SEARCH FOR STANDARD MODEL HIGGS IN TWO PHOTON FINAL STATE AT ATLAS

by

HYEON JIN KIM

Presented to the Faculty of the Graduate School of
The University of Texas at Arlington in Partial Fulfillment
of the Requirements
for the Degree of

DOCTOR OF PHILOSOPHY

THE UNIVERSITY OF TEXAS AT ARLINGTON

August 2010

TO MY FATHER

ACKNOWLEDGEMENTS

I do still remember the overwhelming feeling when I saw the giant ATLAS detector under ground. That feeling held me where I have to be, the unconditional support from my family made me keep focusing on my work, and the help from friends and colleague led me where I am now.

I would like to express my great gratitude to my supervisors, Dr. Jaehoon Yu for his support, valuable advice and trust during all these years. He has been encouraging me to keep doing the work and guided me through the whole years. He always emphasized the importance of having questions and seeking their answers through the collaboration. It makes possible for me to have profound thoughts and expand my vision. I learned not only knowledge but also the attitude as physicist from him.

I would like to thank Dr. Kaushik De for giving me the chance to take part in the assembly of tile calorimeter modules for the ATLAS. I learned the skills of assembling parts of a sub-detector component, gap scintillators with the help with Dr. Jia Li, who passed away on June 25, 2005, and perform its quality test with Rishiraj Pravahan. It was pleasure to work with them. I also thank Ana Henriques and Irene Vichou for their support and help for commissioning of gap scintillators and for its related work.

I want to thank Dr. Alex Weiss, Dr. Andy White, Dr. Kaushik De, and Dr. Zdzislaw Musielak for serving on my defense committee, their valuable suggestions and reviewing my dissertation. I want to thank Giulio Usai, Rishiraj Pravahan,

Heather Brown, and Carlos Medina-Hernandez for taking the time to read my dissertation and correct grammatical and typographical errors.

I appreciate the fruitful discussion and helpful advice on H-matrix study from Dirk Zerwas and Hong Ma. For the work with the analysis of cosmic data and with photon identification efficiency study, I would like to thank Daniel Froidevaux and Guillaume Unal for discussions and suggestions. Also I would like to express my thank to Yaquan Fang. He willingly discussed with me and shared his knowledge with me. I learned from him a lot.

I would like to thank Dr. Mark Sosebee for his kind help, Heuijin Lim, Rajalaksh Sundaramoorthy, for friendly advise and Eric Feng, and Imai Jen-La Plante for being nice friends and their helpful advice. I thank my Korean friends, Jong Duk Lee, Jung Il Lee, Young Shin Park and Byung Do Park who always inspire me with their enthusiasm for studying.

I would like to extend my deepest gratitude to my mother and father. None of this would possible without their incredible support and their faith in me. They allow me to be as ambitious as I wanted. More than all, thanks to unending encouragement from my father while he was alive, I could keep gaining an ability to tackle challenges head on. He would be proud of me if see me where I am now. I also thank my sister, brother and my French family for their trust and love.

Finally I would like to express my appreciation to my husband, Christophe, for his love, patience and for many physics discussions. He provided me strength to complete this work. He was there to cheer me up and is always standing by my side through the good times and bad.

June 25, 2010

ABSTRACT

SEARCH FOR STANDARD MODEL HIGGS IN TWO PHOTON FINAL STATE AT ATLAS

HYEON JIN KIM, Ph.D.

The University of Texas at Arlington, 2010

Supervising Professor: Jaehoon Yu

The Standard Model of particle physics describes very precisely the nuclear strong and weak forces and the electromagnetic interaction, by the exchange of vector bosons. It also describes all matter as composed of quarks and leptons and predicts their interactions. The Higgs boson is the last missing piece of the Standard Model, yet to be observed. The search for the Higgs particle is one of the most important goals of the ATLAS experiment at the Large Hadron Collider (LHC). The ATLAS electromagnetic (EM) calorimeter is a crucial subdetector system of the ATLAS detector in searching for the Higgs boson, in particular its final states that include high p_T photons or electrons. To be able to detect the rare Higgs signals, the EM calorimeter must be not only be able to precisely measure the energy and direction of electrons and photons, but also identify electrons and photons against the overwhelming background from hadronic jets that mimic these particles. The discrimination against these background can be achieved by measuring the detailed shape of the EM showers. The shower shape variables characterizing an EM showers in the calorimeter are

correlated. The covariant matrix technique, or H-matrix method, takes advantage of these correlations for electron and photon identification.

This thesis presents the electron and photon identification algorithms for ATLAS, based on the covariant matrix technique and their performance for single, isolated electrons and photons as well as for photons and electrons from several signal physics processes, along with the rejections against highly electromagnetic jets.

The process $Z \rightarrow \mu\mu\gamma$ is studied as a possible signal in the upcoming ATLAS data to calibrate the photon identification tools. This channel appears promising in terms of statistics given the large integrated luminosity expected at the LHC and could provide a pure sample of photon. This thesis presents the feasibility of the calibration of photon identification using this channel.

Prior to the LHC collisions, high-energy bremsstrahlung photons produced by cosmic ray muons passing through the ATLAS calorimeter provide valuable data that can used to validate the Monte Carlo simulation modeling of the ATLAS detector. The shower shape variables measured in the calorimeter with the cosmic ray data are compared with the prediction from the Monte Carlo simulation.

The Higgs decaying to two photon final state is one of the cleanest discovery channels for the Standard Model Higgs boson in the low mass range $115 < m_H \leq 150$ GeV/c^2. This thesis also presents the prospects for observing $H \rightarrow \gamma\gamma$ and the significance of this signal, when using photon identification algorithm based on covariant matrix.

TABLE OF CONTENTS

LIST OF FIGURES

LIST OF TABLES

CHAPTER 1

INTRODUCTION

The Standard Model of particle physics provides a remarkably successful description of the electroweak interactions up to the energy scales explored to data. It was extensively tested by recent experiments and no appreciable deviations from theoretical predictions have been observed yet. However, the theory is still far from being definitive and the last missing brick of the Standard Model Theory still need to be understood. There is not yet an experimental evidence of the Higgs boson which is responsible of the electroweak symmetry breaking and the fermion mass hierarchy. Moreover other aspects of the theory, as the quadratic dependance on the cutoff parameter of the radiative corrections to the Higgs mass, seem to tell us that still the Standard Model is a low energy effective theory. Therefore more general theories as supersymmetric extensions of the Standard Model (SUSY) or theories based on extra-dimensions, have been formulated as the alternative frameworks.

The Large Hadron Collider (LHC) is planned to test the Standard Model with higher luminosity than Tevatron. By providing proton collisions at a center of mass energy of 14 TeV with an expected luminosity as high as 10^{34} cm^{-2} s^{-1}, LHC will allow the search for the Higgs boson in a wide mass range, from the lower experimental exclusion limit of 114.4 GeV/c^2 [1] up to the theoretical limit of 1 TeV/c^2 [2, 3, 4].

ATLAS is one of the two multipurpose experiments of the LHC. Its main goals are the discovery of the Higgs boson, precision measurements of the electroweak parameters and the search for new phenomena beyond the Standard Model. This

thesis describes the work dedicated to the search of the Higgs boson at the ATLAS experiment.

The second chapter provides the current status of the knowledge about fundamental interactions and constituents. The Higgs mechanism and the Higgs search at LHC are also presented.

The third chapter provides a general overview of the experimental apparatus. The LHC accelerator complex as well as the ATLAS detector and its sub-detectors are described in some detail. The electromagnetic calorimeter which is the main tool in one of the most challenging Higgs discovery channels is described in detail in the chapter.

Chapter 4 provides the information about the reconstructed objects used in the analysis and simulation algorithm.

The covariant matrix based identification method for electrons and photons are described in the fifth chapter. The chapter also provides their performance in some physic process using Monte Calo samples.

Chapter 6 presents the method to measure photon efficiency in data. There are no physics processes to identify photons like $Z \to ee$ for electron. Since the LHC provides high luminosity and center of mass energy, the process $Z \to \mu\mu\gamma$ will be possible. The sufficient statistics of $Z \to \mu\mu\gamma$ events are expected to provide pure photon samples. This chapter shows measurement of photon efficiency in $Z \to \mu\mu\gamma$. Systematic uncertainties on photon efficiency are estimated so that it will be defined what systematic uncertainties can be reduced with larger data sets.

Chapter 7 describes cosmic-ray study to validate shower shape variables used for photon identification. The comparison of shower shape variables of data and of simulation is described. Since the photons in the cosmic data have the different

origin with photon in collision data, they shows different shower profiles. The change of shower shape is presented by photon emission point in the chapter.

Chapter 8 contains the search sensitivity for Higgs decaying in two photons final state mode. The results are discussed in terms of the signal significance for an integrated luminosity of 100 fb^{-1}. Various Higgs messes (115 - 140 GeV/c^2) are considered.

Finally, the last chapter concludes this thesis.

My personal contributions to the ATLAS Collaboration activities in the past 5 years of my PhD program are described in chapter 5, 6, 7 and 8.

CHAPTER 2

THE STANDARD MODEL AND HIGGS BOSON

2.1 Standard Model of Particle Physics

The Standard Model [5, 6, 7] of particle physics provides the best description of elementary particles and their interaction. The elementary particles called *fermions* made up all matter. The interactions between elementary particles (for more details in [8, 9]) are the electromagnetic, the strong and the weak interactions which are mediated by particles called *gauge bosons*. Gravity is not incorporated in the Standard Model due to the technical problem with quantum gravity (more details found in Ref. [10, 11]). The theory called Quantum Electrodynamics (QED) [12] describes electromagnetic interactions and Quantum Chromodynamics (QCD) [13, 14] describes strong interaction. Weak and electromagnetic interactions are unified into an electroweak theory [7, 15], as described later in this chapter.

The Standard Model provides the theoretical framework to calculate physical measurable quantities, explains observed phenomena, and make predictions that can be checked experimentally. The Standard Model of particle physics is a Quantum Field Theory (QFT) based on the principle of local gauge invariance and the electroweak symmetry breaking by the Higgs mechanism.

In this chapter, the different aspects of Standard Model are briefly reviewed and the Higgs mechanism as a model for the spontaneous symmetry breaking is discussed.

2.1.1 Matter Particles and Their Interaction

The knowledge of the fundamental building blocks of matter and their interactions is described by the Standard Model. In the Standard Model, all matter particles, fermions, have half-integer spin. There are 12 elementary fermions which are separated into *leptons* and *quarks* and which obey Pauli exclusion principle[1] and Fermi-Dirac statistics. The fermions have associated antimatter particles, such as the antileptons and antiquarks. The antimatter particles have exactly the same properties but opposite electric charge to that of matter particles. The quarks and leptons are listed in Tab. 2.1 with some of their properties.

Leptons and quarks are grouped into three generations (see Fig. 2.1). The first generation is the electronic leptons (e^- and ν_e), up and down quarks; the second is the muonic leptons (μ^- and ν_μ), charm and strange quarks; and the third is the tauonic leptons (τ^- and ν_τ), top and bottom quarks. Leptons are subject to the electromagnetic force, the gravitational force, and weak interaction, but leptons are not subject to the strong interaction unlike quarks. The strong force is called *color interaction* which is associated with color charge analog to charge in electromagnetic force.

Quarks do not exist as free particles because the color force do not drop off with distance and large amount of energy is required to separate them. There are composite particles called *hadrons* made of quarks. Hadrons must be *colorless* by a phenomenon called color confinement. There are two most common ways to have zero total color charge: three quarks with different colors or a quark with one color and a antiquark with opposite color. The former are called baryons and the latter

[1]There is no two identical fermions that can simultaneously occupy the same quantum state. This is in contrast to bosons with integer spin.

are called mesons. For example, protons (uud) and neutrons (udd) are well known baryons and pions ($\pi^{\pm}$, π^{0}) and J/Ψ are mesons.

Table 2.1. The fundamental particles of the Standard Model and some of their properties. Masses from Ref. [16]. For every particle there is a corresponding antiparticle.

Symbol	**Name**	**Electric charge**	**Spin**	**Mass (GeV/c^2)**
		Leptons		
e	electron	-1	$1/2$	0.511×10^{-3}
ν_e	electron neutrino	0	$1/2$	$< 3 \times 10^{-9}$
μ	muon	-1	$1/2$	0.106
ν_μ	muon neutrino	0	$1/2$	$< 0.2 \times 10^{-3}$
τ	tau	-1	$1/2$	1.78
ν_τ	tau neutrino	0	$1/2$	< 0.02
		Quarks		
u	up	$+2/3$	$1/2$	$0.0015 - 0.003$
d	down	$-1/3$	$1/2$	$0.004 - 0.006$
c	charm	$+2/3$	$1/2$	$1.16 - 1.34$
s	strange	$-1/3$	$1/2$	$0.07 - 0.13$
t	top	$+2/3$	$1/2$	171
b	bottom	$-1/3$	$1/2$	$4.0 - 4.4$

The interactions are mediated by a type of fundamental particle known as *carrier particle*. The carrier particles have integer spin and subject to Bose-Einstein statistics. Th electromagnetic force mediated by the photon and the gravitational force mediated by the hypothetical graviton vary as the inverse square of the distance. But strong and weak forces are short range interactions. The strong force has the gluon as carrier which binds quarks into partons and other hadrons. The carrier particles of the weak nuclear force are W and Z bosons. W bosons can be positive (W^+) or negative (W^-), each being the antiparticle of the other. A Z particle is electrically neutral, and is its own antiparticle. The three interactions described by the Standard Model are summarized in Tab. 2.2. The effective range of electromagnetic

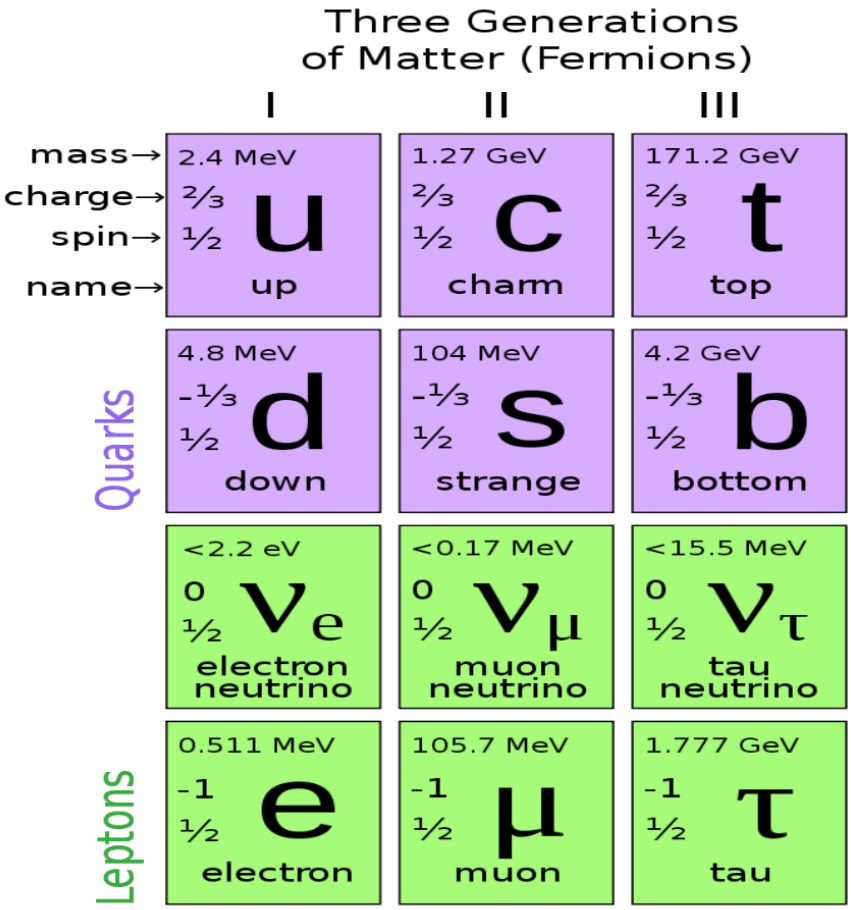

Figure 2.1. The fundamental matter particles (fermions) of the Standard Model grouped into three generations. The main difference between the generations is the masses of their particles.

force is infinite whereas the range of the strong force is limited to the size of a hadron. The range of the weak force is about the size of an atom.

2.1.2 Local Gauge Invariance

In particle physics, the fundamental particle interactions is described by *gauge theory* in which the phase of wave function describing a system is invariant under a continuous group of local transformations (gauge transformations). These inter-

Table 2.2. The particle interactions described by the Standard Model with their carrier particle, electric charge, and mass. The relative strength and effective range of forces are also shown [8, 16].

Interaction	**Bosons**	**Electric charge**	**Mass (GeV/c^2)**	**Effective range (m)**	**Relative strength**
Electromagnetic	photon	0	0	∞	10^{-2}
Weak	$W^{\pm}$	± 1	80.398 ± 0.025	10^{-12}	10^{-12}
	Z	0	91.1876 ± 0.0021		
Strong	gluon	0	0	10^{-15}	1

actions can be described as a combination of three unitary gauge groups, denoted as SU(3) $\otimes$ SU(2) $\otimes$ U(1) [13]. The group of U(1) corresponds to electromagnetic interactions. Similarly, SU(2) and SU(3) describe the weak and strong interactions. SU(2) $\otimes$ U(1) represents the unified weak and electromagnetic interaction.

To ensure that the Lagrangian[2] of a free particle is invariant under a local group transformation, it is necessary to introduce a gauge field. The equations of motion describing the time evolution of a free massless charged fermion are derived from the free lepton Lagrangian[3]

$$\mathcal{L} = i\bar{\Psi}\gamma^{\mu}\partial_{\mu} - m\bar{\Psi}\Psi \tag{2.1}$$

where $\Psi = \Psi(x)$ and $\bar{\Psi} = \Psi(x)\gamma^0$ are complex spinors describing the state of fermions. Since observables depend only on the $|\Psi|^2$, a U(1) local gauge transformation

$$\Psi \rightarrow \Psi' = e^{i\chi(x)}\Psi \tag{2.2}$$

[2]The Lagrangian describes the state of motion of a dynamical system. In the classical mechanics, it is defined as kinetic energy (T) minus the potential energy (V): L = T - V. In field theory, Lagrangian (technically, a *Lagrangian density*) L is a function of the fields ϕ and their position (x, y, z) and time (t) derivatives: $\partial_{\mu}\phi\partial\phi_i/\partial x^{\mu}$

[3]In this chapter, equations are written using "natural" units, where $\hbar = c = 1$.

where $\chi(x)$ is an arbitrary phase which may depend on space and time coordinates, must leave the observables unchanged. If one successively inserts Ψ and Ψ' into Eq. 2.1.

$$\mathcal{L} \rightarrow \mathcal{L}' = \mathcal{L} - \bar{\Psi}\gamma^{\mu}\partial_{\mu}\chi(x)\Psi \tag{2.3}$$

The Lagrangian is clearly not invariant under the transformation of equation 2.2. To maintain the invariance of the Lagrangian a real gauge field, A_{μ}, is introduced whose transformation exactly cancels out the extra term in Eq. 2.3:

$$A_{\mu} \rightarrow A'_{\mu} = A_{\mu} - \frac{1}{e}\partial_{\mu}\chi(x) \tag{2.4}$$

Thus the requirement that Lagrangian is invariant when the charged particle wave function undergoes an arbitrary phase change leads to a suitable change in the photon field. In this case, the invariance leads to the conservation of electric charge and currents.

The new Lagrangian can be written as:

$$\mathcal{L}_{QED} = i\bar{\Psi}(i\gamma^{\mu}\partial_{\mu} - m)\Psi + e\bar{\Psi}\gamma^{\mu}A_{\mu}\Psi - \frac{1}{4}F_{\mu\nu}F^{\mu\nu} \tag{2.5}$$

The first term is the original electron field. The second one is the interaction term between the vector field A_{μ} and the electromagnetic current $e\bar{\Psi}\gamma^{\mu}\Psi$. The new field A_{μ} is thus the photon field and the interaction term appearing in the Lagrangian due to the local gauge invariance describes the electromagnetic interactions mediated through photons. The last term is the kinetic term for the photon for formulated by gauge invariance tensor $F_{\mu\nu} = \partial_{\mu}A_{\nu} - \partial_{\nu}A_{\mu}$.

In an analogous way, one can extend the idea above but replace U(1) transformation on an electron field by SU(3) transformations on a quark color field. The gauge invariant Largrangian is:

$$\mathcal{L}_{QCD} = \bar{q}(i\gamma^{\mu}\partial_{\mu} - m)q - g_s(\bar{q}\gamma^{\mu}T_a q)G^a_{\mu} - \frac{1}{4}G^a_{\mu\nu}G^{\mu\nu}_a \tag{2.6}$$

where $G^a_{\mu\nu} = \partial_{\mu}G^a_{\nu} - \partial_{\nu}G^a_{\mu} - g_s f_{abc}G^b_{\mu}G^c_{\nu}$ as counterpart of $F_{\mu\nu}$. It appears that both mediators, photon and gluon, are required to be massless since the presence of a mass term for gauge fields breaks the gauge invariance of Lagrangian.

The gauge theories introduced above involve only massless gauge bosons. However, the problem will occur when the gauge symmetry is applied to the weak interaction mediated by the gauge bosons ($W^{\pm}$, Z). The W and Z bosons are experimentally massless and their mass have been measured to be $m_W = 80.398 \pm 0.025$ GeV/c^2 and $m_Z = 91.1875 \pm 0.0021$ GeV/c^2 [17]. Experimental search for a mechanism that would allow the gauge bosons to be massive is high priority of particle physics.

2.2 Electroweak Theory

The electromagnetic and weak interactions are unified into a single theory by the Glashow, Salam and Weinberg (GSW) theory. The unified electromagnetic and weak forces, electroweak (EW) theory is based on broken symmetry group SU(2)$_L$ $\otimes$ U(1)$_Y$. Local gauge invariance under SU(2) transformations requires introduction of three massless spin 1 gauge bosons W^+, W^-, and W^0. The conserved quantity is called *weak isospin*. The SU(2) symmetry requires to involve only particles with positive helicity (*left-handed* particles) and denoted SU(2)$_L$ and an additional U(1) symmetry was added to include the electromagnetic interaction in the EW theory. The conserved quantity of the combined SU(2) and U(1) is called *weak isospin*. It requires an additional gauge boson B with spin 1. The weak hypercharge (Y) is

related to the third component of the weak isospin (I_3) and to the electric charge (Q) by the formula

$$Q = I_3 + \frac{Y}{2} \tag{2.7}$$

The quarks and leptons can be arranged in multiplets under the $\mathrm{SU}(2)_L \otimes \mathrm{U}(1)_Y$ symmetry and the local symmetry defines the interactions between the fermion field and gauge fields. The $\mathrm{SU}(2)_L \otimes \mathrm{U}(1)_Y$ multiplets and their quantum numbers are given in table 2.3 for the fermions consisting of the neutrino, the leptons and the quarks, and for the gauge bosons.

Table 2.3. Electroweak $\mathrm{SU}(2) \otimes \mathrm{U}(1)$ quantum numbers. The second column shows isospin and its third components (I_3).

particle	**Weak isospin** (I, I_3)	**Weak hypercharge** (Y)	**Electric charge** (Q)
ν_e	$(1/2, +1/2)$	-1	0
e	$(1/2, -1/2)$	-1	-1
ν_μ	$(1/2, +1/2)$	-1	0
μ	$(1/2, -1/2)$	-1	-1
ν_τ	$(1/2, +1/2)$	-1	0
τ	$(1/2, -1/2)$	-1	-1
u	$(1/2, +1/2)$	$1/3$	$2/3$
d	$(1/2, -1/2)$	$1/3$	$-1/3$
c	$(1/2, +1/2)$	$1/3$	$2/3$
s	$(1/2, -1/2)$	$1/3$	$-1/3$
t	$(1/2, +1/2)$	$1/3$	$2/3$
b	$(1/2, -1/2)$	$1/3$	$-1/3$
γ	$(0, 0)$	0	0
$W^\pm$	$(1, \pm 1)$	0	± 1
Z	$(1, 0)$	0	0

The physical particles mediating the weak neutral interactions (Z) and electromagnetic interaction (the photon) can be found as linear combinations of the neutral gauge particles W^0 and B.

$$\begin{aligned} A &= B\cos\theta_W + W^0\sin\theta_W \\ Z &= B\sin\theta_W - W^0\cos\theta_W \end{aligned} \tag{2.8}$$

The mixing of the gauge particles B and W^0 is a consequence of the fact that $\mathrm{SU}(2)_L \otimes \mathrm{U}(1)_Y$ is a broken symmetry. The weak mixing angle θ_W is generally called the Weinberg's angle and its value is not specified in the theory. It can be measured in the $\nu - e$ diffusion, in the EW interference in e^+e^- processes between γ and Z exchange, by studying the width of the Z boson and from the ratio between masses of the $W^\pm$ and of the Z. The measured value of $\sin^2\theta_W$ from the combined analysis of those experiments is 0.23221 ± 0.00052 [18].

To build a gauge invariant EW Lagrangian we start by writing the Lagrangian for a left-handed fermion doublet and right-handed singlet as

$$\mathcal{L}_{EW} = i\bar{\Psi}_L\gamma^\mu\partial_\mu\Psi_L + i\bar{\Psi}_R\gamma^\mu\partial_\mu\Psi_R \tag{2.9}$$

This Lagrangian once rendered gauge invariant will describe the fermion and gauge boson kinetic energies and their mutual couplings. The form of the Lagrangian in Eq. 2.9 changes by the following local gauge transformation $\mathrm{SU}(2)_L$ for left and right-handed particles

$$\begin{aligned} \Psi_L(x) \rightarrow \Psi_L(x)' &= (1 - ig\boldsymbol{\Lambda}(x)\cdot\boldsymbol{\tau}/2)\Psi_L(x) \\ \Psi_R(x) \rightarrow \Psi_R(x)' &= \Psi_R(x) \end{aligned} \tag{2.10}$$

and $\mathrm{U}(1)_Y$ transformations for the left and right-handed particles.

$$\begin{aligned}\Psi_L(x) \rightarrow \Psi_L(x)' &= (1 - i\frac{g'}{2}\lambda(x)Y)\Psi_L(x) \\ \Psi_R(x) \rightarrow \Psi_R(x)' &= (1 - i\frac{g'}{2}\lambda(x)Y)\Psi_R(x)\end{aligned} \tag{2.11}$$

The functions $\mathbf{\Lambda}(x)$ and $\lambda(x)$ are arbitrary functions of space-time and $\boldsymbol{\tau}/2$ (Pauli matrices) and $Y/2$ are the generators of the $\mathrm{SU}(2)_L$ and $\mathrm{U}(1)_Y$ groups, respectively, as described above. To ensure gauge invariance, the new fields $\mathbf{W}_\mu$ and B_μ must transform correctly:

$$\begin{aligned} SU(2)_L \quad & \begin{cases} \mathbf{W}_\mu \rightarrow \mathbf{W'}_\mu = \mathbf{W}_\mu + \partial_\mu \mathbf{\Lambda}(x) + g\mathbf{\Lambda}(x) \times \mathbf{W}_\mu \\ B_\mu \rightarrow B'_\mu = B_\mu \end{cases} \\ U(1)_L \quad & \begin{cases} \mathbf{W}_\mu \rightarrow \mathbf{W'}_\mu = \mathbf{W}_\mu \\ B_\mu \rightarrow B'_\mu = B_\mu + \partial_\mu \lambda(x) \end{cases} \end{aligned} \tag{2.12}$$

To complete the EW Lagrangian an invariant kinetic energy term for the gauge field is also added to the Lagrangian of the form:

$$\begin{aligned} \boldsymbol{W}_\mu &= \partial_\mu \boldsymbol{W}^\nu - \partial_\nu \boldsymbol{W}^\mu - g\boldsymbol{W}_\nu \times \boldsymbol{W}_\nu \\ B_{\mu\nu} &= \partial_\mu B_\nu - \partial_\nu B_\mu \end{aligned} \tag{2.13}$$

The cross product term in $\boldsymbol{W}_\mu$ is the self-couplings of the weak isospin boson, which contains both three and four bosons interaction terms.

Thus the gauge invariant EW Lagrangian is

$$\begin{aligned} \mathcal{L}_{EW} =& \bar{\Psi}_L \gamma^\mu (i\partial_\mu - g\boldsymbol{\tau}/2 \cdot \boldsymbol{W}_\mu - \frac{g'}{2} Y B_\mu)\Psi_L \\ &+ \bar{\Psi}_R \gamma^\mu (i\partial_\mu)\frac{g'}{2} Y B_\mu \Psi_R - \frac{1}{4}\boldsymbol{W}_{\mu\nu} \cdot \boldsymbol{W}^{\mu\nu} - \frac{1}{4} B_{\mu\nu} B^{\mu\nu} \end{aligned} \tag{2.14}$$

It describes the kinetic energies of the fermions and the gauge bosons and the couplings between them. It should be noticed that mass terms cannot be added to this

Lagrangian without destroying the gauge invariance. However, we know that the W and Z bosons are massive!

2.2.1 Electroweak Symmetry Breaking

The symmetry of $SU(2)_L \otimes U(1)_Y$ requires the presence of massless gauge bosons in the EW theory. This conflicts with experimental measurements of $W^{\pm}$ and Z gauge bosons. Their masses are large; $\sim 85 - 90$ times the mass of a proton, and can not be neglected. A solution has been proposed by F. Englert, R. Brout, P. Higgs and independently G. Guralnik, C. R. Hagen, and T. Kibble [19, 20, 21, 22, 23]. They conjectured that the massless gauge bosons of weak interactions acquire their mass through interaction with a scalar field (the Higgs Field), resulting in a single massless gauge boson (the photon) and three massive gauge bosons ($W^{\pm}$ and Z). This is possible because the Higgs field has a potential function which allows degenerate vacuum solutions with a non-zero vacuum expectation value.

Consider the U(1) gauge invariant Lagrangian, $\mathcal{L}$, of a scalar field ϕ given by the following equation

$$\mathcal{L} = \partial^{\mu}\phi^{*}\partial_{\mu}\phi - V(\phi). \tag{2.15}$$

The first term in Eq. 2.15 is the kinetic energy terms while the last is the potential term. $V(\phi)$ is chosen such that it is an even function of the scalar field, i.e., $V(\phi) = V(-\phi)$ so that the Lagrangian is invariant under the parity transformation $\phi \rightarrow -\phi$. The simplest generalization of the Lagrangian in Eq. 2.15 satisfying these requirement is given by

$$\mathcal{L}' = \partial^{\mu}\phi^{*}\partial_{\mu}\phi - (\mu^2|\phi|^2 + \lambda|\phi|^4). \tag{2.16}$$

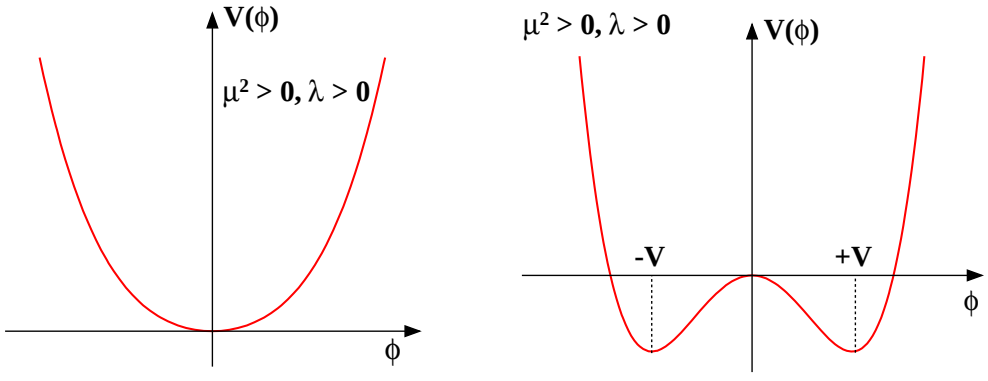

(a) (b)

Figure 2.2. Possible scalar potential $V(\phi) = \frac{1}{2}\mu^2\phi^2 + \frac{1}{4}|\lambda|\phi^4$ for (a) $\mu^2 > 0$, $\lambda > 0$ and (b) $\mu^2 < 0$, $\lambda > 0$ for the given in Eq. 2.16.

The potential is parameterized by λ and μ. Requiring that the vacuum state, lowest energy state is invariant under Lorentz transformations and translations implies that $\phi(x)$ is a constant in this vacuum state. There are two possibilities for the vacuum state depending on the μ^2. If μ^2 is positive, then the minimum of the potential occurs for $\phi = 0$. The shape of the potential $V(\phi)$ for this case is illustrated in Fig. 2.2(a) with the minimum at $\phi = 0$. If instead μ^2 is negative, the minimum energy no longer corresponds to a unique value of ϕ but is degenerate with the minimum as a circle in the complex plane

$$\phi_{\text{min}} = \pm\sqrt{\frac{-\mu^2}{2\lambda}} = \pm v. \tag{2.17}$$

The shape of the potential in this case, shown in Fig 2.2(b), is commonly referred to as a mexican hat or wine bottle potential. Consider the vacuum state $+v$ and defined a new variable $\eta(x) = \phi(x) - v$ to calculate excitations from the ground state. In the transformed coordinates, the Lagrangian may be written as:

$$\mathcal{L}' = \frac{1}{2}\partial_\mu\eta\partial^\mu\eta - |\mu|^2\eta^2 - \frac{|\mu|^2}{v}\eta^3 - \frac{1}{4}\frac{|\mu|^2}{v^2}\eta^4 - \frac{1}{4}|\mu|^2v^2. \tag{2.18}$$

The global U(1) symmetry of the Lagrangian is no longer preserved by this transformation. The vacuum state does not share the symmetry of the Lagrangian and the symmetry is said to be spontaneously broken. The second term in Eq. 2.18 is the mass term of new particle with $m = \sqrt{2|\mu|^2}$. Therefore the first and second term of the equation describes the small oscillation about vacuum state.

2.3 The Higgs Boson

The Higgs particle is hypothetical force-particle proposed to explain how elementary particles acquire mass. The allowed range of Higgs mass by the Standard Model is 114.4 GeV/c^2 $\sim$ 1 TeV/c^2. The Large Hadron Collider is designed for the discovery of Higgs particle and will be able to explore the whole allowed mass range thanks to the high center of mass energy (14 TeV) of the proton-proton collisions, it provides and thanks to its high luminosity (10^{34} cm^{-2}s^{-1}).

In this section, a short introduction to the Higgs mechanism is given and the production and decay channels of a Higgs particle produced at the LHC are discussed at the end of this section.

2.3.1 Higgs Mechanism

As discussed in the previous sections, in order to provide masses to the W and Z bosons, while keeping the photon massless, at least three real scalar fields are required. Simultaneously QED remains an exact symmetry. A single local SU(2) doublet of complex scalar field:

$$\Phi = \begin{pmatrix} \phi^+ \\ \phi^0 \end{pmatrix}, \quad Y_\phi = +1. \tag{2.19}$$

provides four real scalar fields. This doublet has a potential term in the Lagrangian which includes a quartic term in ϕ

$$\mathcal{L}_S = D_{L\nu}\Phi^\dagger D_L^\nu \Phi - V(\phi) = D_{L\nu}\Phi^\dagger D_L^\nu \Phi - \mu^2\Phi^\dagger\Phi - \lambda(\Phi^\dagger\Phi)^2. \tag{2.20}$$

In this formula, $D_{L\mu} = \partial_\mu + i\frac{g_2}{2}\tau_\alpha \cdot W_\mu^\alpha - i\frac{g_1}{2}B_\mu Y$ where $W_\mu^\alpha(x)$ with $\alpha = 1,\ 2,\ 3$ are three gauge fields. The last term of Eq. 2.20 correspond to the potential V with the mass μ and the self coupling parameter λ of the scalar field Φ.

For $\mu^2 > 0$ is required for the potential to be bounded, so that there exists a state of minimum energy. In the case of $\mu^2 < 0$, the potential V has a minimum at $\Psi^\dagger\Psi = -\mu^2/2\lambda$. The scalar field develops an infinite number of ground states. This gives rise to three massless bosons, which can be eliminated through a proper choice of gauge. The fourth boson is the *Higgs boson*, arising from excitation from the ground state. With the expectation value of ground state $v = \sqrt{\mu^2/2\lambda}$ and a physical massive Higgs field $H(x)$, the complex scalar SU(2) doublet Φ may be written as

$$\Phi = \frac{1}{\sqrt{2}}\begin{pmatrix} 0 \\ v + H(x)2 \end{pmatrix} \tag{2.21}$$

After substituting this into Eq. 2.20, new field can be defined by:

$$\begin{aligned} W_\mu^\pm &= \frac{W_\mu^1 \pm iW_\mu^2}{\sqrt{2}}, \\ Z_\mu &= g_1 W_\mu^3 - g_2 B_\mu, \\ A_\mu &= g_2 W_\mu^3 + g_1 B_\mu. \end{aligned} \tag{2.22}$$

The angle $\theta_W = \tan^{-1}(g'/g)$ describes the mixing between the weak boson W_μ^3 and B_μ. It is defined such that the photon field A_μ is massless. The $W^\pm$ and Z bosons acquired masses: the mass of W is given by $M_W = \sqrt{-2\mu^2}$, while the Z mass is

$M_Z = M_W/\cos\theta_W$. The mass of fermions can also be generated by the Higgs boson, if it couples to each of them with a strength proportional to their mass.

The fermion masses are generated by introducing Yukawa coupling between the fermions and the scalar field, Φ in a $\mathrm{SU}(2)_L \otimes \mathrm{U}(1)_Y$ invariant Lagrangian. After the same transformations as for the gauge bosons above one obtains a mass term for every fermion f given by $m_f = \lambda_f v/\sqrt{2}$.

In summary, the masses of fermions and bosons have can be generated by requiring an extra scalar field (Higgs field). By choosing one particular ground state of the Higgs field, the electroweak symmetry is spontaneously broken ($\mathrm{SU}(2)_L \otimes \mathrm{U}(1)_Y \rightarrow \mathrm{U}(1)_Q$) while the $\mathrm{U}(1)_Q$ symmetry is preserved since the photon is massless.

2.3.2 Phenomenology of the Higgs Boson

The theoretical framework presented in the previous section introduces a massive spin 0, the Higgs boson. The Higgs boson has not been observed yet. Therefore it is crucial to prove its existence and the validity of the theory or completely exclude it over the entire allowed mass range. This is one of the main goals of the ATLAS ad CMS experiments at the LHC. Despite prediction of a Higgs boson, the theory does not provide for its mass. The only information available is derived from indirect constraints and direct searches.

The upper limit on the Higgs mass comes from the unitarity requirements for the scattering amplitude of longitudinally polarized W bosons [24]. The processes mediated by the Higgs boson are needed to compensate for the increasing cross-section of the processes including longitudinally polarized W bosons. However, if $m_H > 1$ TeV, the couplings in the W and Z boson sector become so large that the whole concept of the Higgs mechanism as a perturbative expansion around the

vacuum expectation value breaks down. Therefore, the internal consistency of the Standard Model requires an upper limit of $m_H < 1$ TeV.

Tighter theoretical constraints come from one-loop correction to experimentally measure masses and couplings. The masses and couplings in the Standard Model Lagrangian depend on the energy scale [25, 26, 27, 28]. The Higgs boson couples to itself and the quadratic Higgs self-coupling increases with the increasing Higgs mass ($m_H = \sqrt{2\lambda}v$) and become infinite at a certain point. The requirement that the self-coupling remain finite (non zero) at some cutoff energy leads to an upper bound on the Higgs mass known as the *triviality bound*. With this triviality argument and the known top quark mass of 175 GeV, the allowed Higgs mass window would be only 130 - 190 GeV if the Standard Model is required to be valid up to the Planck energy scale ($\Lambda = 10^{19}$ GeV).

The coupling can be small at a certain cutoff scale, at which stage the contribution from the Higgs coupling to the top quark can be dominant and can drive it to a negative value. This leads to a negative scalar potential, which implies an unstable vacuum or a potential energy not bounded from below. In order to have a stable vacuum the Higgs mass must be bounded from below. The lower bound on the Higgs mass with this argument, assuming a cut-off scale to be the EW unification scale ($\Lambda \sim 10^3$ GeV), is $m_H > 70$ GeV. Figure 2.3 shows the upper [29] and lower [30, 31] mass Higgs bounds as a function of cutoff scale, Λ for $m_t = 175$ GeV [29]. These theoretical considerations can favor some mass region for the Higgs boson, but depending on many assumptions, they cannot completely exclude the rest.

In direct constraints on the Higgs mass can be derived from the precision measurements of the parameters of the EW theory in e^+e^- collisions with center of mass energies near the Z-resonance up to 209 GeV at the Stanford Linear Collider (SLC) [] and the Large Electron Positron collider (LEP) [33] at CERN and in pp collisions at

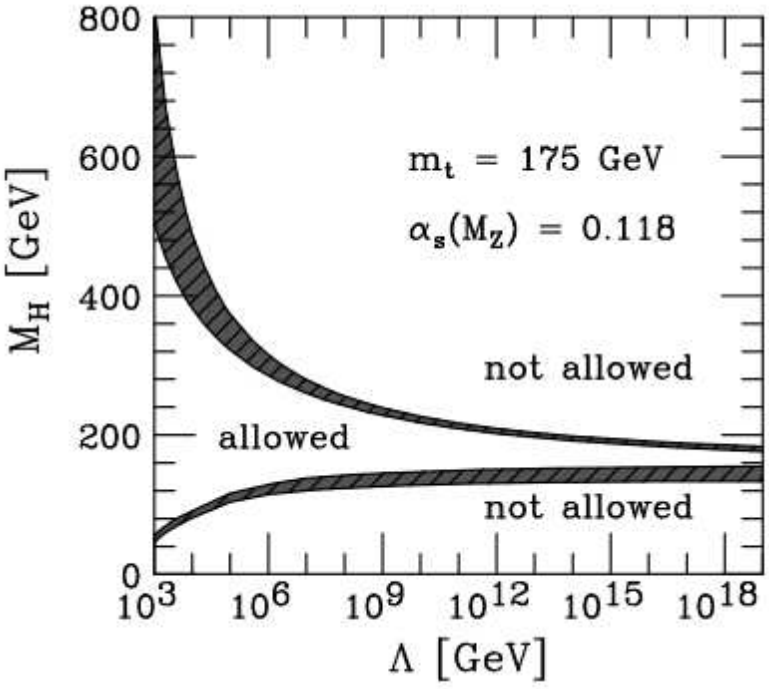

Figure 2.3. Theoretically allowed mass range for the Higgs boson as a function of the validity limit of the Standard Model. The upper solid area presents upper bound in Higgs mass when the mass of top quark is 175 GeV. The lower solid area shows lower bound of Higgs mass from vacuum stability requirements with $m_t = 175$ GeV/c^2 and $\alpha_s = 0.118$ [32].

the Tevatron collider at Fermilab [34]. The measurements of EW observables have reached such a precision that the contributions from EW radiative corrections, including those involving the Higgs boson, can be experimentally introduced. Since these measurements are sensitive to the Higgs mass, m_H, the measurement precision has been sufficient to provide constraints on the Higgs mass [35]. The constraints on the Higgs boson mass are derived from a fit of the Standard Model predictions to the measured observables. Figure 2.4(a) shows the goodness of fit to EW data compared to theory, $\Delta\chi^2 = \chi^2 - \chi^2_{min}$, as a function of the unknown Higgs mass m_H. The yellow band in the figure presents exclusion region from direct search at LEP and Tevatron. The LEP gave a lower limit of $m_H > 114.4$ GeV at 95% confidence level (CL) [1] and

the Tevatron gave the excluded region between 160 GeV to 170 GeV [36]. The blue band indicates the theoretical uncertainty and the solid black line indicates the best $\Delta\chi^2$. These constraints yield a Higgs mass of 87^{+35}_{-26} GeV at 68% CL and < 157 GeV at 95% CL [36].

Higgs boson couples to the heaviest quark, i.e., the top quark and the W boson. For example, the mass of W is sensitive to the mass of the top quark and that of the Higgs boson through higher order loop corrections. The $W^{\pm}$ mass corrections have a logarithmic dependence on the Higgs mass and a quadratic dependence on the top quark mass. This dependence can be used to set experimental constraints on the Higgs mass as shown in Fig. 2.4(b). The red(blue) contour is a 68% CL interval in which the W and top masses are expected to lie from the combined LEP1 and the SLD data (LEP2 and Tevatron data). The green band indicates the functional dependence of W and top masses for a fixed value of Higgs mass. A heavier W mass is measured using the latest Tevatron data which seems to favor (unfavorably to the LEP exclusion limit) a Higgs mass lighter than 114.4 GeV.

2.3.3 Higgs Production and Decay at the LHC

The LHC will open up a broad mass window for new physics searches and allow to find the Higgs boson up to the largest allowed masses. The main production processes for Standard Model Higgs at LHC are :

- Gluon (gg) fusion $gg \rightarrow H$
- Vector boson (W/Z) fusion (VBF) $q\bar{q} \rightarrow W^+W^-, ZZ \rightarrow q\bar{q}H$
- $t\bar{t}$ associated production $q\bar{q}, gg \rightarrow t\bar{t} + H$
- W/Z associated production $q\bar{q} \rightarrow (W,\, Z) \rightarrow (W,\, Z) + H$

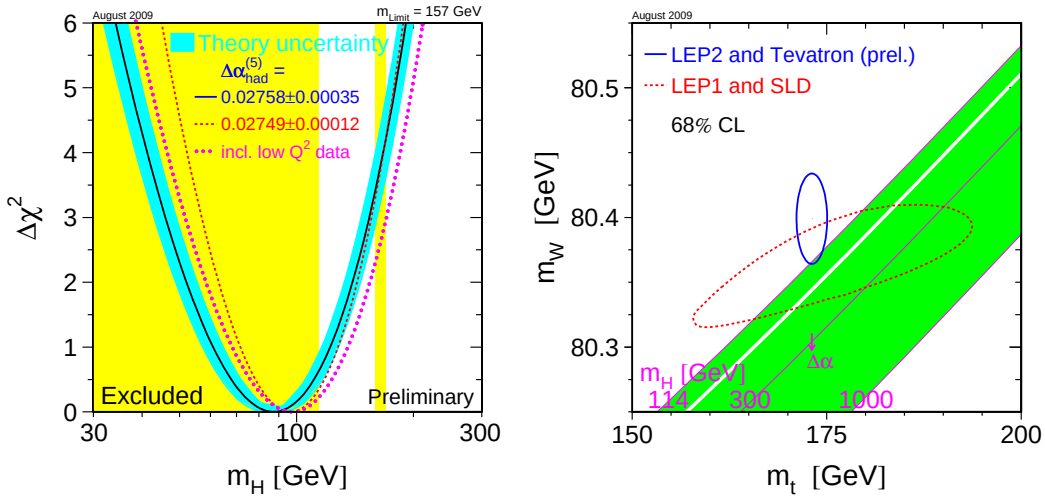

(a) (b)

Figure 2.4. (a) The experimental values of EW precision measurements, $\Delta\chi^2$ ($\equiv \chi^2 - \chi^2_{min}$) curves as a function of the Higgs mass. The band represents an estimate of the theoretical error due to missing higher order corrections. The solid line is the result of the best fit. The vertical band shows the 95% CL exclusion limit on m_H from the direct search. (b) The masses of the top quark and the W boson. The dependence of top quark mass and W boson mass can set constraints on Higgs boson mass. Plots adapted from [17].

The Feynman diagrams for these process are shown in Fig. 2.5 and the cross-sections of the process in Fig. 2.6. The cross-section decrease with increasing Higgs mass. The dominant process is gg fusion as shown in Fig. 2.5 (a), where the Higgs boson is produced from a t or b quark loop over the entire mass range. Its cross section has large higher order QCD corrections and large uncertainties due to the uncertainty of the gluon structure functions. The VBF process (see Fig. 2.5 (b)) has significant contributions from the *next to leading order* (NLO) processes and small QCD correction. It has a cross-section an order of magnitude lower than the gluon fusion for a large fraction of the allowed Higgs mass range. The advantage of this process is the presence of the two spectator jets with high invariant mass in the

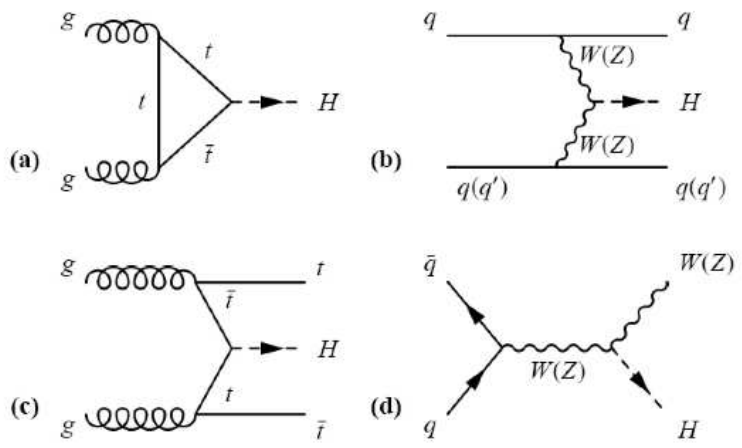

Figure 2.5. Diagrams of the main production processes of the Higgs boson: (a) gluon fusion, (b) Z or W fusion, (c) associated production with $t\bar{t}$ pair and (d) associated production with a Z or W boson.

forward region. The remaining production processes have very small cross sections, orders of magnitude lower than those of gg and VBF. The production with associated production of $t\bar{t}$ or W/Z, as shown in Fig. 2.5 (c) and Fig. 2.5 (d), have very small cross-sections but will be used for the Higgs discovery in association with particular Higgs decay modes which have a clear signature in final states.

Figure 2.7 shows the branching ratios for different Higgs boson decay channels [37, 38] as a function of Higgs mass. The dominant decay mode is through $b\bar{b}$ pairs in the low mass region ($m_H < 140$ GeV/c^2). However, due to the enormous QCD back ground. This channel can only be used in the associated production of Higgs with $t\bar{t}$ pair by requiring in the final state a charged lepton (e, μ). The $\gamma\gamma$ final state, which appears when the Higgs decays via bottom, top and W loops, has a small branching ratio ($\propto 10^{-3}$) but excellent diphoton invariant mass resolution and γ-jet separation make this channel interesting for discovery in the region $m_H < 150$GeV/c^2.

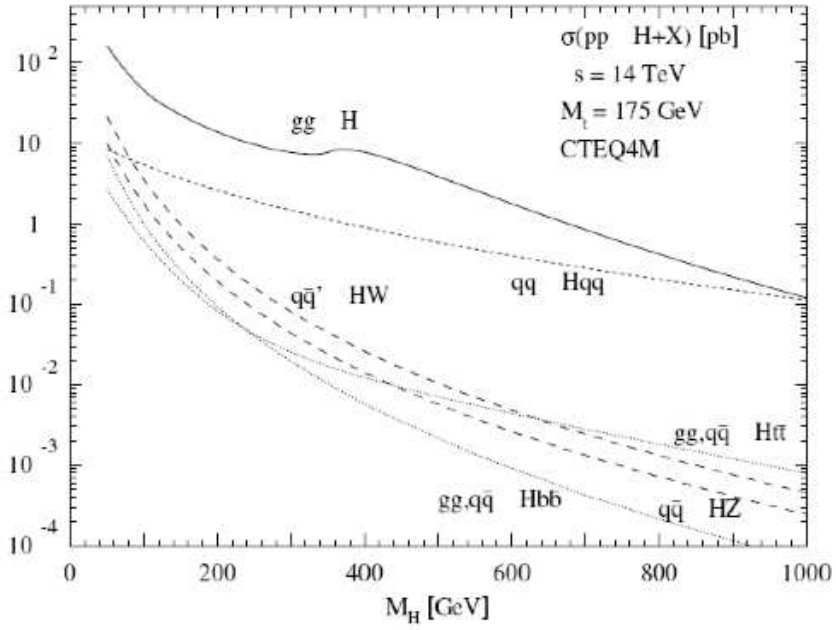

Figure 2.6. Higgs boson production cross-sections at LHC as a function of the Higgs mass.

The $\tau\tau$ decay mode should be visible via VBF production process associated with two high-p_T jets in the forward and opposite regions of the detector.

For larger Higgs masses ($m_H > 2m_W$), the $WW^{(*)}$ and $ZZ^{(*)}$ modes with leptons in their final state are powerful over a large mass range. The clear experimental signature of these channels compensates for their low branching ratio.

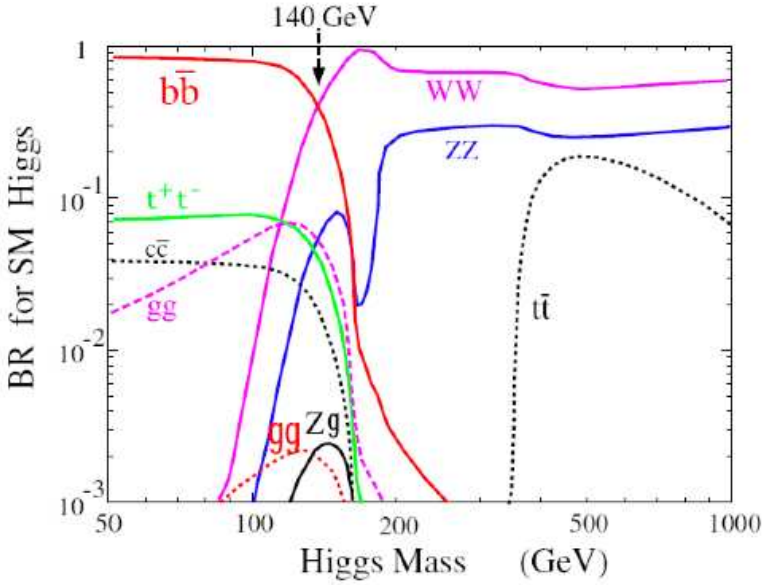

Figure 2.7. Branching ratios of the dominant decay modes of Standard Model Higgs particles.

CHAPTER 3

THE EXPERIMENTAL APPARATUS

The Large Hadron Collider (LHC) [39], a particle accelerator located at CERN near Geneva, Switzerland, was built to study the wide range of Standard Model phenomena and to discover hypothetical new physics at the TeV scale. The LHC is located in the existing LEP (Large electron-positron collider) [33] tunnel with a circumference of 27 km and an internal diameter of 3.7 m in the arcs. This chapter describes an overview of the LHC particle accelerator with a specific focus on the ATLAS (A Toroidal Lhc ApparatuS) [40] detector which is one of four experiments operated at LHC.

3.1 The Large Hadron Collider

The LHC is a proton synchrotron accelerator and proton-proton collider with center of mass energy ($\sqrt{s}$) of 14 TeV. Its purpose is to provide proton-proton collision at $\sqrt{s} = 14$ TeV for the LHC experiment to test predictions made by the Standard Model, including the existence of the Higgs boson and the search for supersymmetry, extra dimensions and other possible of extension of the Standard Model. There are four main experiments operated at the LHC: two with general purpose ATLAS and CMS (Compact Muon Solenoid) [41], and two dedicated detectors ALICE (A Large Ion Collider Experiment) [42] and LHCb (the Large Hadron Collider Beauty experiment) [43] which will study quark-gluon plasma and and B-physics respectively. Figure 3.1 shows the four experimental sites along with the LHC ring. These experiments are described later in more detail.

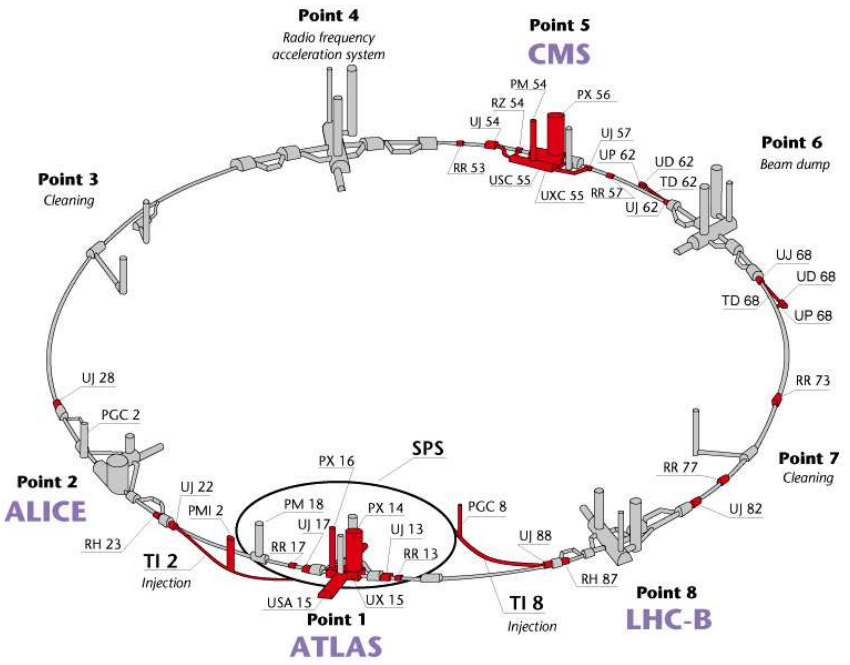

Figure 3.1. Schematic drawing of LHC and SPS accelerators and the four experiments ALICE, ATLAS, CMS and LHCb.

The LHC first beams were successfully circulated on September 10, 2008. On September 19, 2008 the operation was halted due to a serious incident resulting in a large helium leak and damage to several magnets. It took over a year to repair the resulting damages and to install additional safety features. On 20 November 2009 the proton beams were successfully circulated again and 3 days later the first proton-proton collisions at the injection energy of 450 GeV per particle was recorded. On December 18, 2009 the LHC was shut down after its initial commissioning run. This run achieved proton-proton collisions at a center of mass energy of 2.36 TeV, with multiple bunches of protons circulating for several hours and data from over

one million proton-proton collisions. The LHC resumed operations in February 2010, operating at half of the design collision energy for safety reason. On March 30, 2010, LHC set a record for high-energy collisions, by colliding proton beams at a center of mass level of 7 TeV. In 2012, it will be shut down again to deploy additional safety upgrades to reach the full design energy of $\sqrt{s} = 14$ TeV and then it will start up again in 2013.

3.1.1 Design and Operation

The LHC collides proton beams with energies of 7 TeV for each beam and a design luminosity of 10^{34} cm^{-2}s^{-1}. The protons are accelerated in 5 steps using the accelerator chain (see Fig. 3.2). A small linear accelerator (LINAC2) gives the proton beams an initial energy of 50 MeV, then it is boosted to 1.4 GeV by the BOOSTER. The Proton Synchrotron (PS) accelerates the beam up to 26 GeV and the Super Proton Synchrotron (SPS) brings it to 450 GeV sometimes referred to as injection. Finally, the protons from SPS are injected into the LHC ring and are accelerated to 7 TeV. Superconducting magnets generate a field of 8.33 T which keeps the proton beams on the orbits.

The LHC center of mass energy was chosen to be able to produce the Higgs boson over its full allowed mass range. However, due to the small probability of Higgs production the LHC needs to run at high luminosity, $\mathcal{L} = 10^{34}$ cm^{-2}s^{-1}. In one year running at nominal high luminosity the LHC will provide an integrated luminosity of :

$$\mathcal{L} = \int_{10^7 s} L dt \simeq 100 \text{ fb}^{-1} \tag{3.1}$$

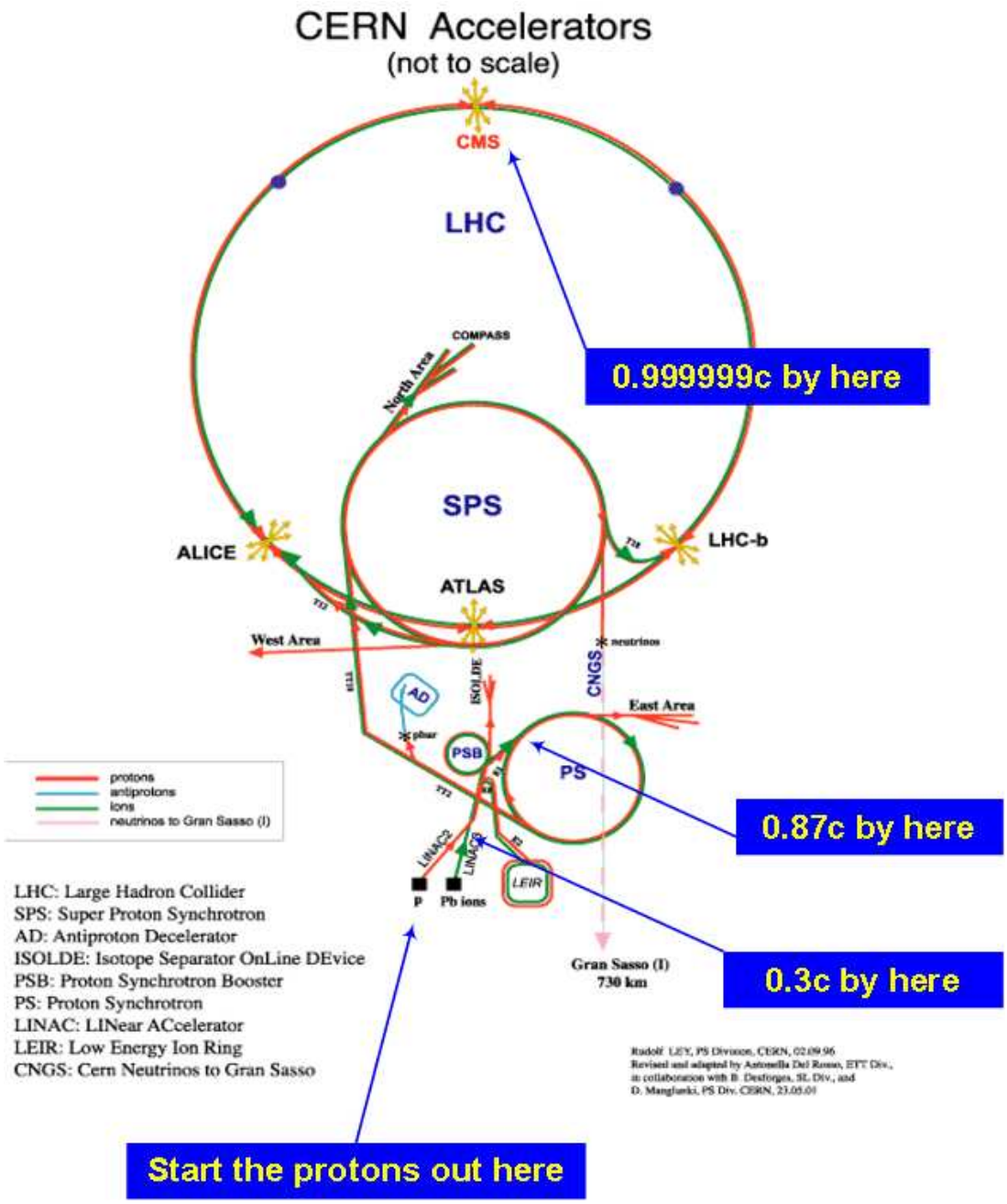

Figure 3.2. The CERN accelerator complex. The proton beams from the SPS are injected into the final LHC ring.

To accomplish such high luminosity the distance between bunches is 7.5 m, corresponding to 25 ns. At high luminosity, the two beams have 2808 bunches each, each bunch containing about 10^{11} protons. The expected event rate R is

$$R = \sigma_{pp}^{tot} \times \mathcal{L} = 80\ mb \times 10^{34}\ \mathrm{cm}^{-2}\mathrm{s}^{-1} \simeq 10^{9}\ \mathrm{s}^{-1} \tag{3.2}$$

where σ_{pp}^{tot} is the total inelastic pp cross-section and its value at a center of mass energy of 14 TeV is about 80 mb. A signal rate of 10^9 Hz corresponds to 22 events occurring per bunch crossing in average. Some parameters of the LHC for pp collisions are given in Tab. 3.1.

Table 3.1. Nominal parameters of the LHC accelerator working with proton beams.

Energy	7 TeV
Energy at injection	0.45 TeV
Number of dipole magnets	1232
Dipole field at 7 TeV	8.33 T
Number of bunches in the ring	2800
Number of particles per bunch	1.1 $\times 10^{11}$
Fraction of filled bunches	0.8
Bunch radius	16 μm
Bunch length	75 mm
Bunch spacing	7.48 m
Bunch separation	25 ns
Bunch crossing frequency	40 MHz
High luminosity	10^{34} $\mathrm{cm}^{-2}\mathrm{s}^{-1}$
Low luminosity	10^{33} $\mathrm{cm}^{-2}\mathrm{s}^{-1}$
Luminosity lifetime	10 h
Energy loss per turn	6.7 KeV

Minimum bias events are the samples that would obtained if all events could be recorded. Such a sample is dominated by low momentum transfer QCD processes. Experiments at the LHC are required fast read-out to prevent measuring

events overlapping from different bunch crossing at the same time because of high rate of interaction. The overlap in time, in the same read out unit is called pileup. It occurs because several minimum bias collisions happen in the same bunch crossing.

3.1.2 Physics Motivation

The primary goal of the LHC experiment is providing the evidence of the existence of Higgs bosons. Beside the Higgs search, the LHC will be also able to study other challenging programs [44] which are summarized in the following list:

- B physics. The study of B hadron final states provides a way to study CP violation. Many B-physics processes are also sensitive to new physics.
- The properties of the top quark. The LHC will produce a very large number of $t\bar{t}$ pairs, allowing to obtain precise measurements of its mass and interactions. For example, a day of running at low luminosity will produce about 10 pb^{-1} of data and thus over 8000 top quarks.
- New physics such as supersymmetry particles, extra dimensions and other signal of physics beyond the Standard Model.
- Improvement of precision measurements of gauge bosons, such as the $W^{\pm}$ bosons,
- Strong interaction. Precision measurements will be carry out the study of the parton structure and the strong coupling constant.

3.1.3 The Experiments at LHC

At the LHC, the two proton beams circulate in opposite directions along two rings and their collision occurs at four interaction points where the experiments are located. The experiments are ATLAS, CMS, ALICE and LHCb which differ in their design depending on their physics goals.

3.1.3.1 ALICE

ALICE as shown in Fig. 3.3(a) is a dedicated heavy-ion collision detector to investigate Pb-Pb collisions and the properties of the quark-gluon plasma (QGP). The goal of ALICE is to study strongly interacting matter at high energy densities where the new phase of matter is expected. The lead ions will be collided with a center of mass energy of 1148 TeV at luminosity of 10^{27} $cm^{-2}s^{-1}$ at the interaction point of ALICE.

The inner tracker of ALICE uses Pixel and Silicon Drift Chambers for vertex reconstruction. The Inner Tracker is surrounded by the main particle tracking device, Time Projection Chamber with a drift volume of 100 m^3. Other sub-detectors of ALICE include a Time of Flight (TOF) measurement system, a Ring Imaging Cerenkov (RICH) detector, a dedicated $PbWO_4$ proton spectrometer (PHOS) and a muon arm. ALICE is designed to deal with the highest particle multiplicities anticipated for Pb-Pb reactions (8000 particles per unit of η).

3.1.3.2 ATLAS

The ATLAS experiment is a general purpose experiment designed for the discovery of new particle predicted by the Standard Model, such as the Higgs boson, and of signatures of physics beyond the Standard Model, such as supersymmetry. With its high-resolution full-solid-angle-coverage detector, ATLAS will provide improved precision measurement of properties of the W bosons and heavy quarks. Figure 3.3(b) shows the layout of the detector. It is described in detail in the next section.

3.1.3.3 CMS

The CMS experiment, shown in Fig. 3.3(c), is a general purpose experiment with a length of 22 m, a diameter of 16 m and weight of approximately 12500 tons. It is built around a high-field solenoid which surrounds the tracker and calorimeters. The CMS tracker uses Silicon Pixel detectors in the regions of high occupancy and Silicon Microstrip detectors where the occupancy is lower. Outside of inner detector a scintillating crystal electromagnetic calorimeter and sampling calorimeter for hadrons are placed. The tracker and the calorimetry are compact enough to fit inside the CMS solenoid which generates a powerful magnetic field of 3.8 T. Outside the magnet are the large muon detectors, which are inside the return yoke of the magnet.

3.1.3.4 LHCb

The LHC-beauty (LHCb) experiment is optimized for the study of B-hadron and CP violation. Since these hadrons are preferentially produced in the direction of the beam, LHCb is designed in the form of a single arm. The detector consists of successively a movable Vertex Locator built near the interaction point, followed by 2 RICH detectors designed for particle identification. Between the two RICH detectors are placed a dipole magnet producing a field of 4 T and a tracker. The electromagnetic calorimeter provide measurement of the energy of electrons, photons, and hadrons. The muon system is located the furthest away from the interaction point. It is composed of Resistive Plate Chambers and Multi-Wire proportional Chambers used to identify and trigger on muons in the events. Figure 3.3(d) shows the layout of LHCb detector.

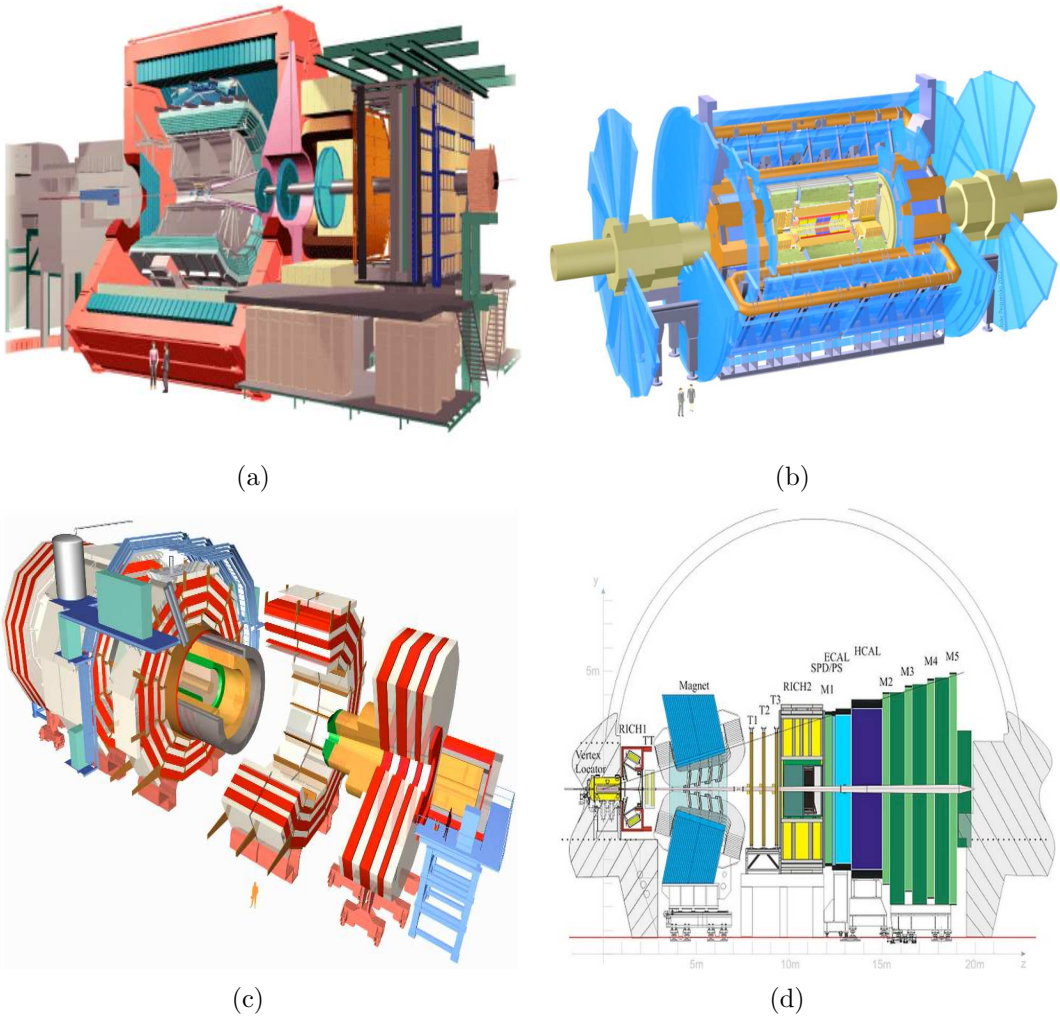

(a) (b)

(c) (d)

Figure 3.3. The four main LHC experiments, (a) ALICE, (b) ATLAS, (c) CMS, and (d) LHCb.

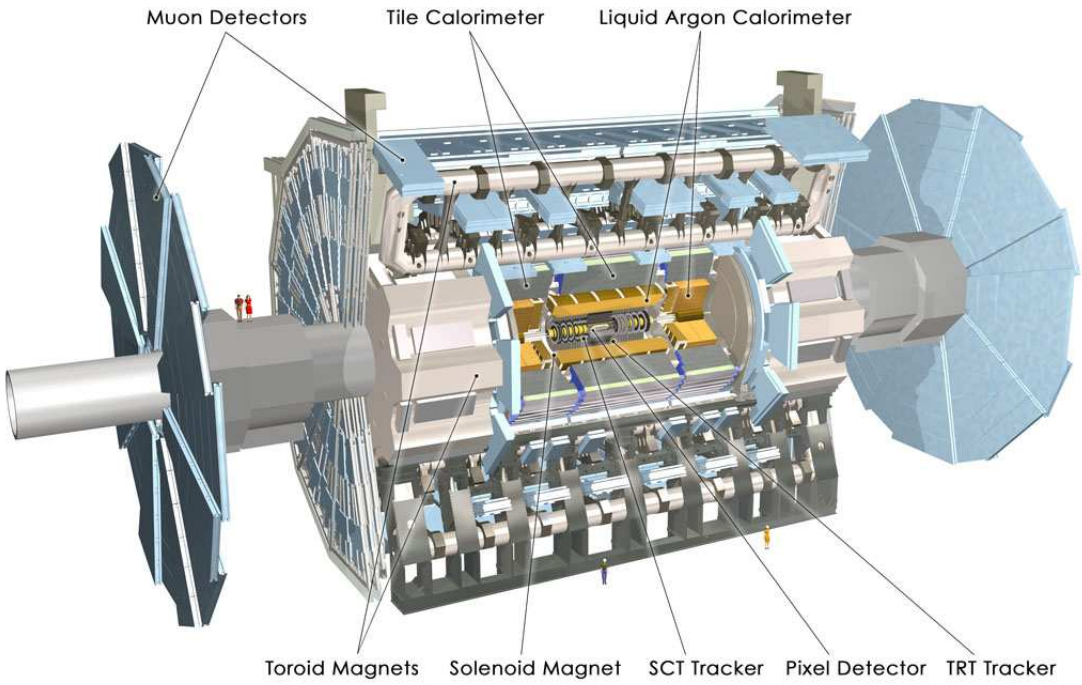

Figure 3.4. View of the ATLAS detector. The sub-detectors are labeled.

3.2 The ATLAS Detector

The ATLAS detector is the largest volume particle detector in the world with a total length of 46 m, a radius of 11 m and a height of 25 m. Its weight reaches about 700 tons. The overall detector layout is shown in Fig. 3.4. The ATLAS detector has a cylindrical shape with sub-detectors arranged coaxially with respect to the beam axis in the barrel region and perpendicularly to the beam axis in the end-cap region. Most of the solid angle around the interaction is covered.

The magnetic system of ATLAS is based on air-core toroid system outside of calorimeter for muon and superconducting solenoid around the inner detector. The inner detector consists with three sub-detectors and measures the momentum of charged particle. The ATLAS calorimetry system uses liquid argon (LAr) [45] sampling calorimetry and scintilling tile calorimetry [46] which measure the energies

of electrons, photons and jets. The muon system is the outermost part of ATLAS and measures and identifies muons.

ATLAS is designed to be able to investigate as much as possible of the new physics at the LHC energy. The bench mark design criteria of ATLAS are defined to allow for Higgs search, study of supersymmetry and search for heavy W and $Z-$like objects. The following criteria on detector structure are needed to match the physics goals [44] and requirements in terms of resolution are given in Tab. 3.2.

- Efficient tracking system for lepton momentum measurement and for particle and charge identifications. Good impact parameter resolution for τ and b-jet tagging.
- Excellent calorimeter system providing precise measurement of electromagnetic showers direction and energy and particle identification allowing for separation between electrons, photons, pions and jets.
- Hadronic calorimeter with accurate jet and missing transverse energy (E_T^{miss}) measurements.
- The muon system with high-precision muon momentum measurements at highest luminosity and momentum.
- Efficient trigger for low-p_T particles with sufficient background rejection.
- Large acceptance in pseudo-rapidity (η) with full azimuthal angle (ϕ).

3.2.1 Reference System and Definitions

ATLAS uses a right-handed reference system with beam direction along the z-axis, the positive x-axis points from the interaction point to the centre of the LHC ring and the positive y-axis points upward. The convenient coordinate system is (R, ϕ, z)

Table 3.2. Required performance of the ATLAS detector.

Detector component	**Required resolution**	**η coverage**
Tracking	$\sigma_{p_T}/p_T = 0.05\%\ p_T \oplus 1\%$	± 2.5
EM calorimeter	$\sigma_E/E = 10\%/\sqrt{E} \oplus 0.7\%$	± 3.2
Hadronic calorimeter		
barrel and end-cap	$\sigma_E/E = 50\%/\sqrt{E} \oplus 3\%$	± 3.2
forward	$\sigma_E/E = 100\%/\sqrt{E} \oplus 10\%$	$3.1 \leq \lvert\eta\rvert \leq 4.9$
Muon spectrometer	$\sigma_{p_T}/p_T = 10\%$ (at $p_T = 1$ TeV)	± 2.7

to measure particle coming from the collision. The description of these variables are the following:

- R is the transverse radius from the beam line, which is defined as $\sqrt{x^2 + y^2}$.
- ϕ is the azimuthal angle and the angle in a plane perpendicular to beam axis. It is measured from the x-axis and its unit is radian.
- The origin of z is at the interaction point. The relation between R and z can be expressed using the polar angle θ.

$$\theta = \arccos \frac{z}{\sqrt{R^2 + z^2}} \tag{3.3}$$

In addition to these, it is useful to define a few other quantities at the hadron collision. Hadrons are composite objects and the original z-momentum of the constituents (or *partons*) interacting in a given collision is unknown. For this reason, it is useful to define the true rapidity of particles, since differences are invariant under longitudinal Lorentz boosts. The definition of the rapidity is

$$y = \frac{1}{2} \ln \left(\frac{E + p_z}{E - p_z}\right) \tag{3.4}$$

This is particularly convenient if the mass of a particle is known; if not, one can refer to the pseudo-rapidity defined as

$$\eta = -\ln\left(\tan\frac{\theta}{2}\right) \tag{3.5}$$

which closely approximates the true rapidity in the relativistic limit for a particle with Lorentz factor $\gamma \gg 1$. Large value of $|\eta|$ correspond to directions close to the beam axis and $\eta = 0$ is a direction in the plane perpendicular to the beam axis. Particles traveling toward higher $|\eta|$ would be described as heading for the *forward* region.

Particles 4-vectors are often described by the parameters (p_T, η, ϕ), where p_T is the transverse momentum with respect to the beam axis. With these notations, the 4-momentum $(\overrightarrow{p}, E)$ can be expressed as following:

$$\begin{pmatrix} \overrightarrow{p} \\ E \end{pmatrix} = E_T \begin{pmatrix} \cos\phi \\ \sin\phi \\ \sinh\eta \\ \cosh\eta \end{pmatrix} \tag{3.6}$$

where E_T is the transverse energy of the particle. The angular distance ΔR between two particles with directions (η_1, ϕ_1) and (η_2, ϕ_2)[1] can be defined.

$$\Delta R = \sqrt{(\eta_1 - \eta_2)^2 + (\phi_1 - \phi_2)^2} = \sqrt{\Delta\eta^2 + \Delta\phi^2} \tag{3.7}$$

3.2.2 Inner Detector

The Inner Detector (ID) is placed in the innermost part of ATLAS as shown in Fig. 3.4. It is designed for precise measurements of a particle's momentum and charge as well as both primary and secondary vertex of charged tracks above given p_T threshold of 0.5 GeV. With a combination of high-precision, high-granularity layers

[1]Throughout this thesis, η and $\Delta\eta$ are in units of pseudo-rapidity and ϕ and $\Delta\phi$ are in units of radian, unless specified otherwise.

in the innermost part and straw tubes in the outer part, tracks of charged particles can be reconstructed in the solenoidal magnetic 2 T within the pseudo-rapidity range $|\eta| < 2.5$.

The main requirements for the ID are:

- The momentum resolution of the inner detector:

$$\sigma_{p_T}/p_T = 0.05\% p_T \oplus 1 \tag{3.8}$$

- Tracking efficiency of 99.9% over full coverage for isolated tracks with $p_T > 5$ GeV and fake-track rate is less than 1%.
- Identification of individual particles in dense jets and of electrons and photons which create similar cluster in the EM calorimeter. Efficiency of photon identification should be greater than 85% with combined ID and EM calorimeter information.
- At least 90% efficiency for reconstructing both primary and secondary electrons.
- Tagging of jets from b-quarks by displaced vertex with efficiency greater than 50% for jet rejection of ~ 1000. The b-jets can be from $t \to Wb$, $H \to b\bar{b}$ decay or decays of supersymmetry particles.
- Decay length reconstruction for CP violation studies in the B-system and for mixing angle of B_s^0

The ATLAS inner detector as shown in Fig. 3.5 is divided into three parts: a pixel detector that provides high granularity near the vertex region, a semiconductor tracker that utilizes silicon micro-strip technology, and a transition radiation tracker that provides continuous track-following with much less material per point. The detector consists of a barrel region and two end-cap regions.

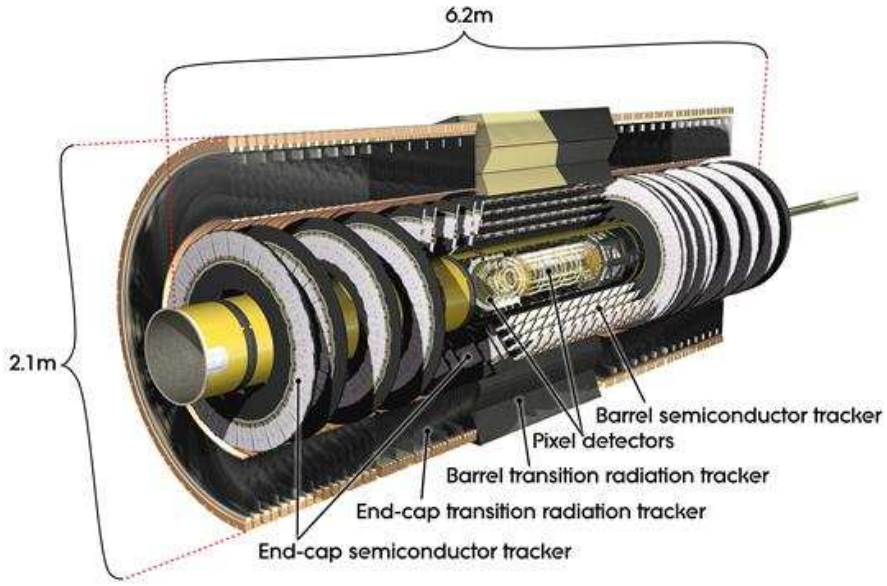

Figure 3.5. Geometrical layout of the ATLAS inner detector.

Pixel Detector

Housed closest to the beam pipe, the pixel detector [47, 48] is built from modules that contain 6,080 pixels of size 50 μm in $R\phi$ and 400 μm in z, providing high-precision measurements with high granularity as close to the interaction point as possible. The system provides three precision points for $\eta = 2.5$, with the possibility to determine the impact parameter and to identify short-lived particles. The pixels are smaller in the $R\phi$ direction in order to improve measurement of particle tracks, thus enhancing the momentum measurement. The pixel detector mostly determines the impact parameter resolution of ATLAS, and the ability of identification of B-hadron decays, of b-tagging in top physics.

This detector consists of three barrel layers, located at radii of 50.5 mm (B-layer), 88.5 mm (the first layer) and 122.5 mm (the second layer), and six disk layers (three on each end-cap). The *B-layer* is designed to be replaced every few years as a result of the received radiation dose being roughly four times higher than that

received by the first layer. The intrinsic resolution of the pixel detector is 10 μm in $R\phi$ and 115 μm in z.

Semiconductor Tracker

The Semiconductor Tracker (SCT) uses silicon microstrip technology for tracking charged particles. It provides eight precision measurements per track, contributing to the measurement of momentum, impact parameters and vertex position. It provides good pattern recognition owing to its high granularity. The SCT consists of four double layers of silicon strips in the barrel and nine disks on each end-cap side. The resolution of the SCT is 17 μm in $R\phi$ and 580 μm in z which can resolve two parallel tracks separated by 200 μm. The layers in the barrel are located at radii 30 cm, 37 cm, 44 cm. One set of strips in each layer is parallel to the beam axis and the other set is off by a 40 mrad angle in order to measure both coordinates. Each disk in the end-cap has one set of strips arranged radially and the other at a 40 mrad angle similar to the barrel layers. The inner radius of the disks is 27 cm and the outer radius is 56 cm.

Transition Radiation Tracker

The Transition Radiation Tracker (TRT) is a drift tube system consisting of *straw* detectors. The TRT has about 370,000 straws with a diameter of 4 mm, which are located along the beam axis in the barrel region and radially in the end-cap to maximize the number of straws passed in all directions pointing away from interaction point. The straws are filled with a xenon gas mixture in order to detect transition-radiation photons created in a radiator between the straws. The number of these photons is proportion to the Lorentz factor, $\gamma = E/m$ where E is the energy and m is the mass of the charge particle. At a given energy, lighter particles like electrons with higher value of γ factor can be distinguished from heavier particles such as

hadrons with lower value of γ factor. Therefore, TRT can provide additional discrimination between electrons and hadrons. The electron identification capabilities are implemented by using a high threshold to detect the enhanced signal for electrons in addition to a low threshold ($p_T > 0.5$ GeV) for identifying standard hits for tracking.

The TRT covers the pseudo-rapidity range of $|\eta| < 0.7$ in the barrel region and $|\eta| < 2.0$ in the end-cap region.

3.2.3 Calorimetry

The ATLAS calorimetry (see Fig. 3.6) is placed outside the central solenoid that surrounds the inner detector, and it precisely measures energy of both charged and neutral particles interacting electromagnetically or strongly. High energy particles entering a calorimeter produce a cascade of secondary particles known as a *shower*. The incoming particle interacts via either the electromagnetic or strong interaction to produce new particles of lower energy which react in a similar fashion, producing a very large number of secondary particles whose energy is absorbed and measured. Calorimeters also provide the measurement of particle direction and the missing transverse momentum per event, particle identification and event selections at the trigger level.

There are two calorimeters in ATLAS, electromagnetic calorimeter and hadronic calorimeter, due to the different interaction behavior between matter and electrons/photons or hadrons. The ATLAS calorimetry system covers the pseudo-rapidity region $|\eta| \leq 4.9$. ATLAS uses liquid argon (LAr) sampling calorimetry [45] and scintillating tile calorimetry [46] technologies. A brief discussion of sampling calorimetry and detailed description of interaction of particles with matter is discussed in section 3.3.3. LAr is used as active medium in the calorimeters close to the beam axis

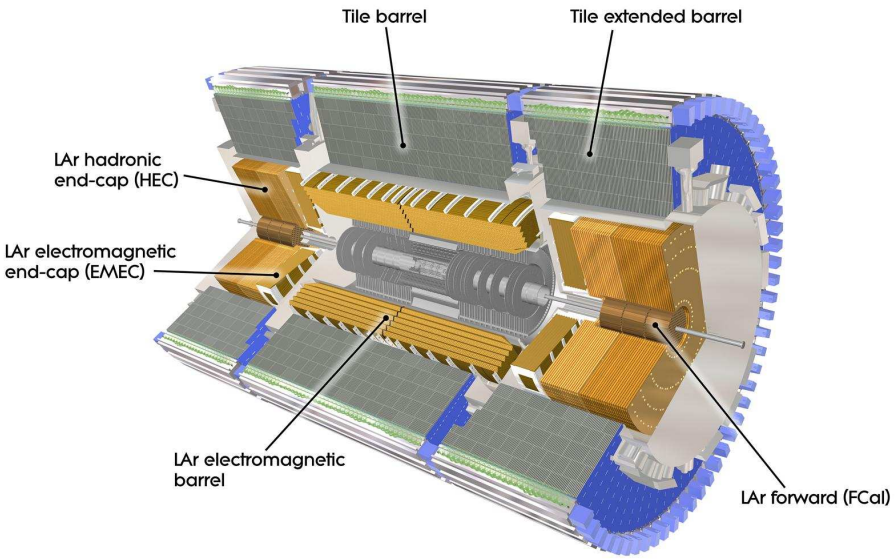

Figure 3.6. Geometrical layout of the ATLAS calorimeter system.

because it has good energy and spatial resolution while it is radiation hard and easy to calibrate.

3.2.3.1 Electromagnetic Calorimeter

The Electromagnetic (EM) Calorimeter is dedicated to the measurement of electron and photon showers. It consists of three layers of *liquid argon accordion calorimeter* and a *presampler*. The EM calorimeter is divided into two identical half-barrels at $|\eta| \leq 1.475$ located between $R = 150$ cm and $R = 197$ cm and two end-cap wheels with an outer radius of 208 cm, covering the range $1.375 \leq |\eta| \leq 3.2$. Given the amount of material upstream of the calorimeter which deteriorates the energy measurements it is necessary to sample showers before the calorimeter. This is done by a presampler placed in front of the calorimeter. The calorimeter design and description are detailed in section 3.3.3.

3.2.3.2 Hadronic Calorimeter

The ATLAS hadronic calorimeters [46] placed behind the EM calorimeters cover the pseudo-rapidity range $|\eta| < 4.9$. Three different technologies are used to meet physics requirements and to tolerate the different radiation levels. The region $|\eta| < 1.7$ is covered by the Tile calorimeter while at larger pseudo-rapidities where radiation tolerance is crucial, the intrinsically radiation hard LAr technology is used in both the Hadronic End-Cap calorimeter (HEC) and the forward calorimeter (FCAL).

The hadronic calorimeters are designed to identify and measure the energy and direction of jets. The required jet-energy resolution depends on the pseudo-rapidity region and is given by the following:

$$\frac{\sigma_E}{E} = \begin{cases} \frac{50\%}{\sqrt{E}} \oplus 3\%, & |\eta| < 3 \\ \frac{50\%}{\sqrt{E}} \oplus 10\%, & 3 < |\eta| < 4.9 \end{cases} \tag{3.9}$$

The hadronic calorimeter must be thick enough to provide good containment for hadronic showers and to keep punch-through into the muon system to a minimum. A thickness of about 10 λ (interaction lengths) provides good resolution for high energy jets. Together with the large pseudo-rapidity coverage, this will also guarantee a good E_T^{miss} measurement which is important for supersymmetry particle searches.

Hadronic Tile Calorimeter

The Tile calorimeter is a sampling calorimeter that uses plastic scintillating tiles as active material and steel plates as absorbers. The scintillating tiles are oriented radially and perpendicular to the beam axis so that an almost seamless azimuthal coverage is possible.

The Tile calorimeter is segmented into one barrel and two extended barrels each consisting of 64 independent azimuthal modules divided in cells and towers.

The barrel tile calorimeter has a length of 5.8 m and two extended barrels have a length of 2.6 m and both have an inner radius of 2.28 m and an outer radius of 4.25 m. The covering range of pseudo-rapidities are $|\eta| < 1.0$ in barrel and $0.8 < |\eta| < 1.7$ in extended barrels. The radial depth of the Tile calorimeter is 7.4 λ which achieve a depth of 9.7 λ of active material in the barrel region together with the EM calorimeter. It is enough to achieve the required resolution for high energy jets.

The Tile calorimeter is required to identify and measure both energy and direction of jets with a relative energy resolution as shown in Tab 3.2 in addition to providing a good measurement of E_T^{miss}.

Hadronic End-cap Calorimeters

The Hadronic End-cap Calorimeter (HEC) is a sampling calorimeter with copper-plate absorbers and LAr as active material. It is designed to provide coverage for hadronic showers in the range $1.5 < |\eta| < 3.2$. The HEC is placed behind the EM end-cap calorimeter and consists of 32 modules in two independent wheels of outer radius of 2.03 m. Each module of the front wheel is made of 24 copper plates with a thickness of 25 mm, while each module of the rear wheel is made of 16 copper plates with a thickness of 50 mm each. The HEC uses parallel plate geometry chosen for the simplicity of its design. The gaps between copper plates are instrumented with a read out structure designed to optimize signal to noise ratio while reducing high-voltage requirements.

Hadronic Forward Calorimeters

The Hadronic Forward Calorimeters (FCAL) is a sampling calorimeter with LAr as active material. The FCAL is segmented into three layers in depth, the first uses copper and the other two uses tungsten as absorber. The first layer is designed for electromagnetic measurements and the others for the measurement of hadronic

interaction. The active gaps are much thinner than with the other LAr calorimeters because of the high counting rate associated with its position. The FCAL covers the very forward region $3.2 < |\eta| < 4.9$ and is located in the inner bore of the hadronic end-cap calorimeter and around the beam pipe. Due to its location, the FCAL is designed to sustain high levels of radiation.

A summary of design parameters for the hadronic calorimeters is provided in table 3.3.

Table 3.3. Design parameters of the hadronic Calorimeters [44]

Hadronic Tile	**Barrel**	**Extended Barrel**
Coverage	$\eta < 1.0$	$0.8 < \|\eta\| < 1.7$
Longitudinal segmentation	3 samplings	3 samplings
Granularity ($\Delta\eta \times \Delta\phi$)		
Sampling 1 and 2	0.1×0.1	0.1×0.1
Sampling 3	$0.2 \times x0.1$	0.2×0.1
Hadronic LAr		**End-cap**
Coverage		$1.5 < \|\eta\| < 3.2$
Longitudinal segmentation		4 samplings
Granularity ($\Delta\eta \times \Delta\phi$)		0.1×0.1 for $1.5 < \|\eta\| < 2.5$
		0.2×0.2 for $2.5 < \|\eta\| < 3.2$
Forward Calorimeter		**Forward**
Coverage		$3.18 < \|\eta\| < 4.9$
Longitudinal segmentation		3 samplings
Granularity ($\Delta\eta \times \Delta\phi$)		$\approx 0.2 \times 0.2$

3.2.4 Muon Spectrometer

The ATLAS muon spectrometer [49] is a drift tube tracker covering pseudo-rapidity range $|\eta| \leq 2.7$. It is based on the magnetic deflection of muon tracks in large superconducting air-core toroid magnet. The muon spectrometer is designed to

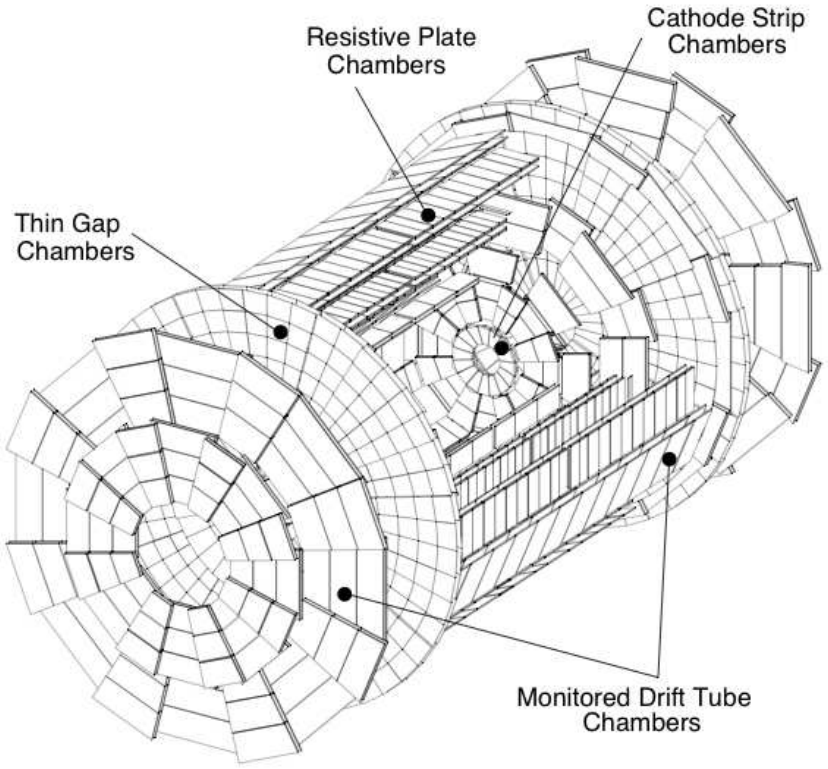

Figure 3.7. View of the ATLAS muon spectrometer.

trigger on high energy muons and to measure the momentum of high energy muons that are not measured well by the inner detector. The momentum measurement of muons are performed by monitored drift tubes (MDT's) over most of the η-range, and using cathode strip chambers (CSC's) at large η-range and at close to the interaction point. Triggering is done using resistive plate chambers (RPC's) in the barrel and thin gap chambers (TGC's) in the end-caps. The trigger system covers the pseudo-rapidity range $\eta \leq 2.4$. The layout of the muon spectrometer, showing the position of the various sub-detectors, is shown in Fig. 3.7. The main parameters of the muon spectrometer are listed in Tab. 3.4.

The precision tracking chambers consists of the MDT and the CSC. The magnetic field is in the ϕ direction over most of the muon detector, and thus muons bend

Table 3.4. Deign parameters for the muon spectrometer.

Muon chambers	**η coverage**	**Function**
Monitored drift tubes	$\|\eta\| < 2.7$ (2.0 for innermost layer)	Precision tracking
Cathode strip chambers	$2.0 < \|\eta\| < 2.7$	Precision tracking
Resistive plate chambers	$\|\eta\| < 1.05$	Triggering, second coordinate
Thin gap chambers	$1.05 < \|\eta\| < 2.7$ (2.4 for trigger)	Triggering, second coordinate

in the R-z plane. The precision measurement provided by the MDT and CSC occurs in this plane.

The MDT's are drift tube chamber of 30 mm diameter and with a 400 μm wall thickness, with a 50 μm diameter central W-Re (tungsten-rhenium) wire. The drift time of the MDTs is 700 ns. The resolution of single wire is 80 μm. The MDT performs precision coordinate measurement in the bending direction of the air-core toroidal magnet and therefore provide the muon momentum measurement. The background hit rates are the highest at the four layers of the MDT.

The CSC's with the higher granularity are used to cope with the demanding rates and backgrounds of higher η. Its position resolution is better than 60 μm. The relative positioning of chambers matches the intrinsic resolution of the precision chambers to meet required momentum resolution in the muon spectrometer. For this reason, an optical alignment system is used to constantly monitor chamber deformations and displacements.

The muon trigger system consists of the RPC in the barrel region ($|\eta| < 1.05$) and the TGC in the end-cap region ($1.05 < |\eta| < 2.4$). The RPC and TGC measure both coordinates of the tracks, one in the bending (η) plane and one in the non-bending plane (ϕ).

The RPC consists of three concentric cylindrical layers around the beam axis. Each of two rectangular layers read out by the η strips parallel to the MDT and by the ϕ strips perpendicular to the MDT. The use of the two orientations allows the measurement of the η and ϕ coordinates. The spatial resolution of the RPC is 1 cm with a time resolution of 1 ns.

The TGC provides the muon trigger capability, the determination of the second azimuthal coordinate in the bending direction. The TGC is a thin multiwire proportional chamber with smaller spacing between cathode and anode than spacing between anode and anode. This allows a short drift time and an excellent response in time of less than 20 ns satisfying identification of bunch crossings at 40 MHz.

3.2.5 Magnet System

The ATLAS magnet system consists of a central solenoid (CS) [50, 51] and three large air-core toroids, one in the barrel (BT) [50, 52] and two in the end-cap (ECT) [50, 53]. The magnet system produces the optimized magnetic field configuration for particle bending around the various detectors while minimizing scattering effects. The whole system is 26 m long and 22 m in diameter and stores an energy of 1.6 GJ. Figure 3.4 shows the general layout, the four main sub-detectors and the four superconducting magnets and Fig. 3.8 shows spiral arrangement of the coil windings.

The CS in Fig. 3.9(a) provides the solenoid field of 2 T along the beam axis for the accurate track momentum measurements (up to 100 GeV) in the inner detector. The CS is placed inside the EM calorimeter. A small magnetic field also reduces the transverse spread of showers. Since the solenoid coil is located between the ID and the EM calorimeter, the amount of the material in the CS has to be minimized to achieve precise energy measurement of particle arriving at the calorimeter. Therefore,

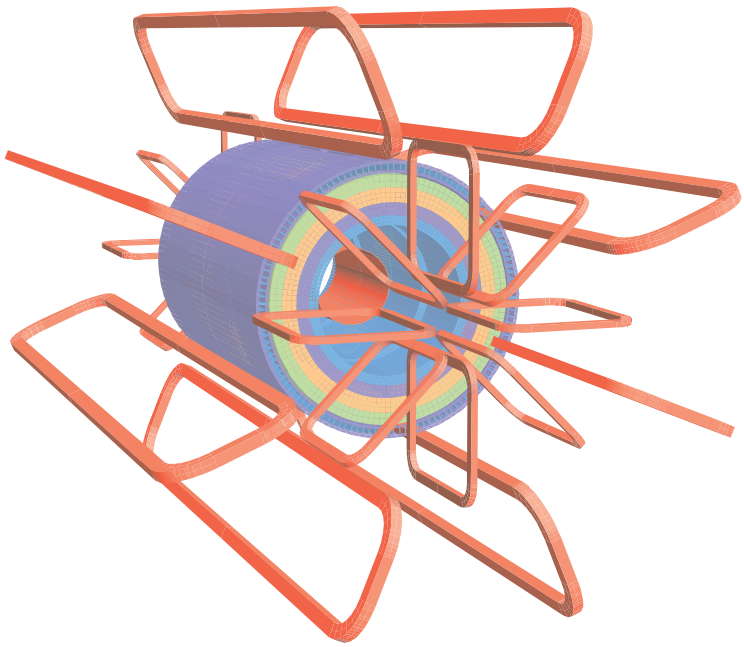

Figure 3.8. Geometry of magnet windings and the tile calorimeter steel. The eight barrel toroid coils, with the end-cap coils interleaved are visible. The solenoid winding lies inside the calorimeter volume.

the solenoid thickness is a 45 mm in spite of a diameter of 2.5 m and a length of 5.3 m.

The toroid magnets, BT and ECT produce magnetic field for momentum measurement in the muon spectrometer. With a toroid field, particles will cross the complete pseudo-rapidity range. It means that the field integral can be kept high even in the end-cap region. This field is generated in the barrel region ($|\eta| < 1.4$) by the BT, in the end-cap region ($1.6 < |\eta| < 2.7$) by the ECT and in transition region by a combination of the two. Each of the three toroids consists of eight coils assembled radially and symmetrically around the beam axis as shown in Fig 3.8. The low number of coils to form the toroid field results in a field strength that varies strongly with the ϕ coordinate. The field in the barrel is 2 T and varies in the end-caps from 4 T to 8 T (at $\phi = 0$).

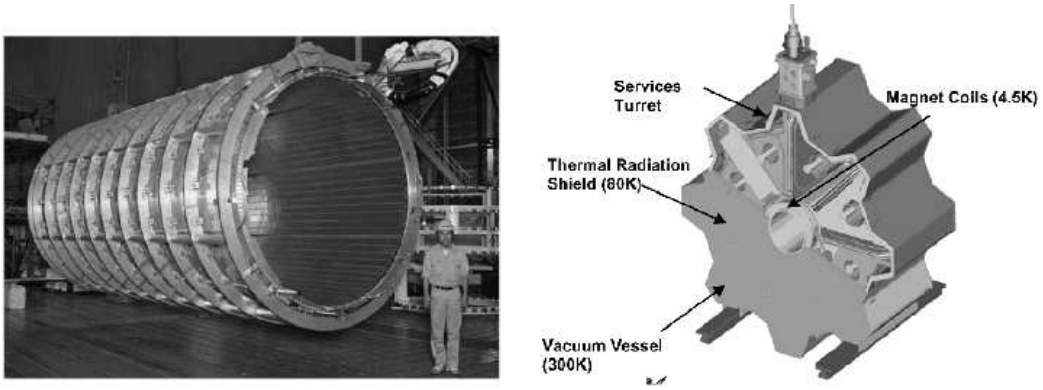

(a) (b)

Figure 3.9. View of the ATLAS magnetic system. (a) Central solenoid is shown after completion of the coil winding. (b) End-cap toroid.

3.2.6 Trigger and Data Acquisition System

In order to allow the studies of rare events LHC is designed to operate at a design luminosity of 10^{34} cm^{-2}s^{-1}. This condition will lead to about 10^9 interactions per second. Most of these interactions are minimum bias events that have a limited interest. Therefore it is necessary to select and register only the interesting events coming from the collisions. The trigger and data acquisition systems have been designed with the challenging role of selecting bunch crossings containing interesting events by reducing the data rate from 40 MHz (collision rate) to 100 – 200 Hz, this is the practical limit for disk storage and offline processing.

The Trigger and Data Acquisition system (TDAQ) of ATLAS has three levels as shown in Fig. 3.10.

- **LVL1** The first level trigger (LVL1) is hardware based and designed to operate at a maximum pass rate of 75 kHz. The LVL1 decision uses information with a reduced granularity of the muon trigger chambers and the calorimeters. It looks for signatures of high-p_T muon, electrons/photons clusters, τ-leptons decays, and large E_T^{miss}. The LVL1 defines the so-called *region of interest* (ROI), where

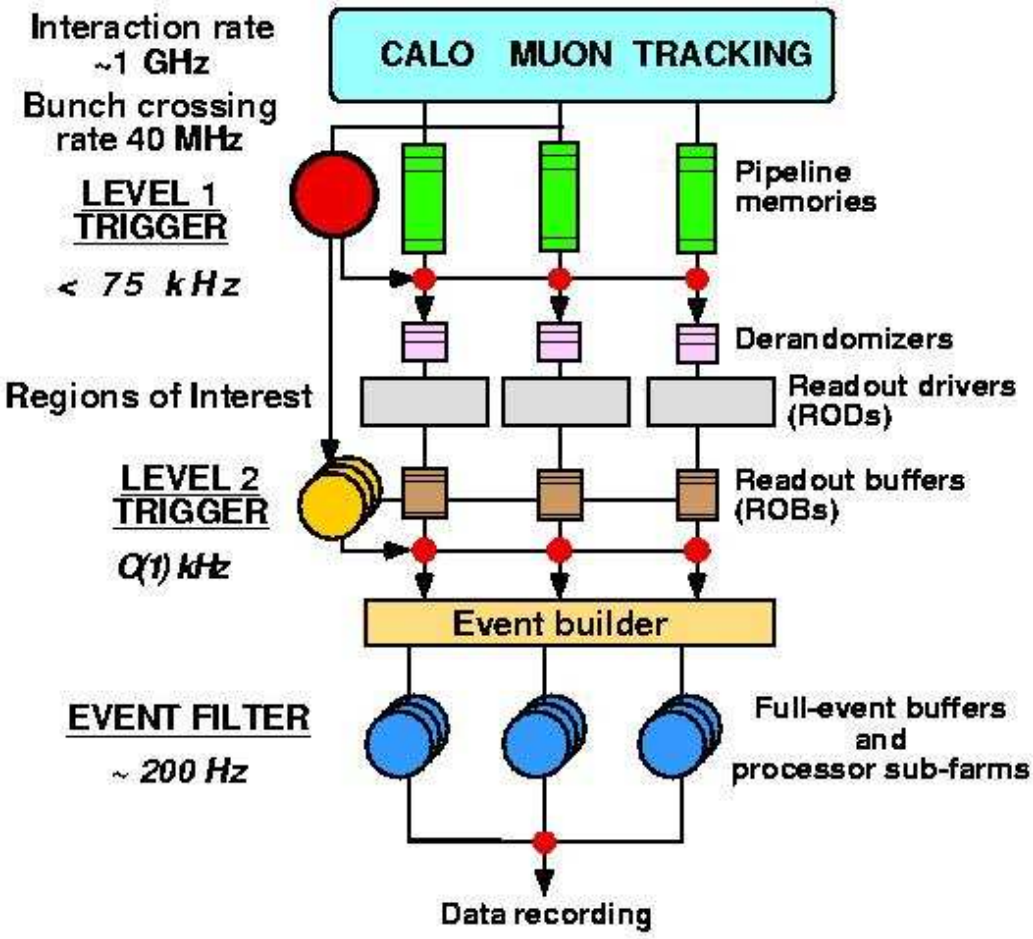

Figure 3.10. Schematic diagram of the ATLAS trigger system.

interesting objects might be exists. Only the full information within ROIs is passed to the second level trigger.

- **LVL2** The second level trigger (LVL2) is software based and reduces further the event rate to a maximum of 3.5 kHz by using full detector granularity within the RoI. The LVL2 uses information from the MDT chambers to improve the muon momentum estimate and calorimeter, and can require a match with a track reconstructed in the inner detector. The LVL2 has a latency from 1 ms to

about 10 ms depending on the complexity of the event. For events accepted by the LVL2, the full event information is collected by the so-called *Event Builder* to form a RAW data event and is passes to the third level trigger, so-called *Event Filter* (EF).

- **LVL3** The EF make decision whether the event is recorded for offline analysis or discarded. It uses complex offline algorithms like tracker reconstruction, vertex finding, jet finding etc., because it has access to the complete event record. It requires relatively long decision time of the order of one second. The recorded data is reconstructed to produce quantities like tracks, energy clusters, jets, E_T^{miss}, secondary decay vertices, etc. For the maximum trigger rate of 100 – 200 Hz the average event processing time is of order four seconds.

3.3 Electromagnetic Calorimetry

A calorimeter [54, 55] is a device that measures the energy deposited by particles. If the calorimeter is thick enough then the particle will be absorbed and its total initial energy can be measured. High energy electrons, photons and hadrons can start a cascade *shower* inside the calorimeter. The shower initiated by muons is usually negligible unless if they have an energy larger than the critical energy $\sim$ 500 GeV. The calorimeter can determine the energy lost by measuring a quantity proportional to the number of particles in the shower. This quantity can be an amount of light, charge or heat.

Showers are usually classified in two types: hadronic showers governed by the strong interaction and electromagnetic showers governed by the electromagnetic interaction. Electromagnetic showers are generated by photons, electrons, but are also a component of hadronic showers. The π^0's produced in hadronic showers decay into two photons which generate an electromagnetic shower inside the hadronic one.

Hadronic particles also cause showers, but they are qualitatively different from the electromagnetic showers caused by electrons and photons. Hadrons lose energy primarily through inelastic collisions with atomic nuclei. These collisions produce secondary hadrons, which can in turn undergo other inelastic collisions. This process is called a hadronic shower and it continues until all particles have either been stopped by ionization losses or absorbed by nuclear processes. The scale for the size of these showers is given by the nuclear interaction length, this is characteristic of the materials. For example, Uranium, $\lambda \approx 10.5$ cm [54]. Hadronic showers are much more extended in space than electromagnetic showers of similar energy.

To optimize the measurement of these two types of showers the ATLAS calorimeter system is divided into a hadronic and an electromagnetic calorimeter. A short description of electromagnetic calorimetry principles is given below, before discussing in more details the ATLAS electromagnetic calorimeter.

3.3.1 Electromagnetic Shower

When a charged particles travel through a material, it loses energy through different processes. Electrons and positrons lose their energy mainly by ionization and bremsstrahlung as shown in Fig. 3.11. Significant sources of energy loss for low energy electrons are ionization, elastic scattering and annihilation process. For high energy electrons the bremsstrahlung is dominant.

For the photons there are three major processes by which they interact with matter: photoelectric effect, Compton effect and pair production (see Fig. 3.12). The photoelectric effect can be considered as an interaction between the photon and the atom. Incident photons whose energy exceeds the binding energy of an electron may be absorbed and consequently the atomic electron may be emitted. Compton effect

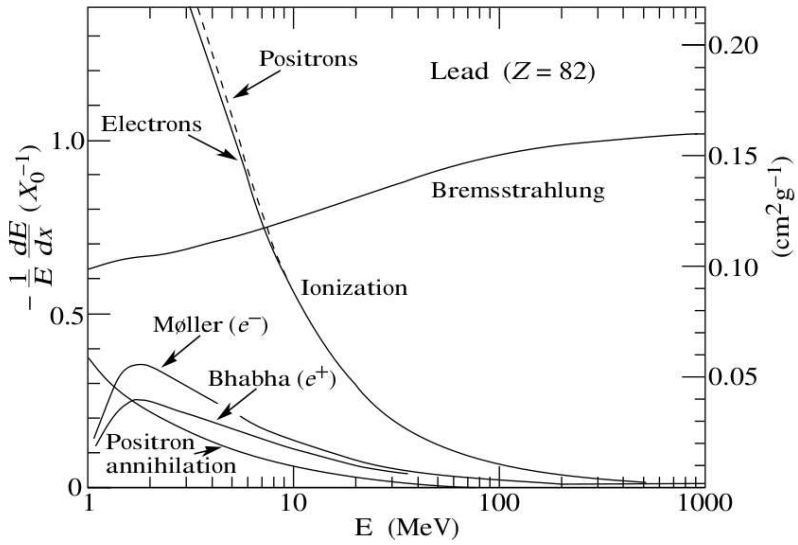

Figure 3.11. Fractional energy loss for electrons and positrons per radiation length in lead (X_0 (Pb) = 6.37 g/cm^2) as a function of the electron or positron energy. Figure extracted from Ref. [16].

involves the scattering of an incident photon with an atomic electron. Pair production leads the production of electromagnetic shower through bremsstrahlung.

High energy electron ($\gg$ 100 MeV) entering in a material interacts with the Coulomb field around a nucleus and emits a photon with a large fraction of the electron's initial energy. A high energy photon, on the other hand, will interact predominately via pair production, in which a photon converts into an electron-positron pair in the vicinity of a nucleus. The particles emitted in these interactions can themselves undergo Bremsstrahlung or pair production. Thus, an energetic electron or photon passing through a dense material will produce electromagnetic shower. As the number of particles in the shower increase the average energy per particles decreases. This process will continue until photons fall below the pair production threshold.

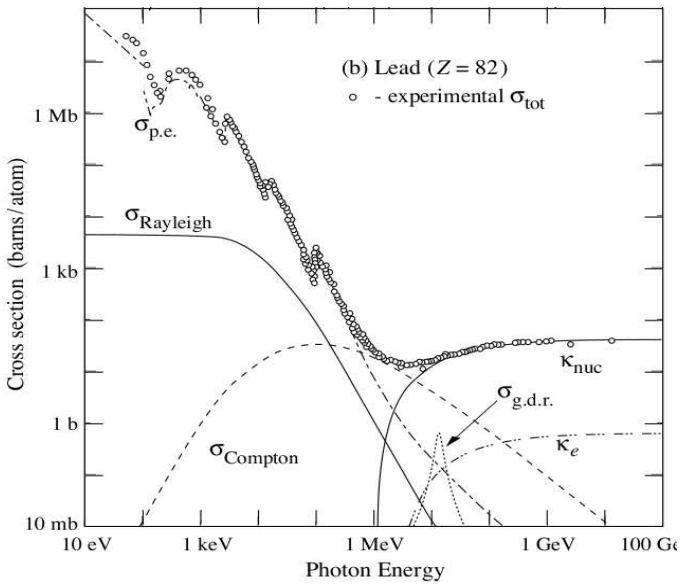

Figure 3.12. Total cross-sections for photons in lead as a function of the photon energy. $\sigma_{p.e}$ is the cross-section for the atomic photoelectric effect, $\sigma_{Rayleig}$ and $\sigma_{Compton}$ for the (coherent) Rayleigh scattering and the (incoherent) Compton scattering, κ_{nuc} and κ_e for the pair production in the nuclear field and the electron field. Figure extracted from Ref. [16].

Critical Energy

The energy losses by ionization, collision, excitation, etc. tend to stop the shower development. These losses become more important than the losses by bremsstrahlung when the energy per particle is lower than the *critical energy*. The critical energy, E_c is defined as the energy at which the energy loss by bremsstrahlung equals that by others source, mainly ionization. An approximate formula by Bethe-Heitler for E_c [56, 57] is given by :

$$E_c[\text{MeV}] = \frac{800}{Z + 1.2} \tag{3.10}$$

where Z is atomic number of the medium. Figure 3.13 shows values for critical energies for some solids and gases.

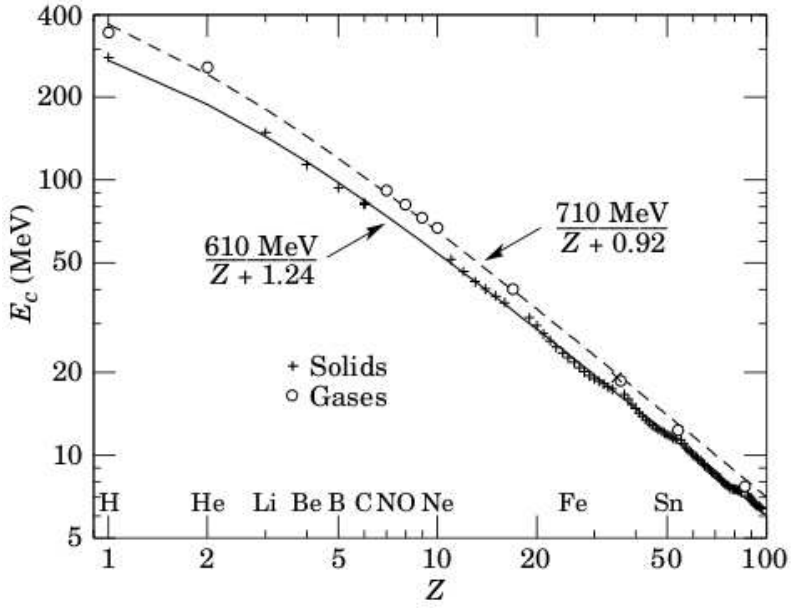

Figure 3.13. Critical energy as a function of atomic number Z. Figure extracted from Ref. [16].

Radiation Length

The energy losses of high energy electrons and photons in matter, due to radiation cause their energy to decrease exponentially with depth. The *radiation length* X_0 is defined as the average length over which an electron loses $1 - \frac{1}{e}$ (i.e. 63%) of its energy due to bremsstrahlung. The radiation length depends on the material and can be approximated by [16] :

$$X_0 \ [\mathrm{g/cm^2}] \cong \frac{761.4A}{Z(Z+1)\ln 287/\sqrt{Z}} \tag{3.11}$$

where A and Z are the atomic weight and the atomic number of the propagation medium. The average absorption length of an electron of a given energy is independent of the material when expressed in radiation length. As an example the radiation length of several materials used in ATLAS are give in table 3.5

Table 3.5. The radiation length of some materials used in ATLAS.

Material	X_0	
	g/cm²	**cm**
Kapton	40.61	28.6
Liquid Argon	19.55	14.0
Aluminium	24.01	8.89
Iron	13.84	1.76
Copper	12.86	1.43
Lead	6.37	0.56

Electromagnetic Cascade

Figure 3.14 shows a simplified electromagnetic cascade model. This model suggests that after t radiation lengths the shower contains 2^t particles . There will be roughly an equal number of electrons, positrons and photons each with an average energy given by the equation

$$E(t) = \frac{E_0}{2^t} \tag{3.12}$$

The cascade process will stop when $E(t)$ equals to E_c (critical energy). The thickness of absorber at which the cascade reach the maximum number of particles, t_{max}, can be written in terms of the initial (E_0) and critical energies (E_c):

$$2^t = \frac{E_0}{E(t)} \tag{3.13}$$

$$\text{If} \quad t = t_{max} \quad \text{when} \quad E(t) = E_c \quad \text{then,} \tag{3.14}$$

$$t_{max} = \frac{\ln E_0/E_c}{\ln 2} = \frac{\ln E_0/E_c}{t_0} \tag{3.15}$$

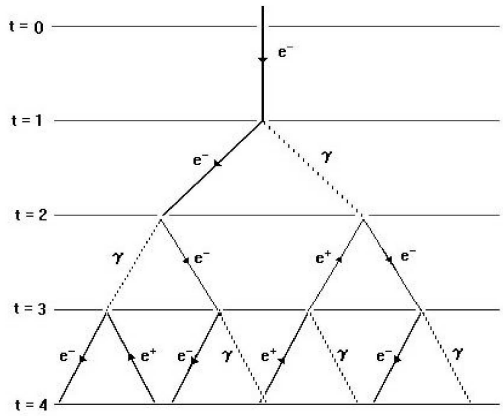

Figure 3.14. Schematic representation of an electron initiated electromagnetic cascade. Values of t represent successive radiation lengths.

It means that maximum shower depth varies as the logarithm of the primary energy. It also predicts that the shower curve should rise rapidly to a peak value and then fall to zero. The broad peak of the experimental curve can be interpreted in terms of a spread of energies of the incoming particles. The logarithmic scaling of the shower depth with the energy of the incoming particle allows compact calorimeters to be built event for very high energy particles.

3.3.2 Sampling Calorimeter

Particle absorption and signal generation can be carried out in a single material or by using two different materials. The former is called homogeneous and the latter is sampling calorimeter. In a homogeneous calorimeter, the entire detector volume is sensitive to the particle and may contribute to shower production. In sampling calorimeter, particle absorption and signal generation are achieved by different materials, called passive and active material.

The active medium can be of various types, for example scintillators, liquid argon ionization chambers or multiwire proportional chambers. The passive medium

is usually a metal and often lead. Since metals have short radiation length, a sampling calorimeter can be compact but still many radiation lengths thick, ensuring a good longitudinal shower containment. The passive and the active medium are in general arranged in alternated layers so that the shower is sampled by an active layer after each passive layer.

The separation of the particle detection and the shower generation tasks allows an optimization of the detector to a particular experiment. The sampling calorimeter are built such that only a fraction of the total energy is deposited in active material. It results in an unmeasured amount of energy in the shower and degraded energy resolution of the calorimeter. The ratio of the measured or sampled energy to the total energy of the shower is obtained by the sampling fraction.

3.3.2.1 Energy Resolution

The basic task of calorimetry is the measurement of the energy of an incident particle through total absorption of the particle and its shower. The response of the calorimeter to an incident particle of a given energy follows approximately a normal distribution if the shower is fully contained. The performance of the calorimeter can be assessed by its energy resolution E/σ where σ is the width of the response distribution at which the energy E of a particle can be measured. The resolution of the calorimeter can be parameterized as a function of energy as

$$\frac{\sigma}{E} = \frac{a}{\sqrt{E_0}} \oplus \frac{b}{E} \oplus c \tag{3.16}$$

where E is the measured energy, E_0 is the initial particle energy and $\oplus$ denotes quadratic summation. The three distinct terms in the parameterization are referred to as the sampling, ectronic noise, and constant terms, respectively. The sampling term a is primarily determined by the sampling quality (fraction and frequency) of

the calorimeter and, in the case of hadronic calorimeters by non-compensation. The term b reflects the electronic noise impact on the resolution. The constant term c ncludes calibration errors, mechanical imperfections and all effects that affect the energy resolution independently of the energy.

With higher energy, the resolution improves and becomes more sensitive to the constant term, while the effect of the electronic noise on the width of the response is energy independent. Since the electronic noise is energy independent, the contribution of b on the resolution is greater at lower energies.

3.3.3 ATLAS Electromagnetic Calorimeter

Isolated electrons and photons with high-p_T in the final state are signatures for many important physics processes at the LHC. The ATLAS EM calorimeter is crucial for good measurements and identification of electrons and photons. The performance of requirement [58, 59] on the EM calorimeter are listed here:

- Particle identification: Excellent electrons/photon identification against a large background of QCD jets is required for many important physics processes at LHC. The required γ/jet seperation with a 80% of photon efficiency is about 3000 and that of π^0 is about 3 for 90% photon efficiency.
- Angular resolution: The beam has certain longitudinal spread at the LHC which contributes to the angular resolution of the invariant mass of diphoton. To reduce this effect photon direction in η is measured with a resolution of about $50\text{mrad}/\sqrt{E}$ (E in GeV). The position measurement in ϕ direction is well constrained with a precision of few micrometer.
- Energy resolution: An excellent energy resolution is required to search for the Higgs boson. The EM calorimeter is required to have sampling term of 10% and

constant term of 0.7%. The noise term includes the electric noise contribution and the pile up noise contribution which depends on luminosity.

- Acceptance: The design of the EM calorimeter is driven by the Higgs search in the channels $H \rightarrow \gamma\gamma$ and $H \rightarrow ZZ \rightarrow e^+e^-e^+e^-$ with high-p_T electrons and photons. An η-coverage up to $|\eta| < 2.4$ and very fine granularity is needed.

A Lead-liquid Argon sampling calorimeter [60, 61] was chosen in ATLAS to achieve the requirements listed. The liquid argon (LAr) technology is tolerant to radiation and allows a full coverage in the ϕ coordinates without crack and dead zone.

3.3.3.1 Geometry and Structure

The ATLAS EM calorimeter is LAr sampling calorimeter. The primary absorber material is lead, with copper and stainless steel used in the large $|\eta|$ regions. The EM calorimeter is designed using *accordion geometry* (see Fig 3.16). The absorber layers and electrodes are shaped like an accordion. This shape allows that the EM calorimeter have seamless geometrical coverage in ϕ.

The EM calorimeter is divided into three parts:

- **Barrel**: covers the region $|\eta| < 1.475$. The barrel calorimeter is a 6.8 m long with an outer radius of 2.25 m, an inner radius of 1.15 m. Its thickness change as function of η from 22 to 33. It consists of two identical half-barrels, separated by a 6 mm gap at $z = 0$. The LAr gap between absorber plates is kept constant by varying the bending angles as a function of the radius. The barrel consists of 32 modules and each module of 1024 accordion-shaped absorbers interlarded with read-out electrodes.

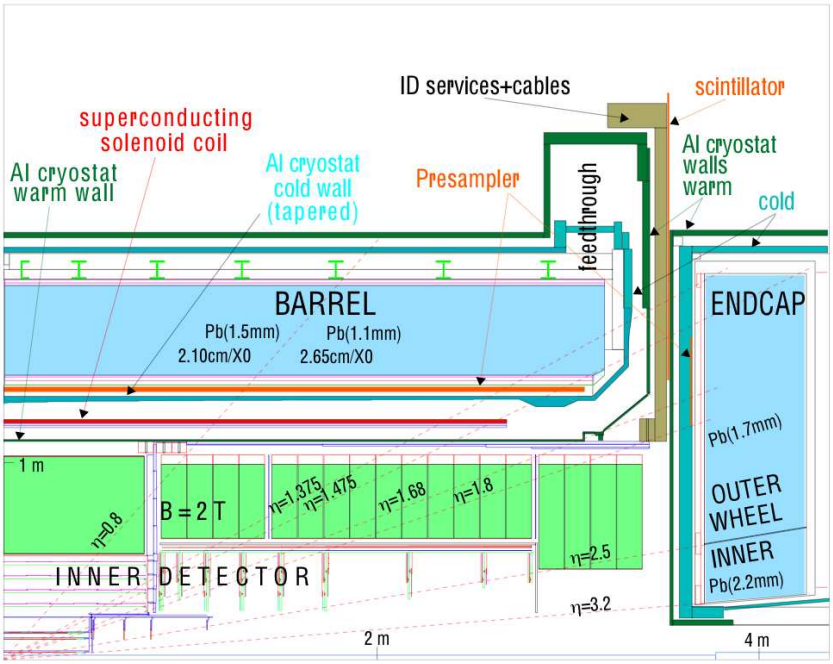

Figure 3.15. Rz view of a quadrant of the ATLAS EM calorimeter.

- **End-caps**: cover the $1.375 < |\eta| < 3.2$ region. The end-caps are placed on each side of the barrel calorimeter. The end-cap extends from an inner radius of 0.3 m to an outer radius of 2 m. Each end-cap is itself divided into two wheels separated by 3 mm. The LAr gaps changes from 2.8 mm to 0.9 mm in inner wheels and from 3.1 mm to 1.8 mm in outer wheels. Its total thickness also varies as function of η from 24 to 38. The inner wheels covers the region $2.5 < |\eta| < 3.2$ and the outer one covers $1.375 < |\eta| < 2.5$.

Due to the complexity of the calorimeter structure (shown in Fig. 3.15) three regions have cracks and the response is degraded with respect to the rest of the detector:

- Gap between the two half barrels: this is located at $\eta = 0$ with a width of 6 mm. Inactive LAr is present.

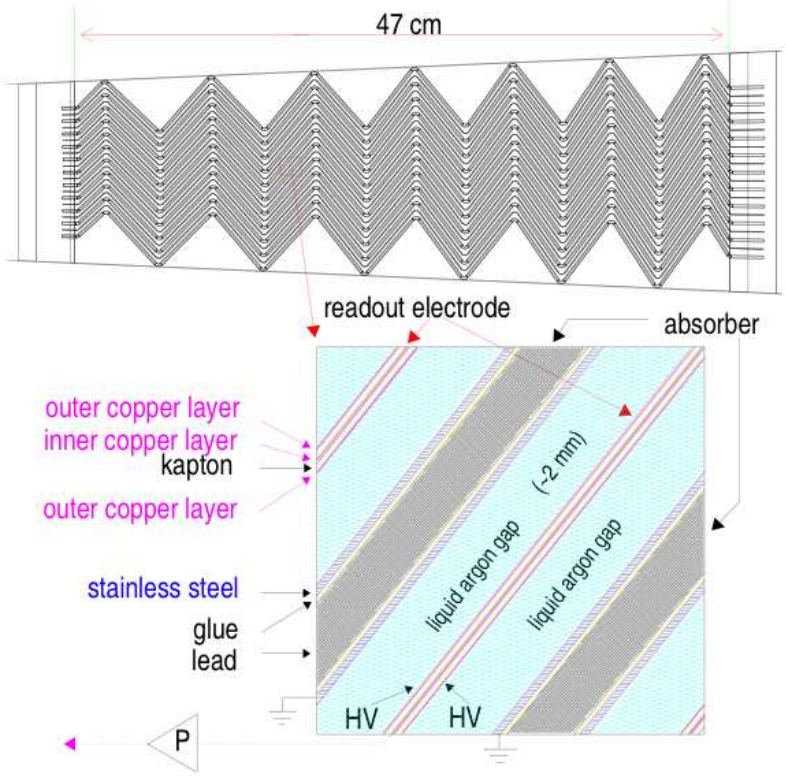

Figure 3.16. Detailed view of a barrel LAr gap Section.

- The transition region between barrel and end-cap: this region placed at about $\eta \sim 1.45$ is used for routing of services and cables of the inner detector. In order to partially recover the energy lost in the passive materials, scintillator detectors are placed between the barrel and end-cap cryostats covering the region $1.0 < |\eta| < 1.6$. These extra devices improve E_T^{miss} resolution and increase the acceptance for precision physics.
- Transition between outer and inner wheel of the end-cap: this region is a 3 mm thick projective gap placed at $\eta = 2.5$. The performance is also degraded by the presence of additional dead material in front due to supports.

Figure 3.16 shows the detailed view of a slice of the barrel calorimeter with the accordion geometry in more detail a LAr gap section. The read out electrodes

are three layers copper-kapton flexible printed circuit boards. The two outer layers are connected to the high voltage while the inner layer is connected to the read-out channel and collects, by capacitive coupling, the current induced by the electrons drifting in the LAr gap.

The absorber electrodes are made of one lead sheet sandwiched between two 0.2 mm thick stainless-steel plates for high mechanical strength. In the barrel calorimeter the lead thickness is 1.5 mm in the region $\eta < 0.8$ and 1.1 mm for $\eta > 0.8$: the thinner lead for $|\eta| > 0.8$ increases the sampling fraction. This compensate for energy resolution degradation due to the decrease of sampling frequency with increasing rapidity.

3.3.3.2 Granularity

Over the region devoted to precision physics ($|\eta| < 2.5$) the calorimeter is segmented in three longitudinal sampling layers and a separate presampler is placed in front of the calorimeter in the $|\eta| < 1.8$ region. The number of layers, the granularity and coverage are summarized in Tab 3.6. A schematic view of the barrel calorimeter segmentation and granularity is shown in Fig. 3.17. The presampler is not shown.

The longitudinal sampling layers are:

- **Presampler**: the presampler consists of an active LAr layer of 1.1 cm and 0.5 cm thickness respectively in the barrel and in the end-cap. The presampler does not have absorber. The purpose is to correct for the energy lost in the material in front of calorimeter. The presampler coverage extend up to $\eta = 1.8$.
- **The first layer (strips)**: The layer is made of narrow strips with a fine granularity providing excellent resolution in the η coordinate. It is used for π^0 rejection up to E_T of 50 GeV or more. In order to limit the number of channels

Table 3.6. Pseudo-rapidity coverage, granularity and longitudinal segmentation of the Atlas EM calorimeters.

EM Calorimeter	**Barrel**	**End-cap**	
Coverage	$\|\eta\| < 1.475$	$1.375 < \|\eta\| < 3.2$	
Longitudinal segmentation	3 samples	3 samples	$1.5 < \|\eta\| < 2.5$
		2 samples	$1.375 < \|\eta\| < 1.5$
			$2.5 < \|\eta\| < 3.2$
Granularity ($\Delta\eta \times \Delta\phi$)			
The first sampling	0.003×0.1	0.025×0.025	$1.375 < \|\eta\| < 1.5$
		0.05×0.025	$1.5 < \|\eta\| < 1.8$
		$0.025 < \|\eta\| < 0.1$	$1.8 < \|\eta\| < 2.0$
		0.003×0.1	$2.0 < \|\eta\| < 2.5$
		0.004×0.1	$2.5 < \|\eta\| < 3.2$
The second sampling	0.006×0.1	0.1×0.1	$1.375 < \|\eta\| < 2.5$
		0.025×0.025	$2.5 < \|\eta\| < 3.2$
The third sampling	0.1×0.1	0.05×0.025	$1.5 < \|\eta\| < 2.5$
Presampler	**Barrel**	**End-cap**	
Coverage	$\|\eta\| < 1.52$	$1.5 < \|\eta\| < 1.8$	
Granularity	$(\Delta\eta \times \Delta\phi)$	0.025×0.1	0.025×0.1

the cells are wider in azimuth with respect to the second and third layer. In the end-caps the bins become narrower when going to larger η: the granularity of the first sampling slightly worse while increasing η due to the fact that for technical reason the strips width can not be made less than 5 mm. The depth of the first layer is chosen to be 6 X_0 based on the condition for π^0 rejection.

- **The second layer (middle)**: The majority of the energy is deposited in the 16 X_0 of the second sampling layer. Showers with energy below 50 GeV are fully contained. The second calorimeter layer is transversally segmented in to squared towers of $(\Delta\eta \times \Delta\phi) \cong (0.025 \times 0.025)$ for the angular measurement.
- **The third layer (back)**: The third layer has the same ϕ granularity as the second one and a twice coarser granularity in the η coordinate. The total thickness varies from 2 to 12 X_0. Only the highest energy electrons will reach

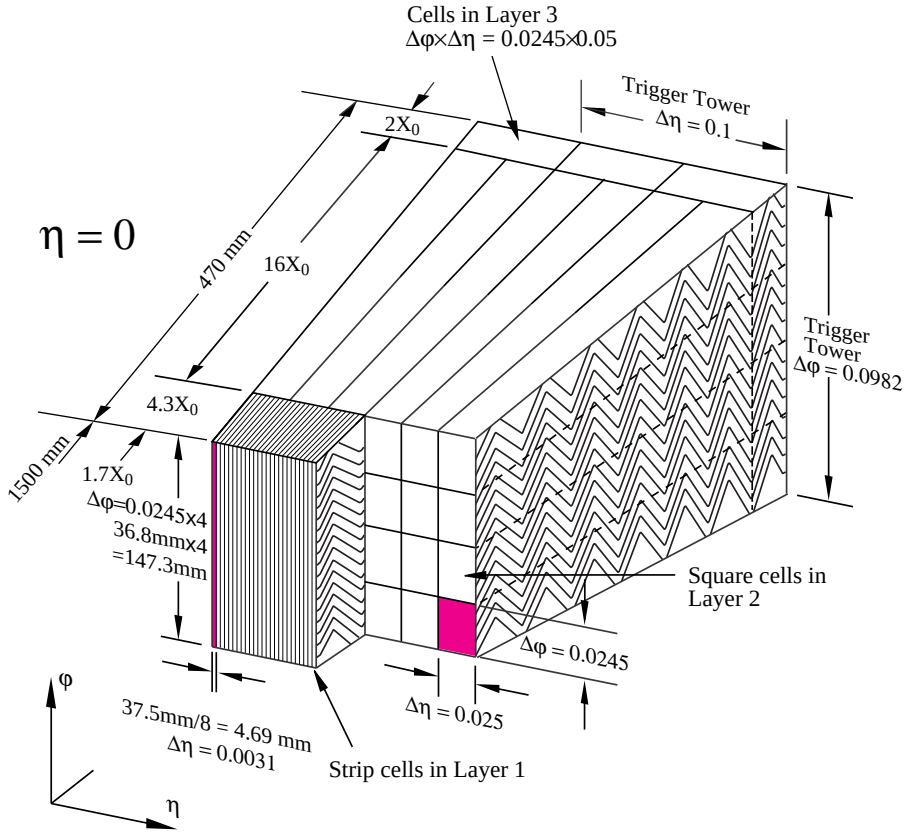

Figure 3.17. Sketch of the accordion structure of the ATLAS EM calorimeter and barrel granularity. The presampler is not shown.

this deep in the calorimeter. Therefore it is used to sample high energy showers and contributes to photon/jet and electron/jet separation. For the end-cap inner wheel ($|\eta| > 2.5$) the calorimeter is segmented in two longitudinal layers only with a coarser granularity.

CHAPTER 4

SIMULATION AND RECONSTRUCTION

4.1 The ATLAS Software Framework

The complexity of the ATLAS detector also demands for complex reconstruction software and thus the development of a common software framework for the experiment which is called Athena [62].

Athena makes communicating within the framework between different software applications, called algorithms. All algorithms have access via the *StoreGate* to results of other algorithms, such as the general event information or the detector description. Moreover, a common framework ensures a common approach of software developing, e.g. messaging or access on disk and reuse of already written code-segments, and a common underlying design of the software packages. These packages consists of Algorithms, Tools, Data objects and Services, which are organized C++ and python classes. The Athena framework is organized in form of plug-in modules allowing flexible configuration of various algorithms to be executed. Using the so-called JobOptions file written in Python scripting, user specific configuration of algorithms is possible. The ATLAS software is used to generate, simulate, digitize and reconstruct proton-proton collisions in the LHC environment. Figure 4.1 shows the a skeleton of organization for the Athena software.

The generation process includes the proton-proton collision, calculating the position and momentum four-vectors of all the particles which are produced in the collision. The generation is based on different Monte Carlo generator programs, which are explained later. The second part is detector simulation which simulates the response

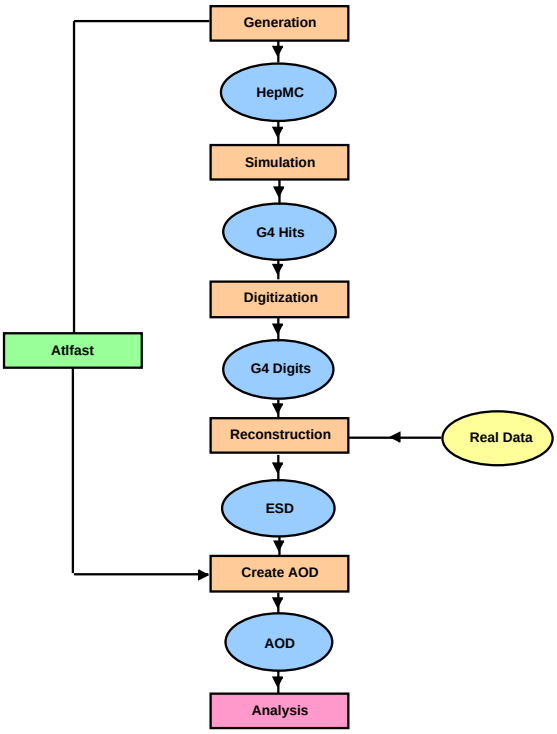

Figure 4.1. Athena software chain including generation, simulation, digitization and reconstruction..

of the produced particle through the detector using the GEANT4 toolkit [63, 64]. GEANT4 simulates interactions with the material of detector (multiple scattering, energy loss, photon conversions) and further decays of unstable particles. GEANT produces *hits* or *hit objects* which represent the position and type of the interaction. During the digitization step, the response of the detector and its electronics is simulated. The final information is stored in so-called digit objects. The reconstruction is based on the digitized information. it includes various algorithms, for pattern recognition, track fitting, vertex determination and energy measurements. It should be noted that the digitized information and the real data are equivalent from a data representation point of view.

4.2 Generation

Theoretical predictions are important part of any particle physics experiment. In order to produce hypothetical events with the distribution predicted by theory, the so-called event generator is used. The generated events allow a realistic estimation of feasibility and to be made to compare data with theoretical predictions. The event generator uses the same framework through which the experimental data are processed. Among more specialized generating programs, many use the matrix elements for some specific set of processes, a few topics such as parton showers or particle decays. There are many event generators in the particle physics. In the following, the generator programs described are used in the analysis.

4.2.1 PYTHIA

PYTHIA [65, 66] is a general purpose generator for hadronic events in pp, e^+e^- and e^+p high-energy colliders. PYTHIA contains around 240 different $2 \to n$ subprocesses, all at leading order. It is mainly optimized for $2 \to 1$ processes and $2 \to 2$ processes. The PYTHIA also includes QCD $2 \to 2$ partonic scattering and heavy flavor, SM processes including γ, Z^0, $W^{\pm}$ singly or in pairs or SUSY processes, among others. The basic partonic processes, initial and final state showers are added to provide more realistic multipartonic configurations. Unstable particles are allowed to decay. In cases where better decay models are available elsewhere, e.g. for $\tau^{\pm}$ with spin information or for B hadrons, such decays can be delegated to specialized packages, as PYTHIAB [67].

The PYTHIA also contains minimum bias of multiple particle interactions, the underlying event process. This has a number of different physical parameters. The basic parameter is the lower limit of the transverse momentum, $p_{T_{min}}$, used in the calculation of 22 *hard* cross section. The minimum p_T is used as a regulating parameter.

In addition, a uniform distribution of matter and a single or double Gaussian matter distribution can be used, introducing fluctuations in the multiplicity distributions, particularly at large multiplicities.

4.2.2 ALPGEN

The ALPGEN [68] is a Monte Carlo generator to produce Standard Model process in a hadron collision. The program performs leading order (LO) QCD exact matrix elements calculations for a large set of parton-level processes of interest in the study of the LHC. Parton-level events are generated providing full information on their color and flavor structure, enabling the evolution of the partons into fully hadronized final states. So, the development of partonic cascades, with the subsequent transformation of the partons into observable hadrons are carried out by Monte Carlo programs such as HERWIG or PYTHIA. The consistent combination of the parton-level calculations with the partonic evolution given by the shower MC programs is the sub jet of extensive work. In the case of $W/Z(\rightarrow ll)$ + N jets process, N can reach at the moment, to approximately 5.

4.2.3 HERWIG

HERWIG [69, 70, 71] is a Monte Carlo event generator to simulate hadronic final states in lepton-lepton, lepton-hadron and hadron-hadron collisions. Using the angular ordered parton shower, the program simulates a large range of hard scattering processes together with initial and final state radiation. It uses the cluster hadronization model and a cluster-based simulation of the underlying event. The HERWIG includes hard $2 \rightarrow n$ scattering processes for both Standard Model and its supersymmetric extension. The following types of processes are included: $2 \rightarrow 2$ QCD scattering processes, including heavy flavor production, electroweak processes,

like $\gamma/\gamma**/Z^0/W^{\pm}/H^0$ production, SUSY, etc. The HERWIG incorporates JIMMY [16] to produce the underlying events.

4.2.4 MC@NLO

The MC@NLO [72, 73] generator simulates the full next-to-leading order QCD corrections in the computation of hard processes. It contains hadronic collisions, with the production of the following final states: W^+W^-, $W^{\pm}Z$, ZZ , $b\bar{b}$, $t\bar{t}$, H^0, etc. In order to provide a better prediction of the rates the NLO matrix elements are incorporated while improving the description of the first hard hadron emission.

The MC@NLO provides a sensible description of multiple soft/collinear emissions. For the same reason, and unlike usual NLO programs, propagation through the shower and subsequent hadronization gives a final state description at the hadron level. The MC@NLO has negative weights (which appear in higher order perturbative calculations, NLO in this case) which is opposed to standard MC's. Thus in unweighted event generation MC@NLO produces unit weight events with a fraction (typically $\sim 15\%$) having weight -1. The MC@NLO is based on the HERWIG generator, so from a technical point of view, the structure of MC@NLO is separated in a NLO former part, which produces an event file, and shower and hadronization part, which is just HERWIG, augmented by the capability of reading the event file.

4.3 Detector Simulation

The full event generations requires the detailed simulation of all particle interactions in each part of the detector. The simulation [74] requires a precise geometrical description of the detector components including the materials used in the manufacture, as well as the magnetic field maps.

There are two types of detector simulation in the ATLAS software framework: GEANT4 full detector simulation and fast simulation (see Fig. 4.1). The former is based on complete detector material description. The latter does not consider detector materials in detail, it only smears the kinematics of the MC particles according to the expected detector performance. The full simulation is needed for the study of tracking performance, energy and E_T^{miss} resolution, photon conversion, electron/photon/muon/tau identification, jet clustering etc. However, the fast simulation is needed for SUSY events and production of large sample of backgrounds (e.g. QCD multi-jets and γ-jets for $H \rightarrow \gamma\gamma$ analysis.), because of the large each events takes several hours to process.

GEANT4 [64, 63] is a common tool used in high energy physics to simulate the particle propagation through the detector and particle interaction with active and passive materials. The GEANT4 takes into account all possible physics process of interactions between particles and detector. Considering finite size of the beam overlap region, the position of the primary vertex is displaced. Then, the GEANT4 simulates the energy loss due to the dead material inside the detector. The outcome of this process is a file of hits which contain information about the type of the detector element traversed, the position and the energy deposited in that element.

In order to mimic the raw data from the real detector, the response of the detector to the hits is simulated in the so-called *digitization* which induces information such as voltages, times, noise etc. Finally, the digitized output (called Raw Data Object) is reconstructed into tracks, energy, etc., using the same reconstruction algorithms that will be applied to real data. The output from the reconstruction is called Event Summary Data (ESD) and a reduced data format called Analysis Object Data (AOD).

4.3.1 Reconstruction

The events recorded after the detector simulation program are stored in raw format (RDO) which contains the digitized information from each sub-detector like the hits in the tracking and muon systems and the digitized counts in the calorimeter cells. In order to convert this raw information to more fundamental physics objects like electrons, and provide useful kinematic as well as quality information, the recorded events are processed through a set of computer algorithms called the offline event reconstruction. The reconstruction depends on the object of interest, and are described in detail elsewhere [75, 76], although the reconstruction of cluster, photons and electrons are described with more details.

4.4 Electromagnetic Particles Reconstruction

The detection and identification of high p_T electrons and photons are primary ATLAS physics aims. However, the conditions of collisions at the LHC make this significantly harder than in previous experiments. For example, the relative rate of QCD jet production compared to inclusive electron production is expected to be between 10 and 100 times higher than at the Tevatron [75]. Then addition, aspects of the detector such as the significant amounts of material in the Inner Detector itself complicate the analysis. The strategies for reconstructing and triggering on electron and photon candidates are described in detail in [76].

The reconstruction of electrons and photons consists of four steps:

1. Identification of suitable energy deposits (cluster seeds) in the calorimeter.
2. Track reconstruction and matching to the cluster seeds.
3. Full calorimeter cluster reconstruction.
4. Application of identification cuts to the electron or photon candidates.

The parameters (p_T, η, isolation, etc) associated with each electron/photon candidate are fixed after the third step. In the forth step, identification cuts are applied, but the candidates themselves are not otherwise altered. To reflect this difference, a distinction will often be made between electron/photon reconstruction (steps 1-3) and its identification (step 4).

For reconstruction of electrons and photons, a calorimeter cluster is to locate suitable cluster seeds. This is done using a sliding window algorithm within the precision region of the calorimeter ($|\eta| < 2.5$). The seeds are rectangular, with a size of 5 cells by 5 cells, which corresponds to $\Delta\eta \times \Delta\phi = 0.125 \times 0.125$ over most of the calorimeter. The algorithm finds local maxima of the energy deposited within this size of window.

If a cluster seed is associated with a reconstructed track in Inner detector, an electron candidate is formed, otherwise a photon candidate is obtained. This association places a very loose requirement on the spatial separation ($\Delta\eta < 0.05$ and $\Delta\phi < 0.1$) between the cluster and the track. In addition, the ratio E/p of the cluster energy and the track momentum must be less than 10, in order to avoid association with very low momentum tracks probably unrelated to the cluster. If, however, the associated track(s) are consistent with a photon conversion, the cluster seed is considered to be a converted photon candidate, not an electron.

After electron/photon classification, the energy and position of the cluster are corrected for known systematic effects. In the case of the position (η and ϕ), these corrections mainly arise from the finite cell granularity. For the energy calculation, deposits of energy in inactive detector components also need to be accounted for. Expressed briefly, the energy of the cluster is

$$E = E_{cal} + E_{front} + E_{back}, \tag{4.1}$$

where E_{cal} is the energy deposited within the calorimeter, and the other two terms, E_{front}, E_{back} describe energy lost before entering the calorimeter and leaking out of the rear, respectively. The calorimeter term, E_{cal}, includes a position-dependent calibration factor, and takes account of energy deposited outside the cluster. The energy lost in front of the calorimeter, E_{front}, is estimated from the depositions within the calorimeter presampler.

Once all corrections have been made, the energy of the electron candidate is obtained by the energy of the cluster, as this is a better measure of the true electron/photon energy for high p_T electrons/photons.

For the electron, the measured p_T uses a combination of the calorimeter and tracking information from inner detector ($p_T = E_{clus} \cosh(\eta_{track})$), while photon uses only calorimeter information.

4.5 Electron and Photon Identification

The standard ATLAS electron and photon identification consists of a series of simple cuts on variables capable of discriminating high p_T isolated electrons and photons from the various background sources, and hence provides a robust selection for early analyses. In the long run, electron and photon performance may be optimized through the use of multivariate techniques.

The standard identification, cut-based algorithm, is based on cuts shower shapes, based on information from the reconstructed track and on the combined reconstruction. The values of cuts are optimized as a function of the measured E_T and $|\eta|$ of the electron and photon and the cuts are applied independently or in groups. For an electron, three cuts are considered depending on signal efficiency and jet rejection [76]:

- loose cuts: consists of simple shower shape cuts and very loose cuts between EM cluster and reconstructed track. The used variables of shower shape are based on the second layer of calorimeter and longitudinal leakage.
- medium cuts: which add shower shape cuts using first layer of EM calorimeter and track quality cuts.
- tight cuts: which add the cut of the energy-to-momentum ratio and use tighter track matching criteria and transition radiation information.

For photon, a single set of cuts, equivalent to "tight cuts" defined for electrons, has been optimized based on the shower shapes in the calorimeter. In addition, a simple track isolation criteria has been added to improve rejection.

The discriminating variables used for loose, medium, and tight cuts are summarized in Tab. 4.1.

Table 4.1. The summary of discriminating variables used for loose, medium and tight cuts [76]. Note that units of $\Delta\eta$ and $\Delta\phi$ are represented in number of cells.

Type	**Description**
Loose cuts	
Acceptance of detector	· $\|\eta\| < 2.4$
Hadronic leakage	· Ratio of E_T in the first layer of the hadronic calorimeter to E_T of the EM cluster
Second layer of EM calorimeter	· Ratio in η of cell energies in 3×7 versus 7×7 · Ratio in η of cell energies in 3×3 versus 3×7 · Lateral width of the shower
Medium cuts (includes loose cuts)	
First layer of EM calorimeter	· Difference between energy associated with the second largest energy deposit and energy associated with the minimal value between the first and second maxima. · Second largest energy deposit normalize to the cluster energy. · Total shower width. · Shower width for three strips around maximum strip. · Fraction of energy outside core of three central strips but within seven strips.
Track quality	· Number of hits in the pixel detector (at least one). · Number of hits in the pixels and SCT (at least nine). · Transverse impact parameter (< 1 mm).
Tight (isol) (includes medium cuts)	
Isolation	· Ratio of transverse energy in a cone $\Delta R < 0.2$ to the total cluster transverse energy.
Vertexing-layer	· Number of hits in the vertexing-layer (at least one). · Track matching $\Delta\eta$ between the cluster and the track (< 0.005). · $\Delta\phi$ between the cluster and the track (< 0.02). · Ratio of the cluster energy E/p to the track momentum.
TRT	· Total number of hits in the TRT. · Ratio of the number of high-threshold hits to the total number of hits in the TRT.
Tight (TRT) (includes tight (isol) except for isolation)	
	· TRT Same as TRT cuts above, but with tighter values corresponding to $\sim 90\%$ efficiency for isolated electrons.

CHAPTER 5

PHOTON AND ELECTRON IDENTIFICATION IN ATLAS WITH A COVARIANT MATRIX BASED METHOD

5.1 Introduction

The main sources of fake isolated high-p_T electrons and photons, at the LHC are QCD processes, with dijet events as the dominant background. To discriminate between real electrons, photons and jets one has to use their characteristic features. In the EM calorimeter, electrons and photons tend to appear as narrow showers while jets tend to have a broader profile and to deposit a significant amount of their energy in the hadronic calorimeter. In some jets most of the transverse momentum is taken by a single neutral meson decaying into photons (mainly $\eta/\pi_0 \rightarrow \gamma\gamma$). These highly electromagnetic jets can be rejected by using variables built from the shower profile in the finely η-segmented first calorimeter layer as shown in section 3.3.3.2.

The ATLAS EM calorimeter is highly segmented with three-fold granularity in depth and with fine transverse segmentation (particularly in the first EM layer). They are assisted by a presampler in front of the calorimeter. This high level of calorimeter segmentation allows for a powerful rejection of jets against the signal of prompt electrons and photons.

This chapter describes a covariant matrix based identification method (H-matrix) for electrons and photons in section 5.2 and its performance for some selected physics processes in section 5.3.

5.2 Description of the Covariant Matrix Method

The discriminating variables for shower shapes defined by calorimeter measurements are correlated. The covariant matrix technique [77, 78, 79] takes advantage of these correlations. The covariant matrix is obtained in the following way:

$$M_{ij} = \frac{1}{N}\Sigma_{n=1}^{N}(y_i^{(n)} - \overline{y}_i)(y_j^{(n)} - \overline{y}_j), \tag{5.1}$$

where indices i and j run over the fourteen variables used as inputs to the discriminant, N is the total number of electrons (or photons) used in the training sample, $y_j^{(n)}$ is the j^{th} variables for the n^{th} electron (photon) in the training sample, and $\overline{y}_i$ is the mean value of variable y_i over all electrons (photons) in the training samples. The sum over index n, runs over all events in the training sample. The training samples are pure single electron or photon Monte Carlo samples, generated with a detailed model of the ATLAS detector, base on GEANT [63].

Since the penetration depth of the photon shower is slightly larger than that of electrons, the longitudinal shower variables have different distributions for photons and electrons as illustrated in Fig. 5.1. Figure 5.2 compares some selected transverse shower variables for electrons and photons. Photons appear to have narrower transverse shower profiles than electrons of the same energy.

In order to take into account the different shower shapes of electrons and photons, two independent covariant matrices are built using single electron and single photon samples as the training samples.

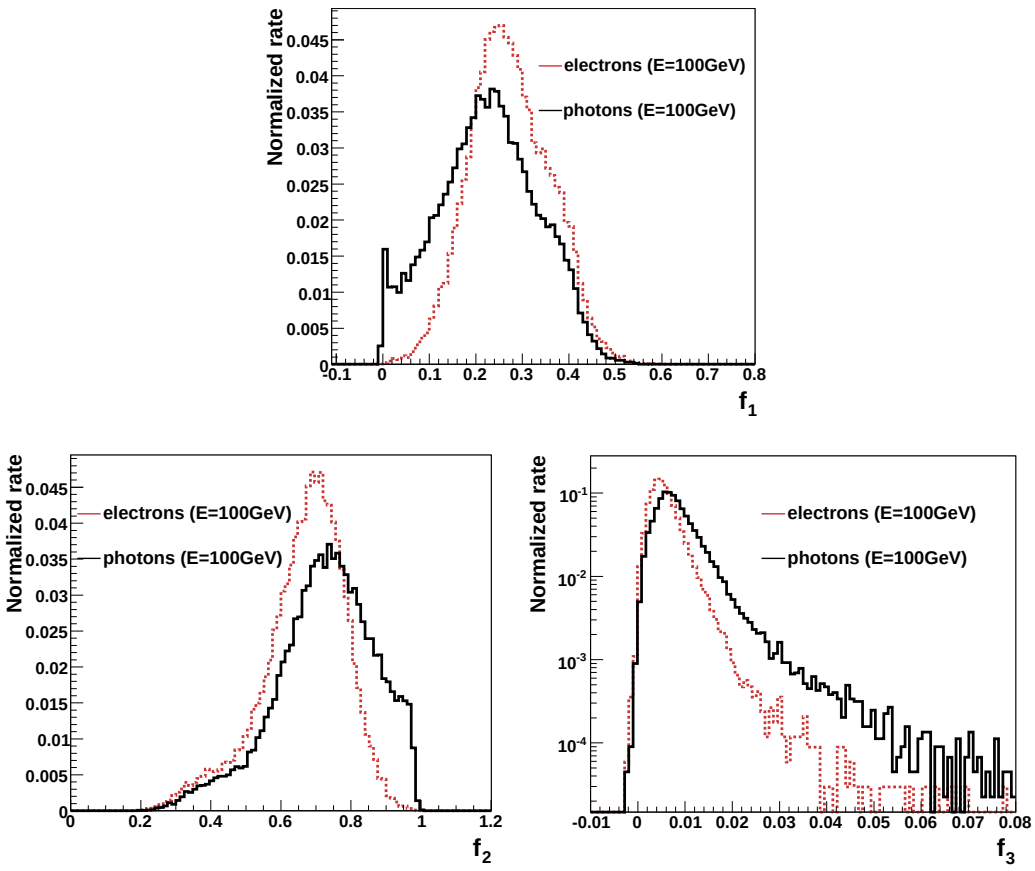

Figure 5.1. Longitudinal shower profile of electrons and photons. The histograms show fractional energies in each layer of the EM calorimeter. Further description of these variables is provided in section 5.2.2. The plots are obtained with 100 GeV electrons (dashed lines) and photons (solid lines) simulated by the geant model of the ATLAS detector.

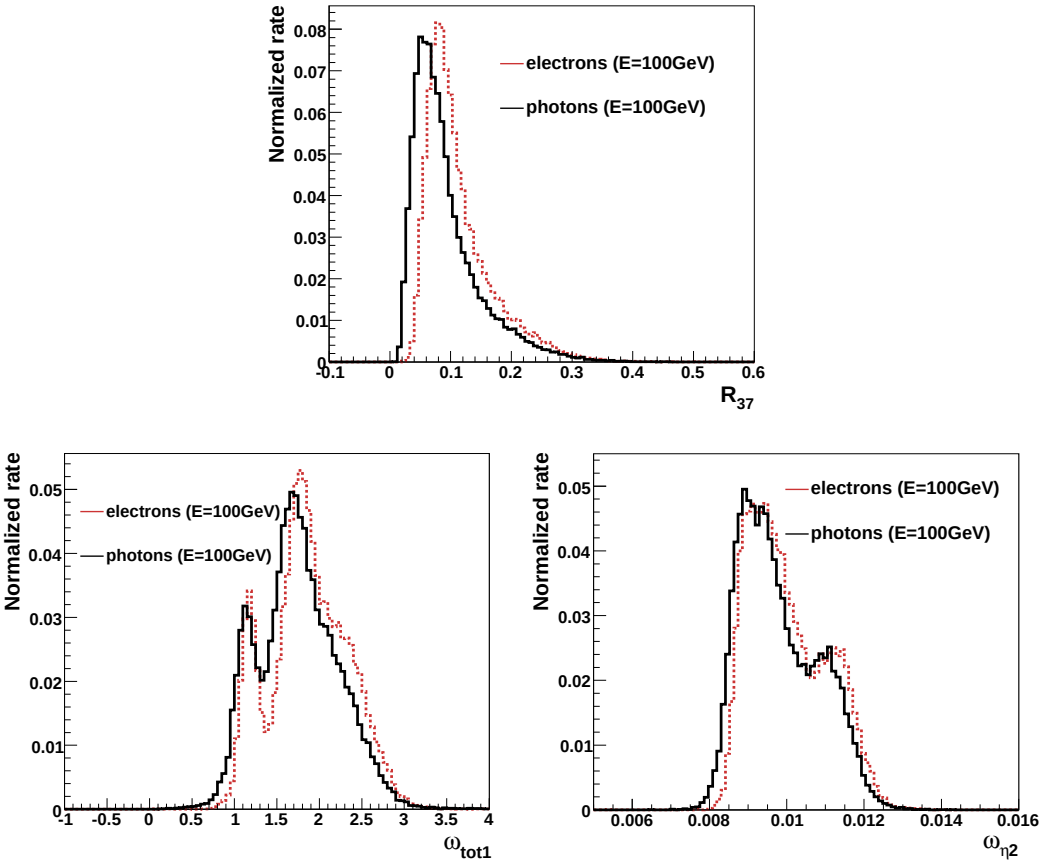

Figure 5.2. Comparison of several transverse shower shape variables for electrons and photons. The distribution of R_{37} characterizing the shower core, ω_{tot1} the shower width in the first layer, and ω_{η_2} the shower width in the second layer of the EM calorimeter. Section 5.2.2 provides further details on the definition of these variables. The plots are obtained with 100 GeV electrons (dashed lines) and photons (solid lines) simulated by the geant model of ATLAS detector.

The electron or photon likeness of an object is quantified by the value of the χ^2 defined as follows:

$$\chi^2 = \Sigma_{i,j=1}^{dim}(y_i - \overline{y}_i)H_{ij}(y_j - \overline{y}_j) \tag{5.2}$$

where $H \equiv M^{-1}$ is the inverse of the covariant matrix defined in Eq. 5.1 and the indices i and j run from 1 to the total number of variables (fourteen) which is also the dimension of the matrix, dim. The y_i are the shower properties for the electron or photon candidate under evaluation. The $\overline{y}_i$ are the mean values of the shower properties for actual electrons or photons as determined in the training samples. They are identical to the $\overline{y}_i$ used in Eq. 5.1

The value of the χ^2 is close to the dimension of the H-matrix for a candidate shower that closely resembles an electron or photon shower. χ^2 for the electron H-matrix is denoted as χ^2_e and χ^2_γ for the photon H-matrix. The discrimination power of the H-matrix between real photons and jets is illustrated in Fig. 5.3, where the χ^2_γ distribution of H-matrix for the jet sample is compared to that obtained on a pure photon sample from $H \to \gamma\gamma$ decays.

5.2.1 Training Samples

The shower development of electrons and photons in each layer of the calorimeter is dependent on the electron or photon energy. For this reason several single electron and photon samples with different energies are used as training samples. The energy of electrons and photons ranges from 10 GeV to 1000 GeV in the samples used for training. All samples are processed with the full ATLAS detector simulation based on GEANT.

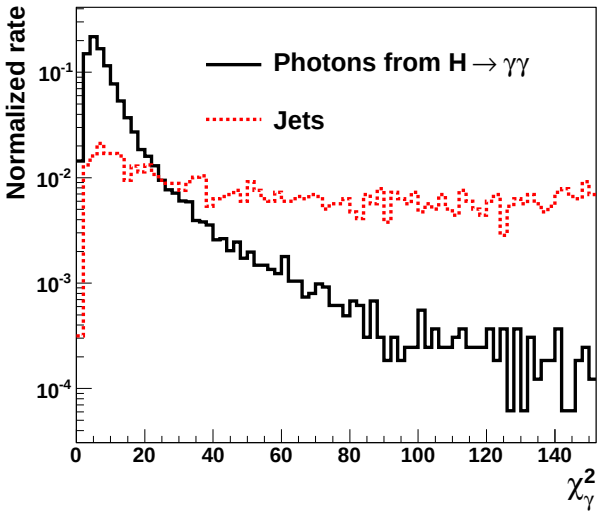

Figure 5.3. The distribution of χ^2_γ for photons from the $H \rightarrow \gamma\gamma$ sample (solid histogram) and for jets from an dijet sample (dashed histogram). Both photons and jets are required to have $E_T > 25$ GeV.

5.2.2 Discriminating Variables

In this section we describe the fourteen variables used in the ATLAS H-matrix to separate electrons or photons from jets. The fourteen variables used in the H-matrix method are the following:

- **Longitudinal shower shape variables :**
  1. The fraction of energy $f_i = E_i/E$ reconstructed in the i-th calorimeter sampling layer, where E_i is the energy deposited by the electron or photon candidate in i-th calorimeter layer and E is the total energy deposited by the electron or photon candidate in the 3 layers of the EM calorimeter plus the energy deposited in the first layer of the hadronic calorimeter. The presampler has index $i = 0$ and $i = 1, 2$ and 3 are the first, second and third layer of the EM calorimeter. The distributions of these variables for photons and jets with $E_T > 25$ GeV are shown in Fig. 5.4.

2. The hadronic leakage f_4 is shown in Fig. 5.5. It is defined as the ratio of the energy in the first layer of the hadronic calorimeter to the total energy E described above. Except for a small fraction of very high energy electrons and photons, electrons and photons deposit all energy in the EM calorimeter, thanks to the large thickness of the EM calorimeter. Jets with a large electromagnetic component will in general penetrate deeper into the calorimeter and deposit a significant amount of energy in the first hadronic layer. As shown in Fig. 5.5, f_4 has a large tail for jets, while photons deposit only a very small fraction of their energy in the first hadronic layer.

- **Transverse shower shape variables using the EM calorimeter:** R_{37} is the ratio of energy deposited outside the window $\Delta\eta \times \Delta\phi = 3 \times 3$ cells to inside a window of 3×7 cells in the all EM calorimeter layers. It is defined by:

$$1 - E(3 \times 3)/E(3 \times 7) \tag{5.3}$$

where $E(3 \times 3)$ is the sum of energies in $\Delta\eta \times \Delta\phi = 1 \times 1$ cell in the presampler and 3×1 cells in the first layer, 3×3 cells in the second layer, and 3×3 cells in the third layer of EM calorimeter. Similarly, $E(3 \times 7)$ equals to $E_0(3 \times 3) + E_1(5 \times 3) + E_2(3 \times 7) + E_3(3 \times 7)$, where the subscript refers to layer of EM calorimeter. Figure 5.6 shows the distribution of R_{37} for photons and jets.

- **Transverse shower shape variables using the second layer of the EM calorimeter:**

1. Electrons and photons deposit most of their energy in a window of $\Delta\eta \times \Delta\phi = 3 \times 7$ cells in the second layer. The lateral shower shape variables R_η (R_ϕ), is given by the ratio of the energy reconstructed in 3×7 (3×3) cells of the second layer to the energy in 7×7 (3×7) cells of the second

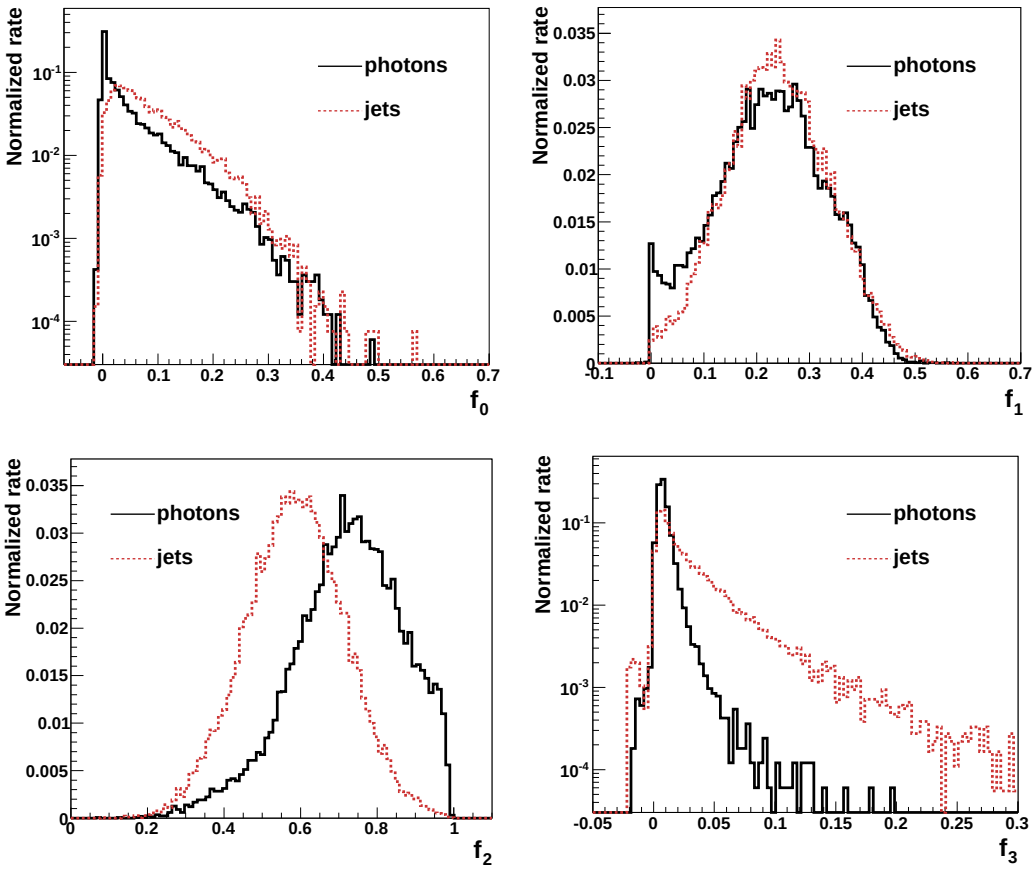

Figure 5.4. The fractional energies f_i in the presampler and the three layers of the EM calorimeter for photons in $H \rightarrow \gamma\gamma$ (solid lines) and jets (dashed lines). Both photons and jets are required to have $E_T > 25$ GeV.

layer. The magnetic field has the effect of widening the shower in the ϕ direction, thus the rejection power of $R_\phi(33)$ is less than that of $R_\eta(37)$. The distribution of $R_\eta(37)$ and $R_\phi(33)$ are shown in Fig. 5.7. It appears that showers from electrons or photons are much better contained (values closer to one) in the windows 3×3 and the 3×7 cells than the jets.

2. The lateral width in η is calculated in a window of 3×5 cells using the energy weighted sum over all cells:

$$\omega_{\eta 2} = \sqrt{\frac{\sum E_i \times \eta_i^2}{\sum E_i} - \left(\frac{\sum E_i \times \eta_i}{\sum E_i}\right)^2}. \tag{5.4}$$

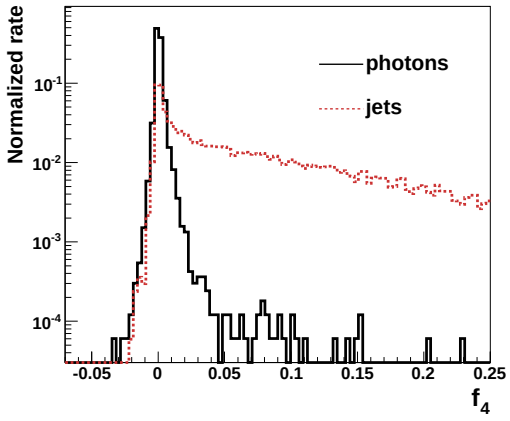

Figure 5.5. The ratio f_4 between the energy deposited in the first layer of the hadronic calorimeter and the total energy deposited E, for photons in $H \rightarrow \gamma\gamma$ (solid line) and jets (dashed line). Both photons and jets are required to have $E_T > 25$ GeV.

where E_i is the energy of the i-th cell and η_i is the pseudo-rapidity of the i-th cell. The shower width ω_{η_2} is thus given in units of pseudo-rapidity. A correction is applied as a function of the impact point within the cell to reduce the bias from the finite cell size. Figure 5.8 shows the distribution of ω_{η_2} as expected, the shower width for jets is significantly larger than for photons.

- **Transverse shower shape variables using the first layer of the EM calorimeter:**

  1. Jets with leading π^0 decays are often found to have two local maxima in terms of energy deposited in the first layer of EM calorimeter. Taking advantage of the fine granularity of the first layer of the EM calorimeter, the shower is studied in a window $\Delta\eta \times \Delta\phi = 0.125 \times 0.2$ around the strip with the most energy. Inside this region one looks for a second energy maximum. If at least two maxima are found, the energy of the second maximum E_{max2} is used to construct two variables:

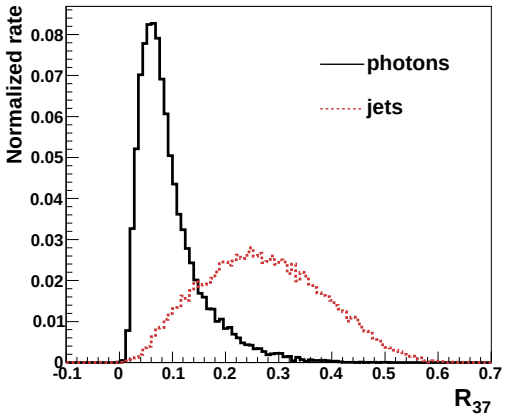

Figure 5.6. Distributions of R_{37} for photons in $H \rightarrow \gamma\gamma$ (solid line) and jets (dashed line). Both photons and jets are required to have $E_T > 25$ GeV.

i. The difference $\Delta E = E_{\rm max2} - E_{\rm min}$ between the energy associated with the second maximum $E_{\rm max2}$ and the energy reconstructed in the local minimum $E_{\rm min}$ between the first and second maxima. The left side of Fig. 5.9 shows distribution of ΔE.

ii. $R_{\rm max2} = E_{\rm max2}/(1 + 9 \times 10^{-3} E_T)$ [GeV], where E_T is the transverse energy of the cluster in the electromagnetic calorimeter and the numerical value has units of GeV^{-1}. The quantity $E_{\rm max2}$ is strongly correlated to the energy of the incoming particle. Thus even in a given of E_T range, $E_{\rm max2}$ still changes with E_T. To reduce its dependence on E_T, $E_{\rm max2}$ is corrected with this linear function of E_T. The corrected variable, $R_{\rm max2}$ is used as input to the H-matrix and its distribution is shown on the right side of Fig. 5.9.

As shown in Fig. 5.9, jets have extremely large values of ΔE and $R_{.\rm max2}$ due to the presence of a second maximum energy in the first layer. However, most photons have vary small value of these variables.

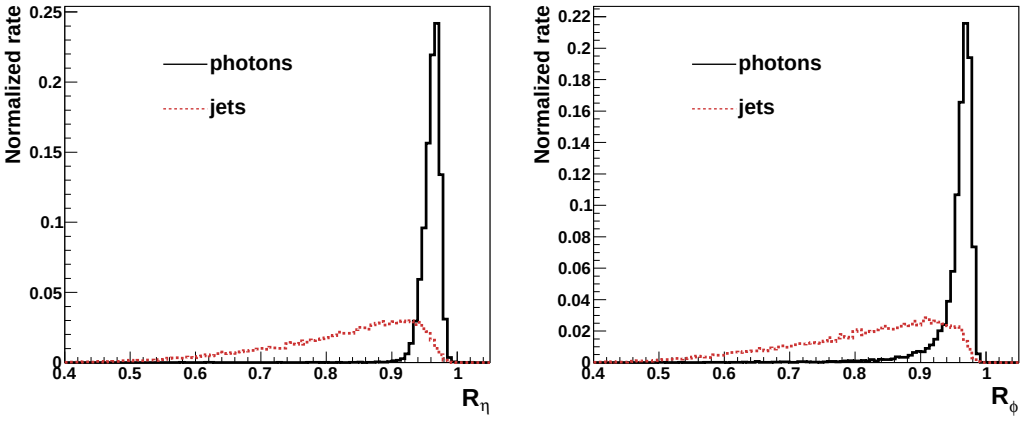

Figure 5.7. Transverse shower shape variables R_η (left) and R_ϕ (right) in the second layer of the EM calorimeter, for photons in $H \to \gamma\gamma$ (solid lines) and jets (dashed lines). Both photons and jets are required to have $E_T > 25$ GeV.

2. F_{side} is defined as the fraction of energy deposited outside the shower core of the three central strips:

$$F_{\text{side}} = \left[E(\pm 3 \text{ strips}) - E(\pm 1 \text{ strips})\right] / E(\pm 1 \text{ strips}), \tag{5.5}$$

where $E(\pm n)$ is the energy deposited in $\pm$ n strips around the strip with the highest energy in the first layer of the EM calorimeter. Figure 5.10 shows the distribution of F_{side} for jets and photons.

3. $\omega_{3\text{strips}}$ is the shower width over three strips around the one with the maximal energy deposit, its distribution is shown on the left side of Fig. 5.11. The shower width $\omega_{3\text{strips}}$ is defined as

$$\omega_{3\text{strips}} = \sqrt{\sum E_i \times (i - i_{max})^2 / \sum E_i}, \tag{5.6}$$

where i is the strip number and i_{max} is that of the most energetic strip in the first layer of EM calorimeter. It is expressed in units of the strip number and corrected for the impact point dependence.

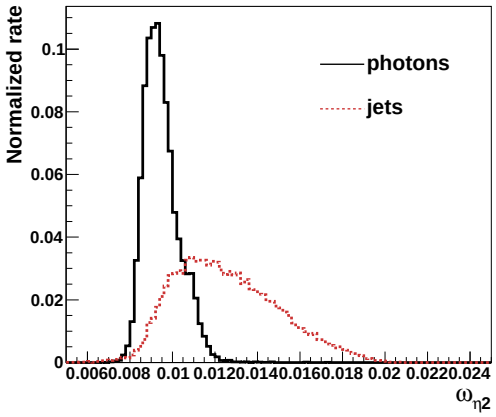

Figure 5.8. Lateral shower width ω_{η_2} in the second layer of the EM calorimeter for photons in $H \rightarrow \gamma\gamma$ (solid line) and jets (dashed line). Both photons and jets are required to have $E_T > 25$ GeV.

4. The total shower width w_{tot1} is the shower width in a window $\Delta\eta \times \Delta\phi = 0.0625 \times 0.2$, which corresponds to 40 strips of the first EM layer in η direction. The shower width ω_{tot1} is defined as

$$\omega_{\text{tot1}} = \sqrt{\sum E_i \times (i - i_{max})^2 / \sum E_i}, \tag{5.7}$$

where i is the strip number and i_{max} that of the most energetic strip in the first layer of EM calorimeter. The distribution of w_{tot1} is shown on the right side of Fig. 5.11 for photons and jets.

In total the H-matrix uses up to fourteen input variables in the fully instrumented sections of the calorimeter. There are five variables based purely on the energy profile measured with the strips in the first layer of the EM calorimeter. The purpose of these variables is to discriminate against charged hadrons but it also has the capability of discriminating against η/π^0, which is not possible with the second and third EM calorimeter layers. The five variables building on the strips are generally correlated but still each of them adds its specific contribution to discriminating power. In addition the correlations among the variables are different for different

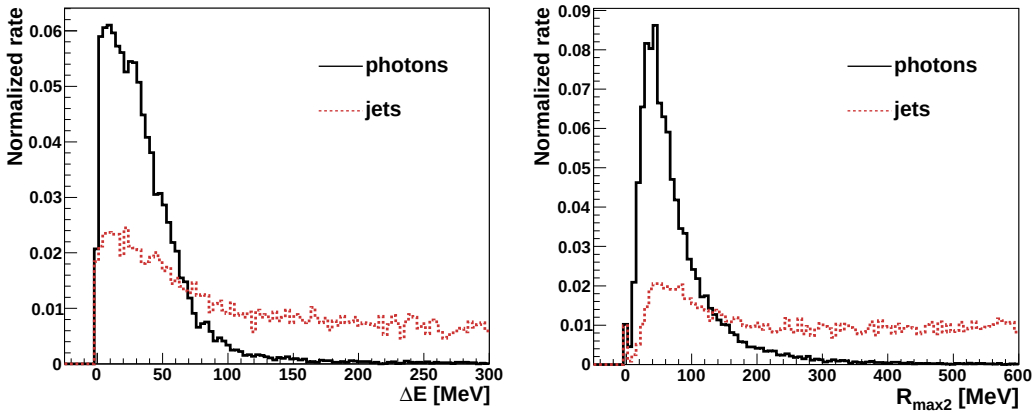

Figure 5.9. The difference ΔE between the second maximum energy and the local minimum $E_{\rm min}$ between the first and second maxima (left) and $R_{\rm max2}$ (right) in the first layer of the EM calorimeter, for photons in $H \rightarrow \gamma\gamma$ (solid lines) and jets (dashed lines). Both photons and jets are required to have $E_T > 25$ GeV.

type of particles, charged pions, η/π^0's or electrons and photons, and the H-matrix is constructed in such a way that it knows what correlations to expect for real electrons and photons. No attempt has been made to reduce the dimensionality of the matrix.

5.2.3 Energy and η Dependence of Discrimination Variables

The shower shape variables vary with η and with the cluster energy, their mean values are obtained separately in 12 bins of η presented in Tab. 5.1.

The subdivision is motivated by the changing granularities (section 3.3.3.2) and increasing amount of material in front of the EM calorimeter as a function of η. The first 7 bins cover the barrel EM calorimeter. The transition region between the barrel and end cap calorimeters, $1.37 < |\eta| < 1.52$ i.e., the crack region is excluded. The quantities calculated using the first EM layer can be used only in the regions $|\eta| < 1.52$ and $1.52 < |\eta| < 2.37$ since there is no first layer present in the crack region or beyond $|\eta| = 2.4$. The quantities calculated using the second and third EM layers, remain valid up to η =2.47. The presampler information is available in the regions

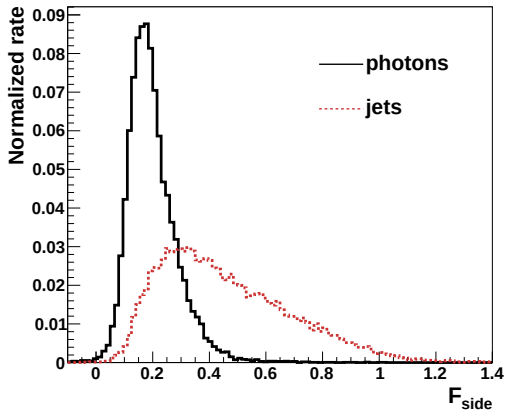

Figure 5.10. Distribution of F_{side}, the fractional energy outside the shower core in the first layer of the EM calorimeter, for photons in $H \rightarrow \gamma\gamma$ (solid line) and jets (dashed line). Both photons and jets are required to have $E_T > 25$ GeV.

$|\eta| < 1.52$ and $1.52 < |\eta| < 1.8$. Therefore, the dimension of the H-matrix will be 13 at $|\eta| > 1.8$ and 8 at $|\eta| > 2.37$ (see Fig. 3.15). The dimension of the covariant matrix is presented in Tab. 5.1 in the different η regions.

Figure 5.12 shows the shower variables R_η, $\omega_{\eta 2}$, F_{side}, for four different η regions and how η affects their shapes. The left figures are obtained for electrons with $E =$ 200 GeV and the right figures are for electrons with $E = 75$ GeV. Similarly, Fig. 5.13 shows the same shower distributions for photons. The photons showers at higher η are generally wider than at lower values of η. It can be noted that the shower appears narrower (F_{side}) at $1.0 \leq |\eta| < 1.2$ than at $0.4 \leq |\eta| < 0.6$ due to the thinner lead absorber starting at $\eta = 0.8$.

The shower variables also depend strongly on the energy of the incident electrons or photons as shown for some selected shower shape variables in Fig. 5.14. It shows the distribution of f_2, f_3 and $\omega_{3\text{strips}}$ for electrons with incident energies 500, 200, 100, 75 and 25 GeV at $0.6 \leq |\eta| < 0.8$ and $1.52 \leq |\eta| < 1.8$. Similarly, Fig. 5.15 shows the same shower distributions for photons. As expected the longitudinal shower shape

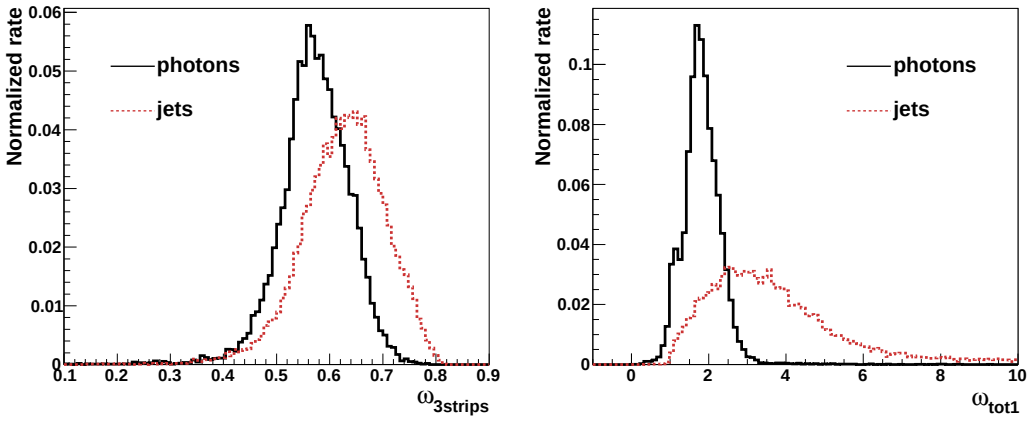

Figure 5.11. The shower width $\omega_{3\text{strips}}$ around the maximal energy deposit in the first layer (left) and the total width w_{tot1} calculated in the first layer of the EM calorimeter (right), for photons in $H \rightarrow \gamma\gamma$ (solid lines) and jets (dashed lines). Both photons and jets are required to have $E_T > 25$ GeV.

variables such as f_2 and f_3 depend strongly on the electron or photon energy. But it appears that even the shower widths in the first layer and the second layer of the EM calorimeter vary strongly with energy.

The energy dependence of the mean value of the shower shape variable $\overline{y}_i$ is studied in the range 10–1000 GeV, and parameterizations of $\overline{y}_i(E)$ are derived using the training samples. Figures 5.16 and 5.17 illustrate how the mean values of the shower variables change as a function of the energy. Each data point shows the mean value of the shower variables f_1 and ω_{tot1} for electrons of different energies. The electrons with higher energies penetrate deeper in the calorimeter leading to a lesser fractional energy f_1 in the first layer. Note that there is no electron or photon at $|\eta| > 1.8$ for $E = 10$ GeV samples because of the lower threshold of E_T (3 GeV)[1]. Therefore the behavior of mean variables at $\eta_8 = (1.6 \leq |\eta| < 1.8)$ and $E = 10$GeV due to low statistics can be explained. The mean values for low p_T electrons or

[1] $E_T = 4$ GeV at $\eta = 1.6$ and $E_T = 3$ GeV at $\eta = 1.8$ for 10 GeV electron or photon. The relation between η and E_T is given in section 3.2.1)

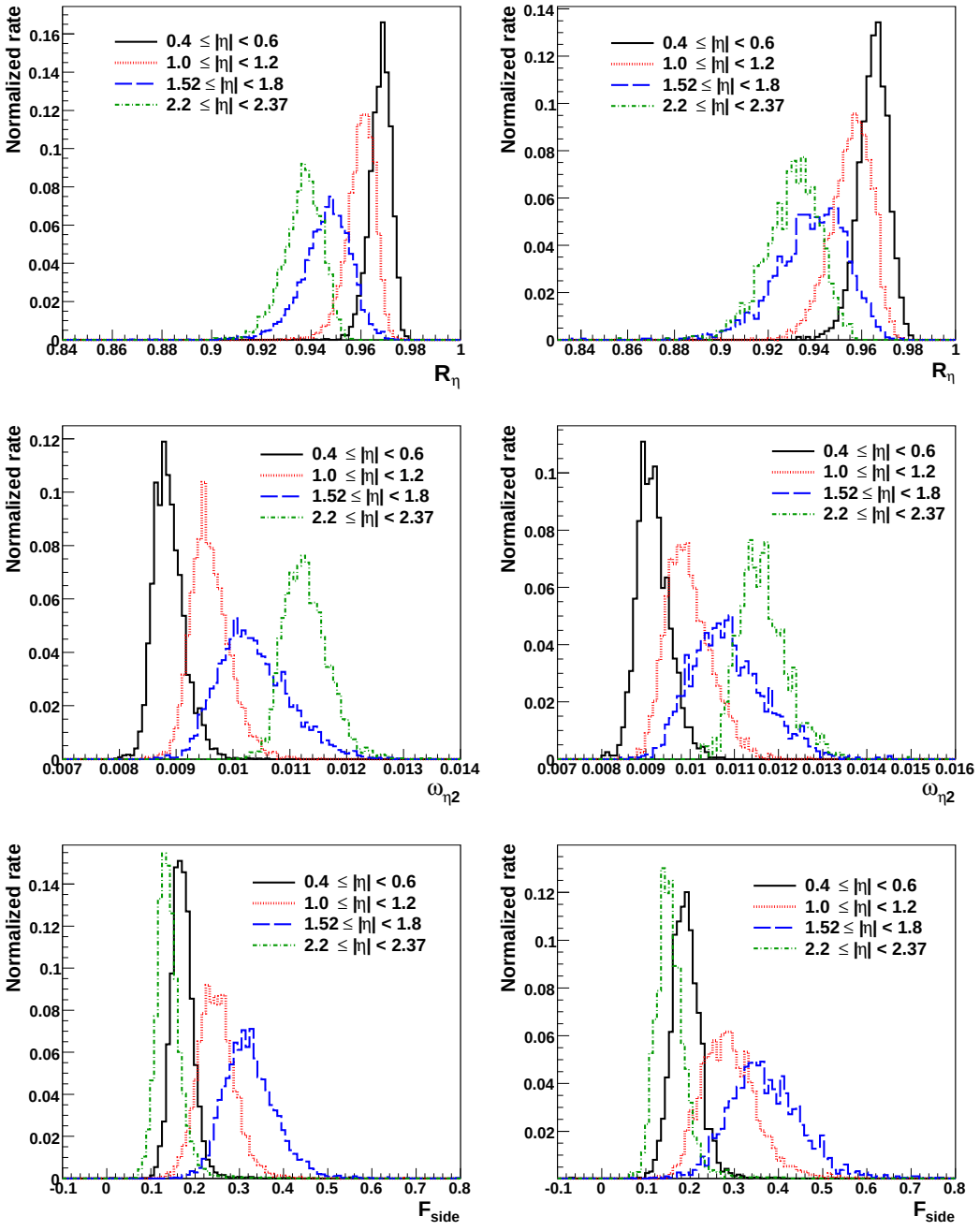

Figure 5.12. Distributions of the discriminating variables R_η, $\omega_{\eta 2}$ and F_{side} in different η regions, for electrons with an energy of 200 GeV (left) and 75 GeV (right).

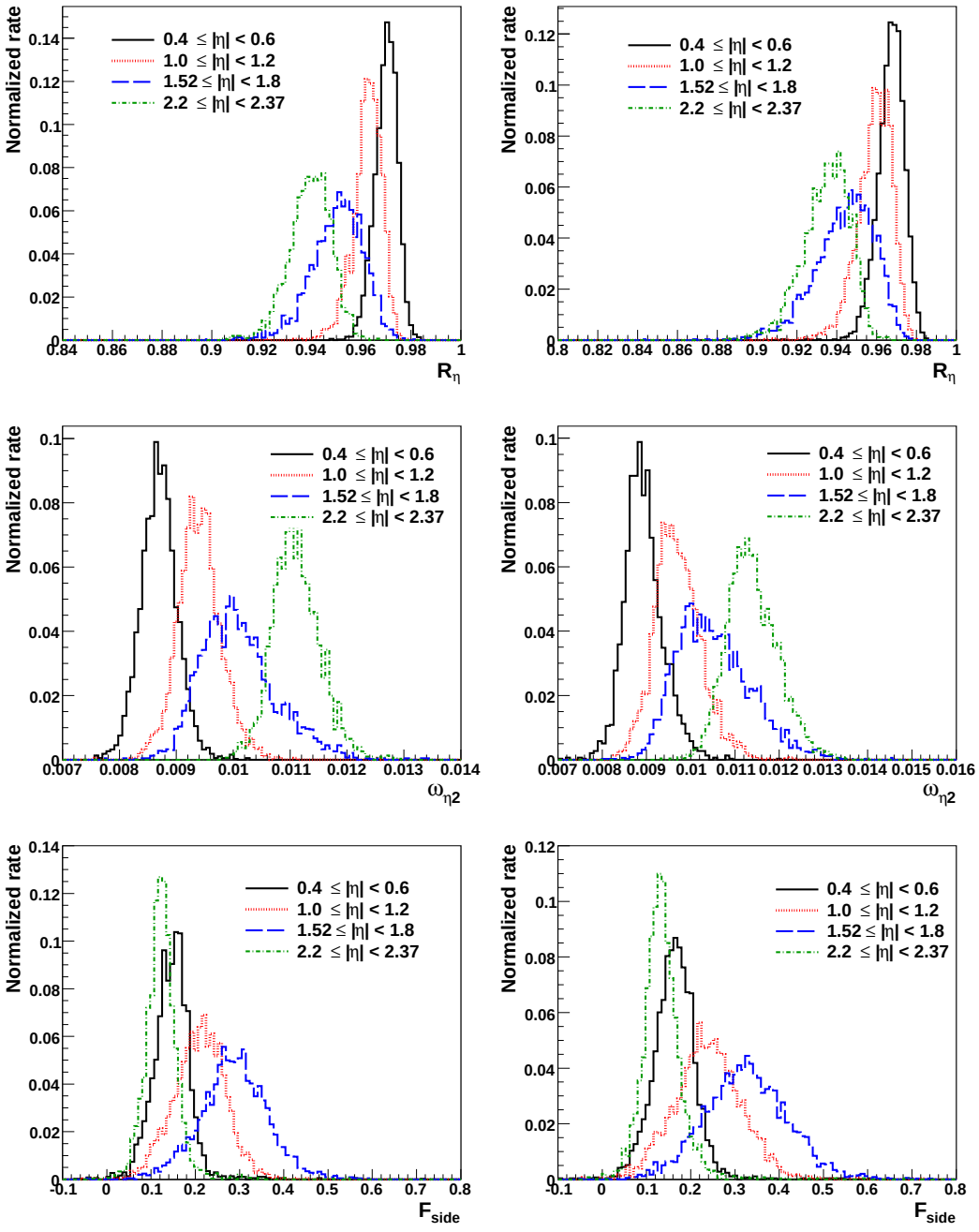

Figure 5.13. Distributions of the discriminating variables R_η, $\omega_{\eta 2}$ and F_{side} in different η regions, for photons with an energy of 200 GeV (left) and 75 GeV (right).

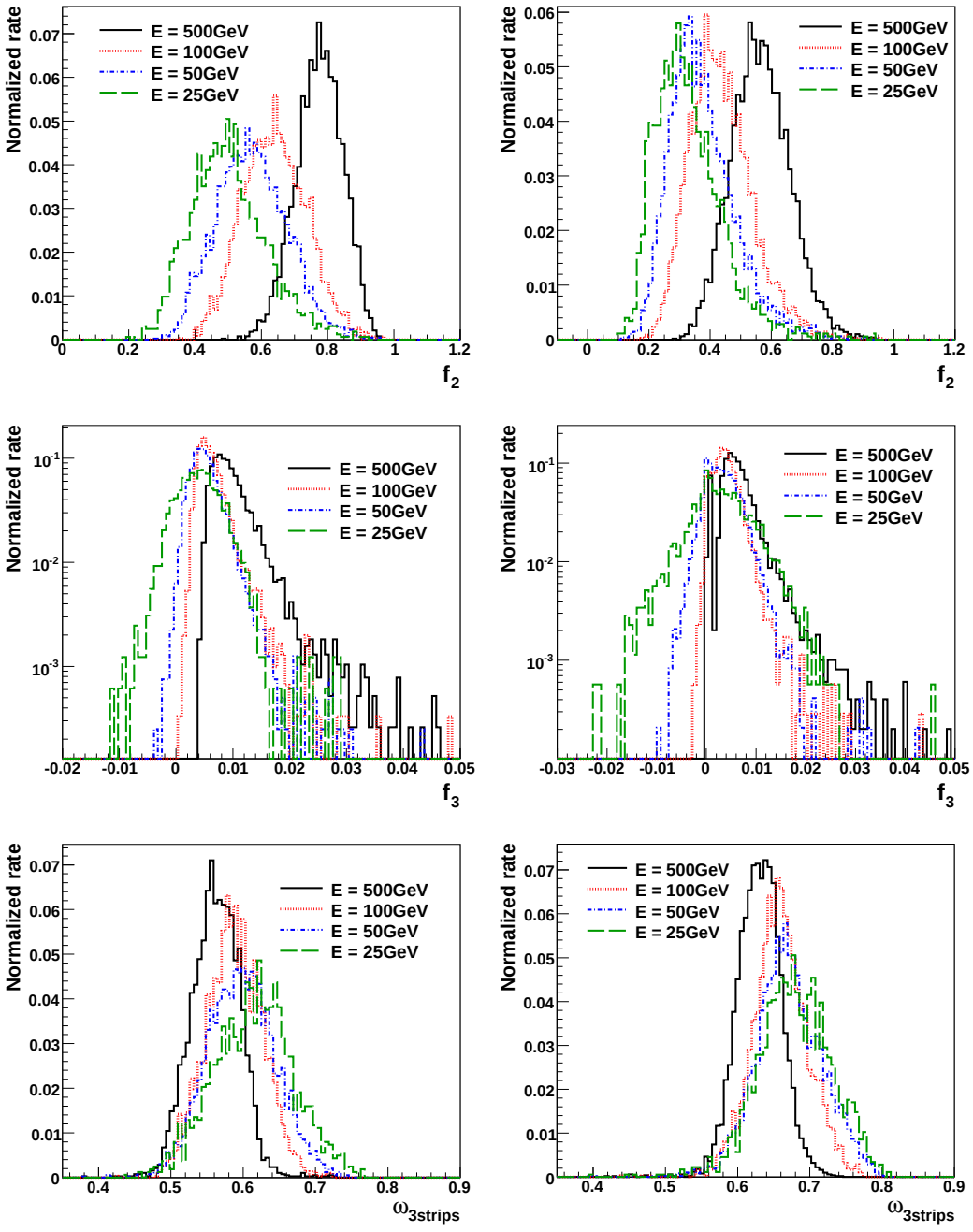

Figure 5.14. Distributions of f_2, f_3 and $\omega_{3\text{strips}}$ for electrons with $E = 500, 100, 50,$ and 25 GeV at $0.6 \leq |\eta| < 0.8$ (left) and $1.52 \leq |\eta| < 1.8$ (right).

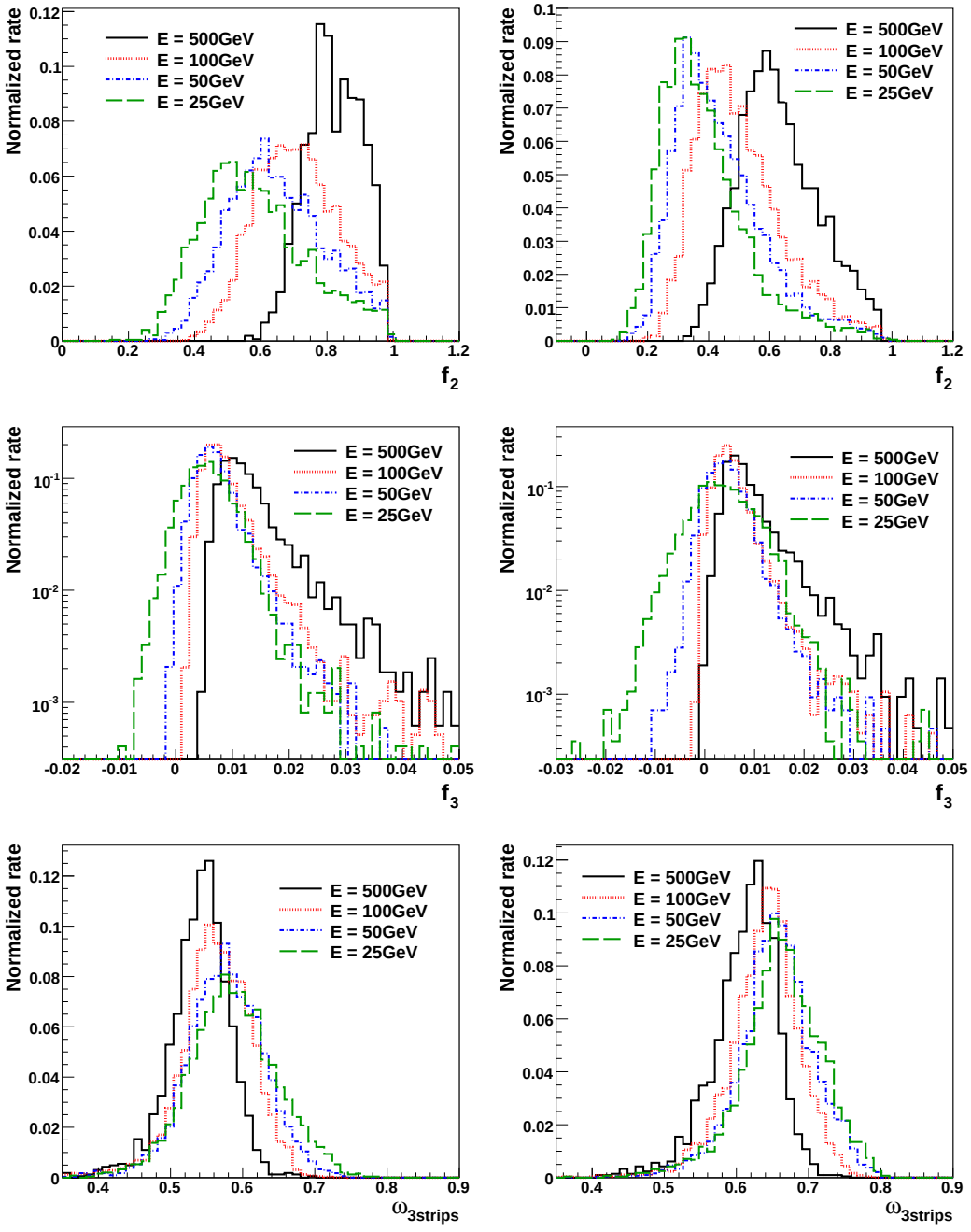

Figure 5.15. Distributions of f_2, f_3 and $\omega_{3\text{strips}}$ for photons with $E = 500, 100, 50$, and 25 GeV at $0.6 \leq |\eta| < 0.8$ (left) and $1.52 \leq |\eta| < 1.8$ (right).

Table 5.1. The twelve η bins considered to construct the electron and photon H-matrix. The η bins are grouped together in regions with the same detector characteristics, for instance the absorber thickness or the calorimeter granularity. The dimension of the H-matrix (dim) is given for each bin.

Dim = 14	Barrel absorber thickness 1
η_1	$\lvert\eta\rvert < 0.2$
η_2	$0.2 \leq \lvert\eta\rvert < 0.4$
η_3	$0.4 \leq \lvert\eta\rvert < 0.6$
η_4	$0.6 \leq \lvert\eta\rvert < 0.8$
Dim = 14	Barrel absorber thickness 2
η_5	$0.8 \leq \lvert\eta\rvert < 1.0$
η_6	$1.0 \leq \lvert\eta\rvert < 1.2$
η_7	$1.2 \leq \lvert\eta\rvert < 1.37$
Crack region $1.37 \leq \lvert\eta\rvert < 1.52$ no H-matrix	
Dim = 14	End-cap with presampler
η_8	$1.52 \leq \lvert\eta\rvert < 1.8$
Dim = 13	End-cap without presampler
η_9	$1.8 \leq \lvert\eta\rvert < 2.0$
η_{10}	$2.0 \leq \lvert\eta\rvert < 2.2$
η_{11}	$2.2 \leq \lvert\eta\rvert < 2.37$
Dim = 8	End-cap without presampler, without strips
η_{12}	$2.37 \leq \lvert\eta\rvert < 2.47$

photons are not measured properly in the forward region. Therefore H-matrix is not available for electron and photons at $|\eta| > 1.6$ for energies below 25 GeV.

Like for f_1 and ω_{tot1}, the mean values of all shower variables have a strong energy dependence. Therefore the mean values $\overline{y}_i$ are parameterized as a function of energy. There is one parameterization per variable and per η bin.

The adopted parameterization for shower variables are the following:

$$\overline{y}_i(E) = a \times \sqrt{E} + b \times \sqrt{\frac{1}{E}} + c. \tag{5.8}$$

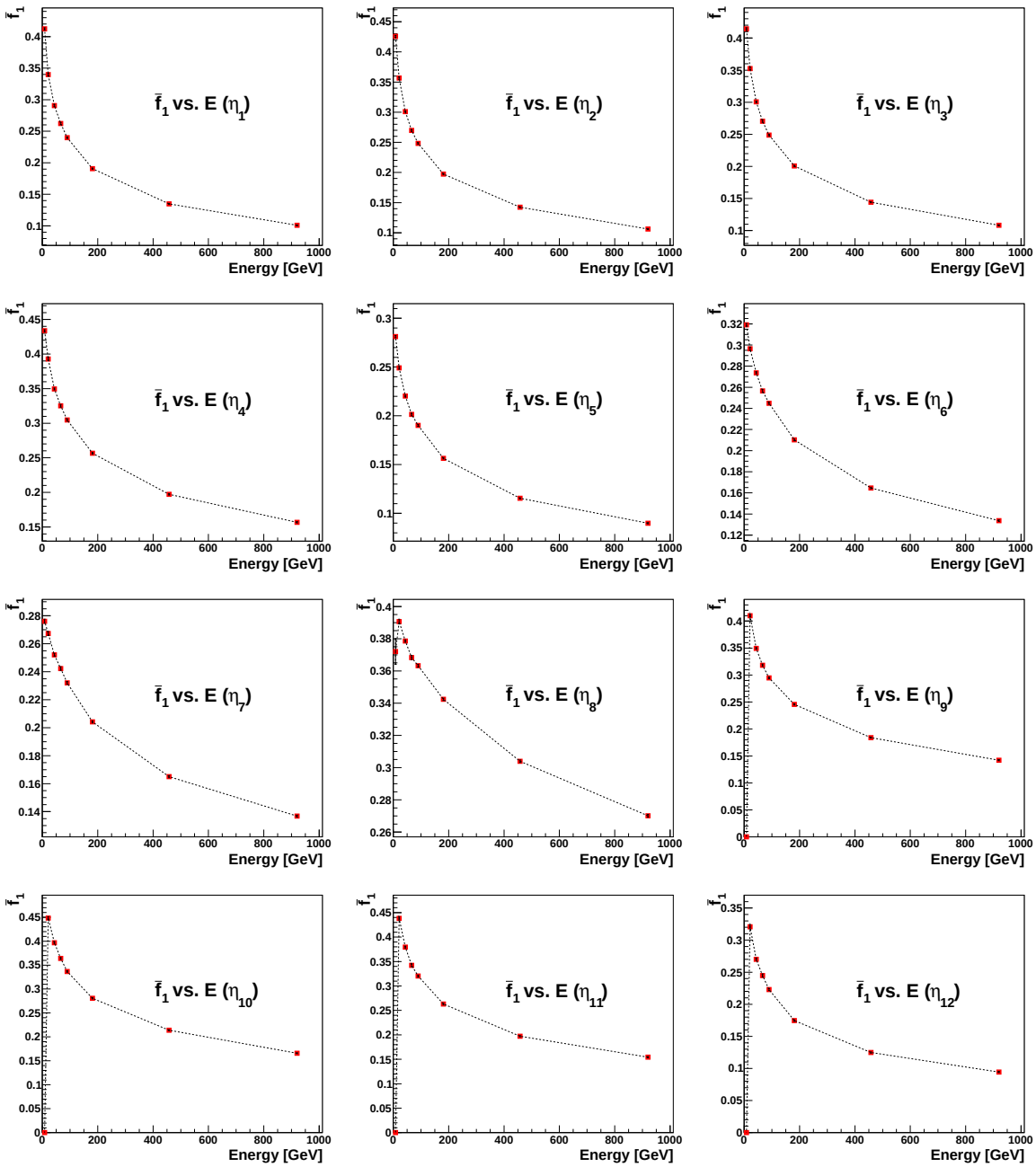

Figure 5.16. Mean value of the fractional energy in the strip layer f_1 as a function of the incident energy of electron/photon in different η bins, here shown for single electrons.

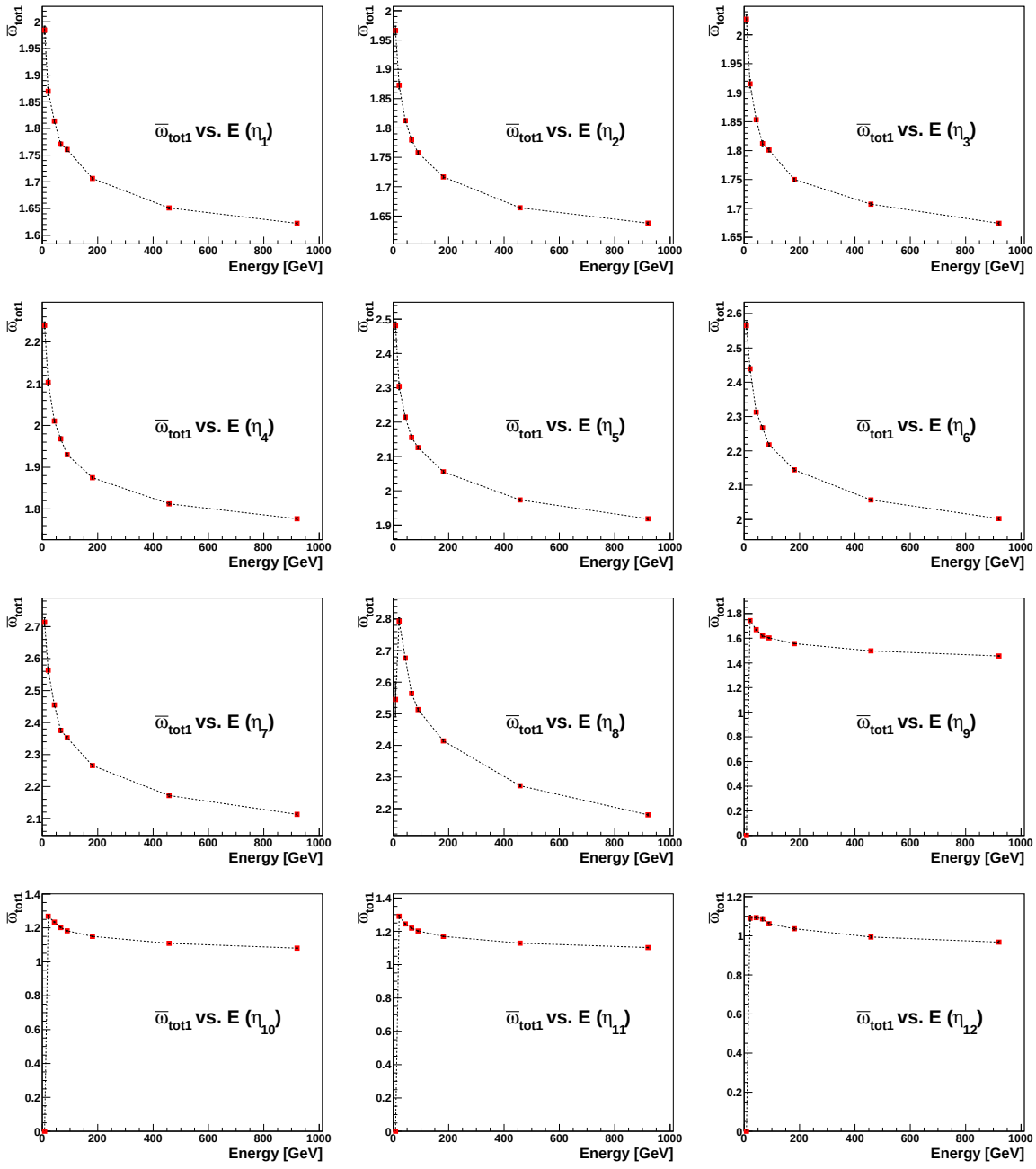

Figure 5.17. Mean value of total width in the strip layer ω_{tot1} as a function of the incident energy of electron/photon in different η bins, here shown for single electrons.

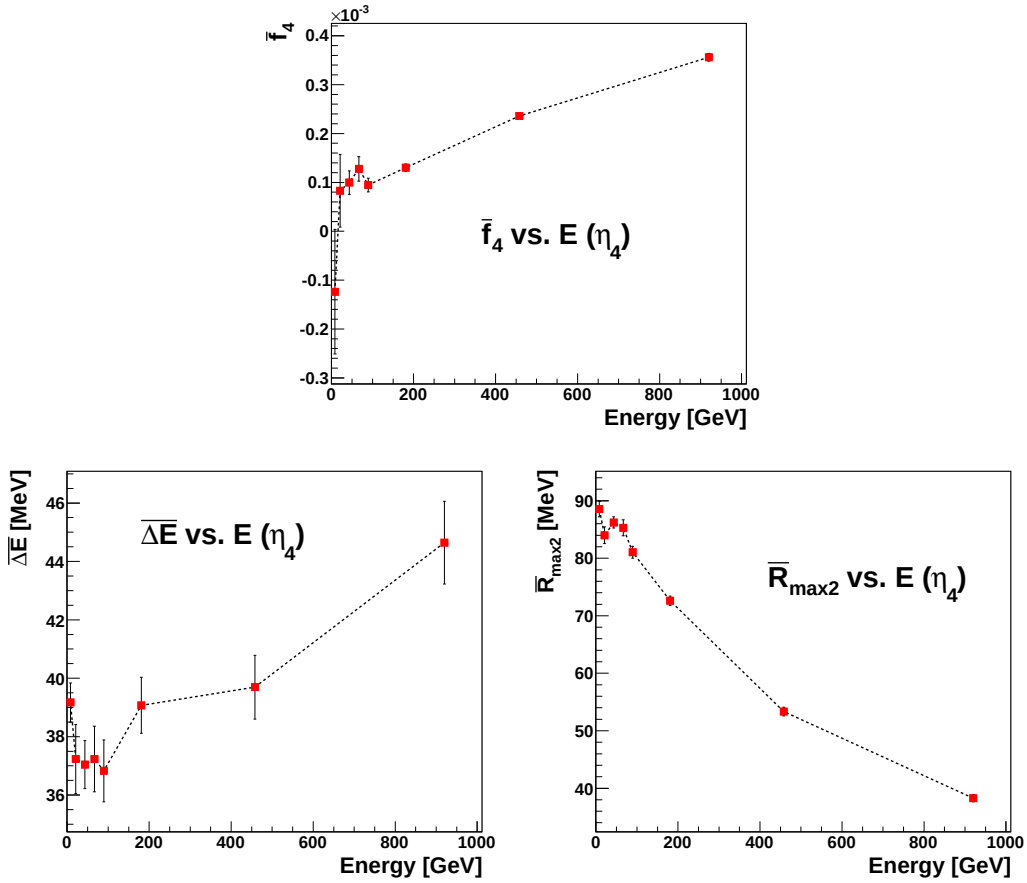

Figure 5.18. Mean values of f_4, $R_{\rm max2}$ and ΔE as a function of the electron energy in the region η_4 ($0.6 \leq |\eta| < 0.8$).

$$\overline{y}_i(E) = a \times \frac{1}{E} + b \times \sqrt{\frac{1}{E}} + c. \tag{5.9}$$

where a, b, and c are the coefficients fitted in each η bin. The shower variable f_3 is parameterized using Eq. 5.8 and the others except for f_4, $R_{\rm max2}$ and ΔE using Eq. 5.9. The parameterizations with equations 5.8 and 5.9 are adopted on all the η ranges. A linear interpolation is used in the case of f_4, ΔE and $R_{\rm max2}$ due to their behavior at the low energies as shown in Fig. 5.18. The linear interpolation between neighboring points is used to parameterize the energy dependence for these three variables.

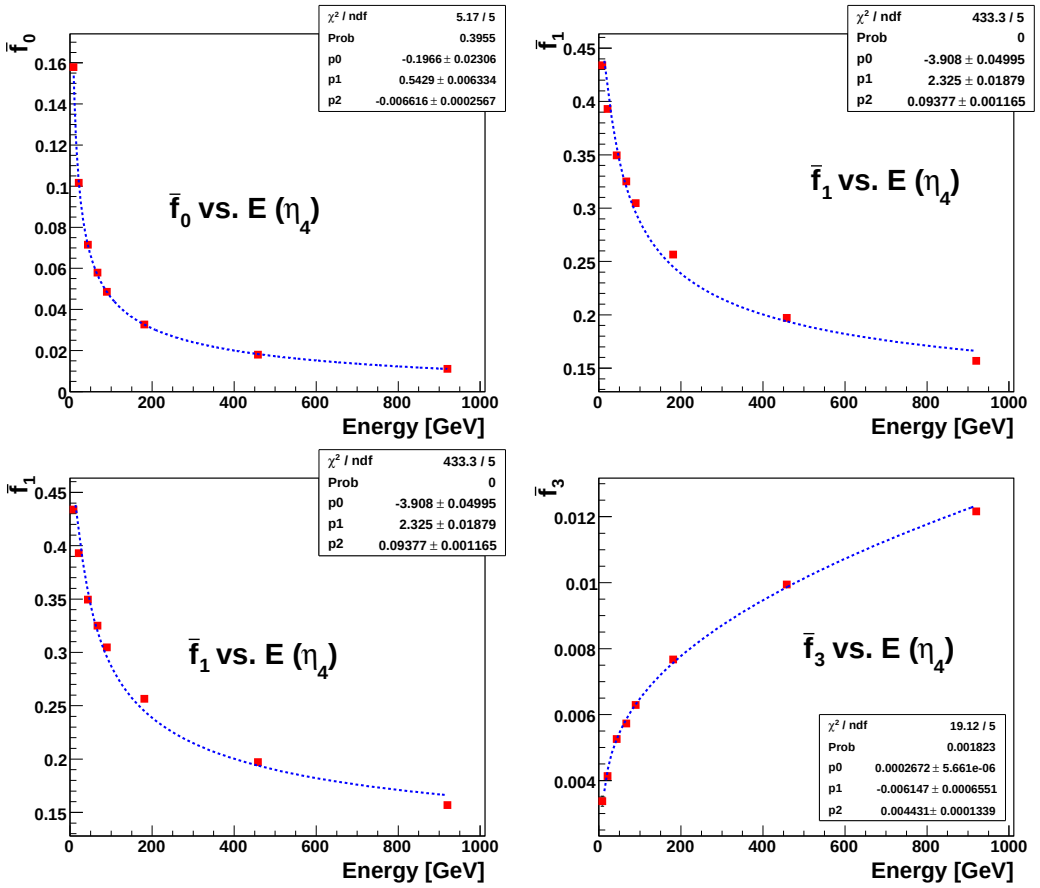

Figure 5.19. The energy dependence of the mean values of f_0, f_1, f_2 and f_3 in the region η_4 ($0.6 \leq |\eta| < 0.8$). The fitted points are the mean values of the variables at different energies. They are fitted by the functions described in Eqs. 5.8 and 5.9. The data points and parameterizations shown here are for electrons.

Figures 5.19, 5.20 and 5.21 show the parameterizations of the mean values for these variables except for f_4, $R_{\max 2}$ and ΔE. These figures show the energy behavior in the η_4 region. The data points are the mean values of the shower variables in the region η_4 and the dashed lines are the chosen parameterizations. The values of $p0$, $p1$, and $p2$ displayed in the figures corresponding to the parameters a, b and c of Eqs. 5.8 and 5.9. As an example, the fitted parameters in the region η_4 are given in Tab. 5.2.

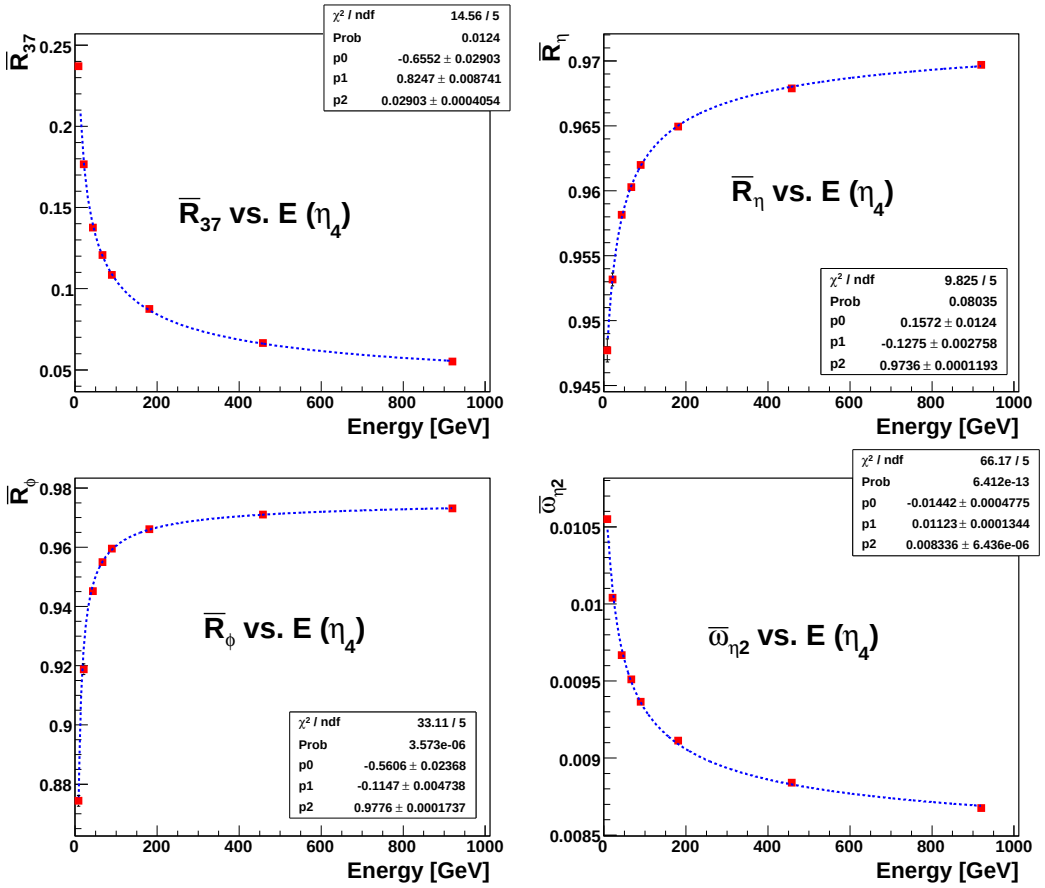

Figure 5.20. The energy dependence of the mean values of R_{37}, R_{η}, R_{ϕ} and ω_{η_2} in the region η_4 ($0.6 \leq |\eta| < 0.8$). The points are the mean values of the variables at different energies. They are fitted by the function described in Eq. 5.9. The points and parameterizations shown here are for electrons.

5.2.4 Covariant Matrix

Once the mean values of the shower variables are parameterized, the covariant matrix, M is built following Eq. 5.1 with $\overline{y}_i(E)$ derived in the previous section.

In certain η regions the dimension of the covariant matrix is reduced as described in Tab. 5.1. For $|\eta| > 1.8$, the dimension of the covariant matrix is 13 because of the absence of presampler in this region and dimension 8 for $|\eta| > 2.37$ where there is no strip layer nor presampler.

As an example, the following element of the covariant matrix:

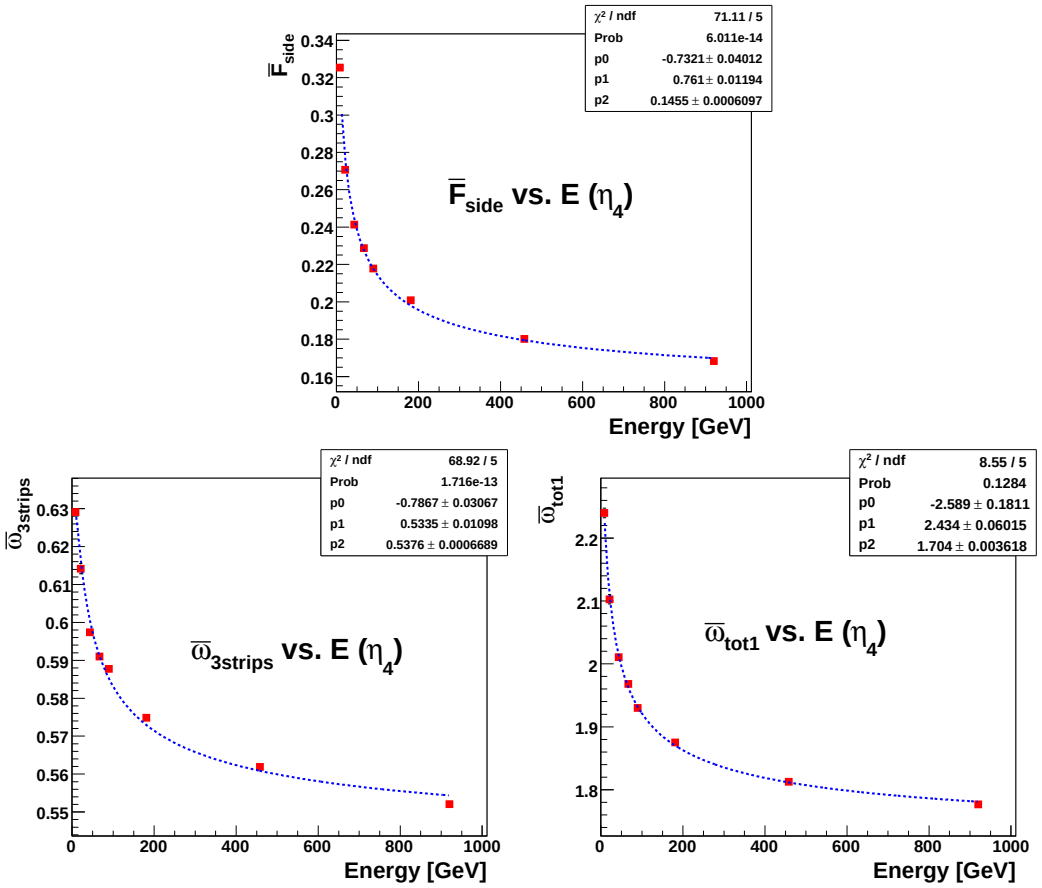

Figure 5.21. The energy dependence of the mean values of $F_{\rm side}$, $\omega_{\rm 3strips}$ and $\omega_{\rm tot1}$ in the region η_4 ($0.6 \leq |\eta| < 0.8$). The points are the mean values of the variables for electrons at different energies and fitted by the function described in Eq. 5.9.

$$M(f1_1, \omega_{\rm tot1}) = (1/N)\Sigma_{n=1}^{N}(f_1^{(n)} - \overline{f}_1)(\omega_{\rm tot1}^n - \overline{\omega}_{\rm tot1}) \tag{5.10}$$

is shown in the regions η_1, η_4, η_7, η_{11} as a function of the electron energy in Fig. 5.22. $\overline{f}_1$ is the mean value of f_1 shown in the Fig. 5.16 and $\overline{\omega}_{\rm tot1}$ is that of $\omega_{\rm tot1}$ shown in the Fig. 5.17.

The Fig. 5.22 confirms that the covariant matrix elements also change with the incident energy and η of electron or photons, but there is no specific trend in the relation between the covariant elements as a function of the energy of the photon or the electron. A simple linear interpolation is used to extract the energy depen-

Table 5.2. The fitted parameters to the mean values of the shower variables as function of energy in the region η_4 for electrons. Since the parameters f_4, R_{emax2} and ΔE are determined by linear interpolation, they are not given in this table. The columns two to four show the results for the fit for a, b and c, corresponding to the parameters of Eq. 5.8 and Eq. 5.9.

Variables	**a**	**b**	**c**
f_0	$-0.20 \pm 2.31 \times 10^{-2}$	$0.54 \pm 6.34 \times 10^{-3}$	$(-6.62 \pm 0.26) \times 10^{-3}$
f_1	$-3.91 \pm 4.99 \times 10^{-2}$	$2.33 \pm 1.88 \times 10^{-2}$	$0.09 \pm 1.17 \times 10^{-2}$
f_2	$4.07 \pm 6.43 \times 10^{-2}$	$-2.83 \pm 2.33 \times 10^{-2}$	$0.90 \pm 1.35 \times 10^{-2}$
f_3	$(2.67 \pm 0.06) \times 10^{-4}$	$-0.01 \pm 6.54 \times 10^{-4}$	$(4.43 \pm 0.13) \times 10^{-3}$
R_{37}	$-0.66 \pm 2.90 \times 10^{-2}$	$0.83 \pm 8.74 \times 10^{-3}$	$0.03 \pm 4.06 \times 10^{-4}$
R_η	$0.16 \pm 1.23 \times 10^{-2}$	$-0.13 \pm 2.74 \times 10^{-3}$	$0.97 \pm 1.19 \times 10^{-4}$
R_ϕ	$-0.56 \pm 2.37 \times 10^{-2}$	$-0.12 \pm 4.74 \times 10^{-3}$	$0.98 \pm 1.74 \times 10^{-4}$
ω_{η_2}	$-0.01 \pm 4.70 \times 10^{-4}$	$0.01 \pm 1.29 \times 10^{-4}$	$(8.32 \pm 0.06) \times 10^{-4}$
ω_{3strips}	$-0.79 \pm 3.07 \times 10^{-2}$	$0.53 \pm 1.10 \times 10^{-2}$	$0.54 \pm 6.69 \times 10^{-4}$
F_{side}	$-0.73 \pm 4.01 \times 10^{-2}$	$0.76 \pm 1.20 \times 10^{-2}$	$0.15 \pm 6.10 \times 10^{-4}$
ω_{tot1}	$-2.59 \pm 1.81 \times 10^{-1}$	$2.43 \pm 6.02 \times 10^{-2}$	$(1.70 \pm 0.36) \times 10^{-2}$

dence of the covariant matrix elements. The straight lines between two points in the Fig. 5.22 represent the linear interpolation and are calculated according to the following equation:

$$f(E) = M_i + (E - E_i) \times \frac{M_i - M_{i+1}}{E_i - E_{i+1}}. \tag{5.11}$$

where (E_i, M_i) are the coordinates of point P_i and (E_{i+1}, M_{i+1}) are the coordinates of point P_{i+1}, where the two points P_i and P_{i+1} are two consecutive points. E is the energy of the electron or the photon. The parameters fixing the energy dependence of the elements of M are obtained in each η bin.

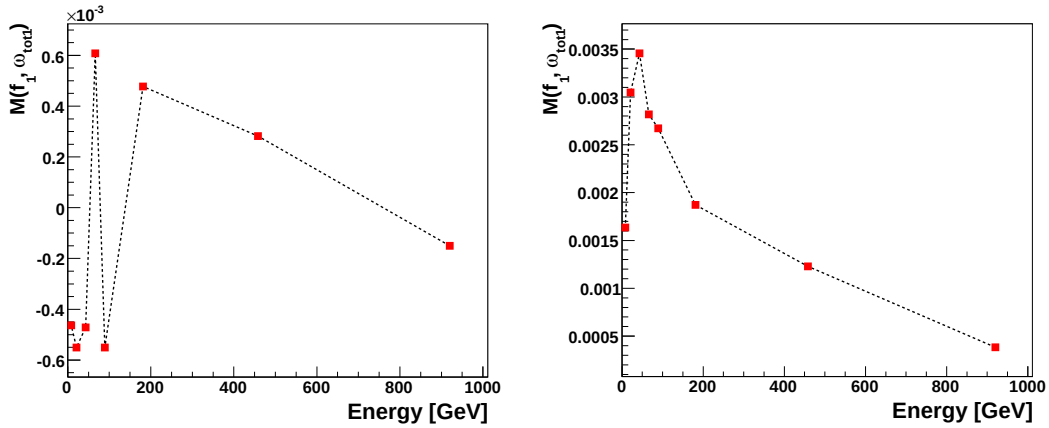

(a)

(b)

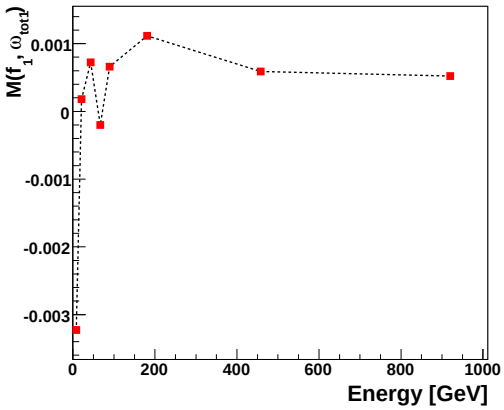

(c)

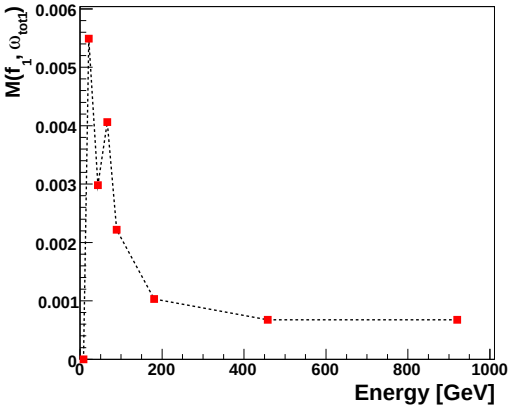

(d)

Figure 5.22. Covariant matrix element M(f_1, ω_{tot1}) in the regions (a) η_1, (b) η_4, (c) η_7 and (d) η_{12} as a function of the electron energy. These plots were produced by single electron samples.

5.2.5 H-matrix for Jets

5.2.5.1 Motivation

The two other ATLAS electron and photon identification methods, log-likelihood ratio and cut-based algorithms are optimized using information of both signal and background (i.e. jets). The log-likelihood ratio uses the exact shapes of background background for p.d.f. construction and the cut-based algorithm sets the cuts values by looking at both the signal and backgrounds shapes. In the case of a H-matrix based discriminant, the way to incorporate the background shape is to build a separate H-matrix discriminant for the background, denoted χ^2_{jet} and then combine it with the signal H-matrix discriminant χ^2_γ [79].

5.2.5.2 Derivation of Jet H-matrix

In order to enhance the performance of the photon H-matrix, a jet H-matrix is built using the shower shape of jets. In this section, the construction of the jet H-matrix is briefly described.

The selected training samples for the jet H-matrix are γ+jet samples generated in different E_T ranges. The training samples are summarized in Tab. 5.3. The γ+jet process where a jet fakes a second photon is one of the main sources of background in the search for the $H \rightarrow \gamma\gamma$ decay channel. For the jet H-matrix derivation, the jet away from the photon is used to extract the shower properties of the jets. It is appropriate to build the jet H-matrix on one of the main sources of background to the $H \rightarrow \gamma\gamma$ signal. These samples are generated with PYTHIA [65] and then run through the GEANT [63] model of the ATLAS detector.

The following steps are applied to select fake photons in the γ+jet samples:

Table 5.3. The γ+jet samples used to build the jet H-matrix with the sample name, the E_T range refers to the E_T range used to generate the hard parton opposite to the photon. The last column gives the cross-section of the sample, taking into account the parton level selections. For the photon, the parton level filter requires photons within $|\eta| < 2.7$ and $E_T > 10$ GeV.

Samples	E_T **range (GeV)**	σ **(pb)**
γ+jet1	17 – 35	$1.49\ 10^5$
γ+jet2	35 – 70	$1.88\ 10^4$
γ+jet3	70 – 140	$2.12\ 10^3$
γ+jet4	140 – 280	$1.87\ 10^2$
γ+jet5	280 – 400	11.6

- Step 1: Select reconstructed photons which must be within $\Delta R < 0.2$ of the corresponding Monte Carlo truth photons.
- Step 2: Select a true jet opposite to the photon selected by step 1. The azimuthal angle ϕ between truth jets and the photons must be larger than 2.7.
- Step 3: Among the jets selected by step 2, only loose photon candidates within $\Delta\ R < 0.4$ of the truth jets are selected as fake photons.

Using the fake photons selected by the steps described above, the mean values of the fourteen shower variables (same variables as for the photon and electron H-matrix) are parameterized and the covariant matrix M is built using Eq. 5.1 in the same η bins as described in Tab. 5.1. Due to the fact that the γ+jets Monte Carlo samples have been generated in bins of E_T, the jet H-matrix is based on the E_T of the photon candidate. The parameterization of the E_T dependence of the mean values of the jet shower shape variables and of the M matrix elements are done by linear interpolation, in the same way as for the electron and photon H-matrix.

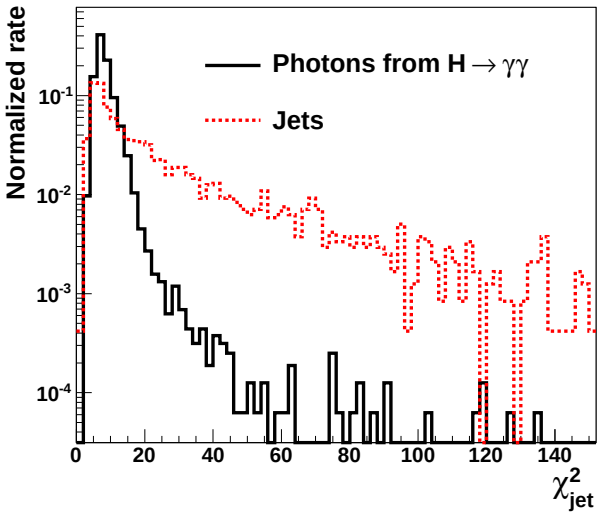

Figure 5.23. The distribution of χ^2_{jet} for photons and jets. The solid line histogram is for true photons from $H \rightarrow \gamma\gamma$, and the dashed histogram is for fake photons found in a dijet sample. The photon candidates are required to have $E_T > 25$ GeV.

Then, χ^2_{jet} for jet H-matrix is calculated using Eq. 5.2. Figure 5.23 shows the χ^2_{jet} distribution for true photons from $H \rightarrow \gamma\gamma$ decay and for fake photons in a dijet sample.

5.3 Performance of the Covariant Matrix Based Algorithm

5.3.1 Data Sets

The efficiency of the photon H-matrix is determined using a $H \rightarrow \gamma\gamma$ Monte Carlo sample generated with $m_H = 120$ GeV/c^2. It provides real photons in the intermediate E_T range. For electron H-matrix efficiency calculation a $Z \rightarrow ee$ sample is used. Finally the rejection power against the background for both electron and photon H-matrices is estimated using a dijet sample, containing all hard-scattering QCD process with $E_T > 15$ GeV. The performance of the H-matrix is compared with the standard ATLAS cut-based algorithm.

5.3.2 Performance of Electron H-matrix

5.3.2.1 Object Selection and Definitions

For performance study, the identification efficiency is defined as follows:

$$\varepsilon = \frac{N_e^{reco}}{N_e^{truth}} \tag{5.12}$$

where N_e^{truth} is the number of true electrons resulting from Z decays and requiring $E_T > 17$ GeV and $0 \leq |\eta| \leq 1.37$ or $1.52 \leq |\eta| \leq 2.47$. N_e^{reco} is the number of reconstructed and identified electron candidates satisfying the following requirements:

- The reconstructed electron must be within $\Delta R < 0.2$ of the Monte Carlo truth electrons resulting from the Z decay.
- The reconstructed electrons must be in the pseudo-rapidity $0 \leq |\eta| \leq 1.37$ or $1.52 \leq |\eta| \leq 2.47$, thus avoiding the calorimeter crack region and requiring the electron to be within the acceptance region.

The jet rejection is defined as follows:

$$R = n\frac{N_{jet}}{N_{fake\,e}} \tag{5.13}$$

where N_{jet} is the total number of jets in analyzed samples and $N_{fake\,e}$ is the number of fake electrons identified in the jet sample. The parameter n is the average number of jets with E_T above 17 GeV and in the calorimeter acceptance volume of $|\eta| < 2.4$, per generated Monte Carlo dijet event. The value of n is 0.74.

5.3.2.2 Performance using the $Z \rightarrow ee$ Monte Carlo sample

The distribution of discriminant χ_e^2 for electrons from Z decays is shown in Fig. 5.24 together with the distribution of χ_e^2 for jets. The χ_e^2 curve for jets shows

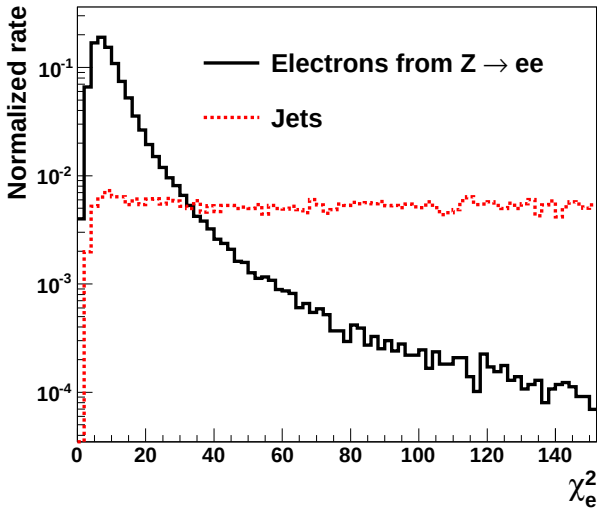

Figure 5.24. Distribution of χ^2_e for electrons and jets. The black solid histogram is for electron from Z decays, the dashed histogram is for jets from a dijet sample. The photon candidates are required to have $E_T > 17$ GeV.

a much wider distribution than that of electrons, and a χ^2_e cut can be adjusted to obtain the desired efficiency for electrons or rejection for jets.

The rejection versus efficiency curve is presented in Fig. 5.25. A tighter cut on χ^2_e helps to increase the rejection against jets, but leads to worsened efficiency. Figure 5.26 shows the efficiency of the H-matrix χ^2_e discriminant for real electrons as function of E_T and η for three different cut values. One observes that in the region with $E_T > 20$ GeV, the efficiency of the H-matrix is constant with E_T and η, for a given χ^2_e cut value. The drop in efficiency around $|\eta| = 1.5$ is due to an edge effect in the proximity of the crack region and the poorer granularity on the first sampling of the calorimeter in this area.

Table 5.4 shows the overall efficiency and rejection for electron H-matrix. The H-matrix has 90%, 91% and 95% overall efficiencies at 22, 25 and 36 of cut values.

In order to compare the performance of the electron H-matrix with the ATLAS cut-based algorithm, the cut value on χ^2_e is tuned in bins of E_T so that in each bin

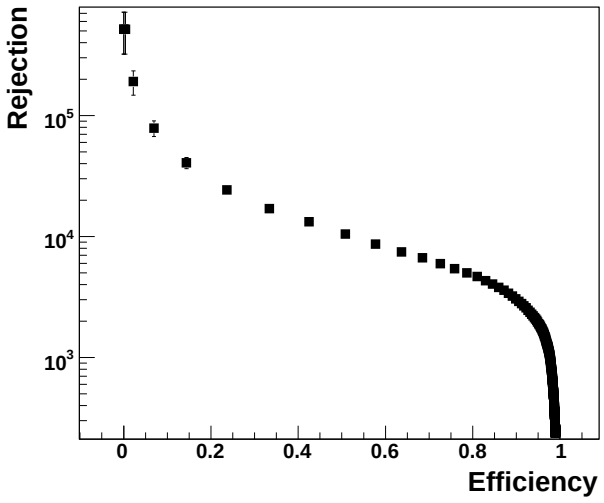

Figure 5.25. Rejection versus efficiency curve for the χ^2_e H-matrix discriminant. For each cut value on χ^2_e the efficiency is calculated for electrons in $Z \rightarrow ee$ and the rejection is calculated with fake electrons in a dijet sample.

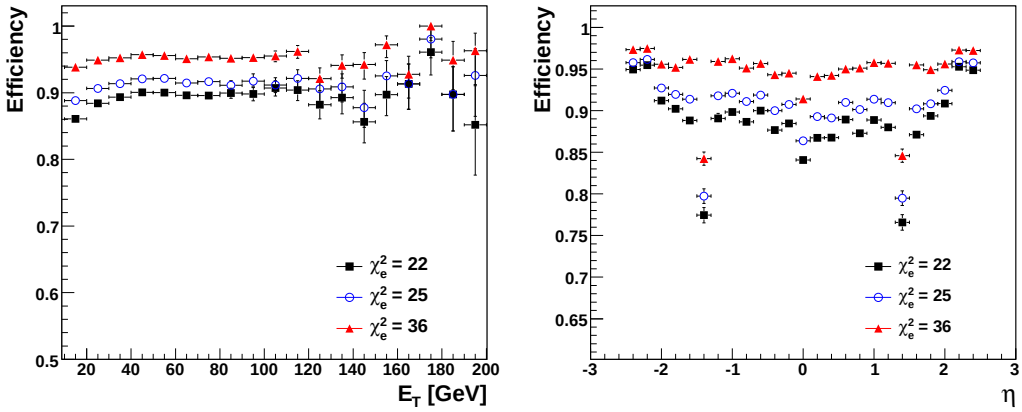

Figure 5.26. Efficiency of the χ^2_e discriminant as function of E_T (left) and η (right) at χ^2_e cut values of 23, 28, and 33.

Table 5.4. Overall χ^2_e discriminant efficiencies and rejections for some selected cut values χ^2_e cuts. The E_T cut on electrons and jets is 17 GeV.

χ^2_e cut value	$\chi^2_e > 22$	$\chi^2_e > 25$	$\chi^2_e > 36$
Efficiency (%)	89.1±0.8	91.2±0.7	95.1±0.5
Rejection	3225±96	2784±77	1901±44

Table 5.5. The tune of χ^2_e cut values in different E_T bins that provide the same efficiency as the ATLAS cut-based discriminant in each E_T bin. Only the calorimeter part of the ATLAS cut-based discriminant is used. For further details see section 4.5.

E_T (GeV)	χ^2_e
$0 < E_T < 17$	20
$17 < E_T < 25$	22
$25 < E_T < 30$	25
$30 < E_T < 40$	30
$40 < E_T < 50$	36
$50 < E_T < 60$	39
$60 < E_T < 70$	44
$E_T > 70$	47

Table 5.6. Electron H-matrix performance compared to the cut-based method. χ^2_e cut was tuned to have the same efficiency as the cut-based method discriminant.

	Electron H-matrix	**Cut-based method**
Efficiency (%)	93.1±0.1	93.3±0.1
Rejection	3027±88	2255± 55

the H-matrix efficiency for electrons is the same as the efficiency of the cut-based algorithm. For a fair comparison between the two discriminants only the calorimeter part of the ATLAS cut-based discriminant is used. The resulting cut values on χ^2_e are listed in Tab. 5.5. With this tune of the χ^2_e cut value, the efficiency is shown in Fig. 5.27(a) as function of E_T. By design the two algorithms have the same efficiency. One can then compare the rejection of the cut-based algorithm with the rejection power of the χ^2_e discriminant, as a function of the jet E_T. This is shown in Fig. 5.27(b) for the χ^2_e cut described earlier. The electron H-matrix achieves higher rejection power than the ATLAS cut-based algorithm for the same signal efficiency. The efficiency and rejection over the entire signal and background samples are given for the cut-based and the χ^2_e discriminants in Tab. 5.6

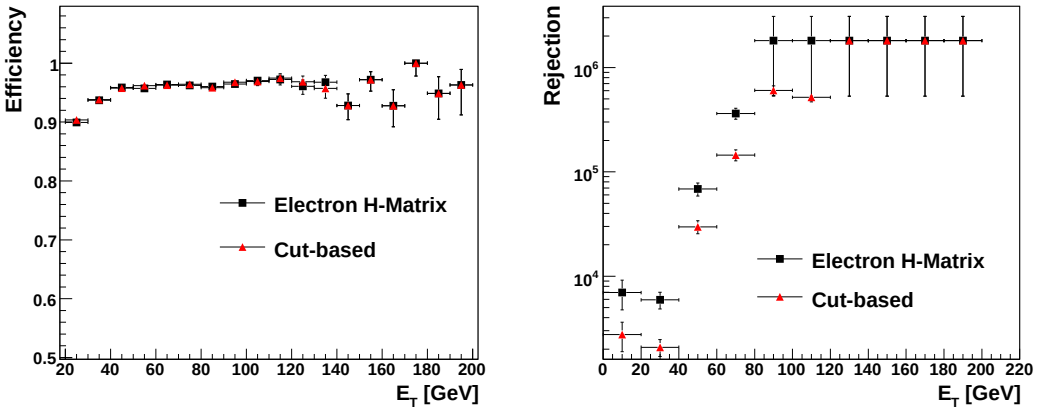

(a) (b)

Figure 5.27. (a) Efficiency and (b) Rejection of the χ^2_e discriminant (close square) compared to that of the cut-based algorithm (close triangle). The cut on χ^2_e is tuned in bins for E_T to have same efficiency as the cut-based algorithm.

5.3.3 Performance of Photon H-matrix

As described in section 5.2.5, the photon H-matrix incorporates a jet H-matrix. The χ^2 is obtained from combined photon-jet H-matrix and defined as

$$\chi^2_{\gamma-\text{jet}} = \frac{1}{2}(\chi^2_\gamma - \chi^2_{jet}) \tag{5.14}$$

where χ^2_γ is obtained from photon H-matrix and χ^2_{jet} from jet H-matrix.

5.3.3.1 Object Selection and Definitions

In order to obtain the photon efficiency for H-matrix, photons from $H \rightarrow \gamma\gamma$ decays are used and the criteria for photon candidates from this signal sample are as follows:

- The reconstructed photons must be within $\Delta R < 0.2$ of the Monte Carlo truth photons resulting from the Higgs particle decay with mass of 120 GeV. The true

photons are required to pass the following kinematic cuts: $E_T > 25$ GeV and $0 \leq |\eta| \leq 1.37$ or $1.52 \leq |\eta| \leq 2.37$.

- The reconstructed photons must be in $0 \leq |\eta| \leq 1.37$ or $1.52 \leq |\eta| \leq 2.37$ to avoid the crack region or calorimeter regions with poorer granularity. The photon H-matrix algorithm can in principle produce a H-matrix χ^2 in the whole range up to $|\eta| < 2.47$. For the sake of comparison with the cut-based photon identification, the performance of the H-matrix is estimated in a more restricted region, corresponding to the region where the cut-based discriminant is defined, namely $|\eta| < 1.37$ or $1.52 < |\eta| < 2.37$.

Using the photon sample selected as above, the efficiency is defined as $\varepsilon = N_\gamma^{reco}/N_\gamma^{truth}$, where N_γ^{truth} is the number of true photons and N_γ^{reco} is the number of loose photon candidates.

The jet rejection is defined in a way similar to that for the electron H-matrix, as follows:

$$R = \frac{N_{jet}}{N_{fake\gamma}} n \frac{1}{\varepsilon_{\gamma-filter}} \tag{5.15}$$

where N_{jet} is the total number of jets in the analyzed sample and $N_{fake\ \gamma}$ is the number of fake photons identified in the jet sample. Note that photon candidates matched to a true photon from QCD process or a quark bremsstrahlung are removed prior to the rejection calculation. The parameter n has the same definition as for the rejection in the electron H-matrix. The value of n for jets in the fiducial volume of $|\eta| < 1.37$ or $1.52 < |\eta| < 2.37$ is 0.226 for jets with $E_T > 25$ GeV and 0.042 for jets with $E_T > 40$ GeV. The quantity $\varepsilon_{\gamma-filter}$ is the efficiency of the Monte Carlo generation with respect to the parton selections applied to the sample. Its value is 8.2.

5.3.3.2 Track Isolation

The background from charged hadrons is removed after the shower shape cut, but the contamination from high-p_T π_0 meson still remains. For the this reason the track isolation [80] variables are considered in order to remove the remaining background and it is expected to achieve additional rejection of 1.5 to 2 with small loss on efficiency. The track isolation is defined as the sum of the p_T of all tracks with p_T above 1 GeV within $\Delta R < 0.3$ where ΔR is the distance between the track direction at the vertex and the cluster centroid. In this study, the track isolation value is required to be less than 4 GeV.

5.3.3.3 Performance using $H \rightarrow \gamma\gamma$ sample

The photon efficiency and jet rejection calculations are estimated once using the pure photon H-matrix and then estimated again with the combination of jet and photon H-matrix.

Photon H-matrix

The efficiency for true photons from the Higgs decay $H \rightarrow \gamma\gamma$ is derived on reconstructed photon candidates which satisfy preselection criteria described in 5.3.3.1. The rejection of the H-matrix for jets and π^0's are calculated using the dijet sample with $E_T > 17$ GeV.

Figure 5.28 shows the efficiency versus the photon candidate E_T and η for some selected χ^2_γ cut values. The photon H-matrix efficiency is somewhat E_T dependent, as shown in Fig 5.28(b). To keep the efficiency of the photon H-matrix constant, the χ^2_γ cut value can be adjusted in different E_T bins to make the efficiency constant with respect to the E_T of the photon. The efficiency can be adjusted by changing the χ^2_γ cut value as shown in Fig. 5.28(a). It appears as in the electron H-matrix case

Table 5.7. Overall photon H-matrix efficiencies and rejections with different χ^2_γ cut values. The E_T cut on photons and jets are 25 GeV.

photon H-matrix cut	$\boldsymbol{\chi^2_\gamma > 13}$	$\boldsymbol{\chi^2_\gamma > 17}$	$\boldsymbol{\chi^2_\gamma > 22}$
Efficiency (%)	76.0±0.3	83.5±0.3	88.1±0.3
Rejection	4132±252	3741±217	2593±125

that the efficiency is lower around $|\eta| = 1.5$ due to on edge effect in the proximity of the crack region. The values of the efficiencies are 76%, 83%, and 88.1% for the χ^2_γ cut values of 13, 17 and 22. The corresponding values of the rejection are listed in Tab. 5.7

The sensitivity to a $H \to \gamma\gamma$ signal is maximized by selecting two photons, one with $E_T > 40$ GeV and a second photon with $E_T > 25$ GeV [81]. For this reason the efficiency and rejection of the H-matrix are derived in two different E_T regions, $p_T > 25$ GeV and $E_T > 40$ GeV.

Figure 5.29 shows the rejection versus efficiency of photon H-matrix for photons and jets of E_T above 25 GeV and 40 GeV. The plots in the Fig. 5.29 also show how performance changes with track isolation cut. The track isolation provides additional rejection against jets, but leads to slightly lower efficiency.

The rejection of the H-matrix against jets is compared with that of the cut-based photon identification, after tuning the H-matrix χ^2_γ cut in bins of E_T, to have the same efficiency as the cut-based algorithm in each bin of E_T. The resulting efficiency is shown as a function of E_T in Fig. 5.30(a). For the same cut tune, Fig. 5.30(b) shows the rejection curves versus E_T for the photon H-matrix and the cut-based method. The rejection power of the H-matrix is slightly lower than that of the cut-based algorithm. For this reason the jet H-matrix is used to provide additional rejection against jets.

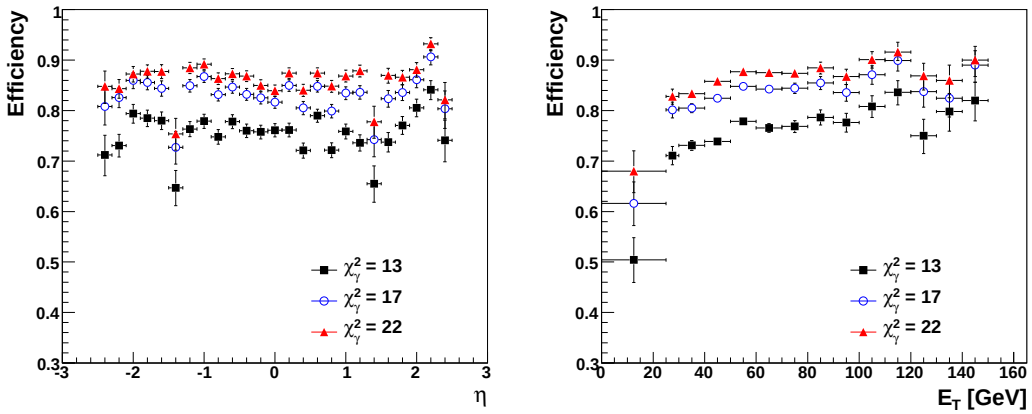

(a) (b)

Figure 5.28. Efficiency of the photon H-matrix as a function of (a) η and (b) E_T for the following χ^2_γ cut values: 13, 17 and 22.

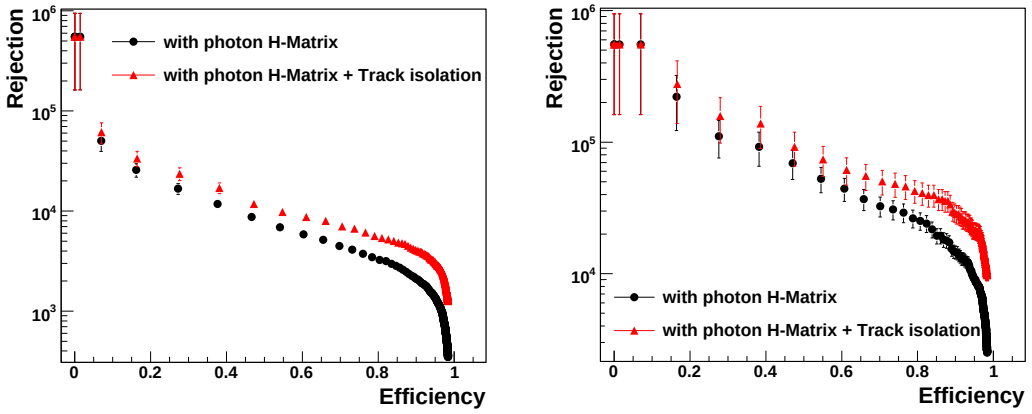

(a) (b)

Figure 5.29. Jet rejection versus photon efficiency for (a) $E_T > 25$ GeV and (b) $E_T > 40$ GeV cut. The closed circles show the rejection versus efficiency curve without track isolation. The closed triangles show the efficiency versus rejection curve with the track isolation cut.

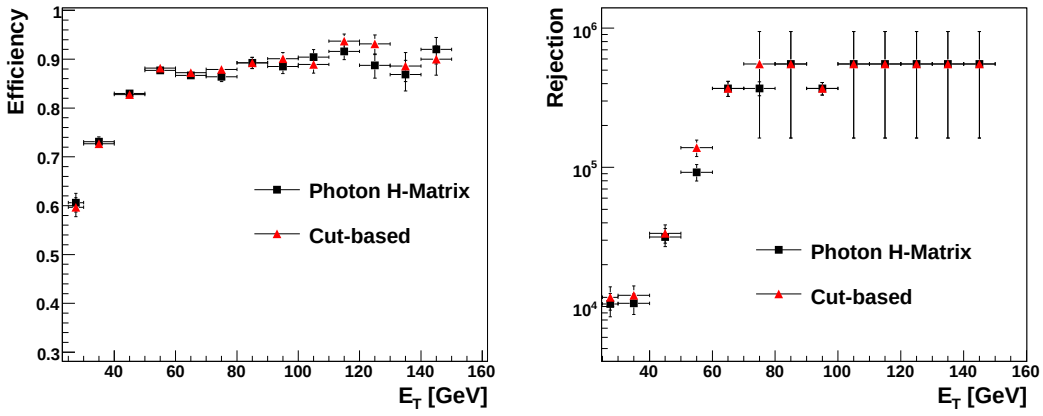

(a) (b)

Figure 5.30. (a) Photon efficiency as a function of E_T and (b) Photon rejection as a function of E_T. Both (a) and (b) are produced with the χ^2_γ cut values tuned to have the same efficiency as with the cut-based method.

Combined Photon and Jet H-matrix

To enhance the performance of the photon H-matrix, it is combined with the jet H-matrix according to Eq. 5.14. Figure 5.31 shows the $\chi^2_{\gamma-\text{jet}}$ distribution for photons from $H \rightarrow \gamma\gamma$ and for jets. The distribution for true photons has a sharp peak at low values of $\chi^2_{\gamma-\text{jet}}$ while the jets have a rather flat distribution. One can observe that the peak for the photons is in fact much sharper for $\chi^2_{\gamma-\text{jet}}$ than for χ^2_γ shown in Fig. 5.3. This indicates that $\chi^2_{\gamma-\text{jet}}$ will provide better rejection against jets.

Figure 5.32 shows the rejection versus efficiency for the χ^2_γ discriminant (triangles) and for $\chi^2_{\gamma-\text{jet}}$ (solid circle). The combination with the jet H-matrix clearly improves the performance. In particular, the rejection power is improved significantly at low efficiencies.

Figure 5.33 shows the rejection power of the $\chi^2_{\gamma-\text{jet}}$ discriminant against jets, and its comparison with the cut-based method. The $\chi^2_{\gamma-\text{jet}}$ cut values have been tuned in bins of E_T, to give the same efficiency as the cut-based discriminant in each bin of E_T. The cut tunes are listed in Tab. 5.8. The left plot in the Fig. 5.33 shows that

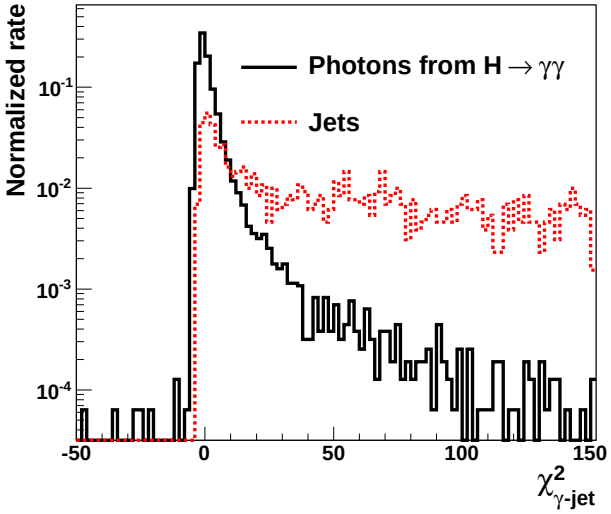

Figure 5.31. Distribution of $\chi^2_{\gamma-\mathrm{jet}}$ for combined photon and jet H-matrix. Solid histogram represents real photons from $H \rightarrow \gamma\gamma$ and dashed one fake photon with $E_T > 25$ GeV from dijet sample.

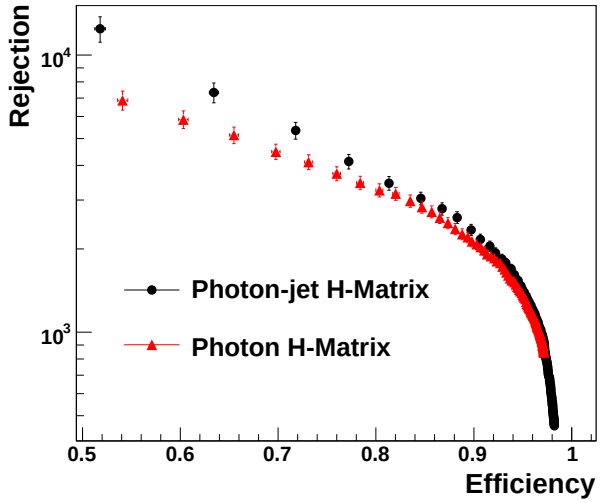

Figure 5.32. Rejection versus efficiency for the photon H-matrix χ^2_γ (solid circles) and for the photon-jet H-matrix $\chi^2_{\gamma-\mathrm{jet}}$ (solid triangles).

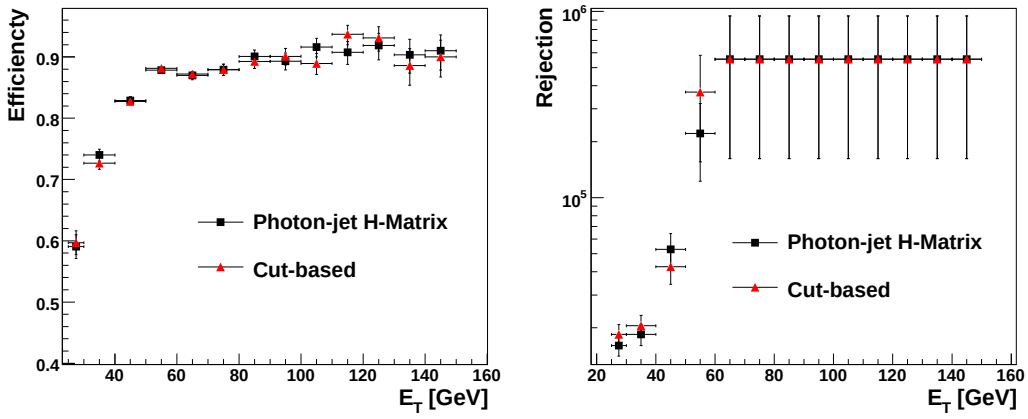

Figure 5.33. Performance comparison of photon-jet H-matrix (close square) and cut-based algorithm (close triangle). The $\chi^2_{\gamma-\text{jet}}$ cut values are chosen to have the same efficiency for the two methods as shown in the left plot. The right plot shows rejection as a function of E_T of fake photons.

the resulting efficiencies for $\chi^2_{\gamma-\text{jet}}$ and the cut-based discriminants are the same as expected. The right plot shows the corresponding rejection as a function of E_T for the $\chi^2_{\gamma-\text{jet}}$ discriminant (square) and for the cut-based algorithm (triangles).

Table 5.9 provides numerical comparisons of jet rejection for two the methods at similar efficiencies. The rejections of the $\chi^2_{\gamma-\text{jet}}$ H-matrix and cut-based discriminants for photons with $E_T > 25$ GeV and $E_T > 40$ GeV are given in the fourth row of Tab. 5.8. As can be seen from Fig. 5.33, the cut-based algorithms and the $\chi^2_{\gamma-\text{jet}}$ H-matrix have comparable performance both in terms of efficiency and rejection. Still the H-matrix discriminant has the advantage that the cut value can be adjusted to the need of a particular analysis, while the cut-based discriminant provides only a single point in the rejection, efficiency plane.

Table 5.8. $\chi^2_{\gamma-\text{jet}}$ cut tunes in E_T bins which provide the same efficiency as the cut-based algorithm in each bin.

E_T (GeV)	$\chi^2_{\gamma-\text{jet}}$
$0 < E_T < 25$	2
$25 < E_T < 30$	2
$30 < E_T < 40$	3
$40 < E_T < 50$	4
$50 < E_T < 60$	5
$50 < E_T < 70$	4.5
$70 < E_T < 80$	4
$E_T > 80$	5

Table 5.9. Comparison of the photon-jet H-matrix rejection with the cut-based method when the H-matrix has same efficiency as the cut-based method. These results are produced without isolation cut.

	$E_T > 25$		$E_T > 40$	
	$\chi^2_{\gamma-\text{jet}}$ H-matrix	cut-based	$\chi^2_{\gamma-\text{jet}}$ H-matrix	cut-based
Efficiency (%)	84.2±0.3	83.9±0.3	86.9±0.3	86.4±0.3
Rejection	4614±298	4692±368	4379±638	4200±600

5.4 Systematic Uncertainties

In this section two effects are investigated which might lead to a different performance of the H-matrix in data compared to what has been established on the Monte Carlo simulation in this chapter.

5.4.1 Effect of Data to Simulation Discrepancies in Shower Shapes

The H-matrix is constructed using training samples of single electrons and photons generated from Monte Carlo. It is is possible that some of the shower properties in the data differ from their distributions in the Monte Carlo. In this case this will reduce the ability of the H-matrix to identify electrons or photons in the data. One of the main reasons for differences of shower shape variables between data and Monte Carlo is the possibility that the amount and distribution of material in the simulation does not reflect exactly what it is in the actual detector. As an example, material upstream of the calorimeter will lead to wider showers in the first layer of the calorimeter.

In Chapter 7, the ATLAS cosmic-ray data is compared with the simulation. Some discrepancies are observed between data and simulation. The size of these discrepancies are used as a benchmark to measure the potential effect of data to simulation discrepancies on the performance of the H-matrix.

Figure 5.34 shows the ratio of data to simulation for two selected shower shape variables, as measured using the cosmic ray data taken by ATLAS. The same type of ratios are derived for all of the fourteen variables used as input to the H-matrix.

The ratio of data to simulation can be used as a weight (correction) factor to the Monte Carlo distributions, to make them data-like. Figure 5.35 shows the effect of applying the data to the simulation ratio to some photon shower variables as observed in a $H \rightarrow \gamma\gamma$ Monte Carlo sample. The solid histograms represent

distributions of R_ϕ and ω_{η_2} for photons from $H \rightarrow \gamma\gamma$ and the dashed histogram represents the corresponding weighted distributions. The same weighting procedure is applied to each of the fourteen input variables of the H-matrix. The efficiency of the photon H-matrix is computed on the non weighted $H \rightarrow \gamma\gamma$ sample and then again but using the weighted distributions. One can then quantify the resulting effect on the photon H-matrix efficiency. The most significant effects on the H-matrix efficiency are summarized in Tab. 5.10. All contributions are rather small and summed quadratically lead to a – 0.3% effect, indicating that the H-matrix is robust to small discrepancies in shower shapes between the shapes used to build the H-matrix and the actual shapes of the electron or photon candidate under evaluation.

Table 5.10. Effect in % of the Monte Carlo to data reweighting on the H-matrix photon efficiency, computed on the $H \rightarrow \gamma\gamma$ sample. Only the significant variations in efficiencies are listed. The last line shows the quadratic sum of all contributions

Variables	**Relative variation**
f_0	– 0.1%
f_4	– 0.1%
R_ϕ	– 0.2%
R_{max2}	– 0.1%
ΔE	– 0.2%
Total	– 0.33%

5.4.2 Effect of Different EM Scales in Data and Simulation

The purpose of the electromagnetic scale (EM scale) is to understand the measured energy of electrons and photons, such that for instance electrons with a true energy E_{true}=10 GeV will be measured on average to have an energy of E_{measured}10 GeV.

In the early period of ATLAS data taking the EM scale is known to about 2%[2] known from test beam studies [82]. This means that the ratio $E_{\text{measured}}/E_{\text{true}}$ is 1.00±0.02.

The shower shape variables are energy dependent and to calculate the H-matrix for a given photon or electron candidate one needs to know its energy. Effectively the H-matrix compares the shower shape of a measured photon of true energy E_{true} but of measured energy E_{meas} to the ideal shower shape of photons with energy E_{meas}. Thus if the difference between E_{meas} and E_{true}, the H-matrix compares the shower shapes of the electron or photon to the wrong reference shapes, thus reducing the photon or electron identification capability.

The effect of an unknown EM energy scale within 2% is estimated by taking a sample of photons and scaling their energy up and down by 2% and measure the resulting effect on the on photon efficiency. Figure 5.36 shows the relative variation in photon efficiency as function of the photon E_T when the EM scale is varied up (closed square) or down (close triangle) by 2%. The resulting effect is less than 0.2% overall, thus showing that the H-matrix is robust to the EM scale. Table 5.11 shows the estimated systematic uncertainties and their effect on the H-matrix efficiency.

Table 5.11. Systematic uncertainties from each sources on H-matrix efficiency

Source	**Relative error**
Electromagnetic energy scale	±0.2 %
Data to simulation discrepancies	±0.33%
Total	±0.4%

[2]For the long term EM scale precision should be 0.5%.

5.5 Conclusions

Two covariant based H-matrix discriminants have been developed to identify photons and electrons in ATLAS in the range 10 – 1000 GeV. They exploit the high granularity of the ATLAS electromagnetic calorimeter by combining up to fourteen different shower shape variables, to achieve a high rejection against jets while keeping high efficiency for electrons and photons. The electron H-matrix provides higher rejection than the standard ATLAS cut-based electron discriminant at equal efficiency. The photon H-matrix incorporates a jet H-matrix to increase the rejection against jets. Its performance is equivalent to that of the ATLAS cut-based photon discriminant. Additionally the H-matrix discriminant has the advantage of providing a continuous variable to cut on, thus allowing to adapt the working point in the efficiency, rejection plane, to the needs of a particular analysis. The ATLAS cut-based discriminant provides less flexibility. Finally the efficiency of the H-matrix has been tested against variations in shower shapes, corresponding in size to the type of discrepancies observed between data and simulation in cosmic ray showers. The H-matrix efficiency is robust to such variations in the shapes of the shower shapes. The H-matrix efficiency is also robust to variations of the EM scale of 2%.

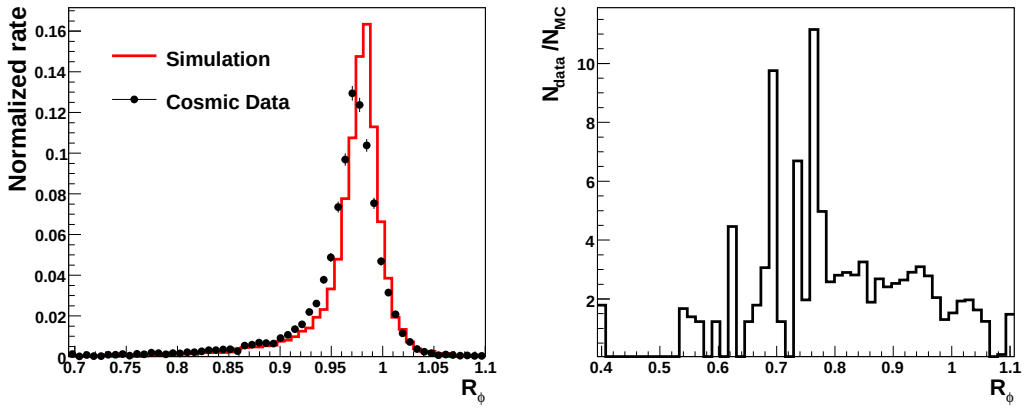

(a)

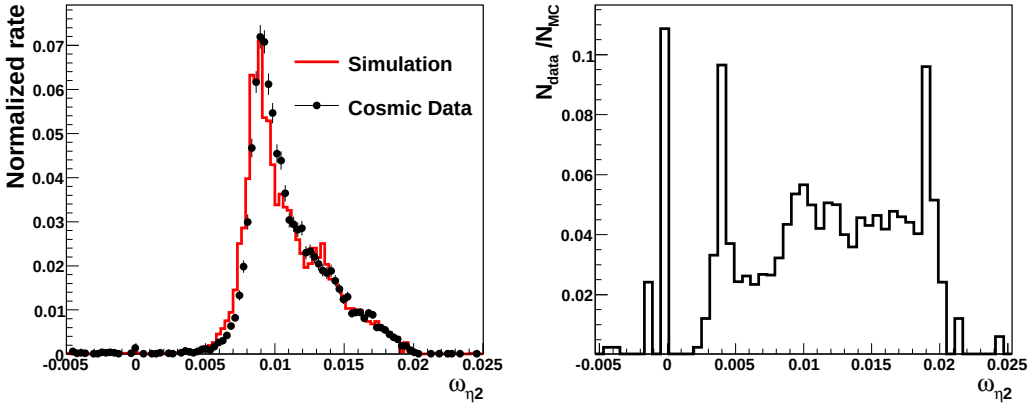

(b)

Figure 5.34. (a) Distribution of R_ϕ in cosmic data (close circle) and in simulation (solid line), and its correction factor. (b) Distribution of ω_{η_2} (left) in cosmic data (close circle) and in simulation (solid line), and its correction factor. For both (a) and (b), correction factor is event ratio between data and MC.

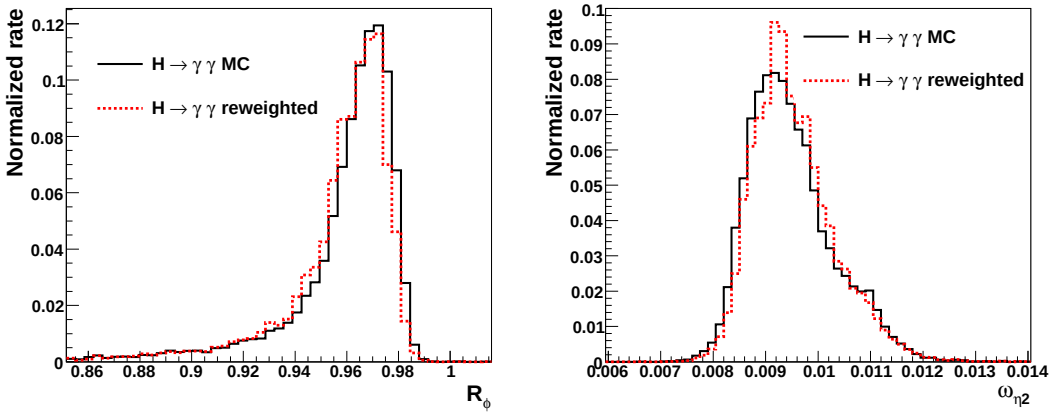

(a) (b)

Figure 5.35. Distributions of (a) R_ϕ and (b) ω_{η_2} in $H \rightarrow \gamma\gamma$. The solid line represents distribution in simulation and dashed histogram reweighted distribution using correction factor as shown in Fig. 5.34 from $H \rightarrow \gamma\gamma$.

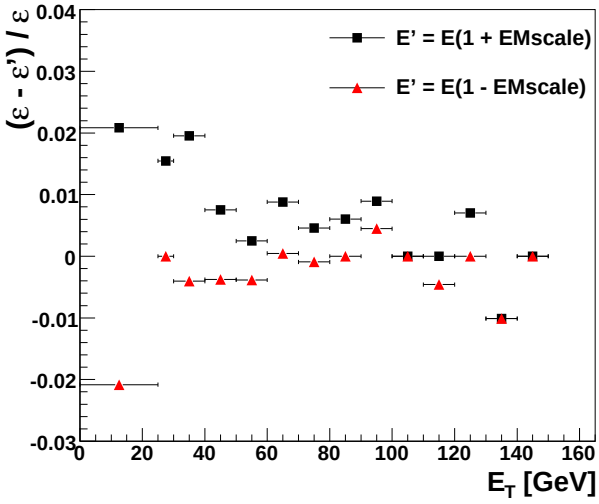

Figure 5.36. Relative error, $(\varepsilon - \varepsilon')/\varepsilon$ due to the EM energy scale, where ε is efficiency for uncorrected energy (E) and ε' is efficiency for corrected energy (E′) with EM energy scale. Closed square is the case of EM scale varied up and close triangle EM scale down..

CHAPTER 6

A DATA DRIVEN METHOD FOR PHOTON IDENTIFICATION EFFICIENCY MEASUREMENT

6.1 Introduction

ATLAS has developed several advanced tools and discriminants to identify photons by combining a large number of electromagnetic shower shape variables. It is important to measure the efficiency of the photon identification tools using data. To be able to perform the measurement in data it is necessary to have a clean experimental signature that allows to select a pure photon sample. To allow for efficiency measurements the clean photon sample needs to be selected without requiring the full photon selection based on the whole set of shower shape variables. The purity of the photon sample needs to be achieved by other means than the full photon identification techniques, by for instance using a well recognizable physics process.

For electrons it is well known that such a signal is available in the form of the $Z \to ee$ process, and its characteristic dielectron mass peak at the mass of the Z boson (m_Z). However, there is no equivalent of a usable physics process with a heavy resonance decaying into two photons that would be easily identifiable from backgrounds. The 3-body decay of a real Z boson, $Z \to \mu\mu\gamma$ where the photon is produced as a final state radiation off a muon could provide a clean source of photons for the in-situ measurement of photon identification efficiencies. The unprecedented luminosity and center of mass energy of the LHC, makes this process for the first time a usable calibration tool.

This chapter describes a feasibility study that demonstrates how to use this new signal for the measurement of the photon identification discriminants. In order to be a usable signal for photon efficiency measurements, three conditions have to be met. First the properties of the photons found in the $Z \to \mu\mu\gamma$ events should be equivalent to that of the photons found in for instance $H \to \gamma\gamma$. The muons deposit very little energy in narrow regions of the calorimeter, thus leaving very little activity in the calorimeter that could disturb the photon shower shapes. The second condition to be met is that the number of $Z \to \mu\mu\gamma$ events should be large enough for statistically significant measurements of the photon efficiency in bins of photon E_T. Finally one needs to demonstrate that there exists a set of selections than can retain the $Z \to \mu\mu\gamma$ signal while keeping only a small fraction of backgrounds. The remaining fraction of background will spoil the measurement of the photon efficiency and thus has to be kept as low as possible. Alternatively, the contamination could potentially be measured in data and its contribution could be taken into account.

The present chapter is organized as follows. The section 6.2 describes the $Z \to \mu\mu\gamma$ process. In section 6.3 some details are given concerning the Monte Carlo samples used in the present study. Some characteristic features of the $Z \to \mu\mu\gamma$ signal that can be exploited for its selection are discussed in section 6.4 and the proposed selections to extract this signal in the ATLAS data are described in section 6.5. In section 6.6 the shower shapes obtained for photons from $Z \to \mu\mu\gamma$ after selections are compared with the shower shapes for prompt photons in $H \to \gamma\gamma$ events. In section 6.7 the efficiency is computed both on the $Z \to \mu\mu\gamma$ and in $H \to \gamma\gamma$ Monte Carlo samples and are compared. Finally the contamination by other Standard Model processes or by sources of fake photons in $Z \to \mu\mu$ events is estimated in section 6.8.

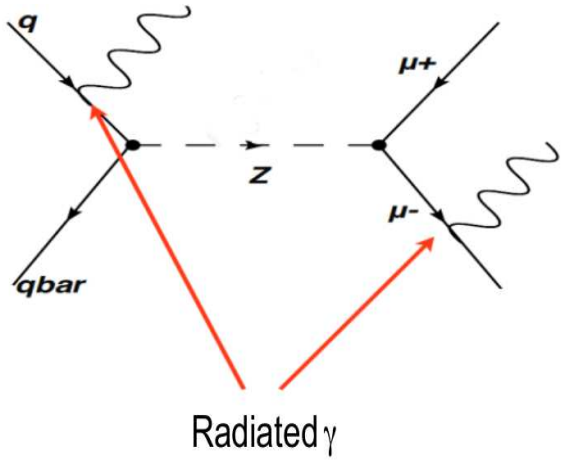

Figure 6.1. Illustration of the production of an initial state radiation photon (photon emitted on the left side of the figure), and of the production of an inner bremsstrahlung photon (photon emitted on the right side of the figure).

6.2 The $Z \to \mu\mu\gamma$ Process

There are several processes that can lead to the presence of a $Z \to \mu\mu$ and a photon in the final state, most of which are in fact backgrounds to the present study.

The $Z \to \mu\mu$ events can contain a photon from initial state radiation (ISR), as illustrated in Fig. 6.1. In this case the photon and the muon directions are uncorrelated, the invariant mass of the two muons $m_{\mu\mu}$ is close to m_Z and there is no particular relationship between the photon and the muons from the Z decay.

The $Z \to \mu\mu$ decays of an on-shell Z into two real muons can also contain a photon produced by bremsstrahlung off one of the muons interacting with the material inside the detector. The vast majority of these photons is very close to the muon track as shown in the darker histogram of Fig. 6.2. The main characteristic of these events is that the distance $\Delta R_{\mu\gamma}$ between the photon and one of the muons is very small. The invariant of the two muons is in general compatible with m_Z unless the photon carries a large amount of energy, in which case $m_{\mu\mu}$ will be smaller than m_Z. This process is referred to as "detector bremsstrahlung".

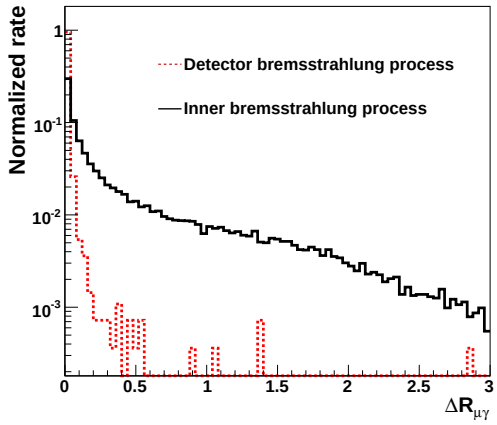

Figure 6.2. Distribution of $\Delta R_{\mu\gamma}$ for the inner bremsstrahlung process (solid line histogram) and for the detector bremsstrahlung (dashed line histogram), obtained with the $Z \rightarrow \mu\mu$ PYTHIA sample. The detector bremsstrahlung is significantly more peaked at small values of $\Delta R_{\mu\gamma}$. This figure is obtained using the Monte Carlo truth information, thus no lower E_T cut is applied on the photon.

Finally an on-shell Z boson can decay to two muons, one of which is off mass and then becomes real while producing an inner bremsstrahlung photon. This is effectively a 3-body decay of the Z boson. In this case there is no interaction with the detector material required. This process is referred in the rest of this chapter as the process of "inner bremsstrahlung". In this case the direction of the photon is also correlated with muon directions, but the distribution is much less peaked to small $\Delta R_{\mu\gamma}$ values as it is the case for the detector bremsstrahlung. The distribution of $\Delta R_{\mu\gamma}$ in the Monte Carlo truth for the inner bremsstrahlung process is compared to that of the detector bremsstrahlung in Fig. 6.2. For this process the invariant mass of the two muons $m_{\mu\mu}$ is generally smaller than m_Z, while the invariant mass of the two muons together with the photon ($m_{\mu\mu\gamma}$) will be close to m_Z.

As discussed further in section 6.4, the inner bremsstrahlung process has characteristics which allows to select a pure photon sample without using the full photon identification tools. It is considered as the main signal process in the present study.

6.3 Simulation Samples

The present study is carried out with Monte Carlo samples generated for a proton-proton center of mass energy of $\sqrt{s}$=10 TeV for all considered processes. The $Z \rightarrow \mu\mu$ process is generated with the PYTHIA [65, 66] event generator. It contains the final states with photons from initial state radiation and inner bremsstrahlung. The detector bremsstrahlung photons are instead produced by the ATLAS detector simulation based on GEANT [63, 64]. All Monte Carlo samples used in the present study have been run through the detailed ATLAS detector simulation based on GEANT. The cross section of the process $Z \rightarrow \mu\mu$ at the considered center of mass energy is 1144 pb.

In order to estimate the uncertainty due to Monte Carlo modeling on the event yield calculation, the number of $Z \rightarrow \mu\mu\gamma$ is evaluated both with the PYTHIA sample mentioned earlier and with a second $Z \rightarrow \mu\mu$ sample generated with ALPGEN [68]. The ALPGEN generator includes leading order electroweak and QCD effects for multiparton hard processes. It contains the matrix elements for Z production in association with up to 5 jets. In the present study we consider Z production with zero and one jet. For the ALPGEN samples the parton showering and fragmentation are simulated with HERWIG [69, 70, 71].

The other Standard Model background processes considered in this analysis, are $t\bar{t}$, diboson and $b\bar{b}$ production. Table 6.1 summarizes the samples used in this chapter with their cross-section and the event generators used for their simulation.

The MC@NLO [72, 73] generator includes the full next to leading order QCD corrections, it has been used to simulate $t\bar{t}$ production. The generator is interfaced to the HERWIG + JIMMY for parton showering, fragmentation, underlying events and multiple interaction. Only $t\bar{t}$ simulated events containing at least one isolated lepton in the final state are used. This is consistent with the event selection described later

Table 6.1. Samples used for the $Z \to \mu\mu\gamma$ study and corresponding backgrounds with the generators used, their cross-sections (X-section) and number of events available.

Process	**Generator**	**x-section (pb)**	**Events**
$Z \to \mu\mu$	PYTHIA	1144	246k
$Z \to \mu\mu + 0$ parton	ALPGEN	900.21	242k
$Z \to \mu\mu + 1$ parton	ALPGEN	205.21	50k
$t\bar{t}$	MC@NLO + JIMMY	373.6	521k
$gg \to WW \to \mu\mu$	gg2WW + JIMMY	31.51	9k
$b\bar{b} \to \mu\mu$	PYTHIAB	88500	40k

in section 6.5, since two isolated muons are required in the events selected in this analysis.

The $b\bar{b}$ background sample is generated using PYTHIAB [67]. During generation, the $b\bar{b}$ events are required to contain at least one muon with $p_T > 15\ GeV$ within $|\eta| < 2.7$.

The WW background was generated using the gg2WW [83] event generator and interfaced to JIMMY [84]. This diboson process has a small cross-section compared to the previously discussed background processes. The WW production via quark-quark and quark-gluon are much smaller than gluon-gluon and are therefore neglected. The other diboson processes WZ and ZZ have much lower cross sections than WW and are therefore negligible.

The uncertainty on the production cross section can be estimated by comparing predictions of different Monte Carlo generators and the generator parameters. The uncertainty on the Z, $t\bar{t}$ and WW production cross sections is taken to be 20% and 50% for the $b\bar{b}$ production as prescribed in Ref. [85].

6.4 Properties of Inner Bremsstrahlung $Z \to \mu\mu\gamma$ Events

In this section the most important event properties which allow to select a clean photon sample using inner bremsstrahlung events are reviewed. They rely essentially on the fact that this is a 3-body decay of the Z boson. The main differences with the detector bremsstrahlung and initial state radiations are underlined.

- The invariant mass of the photon and the two muons ($m_{\mu\mu\gamma}$) is consistent with m_Z, within experimental resolutions for photons and muons. For the ISR and detector bremsstrahlung events $m_{\mu\mu\gamma}$ is higher than m_Z except when the photon energy is so low that it does not affect $m_{\mu\mu\gamma}$ in a significant way compare to m_Z.
- The invariant mass of the two muons $m_{\mu\mu}$ is lower than m_Z in the case of inner bremsstrahlung. For the ISR $m_{\mu\mu}$ is consistent with m_Z. In the case of the detector bremsstrahlung most of the photons have very low momentum and $m_{\mu\mu}$ will not be significantly affected by this momentum loss. If the detector bremsstrahlung photon takes away a significant fraction of the muon momentum, then the measured $m_{\mu\mu}$ will be significantly lower than m_Z.

  In the vast majority of the detector bremsstrahlung events the photon is produced in the calorimeter which corresponds to the most significant chunk of material traversed by the muon. This means that in principle one could also detect that the muon track measured inside the inner detector has more momentum than the muon track measured in the muon spectrometer. This was not studied in this analysis but could potentially be exploited to reduce further the detector bremsstrahlung contribution.

  The Fig. 6.3(a) shows the two dimensional distribution of the invariant mass $m_{\mu\mu}$ as function of $m_{\mu\mu\gamma}$ for the fully simulated PYTHIA $Z \to \mu\mu$ sample. This

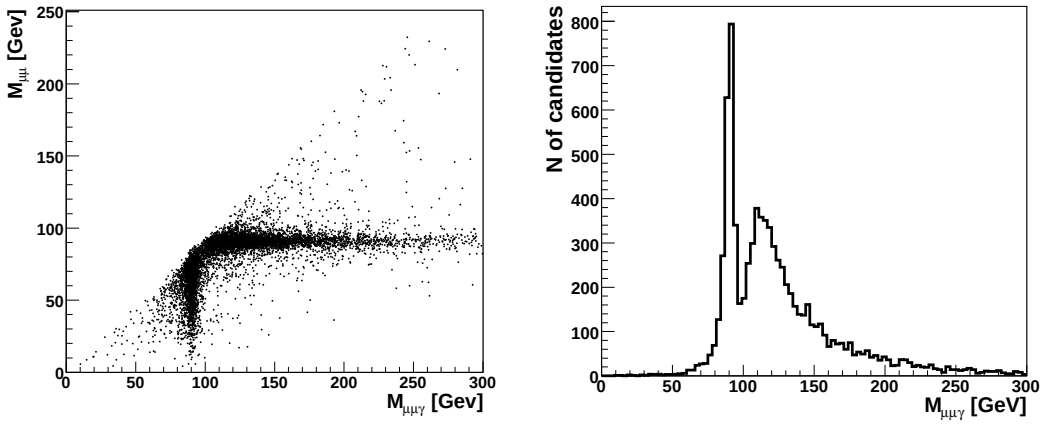

(a) (b)

Figure 6.3. (a) The two dimensional distribution of $m_{\mu\mu}$ as function of $m_{\mu\mu\gamma}$ for $Z \rightarrow \mu\mu$ PYTHIA events containing two muons of $p_T > 20$, 6 GeV and a loose photon candidate with $E_T > 10$ GeV. The invariant mass distribution $m_{\mu\mu\gamma}$ is shown in (b) for the same class of events.

distribution is obtained after requiring two muons with p_T larger than 20 GeV and 6 GeV and requiring a loose photon candidate with $E_T > 10$ GeV. There is a clear horizontal band at $m_{\mu\mu} \sim m_Z$, which corresponds to ISR and detector bremsstrahlung events. Since only a loose photon candidate is required it is also possible that the photon candidate is in fact a highly electromagnetic jet in the event. One can also observe a vertical band at $m_{\mu\mu\gamma} \sim m_Z$ which corresponds to inner bremsstrahlung events. For this class of events one has generally $m_{\mu\mu} < m_Z$.

By selecting events with $m_{\mu\mu\gamma} \sim m_Z$ both the ISR and detector bremsstrahlung contributions can be reduced. Figure 6.3(b) shows the distribution of $m_{\mu\mu\gamma}$ in the same class of events and the peak of the 3-body Z decays appears clearly. The excess of events at higher values of $m_{\mu\mu\gamma}$ corresponds to 2-body decays where the two muons have been combined with a 10 GeV photon from ISR or detector bremsstrahlung photon from a highly electromagnetic jet.

- As already shown in Fig. 6.2 the distribution of distance $\Delta R_{\mu\gamma}$ between the photon and the muon is very narrow and close to zero for the detector bremsstrahlung photons. In the case of photons from inner bremsstrahlung the distribution $\Delta R_{\mu\gamma}$ extends to large values, although it also peaks at small angles.

  Figure 6.4 shows the two dimensional distribution of $\Delta R_{\mu\gamma}$ versus the invariant mass $m_{\mu\mu\gamma}$, for events with two muons with $p_T > 20$, 6 GeV and a loose photon candidate with $E_T > 10$ GeV. The vertical band at $m_{\mu\mu\gamma} \sim m_Z$ corresponds to the inner bremsstrahlung, for which $\Delta R_{\mu\gamma}$ extends up to about three. The cloud of points at $m_{\mu\mu\gamma} > m_Z$ corresponds to events where the muons of the 2-body Z decay are combined with an ISR photon or a highly electromagnetic jet. It appears also that the number of entries at $\Delta R_{\mu\gamma} \sim 0$ is rather small, indicating that the detector bremsstrahlung photons are suppressed by the $E_T > 10$ GeV selection.

For high energy photons the fraction of inner bremsstrahlung becomes much more important that of detector bremsstrahlung photons. To search for the decay $H \rightarrow \gamma\gamma$ in ATLAS one looks for events with two photons with $E_T > 40$ and 25 GeV.

The detector bremsstrahlung photons also suffer from two disadvantages, which make them less interesting for photon efficiency in-situ measurements. First, due to their very small angle to the muon, the energy deposited by the muon in the calorimeter can spoil the shower shape variables that are supposed to reflect the properties of a pure photon samples. This is illustrated by Fig. 6.5, where the distribution of f_4, the fraction of energy deposited in the first hadronic layer is shown. The distribution of f_4 for detector bremsstrahlung photons is significantly shifted towards positive values due to the presence of the energy deposited by the muon in the first hadronic layer.

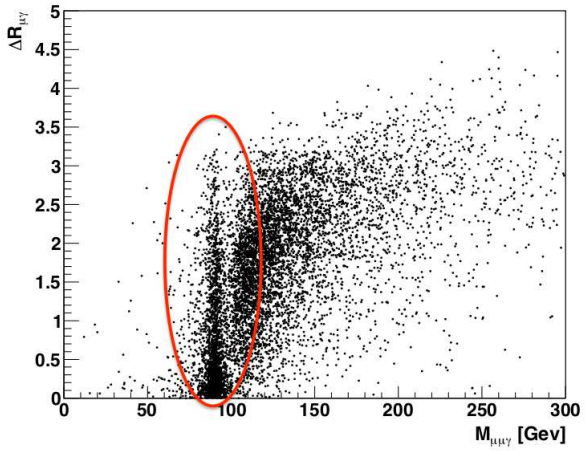

Figure 6.4. Distribution of $\Delta R_{\mu\gamma}$ versus $m_{\mu\mu\gamma}$ obtained in the $Z \rightarrow \mu\mu$ PYTHIA sample, after requiring two muons with $p_T > 20$, 6 GeV and a loose photon with $E_T > 10$ GeV.

The value of f_4 is essentially zero for actual isolated photons as those observed in $H \rightarrow \gamma\gamma$.

The detector bremsstrahlung photons are most likely to be produced in the calorimeter volume, thus due to their late production they cross less material than a prompt photon coming from the interaction point. This leads to significant differences in shower shapes between detector bremsstrahlung photons and prompt photons such as those produced by the inner bremsstrahlung or the $H \rightarrow \gamma\gamma$ process.

6.5 $Z \rightarrow \mu\mu\gamma$ Event Selection

Based on the observations in the previous sections, this section gives the selections used to select the inner bremsstrahlung events, that will be used in section 6.7 to derive the photon identification efficiency. The selected events are required to have two muons and a loose photon candidate. Loose photon candidates are defined by a cluster of cells in the electromagnetic section of the calorimeter, without a matching

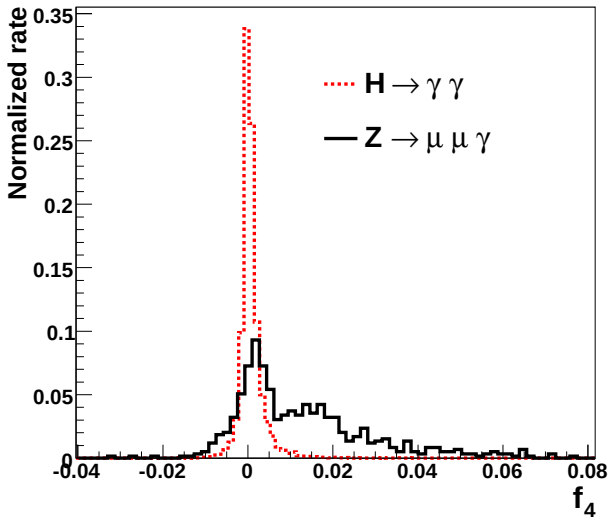

Figure 6.5. Shower variable f_4 for photons in $Z \rightarrow \mu\mu\gamma$ selected by requiring two muons with $p_T > 20$, 6 GeV, a loose photon with $E_T > 10$ GeV and $\Delta R_{\mu\gamma}$ <0.2 (solid line histogram) and for photons in $H \rightarrow \gamma\gamma$ (dashed line histogram). The higher values of f_4 are caused by the energy deposited by muon the in the first hadronic layer.

inner detector track. No selections on the shower shape in the calorimeter are applied.

The inner bremsstrahlung events are selected by applying the following requirements:

Cut A: The transverse momentum p_T of the 2 muons must be larger than 20 GeV for the leading muon and larger than 6 GeV for the second leading muon. The momentum selection on the muons must be at least as hard as the ATLAS trigger selections. The 20 GeV muon trigger is expected to be kept unprescaled up to a luminosity of at least 10^{33} cm^{-2} s^{-1}.

Cut B: The two muons are required to be isolated from calorimeter activity, by demanding that the energy deposited in the calorimeter in a cone of radius $\Delta R = 0.2$ around each muon contains less than 5 GeV of transverse energy.

Cut C: The transverse energy of the photon, E_T must be greater than 10 GeV.

Table 6.2. Expected number of $Z \rightarrow \mu\mu\gamma$ events which survive the selection criteria for an integrated luminosity of 200 pb^{-1} and 1 fb^{-1} for a center of mass energy of $\sqrt{s} = 10$ TeV.

Selection	N_{event}	
	200 pb^{-1}	**1 fb^{-1}**
cut A	120292	601460
+ cut B	114094	570470
+ cut C	3670	18350
+ cut D	3354	16770
+ cut E	1148	5740

Cut D: The photon must not be collinear to any of the muons. If ΔR_1 and ΔR_2 are defined as the $\Delta R_{\mu\gamma}$ distance for the leading and second leading muon, then it is required that Min(ΔR_1, ΔR_2) > 0.2.

Cut E: The invariant mass of the triplet made of the two muons and the loose photon is consistent with m_Z, thus requiring 81 GeV $< M_{\mu\mu\gamma} <$ 101 GeV.

The number of expected $Z \rightarrow \mu\mu\gamma$ after each selection and for an integrated luminosity of 200 pb^{-1} is presented in Tab. 6.2. With all selection cutA to cutE, we anticipate 1148 $Z \rightarrow \mu\mu\gamma$ events for an integrated luminosity of 200 pb^{-1} and 5740 events for an integrated luminosity of 1 fb^{-1}.

6.6 Shower Properties for Photons from Inner Bremsstrahlung and for Prompt Photons

To become a usable signal for in-situ determination of the photon identification efficiencies, the inner bremsstrahlung photons must have shower properties identical to that of prompt photons from for instance $H \rightarrow \gamma\gamma$.

The Fig. 6.6 compares the kinematic properties of inner bremsstrahlung photons with the photons from Higgs boson decay. As expected the total energy in the photon calorimeter cluster and the first layer of hadron calorimeter E and the photon transverse energy are significantly higher for photons from Higgs boson decay. The E_T spectrum of the inner bremsstrahlung photons falls steeply at higher E_T, this will lead to higher statistical uncertainties on the efficiencies derived in-situ. The η distribution for inner bremsstrahlung photons is very similar to that of photons from Higgs decays.

The shower variables used as input to the H-matrix discriminant are compared to those of photons from $H \rightarrow \gamma\gamma$. To allow for a fair comparison, an additional E_T cut of $30 < E_T < 40$ GeV is applied to the photons on both samples, to remove the effect of very different E_T spectra between inner bremsstrahlung and Higgs decay photons. The solid line histograms in Fig. 6.7, Fig 6.8 and Fig 6.9 present the shower shapes for inner bremsstrahlung photons and agree well with photons from the $H \rightarrow \gamma\gamma$ decay presented in the dashed line histograms.

One can thus conclude that the photons produced by the inner bremsstrahlung process in $Z \rightarrow \mu\mu$ events have the same shower properties as prompt photons seen for instance in $H \rightarrow \gamma\gamma$ decays. The η distributions for photons in Higgs decay and inner bremsstrahlung photons from Z decays are incidentally the same, which means that the efficiency will not need to be parameterized as function of η. On the other hand the very different E_T spectra between the two samples implies that the photon efficiency has to be derived in bins of photon E_T in the inner bremsstrahlung photon sample before it can be applied to the $H \rightarrow \gamma\gamma$ sample. If the in-situ efficiency is applied to another physics process such as γ+jets production the actual η and E_T spectra of the photons will need to be taken into account.

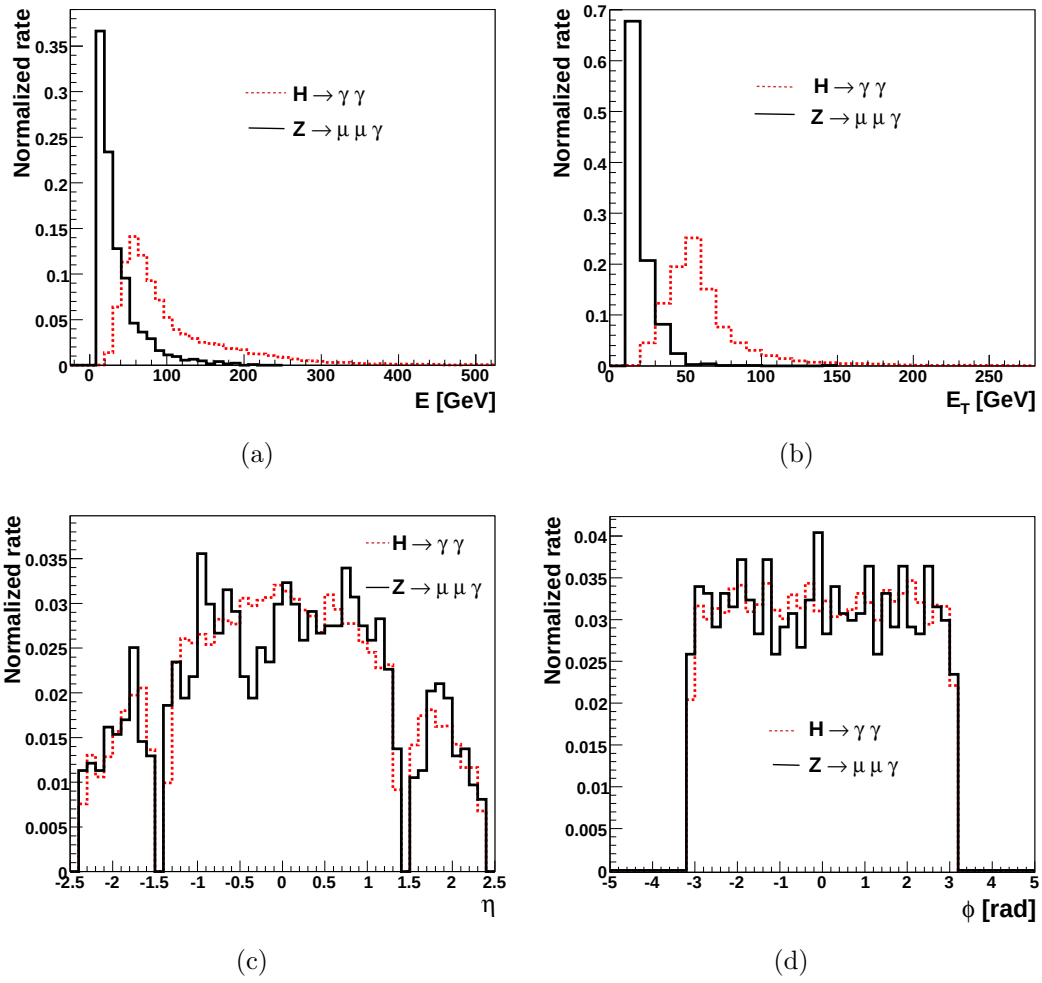

Figure 6.6. Distributions of kinematic variables (a) total energy E (see section 5.2.2), (b) E_T, (c) η and (d) ϕ for photons in $Z \rightarrow \mu\mu\gamma$ events (solid line histograms) are compared with kinematic variables of photons from $H \rightarrow \gamma\gamma$ (dashed line histograms), after Cut E. Most of photons in $Z \rightarrow \mu\mu\gamma$ events have low E_T.

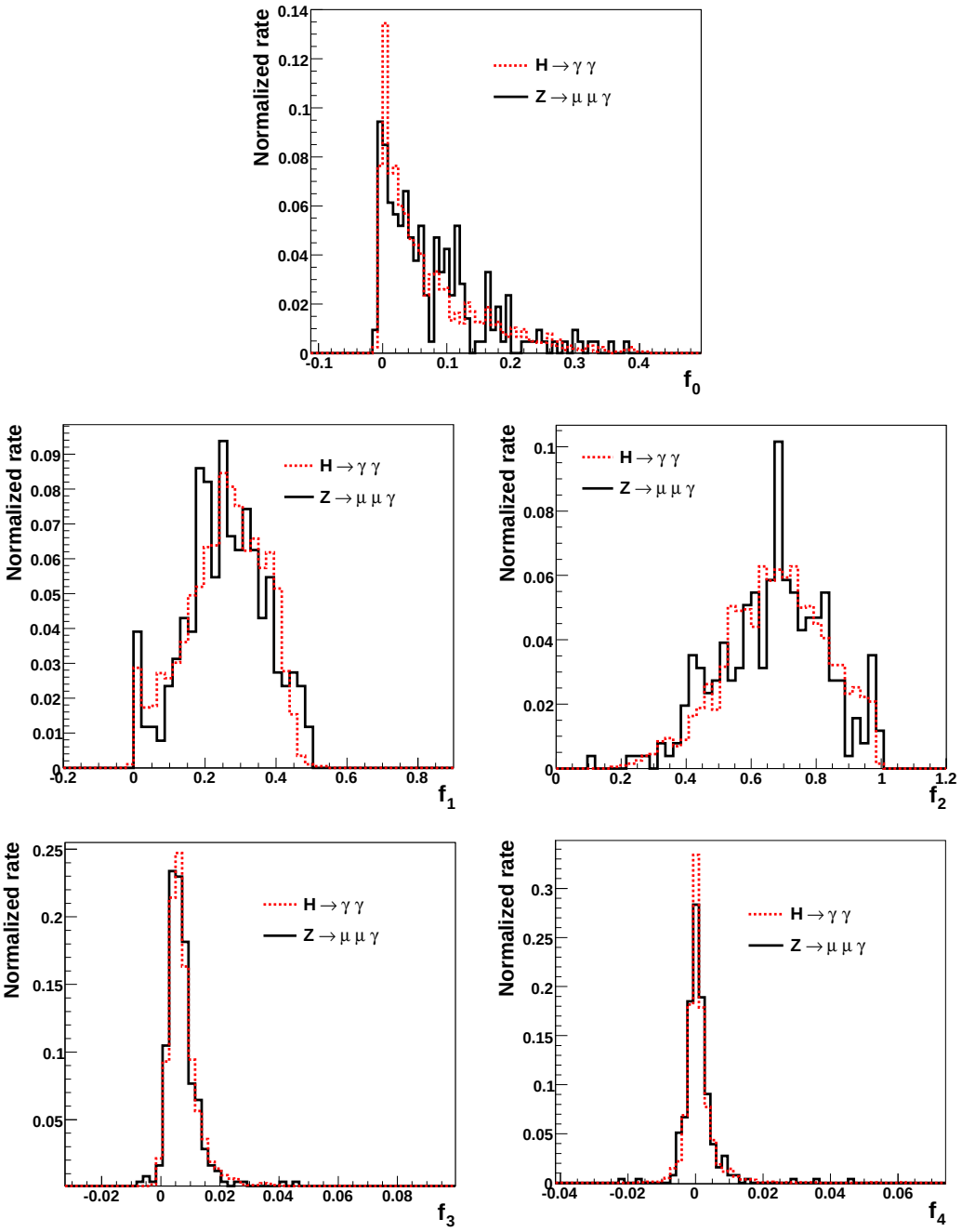

Figure 6.7. Longitudinal shower variables for inner bremsstrahlung photons from $Z \rightarrow \mu\mu\gamma$ decays (solid line histograms) and from $H \rightarrow \gamma\gamma$ decays (dashed line histograms) after Cut E. For both samples the E_T of the photon is required to be between 30 and 40 GeV.

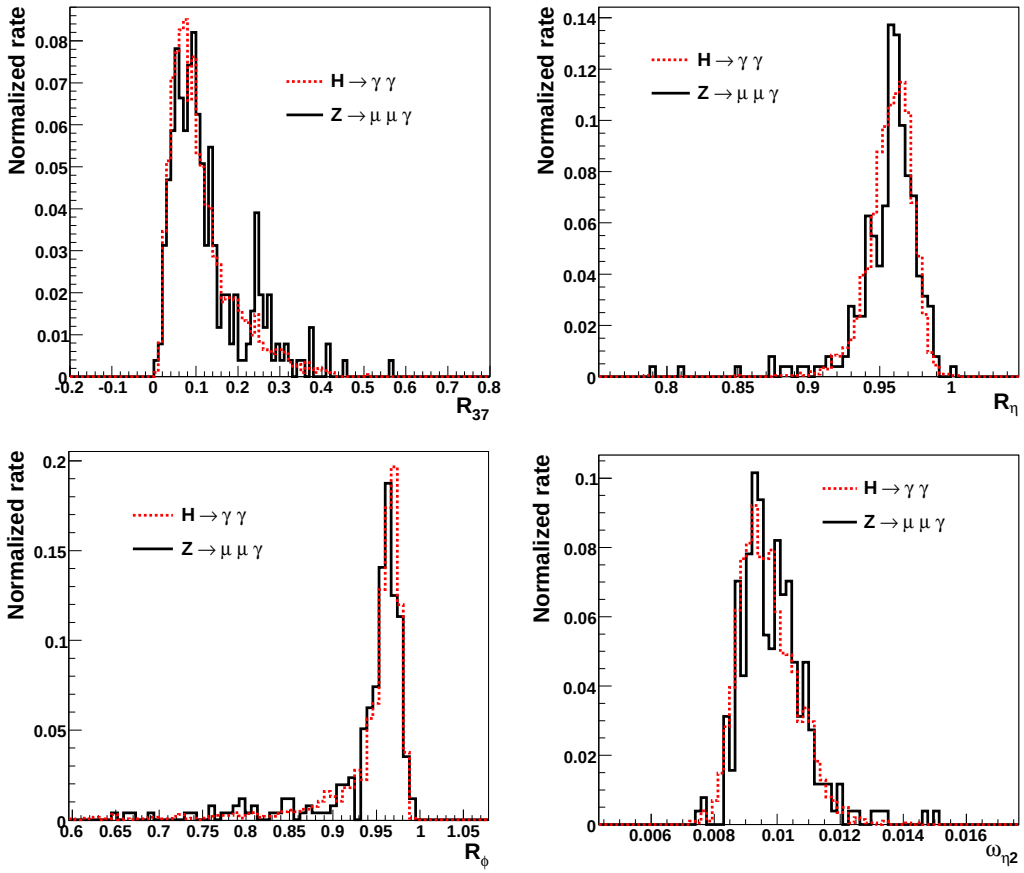

Figure 6.8. Transverse shower shape variables of the second layer of EM calorimeters for inner bremsstrahlung photons from $Z \rightarrow \mu\mu\gamma$ decays (solid line histograms) and from $H \rightarrow \gamma\gamma$ decays (dashed line histograms) after Cut E. For both samples the E_T of the photon is required to be between 30 and 40 GeV.

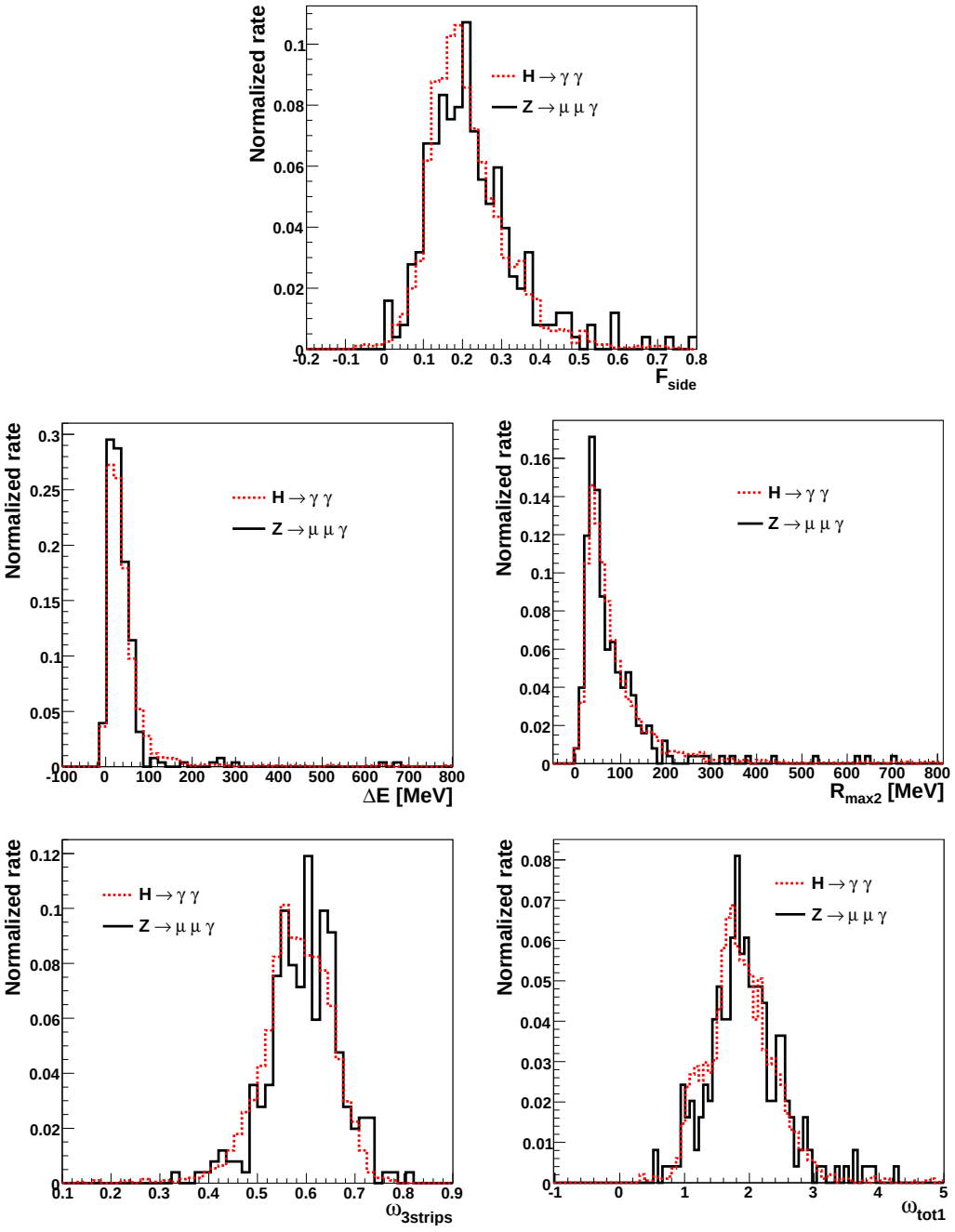

Figure 6.9. Transverse shower shape variables of the first layer of EM calorimeters for inner bremsstrahlung photons from $Z \to \mu\mu\gamma$ decays (solid line histograms) and from $H \to \gamma\gamma$ decays (dashed line histograms) after Cut E. For both samples the E_T of the photon is required to be between 30 and 40 GeV.

6.7 Measurement of Photon Identification Efficiency

The total efficiency ε to identify a photon in ATLAS can be decomposed as follows:

$$\varepsilon = \varepsilon_{\gamma}^{\mathrm{ID}} \times \varepsilon_{\gamma}^{\mathrm{loose}} \tag{6.1}$$

where $\varepsilon_{\gamma}^{\mathrm{loose}}$ is the probability to reconstruct a loose photon candidate in the presence of a photon, and $\varepsilon_{\gamma}^{\mathrm{ID}}$ is the probability for a true photon, that passes the loose photon criteria, to also pass the full photon identification criteria. The full photon identification criteria can be for instance the ATLAS standard cut based photon discriminant or the H-matrix discriminant. The first part of the efficiency $\varepsilon_{\gamma}^{\mathrm{loose}}$ is a general quantity that is common to all photon identification algorithms, which is essentially the probability to find a cluster of cells in the EM calorimeter. This part of the efficiency could be determined for instance using a tag and probe method [86, 87]. The second part of the efficiency $\varepsilon_{\gamma}^{\mathrm{ID}}$ is specific to the discriminant used to reject jets and select pure photons. This section concentrates on the calculation of $\varepsilon_{\gamma}^{\mathrm{ID}}$ for the ATLAS standard cut based and the H-matrix discriminants.

The efficiency $\varepsilon_{\gamma}^{\mathrm{ID}}$ can be obtained by using $\varepsilon_{\gamma}^{\mathrm{ID}} = N_{\gamma}^{ID}/N_{\gamma}^{\mathrm{loose}}$, where $N_{\gamma}^{\mathrm{loose}}$ is the number of loose photon candidates and N_{γ}^{ID} is the number of photons that satisfy the loose photon selection as well as the full photon discriminant (ATLAS standard cut based or H-matrix). This ratio can be computed for both discriminants as function of the photon transverse energy, using photons from $H \rightarrow \gamma\gamma$ and from inner bremsstrahlung in $Z \rightarrow \mu\mu\gamma$ decays. The result is shown in Fig. 6.10 for the H-matrix discriminant (Fig. 6.10(a)) and for the standard ATLAS cut-based discriminant (Fig. 6.10(b)). For both discriminants, the efficiencies obtained with the inner bremsstrahlung photons are in good agreement with the efficiencies obtained with the prompt photons in the $H \rightarrow \gamma\gamma$ sample. The statistical errors in Fig. 6.10 are deter-

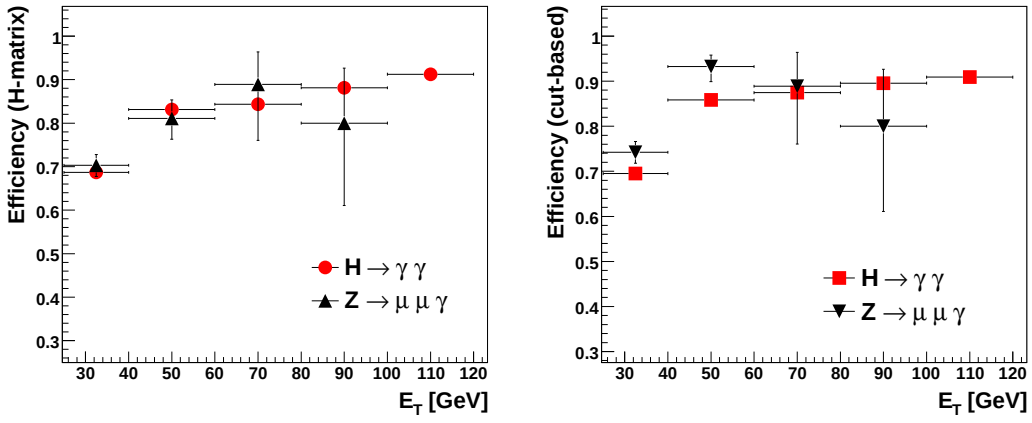

(a) (b)

Figure 6.10. Efficiency $\varepsilon_\gamma^{\mathrm{ID}}$ versus E_T for H-matrix (a) and the ATLAS cut-based discriminant (b). In each case the efficiency is compared between the inner bremsstrahlung photon sample in Z decays and the photons from Higgs boson decay.

mined by the Monte Carlo statistics of each sample. Figure 6.11 shows the expected statistical error in each E_T bin as function of the available integrated luminosity. For 200 pb^{-1} the statistical error is expected to be 2% for $10 < E_T < 20$ GeV, 3% for $20 < E_T < 40$ GeV, 4% for $40 < E_T < 60$ GeV. For integrated luminosities of several fb^{-1}, there should be enough statistics to derive the efficiency $\varepsilon_\gamma^{\mathrm{ID}}$ in bins of η as well.

6.8 Systematic Uncertainties

One important source of systematic uncertainty when deriving the photon efficiency in data is the potential contamination by either fake photons in a $Z \to \mu\mu$ event or contamination by other Standard Model processes such as WW, $t\bar{t}$ or $b\bar{b}$ production. In this section the size of these backgrounds is quantified.

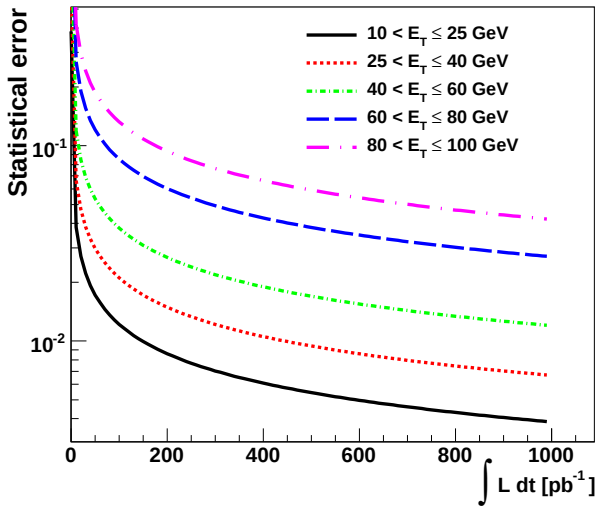

Figure 6.11. Expected statistical error versus an integrated luminosity for different E_T bins. This graph takes only into account the $1/\sqrt{N}$ behavior of the statistical error in each bin.

6.8.1 Sources of Background Photons in $pp \to Z \to \mu\mu$ Events

The sources of photons in $Z \to \mu\mu$ events are investigated by using the $Z \to \mu\mu$ PYTHIA Monte Carlo sample. The events are selected by applying Cuts A to E. The highest E_T loose photon candidate is then matched to Monte Carlo truth information. The matching is done by computing the ΔR distance between the reconstructed loose photon candidate with any Monte Carlo truth particle. The Monte Carlo truth particle with the smallest ΔR to the loose photon candidate is then selected and considered to be matched to the loose photon candidate.

The parentage tree of the selected truth particle is then followed backward to find its origin up to the hard scatter. When the selected truth particle is a photon that can be traced back to a Z via a muon, through a chain of the type $Z \to \mu \to \mu\gamma$, then the reconstructed photon is classified as coming from true inner bremsstrahlung. About 10% of the matching truth particles are photons or electrons that can be traced back to an inner bremsstrahlung photon from Z, after one or several steps of

showering and conversion. These photons are real photons coming indirectly from the inner bremsstrahlung and should legitimately be included in the efficiency calculation, since it is expected that a fraction of prompt photons does undergo early showering in the detector before it reaches the calorimeter. Finally in a fraction of events the reconstructed photons arises from hadron decays ($\omega, \eta, \eta', \pi^0$). These are fake prompt photons, which will degrade the efficiency measured in the $Z \to \mu\mu\gamma$ sample.

Figure 6.12 displays the distribution of the radius of production of the selected truth particle. The radius of production is measured with respect to the beam line. The different processes are also indicated. The bulk of the selected truth particles come from actual inner bremsstrahlung photons and have correspondingly a radius of emission at zero. Most of the other photons are radiated by detector bremsstrahlung and early showering outside the beam pipe. Finally a few photon arise from hadron decays. The exact composition of the loose photon candidates is given in Tab. 6.3 for two different sets of cuts on $m_{\mu\mu\gamma}$, using $81 < m_{\mu\mu\gamma} < 101$ (Cut E) and $85 < m_{\mu\mu\gamma} < 95$. In the case of Cut E, the contamination by fake photons is 13.8% of the sample and 6.6% for the tighter $m_{\mu\mu\gamma}$ selection.

The effect of the contamination by fake photons on the efficiency computed in section 6.7 is estimated by assuming that the photon discriminant (H-matrix or ATLAS cut-based discriminant) have zero efficiency for the fakes. A contamination of the photon sample by 6.6% fake photons would thus lead to an underestimate of the photon efficiency by about 6.6%. If c is the fraction of fakes contaminating the loose photon sample then the correct true photon efficiency is given as function of the measured efficiency $\varepsilon_\gamma^{\mathrm{ID}}$ by:

$$\varepsilon_\gamma^{\mathrm{IDCorrected}} = \frac{\varepsilon_\gamma^{\mathrm{ID}}}{1-c} \tag{6.2}$$

For the $81 < m_{\mu\mu\gamma} < 101$ GeV selection this leads to a 13.8% underestimate of the photon identification efficiency. To deal with this large effect there are several options. First the contamination could be estimated from Monte Carlo simulation and the estimated contamination c could be used to correct the measured efficiency. This would correct the systematic underestimate of the efficiency, but instead one would have to take into account the uncertainty on the Monte Carlo driven estimate of the contamination c.

One can also observe that a large fraction of the fake photons are back-to-back with the Z momentum with an angle $\Delta\phi_{Z\gamma}$ between the Z momentum and the photon candidate close to π. Thus fake photon candidates arise due to the hadronic activity opposite to the Z boson. By removing loose photon candidates back-to-back with the Z momentum direction the contamination could be decreased. Ultimately the selection on $m_{\mu\mu\gamma}$ together with a possible cut on $\Delta\phi_{Z\gamma}$ should be optimized simultaneously to maximize efficiency and purity.

6.8.2 Contamination by Other Standard Model Processes

It is possible that other physics processes than the desired $Z \to \mu\mu\gamma$ pass the selections A to E. In this section the processes $WW \to \mu\mu$, $t\bar{t} \to \mu\mu$ and $b\bar{b} \to \mu\mu$ are considered. The selections A to E are applied to the corresponding Monte Carlo samples described in section 6.3. The processes are then weighted for there cross sections and an integrated luminosity of 200 pb^{-1} is considered. Table 6.4 summarizes the estimated number of $\mu\mu\gamma$ events from signal and background processes.

The uncertainties given on the yield predictions are derived from the uncertainties on the cross sections mentioned in section 6.3. The number of $b\bar{b}$ events after final selection is estimated by deriving the efficiency of the Cut E alone on this process, without applying the muon isolation and then applying this efficiency to the number

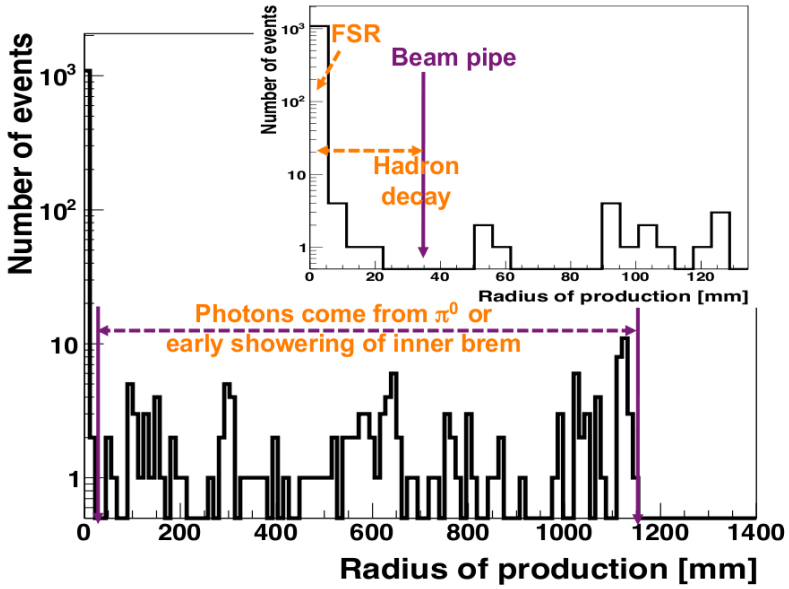

Figure 6.12. Radius of production of the truth particle matched to the reconstructed loose photon candidate. This distribution is made using the $Z \to \mu\mu$ PYTHIA sample.

Table 6.3. Sources of photon in $Z \to \mu\mu$ with requiring mass of 2 muons and one photon within 81 and 101 GeV and 85 and 95 GeV

Process	**$10 < E_T < 25$ GeV**	**$E_T > 25$ GeV**	**$E_T > 10$ GeV**
	$81 < m_{\mu\mu\gamma} < 101\ GeV$		
Inner bremsstrahlung	343	857	1200 (75.9%)
Showering and conversion of inner bremsstrahlung	48	115	163 (10.3%)
Hadron decay (ω, η, η', π^0)	6	203	209 (13.2%)
ISR or FSR from partons	0	10	10 (0.6%)
	$85 < m_{\mu\mu\gamma} < 95\ GeV$		
Inner bremsstrahlung	297	722	1019 (82.8%)
Showering and conversion of inner bremsstrahlung	40	89	129 (10.5%)
Hadron decay (ω, η, η', π^0)	4	75	79 (6.4%)
ISR or FSR from partons	0	3	3(0.2%)

of $b\bar{b}$ events found after isolation but before Cut E. This yields an estimated 54 events. The $b\bar{b}$ event yield was also estimated by deriving the efficiency of the $\Delta R_{\mu\gamma}$ (Cut D) on the $b\bar{b}$ events before muon isolation and then applying this efficiency to the $b\bar{b}$ yield after isolation. This yielded 13 $b\bar{b}$ events after all cuts. The most conservative of the two estimates was chosen for Table 6.4.

With cuts A to E about 7% of the selected $Z \rightarrow \mu\mu\gamma$ sample would in fact come from other Standard Model processes. Once the WW and $t\bar{t}$ cross sections will have been measured at the LHC center of mass energy, these contributions could be subtracted with good precision. The $b\bar{b}$ background could be estimated by using a data driven technique based on the isolation of the muons [88] or could possibly be reduced by tightening the muon isolation.

Figure 6.13 shows the invariant mass of the two muons and the loose photon for the signal and background processes scaled to the integrated luminosity of 200 pb^{-1} before Cut E. It is possible by using a side band technique to subtract the number of events below the $m_{\mu\mu\gamma}$ peak. By estimating the area under the peak before and after applying the full photon identification, it is possible to derive the efficiency $\varepsilon_{\gamma}^{\mathrm{ID}}$.

6.8.3 Extrapolation to Other Samples, Different η Distribution

The photon identification efficiency is dependent on η of the photon. Therefore if the photon efficiency derived from the inner bremsstrahlung photons from $Z \rightarrow \mu\mu\gamma$ is applied to samples with different η distribution then the total efficiency will not be correct. To estimate the size of this effect, the photon efficiency is calculated in a γ+jet sample in different η bins and compared to that of the $Z \rightarrow \mu\mu\gamma$ samples. Figure 6.14 shows the comparison of photon η distribution from γ+jet and $Z \rightarrow \mu\mu\gamma$. The photons in the $Z \rightarrow \mu\mu\gamma$ samples are more central than for γ+jet.

Table 6.4. Expected number of events for $Z \to \mu\mu\gamma$ and Standard Model backgrounds, for integrated luminosity of 200 pb^{-1} and 1 fb^{-1} at $\sqrt{s} = 10$ TeV. The uncertainties on the event yields are derived from the uncertainties on the cross sections as discussed in section 6.3. For clarity the error bars are given explicitly only for the last cut level, but the relative uncertainties are the same for all cut levels

	$Z \to \mu\mu$ PYTHIA	$Z \to \mu\mu$ ALPGEN	$WW \to \mu\mu$	$t\bar{t}$	$b\bar{b} \to \mu + X$
	$\int Ldt = 200\ pb^{-1}$				
cut A	120292	113032	117	2548	289851
cut B	114094	107669	107	910	28621
cut C	3670	2837	6	180	1363
cut D	3354	2597	5	168	454
cut E	1148±230	1078±216	0.6±0.2	24±4.8	54±27
	$\int Ldt = 1\ fb^{-1}$				
cut A	601460	585160	585	12740	1449255
cut B	570470	538345	535	4550	143105
cut C	18350	14185	30	900	6815
cut D	16770	12985	25	840	2270
cut E	5740±1150	5390±1080	3±1	120±24	270±135

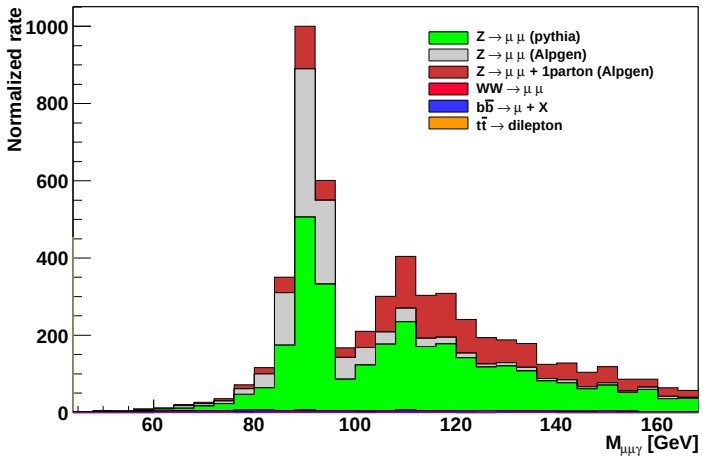

Figure 6.13. Invariant mass of two muon and a photon ($m_{\mu\mu\gamma}$) after applying all cuts except $m_{\mu\mu\gamma}$ cut. The distributions are shown for signal and various background for luminosity 200 pb^{-1}.

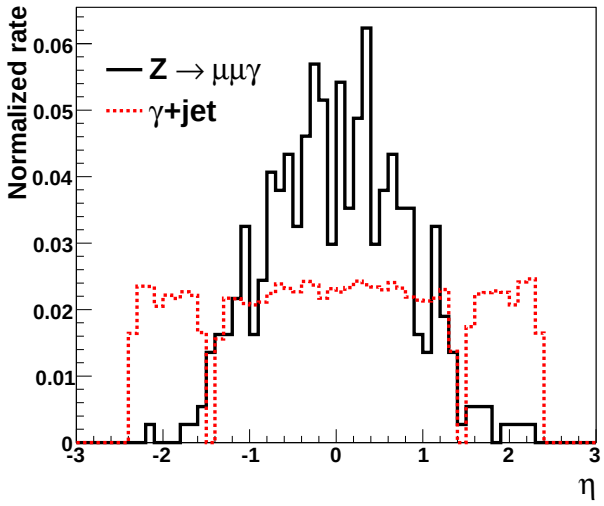

Figure 6.14. η distribution of photons from γ+jet and $Z \rightarrow \mu\mu\gamma$ events.

Figure 6.15 shows the observed difference in photon efficiency between the actual photon efficiency in γ+jet and the efficiency that would be derived if using $Z \rightarrow \mu\mu\gamma$ inner bremsstrahlung photons. The resulting bias in photon efficiency is less than 8% for photons up to E_T of 40 GeV. The bias in photon efficiency decreases tp 2% at larger E_T. Since most photons in the γ+jet samples are significantly more forward than for $Z \rightarrow \mu\mu\gamma$ for lower E_T region, the bias in photon efficiency is much highter than one for high E_T region. Once several fb^{-1} of integrated luminosity are recorded by ATLAS, it will be important to derive the photon efficiency also in bins of η of the photon, using the inner bremsstrahlung photons from the $Z \rightarrow \mu\mu\gamma$ process.

6.9 Conclusions

A new calibration process has been presented that will allow to measure the photon identification efficiencies directly with the ATLAS data, by utilizing inner bremsstrahlung photons in the process $Z \rightarrow \mu\mu\gamma$. By selecting the inner bremsstrahlung photons one obtains a sample of prompt photons. Already with a few hundreds pb^{-1} it

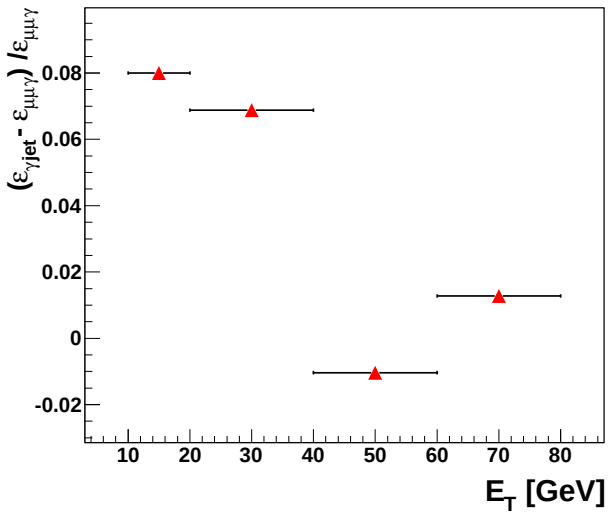

Figure 6.15. Photon efficiency difference, $\varepsilon_{\gamma jet} - \varepsilon_{\mu\mu\gamma}$ at given E_T bins due to the difference of η distribution. The $\varepsilon_{\gamma jet}$ is the actual photon efficiency in γ+jet and the $\varepsilon_{\mu\mu\gamma}$ is derived from $Z \to \mu\mu\gamma$.

should be possible to precisely extract efficiencies for photons with E_T below 40 GeV. The contamination by other Standard Model processes is about 7% with the presented selection and between 6.6% and 13.8% for fake photons inside $Z \to \mu\mu\gamma$ depending on the tightness of the selection on the $m_{\mu\mu\gamma}$ mass. The final sample composition obtained after the presented selection is summarized in Table 6.5. The contamination by other processes or by fake photons would lead to an underestimate of the in-situ photon efficiency if it is not taken into account or reduced to a negligible level. Ultimately a combination of both might be necessary. Several handles are available to reduce the backgrounds further like the angle $\Delta\phi_{Z\gamma}$ between the Z momentum and the photon candidate, or tighter cuts on $m_{\mu\mu\gamma}$, or $m_{\mu\mu}$. Once the cross sections for Standard Model processes such as $t\bar{t}$ and WW are measured at the LHC center of mass, their contribution to the signal sample could be subtracted with good precision from the signal sample. The total background contribution in data could also possibly

Table 6.5. Expected number of events after all selections (Cut E) for signal and backgrounds, for an integrated luminosity of 200 pb^{-1} and 1 fb^{-1} at $\sqrt{s}$ =10 TeV. The first column gives the actual useful inner bremsstrahlung contribution of $Z \to \mu\mu$, the second column gives the contribution from fake photons in $Z \to \mu\mu$, and the other column indicate the Standard Model backgrounds. The uncertainty on the $Z \to \mu\mu$ yield is the quadratic sum of the uncertainty from the Z production cross section (20%) and an uncertainty taken from the observed difference in yields after all selections between PYTHIA and ALPGEN.

$\int Ldt$	$Z \to \mu\mu\gamma$ (signal)	$Z \to \mu\mu\gamma$ (background)	$WW \to \mu\mu$	$t\bar{t}$	$b\bar{b} \to \mu + X$
200 pb^{-1}	990±208	158±32	0.6±0.2	24±4.8	54±27
1 fb^{-1}	4960±1040	790±160	3±1	120±24	270±135

be removed using side band technique to measure the area under the $m_{\mu\mu\gamma}$ mass peak at m_Z, before and after the selection on H-matrix or cut-based photon discriminant.

In conclusion the presented channel is promising in terms of statistics and with many possible handles that can be used to adjust the purity of the photon sample. Before the 1 fb^{-1} LHC target is reached at the end of 2011, the inner bremsstrahlung photon signal should become an important calibration tool for in-situ photon efficiency calculations in ATLAS.

CHAPTER 7

PHOTON SHOWERS IN ATLAS COSMIC-RAY MUON DATA

7.1 Introduction

The ATLAS EM calorimeter is a crucial sub-detector of ATLAS for search of the Higgs particle. Some decay channels of the Higgs particle lead to the presence of high energy photons or electrons in the final state. To be able to detect the rare Higgs boson signals, EM calorimeter must be able to precisely measure the energy of electrons or photons and discriminate between electron or photon objects and the large background from jets. The discrimination against the backgrounds is achieved by measuring the detailed shape of the EM showers and check whether it resembles more electron/photon object or the jets. It is therefore crucial to show that the shower shape variables are well modeled by the simulation and check that the calorimeter indeed provide the expected discrimination against the background. Discrepancies between the simulation and the data could for instance indicate differences between the actual distribution of the dead material in the installed detector and in the simulations.

Prior to the LHC collisions, the high-energy bremsstrahlung photons produced by cosmic-ray muons passing through the ATLAS calorimeter would provide valuable information that can be used to compare the shape of the EM showers in actual detector and in the simulation.

The lateral and longitudinal shower shapes measured in the first and second layers of the EM calorimeter are very important for photon identifications. However, there are some limitations. Unlike muon from collision, cosmic muons arrive at the

detector from random direction and random times. They can travel either both hemisphere or only a small part of detector depending on their energies and directions. Therefore, the places where photon are emitted could be anyplace of detector and the energy profile at each layer of calorimeter could be different from that of photon from collision. Therefore, the shower shapes may differ from those coming from LHC collision events due to their different origins (not interaction point, cosmic muons).

Since ATLAS has a cylindrical symmetry about the beam axis, one can characterize the vertex $\mu \rightarrow \mu\gamma$, or the point of photon emission by its distance R_γ in the transverse plane to the beam axis. A measurement of R_γ was developed using the information by combining the muon tracks measured by both the ATLAS muon spectrometer and the Inner detector with the EM shower positions measured by the EM calorimeter. Based on the value of R_γ, one can compare different configurations of photon emissions in data and simulation.

7.2 Samples of Cosmic-Ray Data and Simulation

7.2.1 Cosmic-Ray Data

The ATLAS cosmic-ray data used in this analysis were collected during the ATLAS global run between September and November 2008, with all ATLAS subsystems included in the data acquisition. Data were taken with and without the solenoid turned on. Figure 7.1 shows the accumulated statistics during a combined global run in autumn 2008 produced by different trigger streams (over 200 millions events).

The vast majority of these events were triggered with the barrel muon trigger which has a very large size and can provide up to 1 kHz of pure cosmic muons. Due to the very large acceptance of the muon system and the fact that the muon trigger had

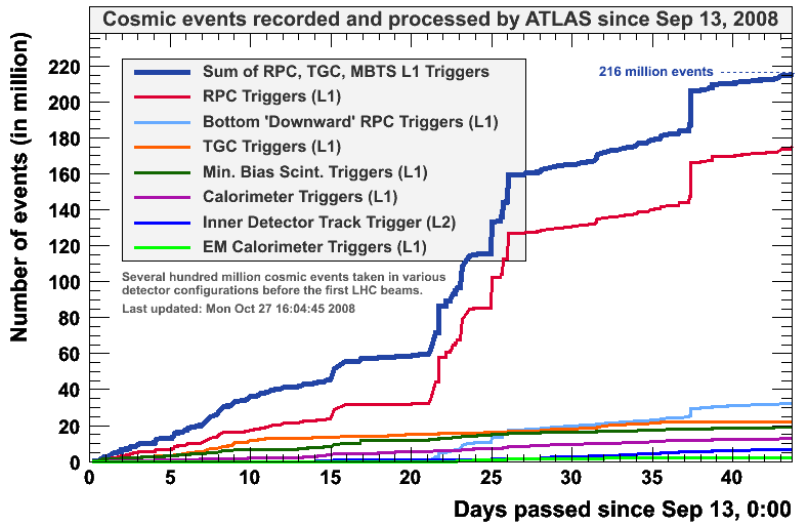

Figure 7.1. Cosmic data recorded by ATLAS since Sept 13, 2008, 216M events, were recorded in 400,000 files.

no or loose pointing requirement at the time, most of the triggering the muons do not cross the calorimeter volume. The rate of cosmic-ray muons crossing the calorimeter volume is at most 10-20 Hz or as testified by the L1Calo trigger rate during the cosmic runs. rates during cosmic runs, while the rate of events with a track crossing the pixel volume is about 0.5 Hz. The events containing a high energy photon must have a significant energy deposited in the calorimeter. Therefore the data stream of events passing one of the calorimeter triggers, called L1Calo stream, was used for this analysis. The second data stream, called IDCosmic stream. This stream is generated by sending all events trigger by any L1 trigger into the high level trigger where an inner detector track is searched for. The remaining events with a track found at L2 constitute the IDCosmic stream. The L1Calo stream and IDCosmic stream contain, respectively, 3.7 million events and 3.6 million events, of which only events with an electromagnetic cluster above 5 GeV are selected.

7.2.2 Cosmic Simulation

The cosmic-ray raw hits are simulated using detector simulation (GEANT4). These hits are digitized and reconstructed by Atlas simulation program (see chapter 4). The cosmic generator constrains the production vertex and direction of generator-level tracks, requiring simulated hits inside a certain volume, such as TRT barrel volume, inner detector volume, or Muon detector volume.

The simulation sample used this study is produced with inner detector volume. It is composed of 11.7 million cosmic-muons following the known energy and angular spectrum and tracked from the top surface to the bottom of the ATLAS detector.

7.3 Photon Emission Point Determination

The shower shape variables are sensitive to where the photon was emitted along the cosmic-ray muon track, because the point of the photon emission (the location of the $\mu \rightarrow \mu\gamma$ vertex) will determine how much material will have been crossed by the photon before it reaches the EM calorimeter where it is measured. This is also one of the main differences between the high energy photons in cosmic and the photons produced in the LHC pp collisions. While the pp collisions will yield photons mostly coming from the interaction point at the center of the experiment, the photons in cosmic-ray events can come from a large range of directions, and can be produced in the hadronic part of the calorimeter or in the middle of the EM calorimeter. For instance photon produced inside inner detector volume are potentially more alike photon from collisions than photon produced in the top hadron calorimeter. It is therefore important to compare EM showers in simulation and in cosmic data, as a function of the photon emission point.

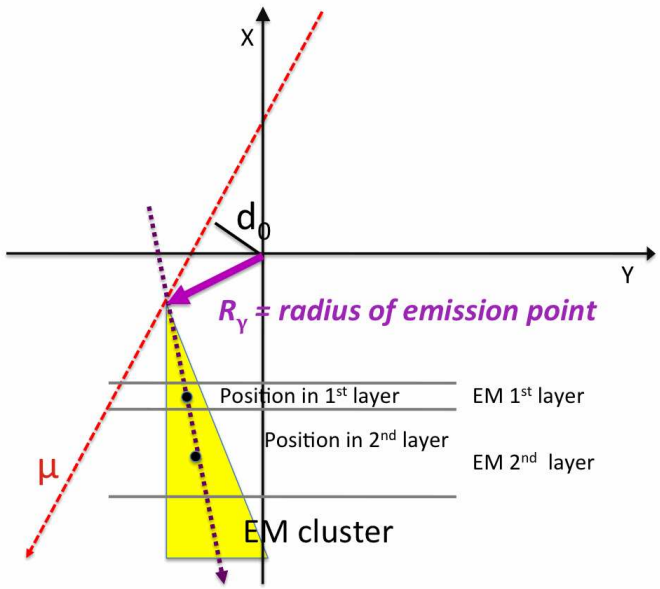

Figure 7.2. Sketch of the photon line of flight obtained from the EM shower measured in the calorimeter, intersecting with the muon trajectory.

7.3.1 Measurement of Photon Emission Point

The transverse coordinates of the emission points of the photons from $\mu \rightarrow \mu\gamma$ are referred to as X_γ and Y_γ, thus $R_\gamma = \sqrt{X_\gamma^2 + Y_\gamma^2}$. This point is defined by the intersection between the muon track and the line of flight of the photon. The parameters of the muon trajectory are obtained by combining the track measured in the muon system and in the inner detector. The line of flight of the photon is defined by the line going through the middle of the EM clusters in the first and second layer of the EM calorimeter. Exploiting the fine granularity of the EM calorimeter, the positions are measured precisely. The distance of the photon emission to the beam axis is R_γ. Figure 7.2 illustrates the intersection between the muon track and the photon line of flight. This point indicated by the arrow in the sketch corresponds to the photon emission point, its distance from beam axis is R_γ.

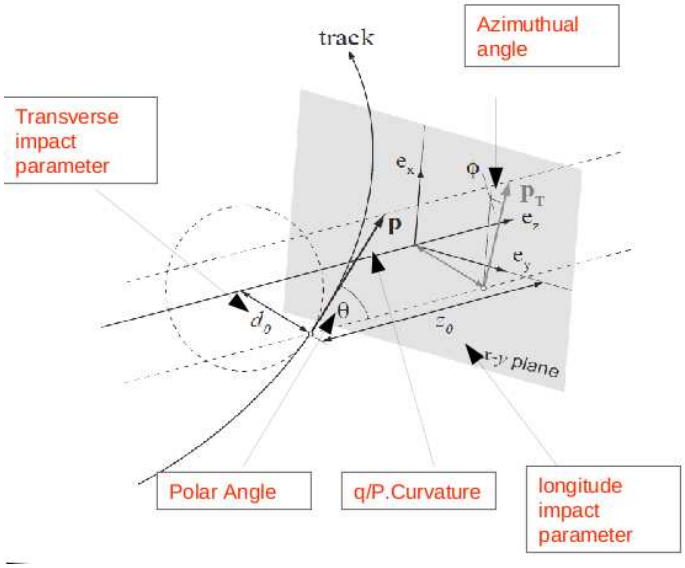

Figure 7.3. Definition of transverse impact parameter (d_0) and its sign. When the angle between the x axis and the line between center of beam axis and the point of closest approach of the track is lower (greater) than $\pi/2$ the sign is positive (negative).

Our observables are the muon transverse impact parameter d_0 and its ϕ position for determining the direction of the muon track and photon positions in η and ϕ at the first and second layers of EM calorimeter for direction of photon trajectory in x-y plane. The variable, d_0 is defined as the smallest distance of the closest approach to the beam axis as shown in Fig. 7.3. The sign of d_0 is based on the angle between the x-axis and the line between center of beam axis. The point of d_0 is lower (greater) than $\pi/2$ the sign is positive (negative).

Figure 7.4 shows the distribution of transverse impact parameter, d_0 (left) and ϕ (right) for muon track in data. The d_0 is smaller than 1000 mm. For those muon the track can be precisely measured with the help of the inner detector. This is also a configuration where the showers do not deviate too much from pp collision photons if photon is produced within inner volume.

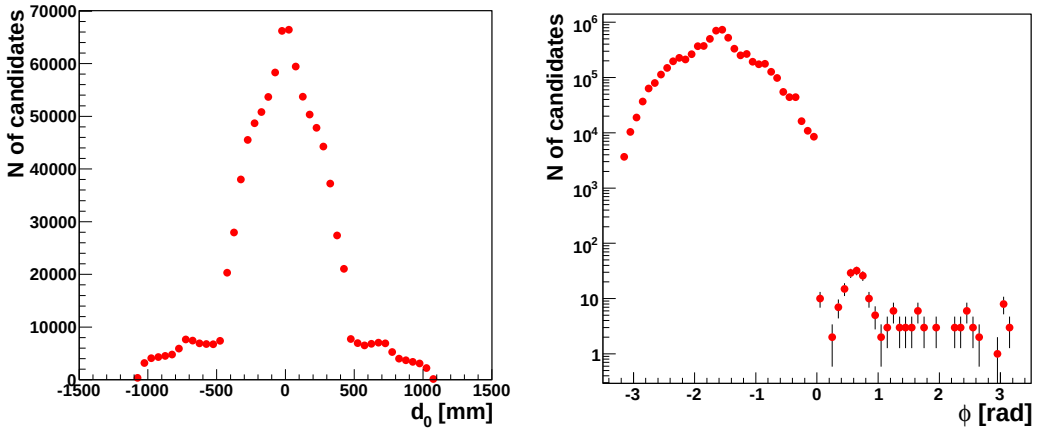

(a) (b)

Figure 7.4. Distributions of (a) d_0 and (b) ϕ for muon in cosmic-ray data.

The ϕ position of cosmic muon assigned to negative because the muon travel from upper to lower hemispheres of detector.

The other parameters η and ϕ for photons are shown in Fig 7.5 which are used for determining photon trajectory in EM calorimeter. For both plots in the figure, solid histograms shows distribution of η and ϕ in the first layer and dashed histograms shows ones in the second layer of EM calorimeter.

Figure 7.6 shows the energy difference between the first and third layers for photon from cosmic muon and simulated single photon originating from the center of the detector. For photons from collisions, their EM shower develops primarily in the second layer of EM calorimeter, and energy deposited in third layer is always bigger than in the first layer. Therefore, to select photons like the one from collision, a cut on difference energy deposited in between the first and third layers, $E_1 > E_3$ is applied.

After requiring the selection, $E_1 > E_3$, R_γ is calculated by algorithm as described in Appendix B. Figure 7.7 shows the resulting distribution R_γ distribution computed as using simulated cosmic muon events and cosmic data and Fig. 7.8 shows

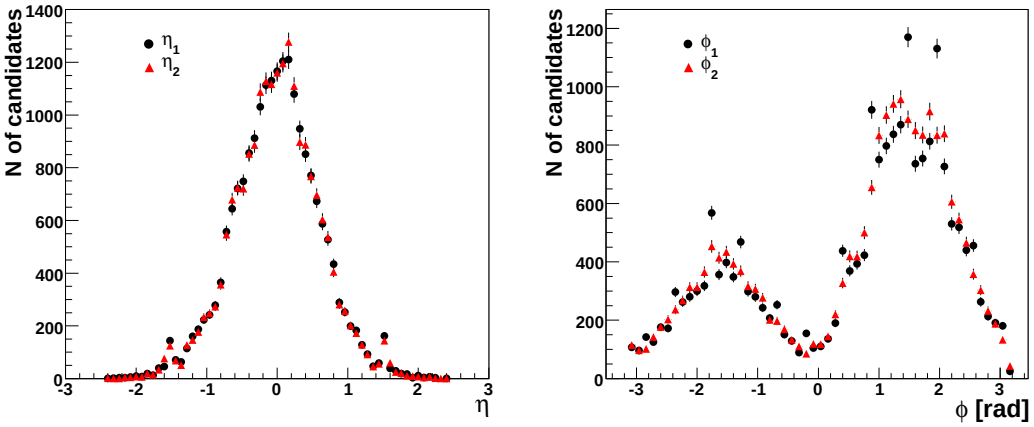

(a) (b)

Figure 7.5. Distribution of (a) η position and (b) ϕ position for photons. η_1 and ϕ_1 are measured in the first (closed line) layer of EM calorimeter and η_2 and ϕ_2 in the second layers (dashed line) of EM calorimeter, which are used to determine photon line of flight.

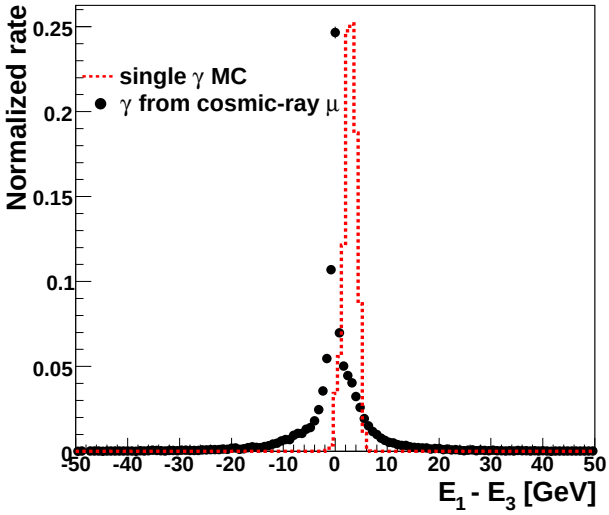

Figure 7.6. Distribution of the difference between E_1 and E_3.
Distribution of the difference of energies deposited in between the first layer (E_1) and third layer (E_3) of the EM calorimeter. Dashed histogram shows $E_1 - E_3$ for photon from center of the vertex and closed circle for photon from cosmic muon

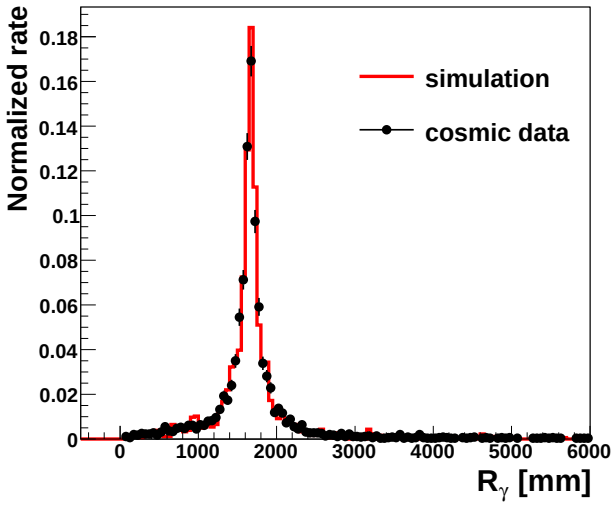

Figure 7.7. Distribution of R_γ calculated on the simulated cosmic-ray sample (histogram) and data (closed circles)..

Y_γ verses X_γ for simulated cosmic muon events. Each circles on the Fig. 7.8 indicates the position of beam, inner detector (ID), EM calorimeter (EMcal) and hadron calorimeter (HadCal) from center.

One observes that the most probable value for R_γ (or position in X_γ-Y_γ plane) corresponds to the second layer of the EM calorimeter, due to the fact that the photon will have a less probability to be recognized as a photon if the shower occurs in a different part of the ATLAS detector.

7.3.2 Validation of Photon Emission Point

Comparison of the calculated X_γ (Y_γ) and the true value of the $\mu \rightarrow \mu\gamma$ vertex position $X_{\rm vertex}$ ($Y_{\rm vertex}$) is needed for validation of photon emission point algorithm.

First of all, the parameters used for X_γ (Y_γ) calculation are studied to evaluate photon emission point algorithm. Figure 7.9 shows the comparison of reconstructed and truth d_0 and ϕ for muons. These are reasonably well reconstructed given the fact

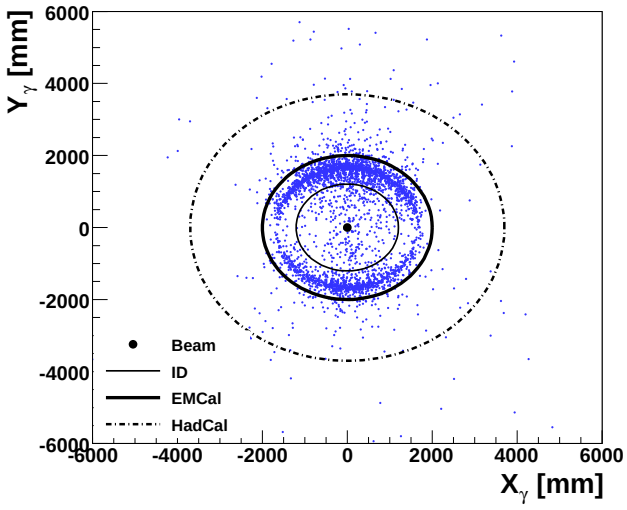

Figure 7.8. Distribution of Y_γ vs. X_γ calculated on the cosmic data. The position of ATLAS sub-detectors are shown in the plot. Most photons are radiated in the middle of EM calorimeter.

that the muons can pass up to 1 m away from the beam axis. Similarly Fig. 7.10 shows the reconstructed and truth ϕ for photons. Since traveling direction of photon is downward in the ATLAS truth photons have $-\phi$. While the reconstructed photons have $+\phi$ or $-\phi$ depending on where they measured in the top or bottom of detector, respectively. However the values of ϕ for photon are vary close to what true photons have.

Then, the difference on an event by event basis between X_γ (Y_γ) and their truth values of the vertex position X_{vertex} (Y_{vertex}) in the simulation are calculated and Fig. 7.11 shows its distribution. Due to the small angle between the muon track and the photon direction, the precision on Y_γ is worse than the precision on X_γ. Cosmic-ray muon comes to ATLAS with small angle therefore the measurements on y-axis bigger than on x-axis. In this reason, the accuracy of Y_γ is worse than that X_γ. Finally, Fig. 7.12 shows difference between R_γ and R_{vertex} and ΔR_γ is about 450 mm.

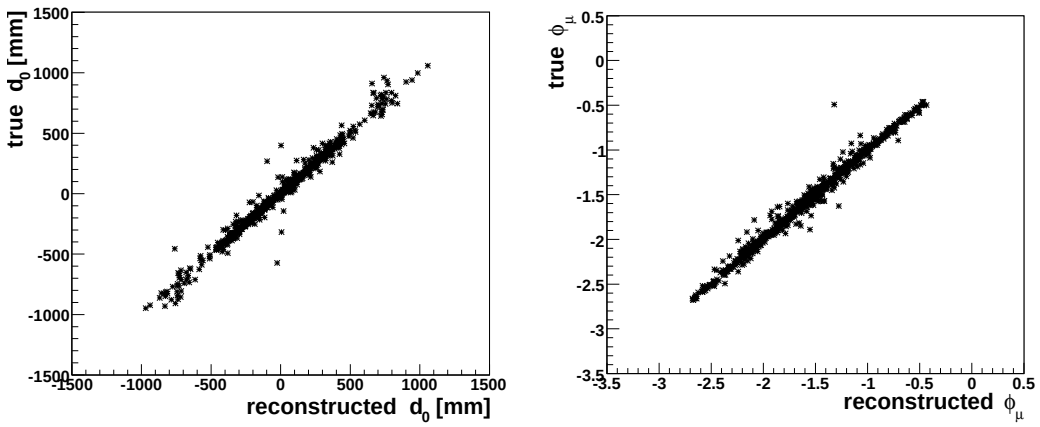

(a) (b)

Figure 7.9. Comparison of reconstructed and truth values of (a) d_0 and (b) ϕ for muons. Y-axis is their true values and X-axis their reconstructed values.

7.4 Photon Selection in Cosmic-Ray muon

The basis for the study of bremsstrahlung photons in ATLAS cosmic-ray data is a sample of 7.3 million cosmic-ray which consists of 3.7 million events in IDCosmic data stream and 3.6 million events in L1Calo data stream. The events are required to have at least one muon and one photon candidate with $E_T^\gamma > 5$ GeV. The cosmic-ray muon is identified both in the inner detector volume and in the muon system. The two data streams are merged and double counted events are removed. Table 7.1 summarizes the number of events obtained after applying the selection cuts on cosmic-ray data and simulation.

After requiring the selection described in Tab. 7.1 and the additional cut ($E_1 > E_3$) already mentioned in section 7.3.1), kinematic variables and shower shape variables is compared to ones produced from simulation.

Figures 7.13(a) to 7.13(c) show the distributions of the transverse energy (E_T), η and ϕ for photon candidates in simulation (histogram) and in data (closed circles),

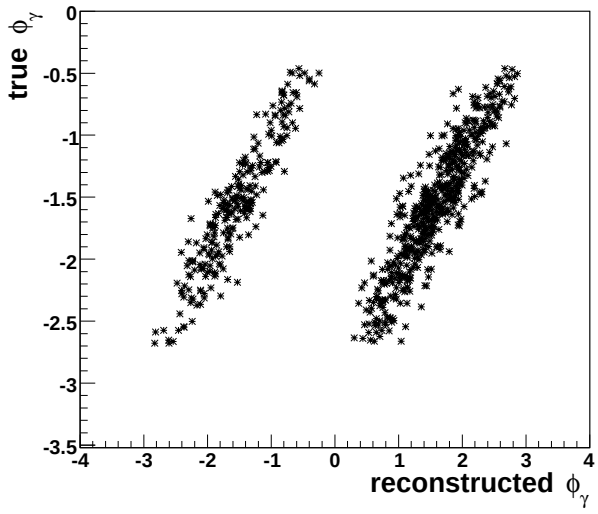

Figure 7.10. Comparison of reconstructed and truth values of ϕ for photon radiated cosmic-ray muons. Y-axis is their truth values and X-axis their reconstructed values.

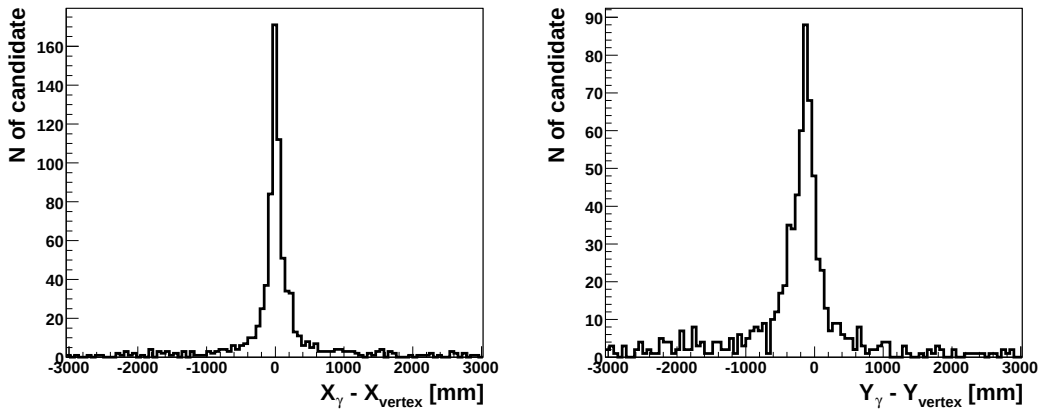

(a) (b)

Figure 7.11. (a) Distribution of the difference between the calculated X_γ and the true coordinate X_{vertex} of the simulated $\mu \to \mu\gamma$ vertex. (b) is the same for the Y_γ coordinate.

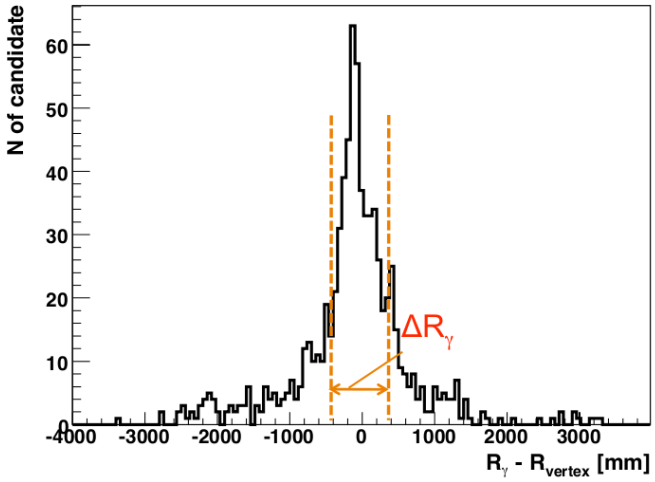

Figure 7.12. Distribution of the difference between the calculated R_γ and the true distance R_{vertex} of the simulated $\mu \to \mu\gamma$ vertex to the beam axis.

Table 7.1. Number of events after cuts

Cuts	**Data**		**Simulation**
	IDCosmic	L1Calo	
at least one μ/event	3.7×10^6	3.6×10^6	9.1×10^6
only one γ with$E_T^\gamma > 5$GeV	20778	170429	26584
μ has ID track	7276	8449	5699
removing duplication	9241		5699

respectively. These distributions from cosmic data and simulation are in excellent agreement with the simulation.

The d_0 variable from cosmic data is also compared to one from simulation. Simulation has more flat distribution than that in data as Fig. 7.13(d). The slight difference in the center ($\eta \sim 0$) could be caused by the difference of trigger and tracking efficiencies in data and simulation.

7.5 Photon Shower in the Inclusive Cosmic-ray Sample

After applying the event selection criteria described in section 7.4, the discriminating variables were computed for 9241 photon candidates in data and 5699 candidates in the simulation.

With these samples, the comparison of shower variables in cosmic data and in simulation is studied. Figures 7.14 to 7.16 show the distributions of fourteen shower variables used for H-matrix (see section 5.2.2.) In the following figures, shower shape variables in simulation are presented by histograms and those in data by closed circles. As expected the shower profile for photon from cosmic-ray muon shows different one for photon from collision. For the cosmic shower also developed from back of calorimeter not only from front. Therefore, longitudinal shower shape has longer tail and transverse shower shape are wider comparing with shower shape for photon from collision. However, all distribution from cosmic data and simulation shows good agreement.

It is expected the shower starts at the bottom of the EM calorimeter ($\phi < 0$) are more like what one from collisions. Figure 7.17 shows the different distributions for shower where it develops from the back of the EM calorimeter (left plots in the figure) and from the front (right plots in the figure). If shower start from the back the amount of energy deposited in the first layer is smaller than the case of shower starting from the front. While for energy in the second layers it is contrary.

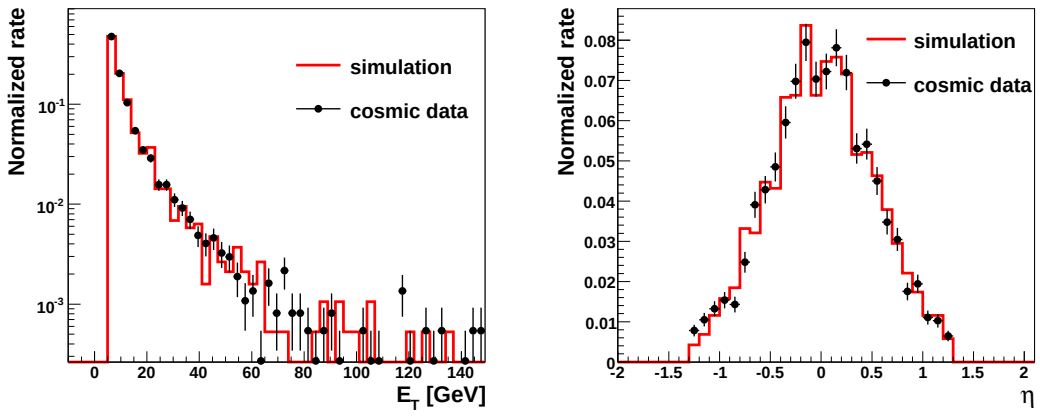

Figure 7.13. Distributions of kinematic variables, (a) E_T, (b) η and (c) ϕ, for photon candidate and (d) distribution of d_0 of muon track in cosmic data (closed circles). These variables are compared to simulation (line histogram). The cosmic data are in good agreement with the simulation.

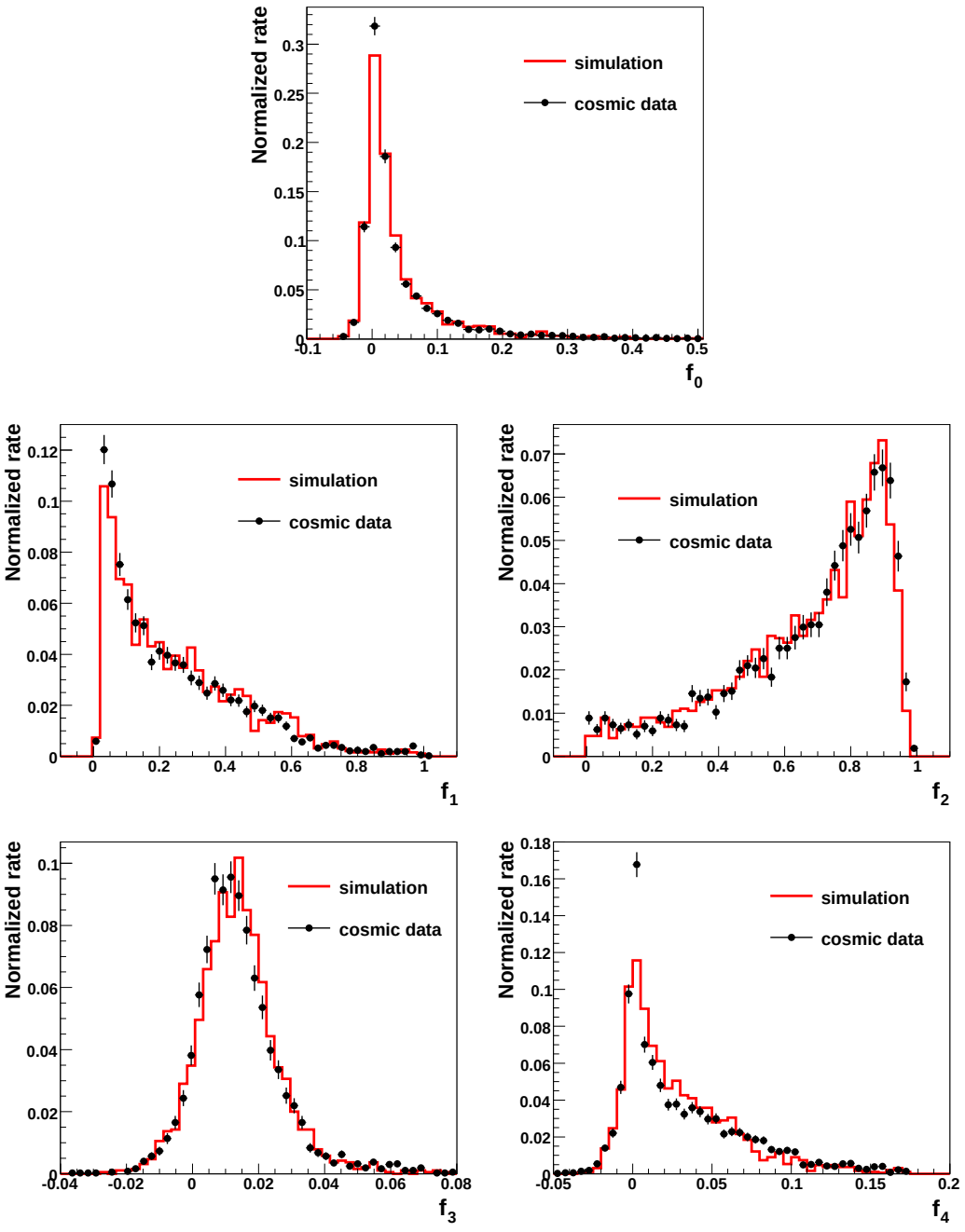

Figure 7.14. Distributions of longitudinal shower shape variables f_0, f_1, f_2, f_3 and f_4. See section 5.2.2for more detail about these variables. Histograms are from simulation and closed circles from cosmic data..

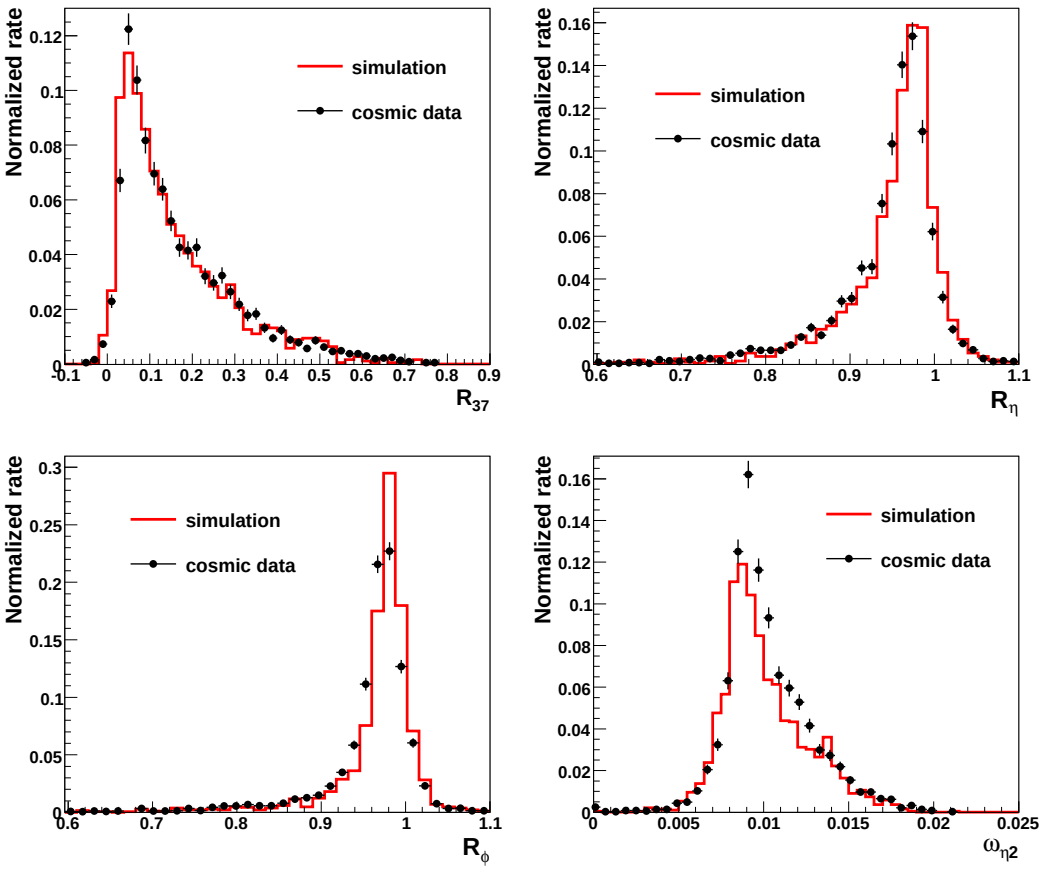

Figure 7.15. Distributions of R_{37} characterizing shower core and transverse shower shape variables in the second layer of EM calorimeter. See section 5.2.2 for more detail about these variables. Histograms are from simulation and closed circles from cosmic data..

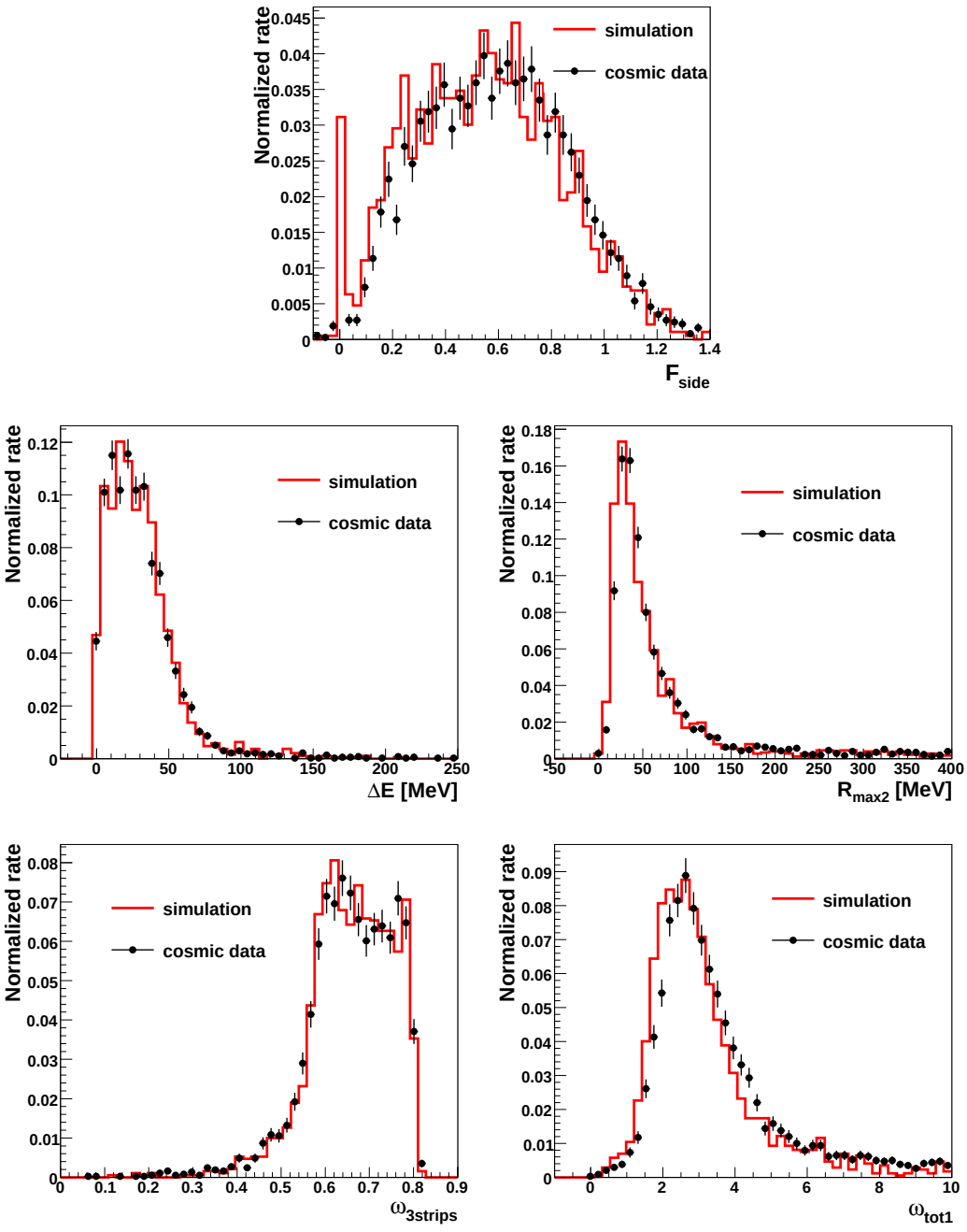

Figure 7.16. Distributions of transverse shower shape variables in the first layer of EM calorimeter. See section 5.2.2 for more detail about these variables. Histograms are from simulation and closed circles from cosmic data.

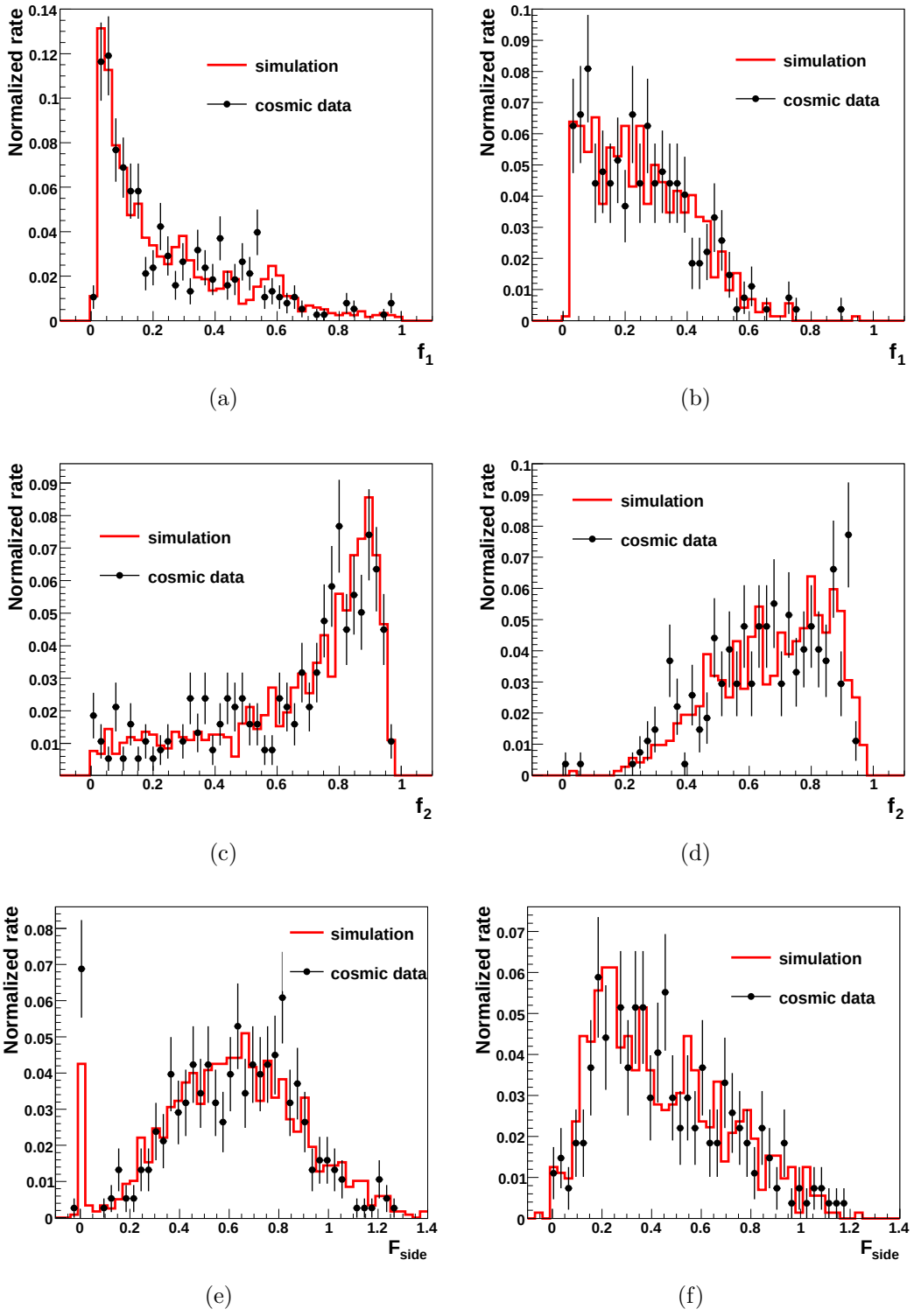

Figure 7.17. Distributions of shower shape variables at $\phi > 0$ (a, c, and e) $\phi < 0$ (b, d, and f). Shown are f_1, f_2 and F_{side} for photon candidates from cosmic-ray data and simulation.

7.6 Photon Showers as Function of Point of Emission

In the previous section, the shower shapes are integrated over all photon point of emission. In this section, we select photons produced inside the inner detector volume, requiring R_γ is smaller than the outer radius of the inner detector $R_{ID} = 1.4$.

The shower variables are very sensitive to where the shower stars to develop as show in Fig. 7.17. Therefore it is important how shower variables are changed by R_γ. The photon candidates are divided to 3 samples.

- sample A : photon radiated inside of ID detector,$R_\gamma < 1.4$ m. This sample is indicated by closed circle in the following plots.
- sample B : photon radiated outside of ID detector and reconstructed on top of detector, $R_\gamma > 1.4$ m and $R_\gamma > 0$. This sample is indicated by open square in the following plots.
- sample C : photon radiated outside of ID detector and reconstructed on bottom of detector, $R_\gamma > 1.4$ m and $R_\gamma < 0$. This is indicated by closed triangle in the following plots.

Figure 7.18(a) shows $F_{\rm side}$ based on R_γ. Clearly one can see expectedly, that the shower shape variables in sample B are wider than in sample C because showers in sample B initiate in back of EM calorimeter or Hadron calorimeter and showers in initiate in first layer of EM calorimeter. But samples A is more similar to sample C not sample B. Figures 7.18(b), 7.18(c) and 7.18(d) show $F_{\rm side}$ distribution of data and simulation for the cases of samples A, sample B and sample C, respectively. As shown in these figures, even though these two shower variables have different shower shapes depending on R_γ they still show good agreement between data and simulation for each samples. Similarly, Fig. 7.19 show the distributions of $\omega_{\rm tot1}$ for 3 samples. For $\omega_{\rm tot1}$ we still see the change by R_γ.

For further investigation, the more detail shower shapes study is carried out. The sample A is divided into two samples, $\phi > 0$ and $\phi < 0$ again. Figure 7.20 shows the distributions of f_2 and ω_{tot1} for two subsamples of sample A (open circles for $\phi > 0$ and closed ones for $\phi < 0$) and comparison to single photon sample with energy of 10 GeV (line histogram). As shown in the figure, some photons in the sample A shows the characteristics of shower which are developed from back of EM calorimeter or hadron calorimeter even they are emitted from muon inside of inner detector.

7.7 Conclusions

A sample of highly energetic bremsstrahlung photons off cosmic ray muons traversing the ATLAS detector have been isolated and used to study the shower shapes of the photons in the calorimeter. Of 300 millions cosmic rays recorded in 2008, 7 millions passed the L1 Calorimeter trigger or a track trigger in the High Level Trigger. After selections a sample of nearly 10000 photons with E_T >5 GeV could be isolated and used to compare the shower shape variables in the calorimeter with the Monte Carlo simulation. No significant discrepancy was found. It illustrates a good initial understanding of shower shape variables in real data. The shower shapes show different profiles depending on where the shower is initiate. Classes of photons were selected based on their emission point along the muon track. Even in this case the particular distributions are in good agreement with the cosmic simulation. These results give good confidence that the simulation already gives an accurate description of the material distribution in ATLAS.

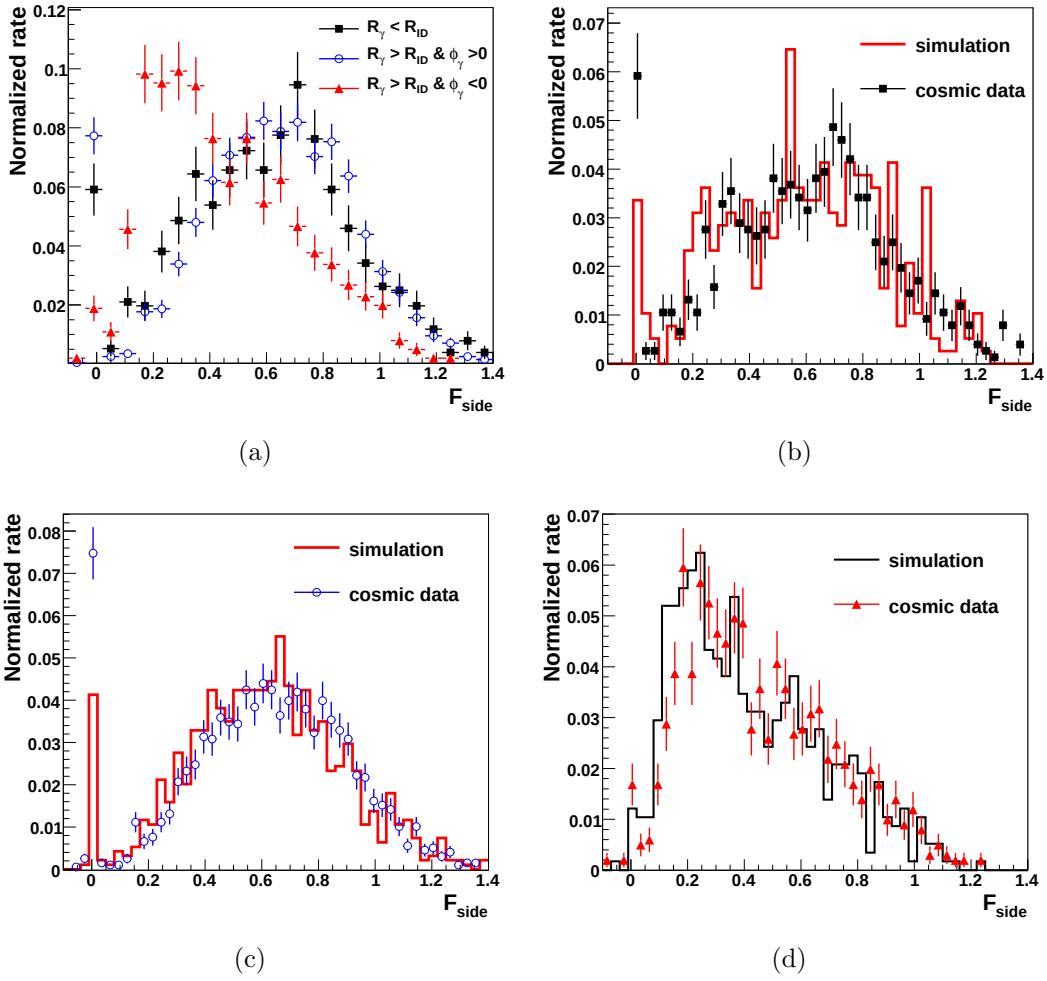

Figure 7.18. (a) $F_{\rm side}$ distributions for sample A ($R_\gamma < R_{ID}$), sample B ($R_\gamma > R_{ID}$ and $R_\gamma > 0$) and sample C ($R_\gamma > R_{ID}$ and $R_\gamma < 0$) from data. The comparison of $F_{\rm side}$ distributions in data and simulation are shown in (b), (c) and (d) for sample A, B and C, respectively.

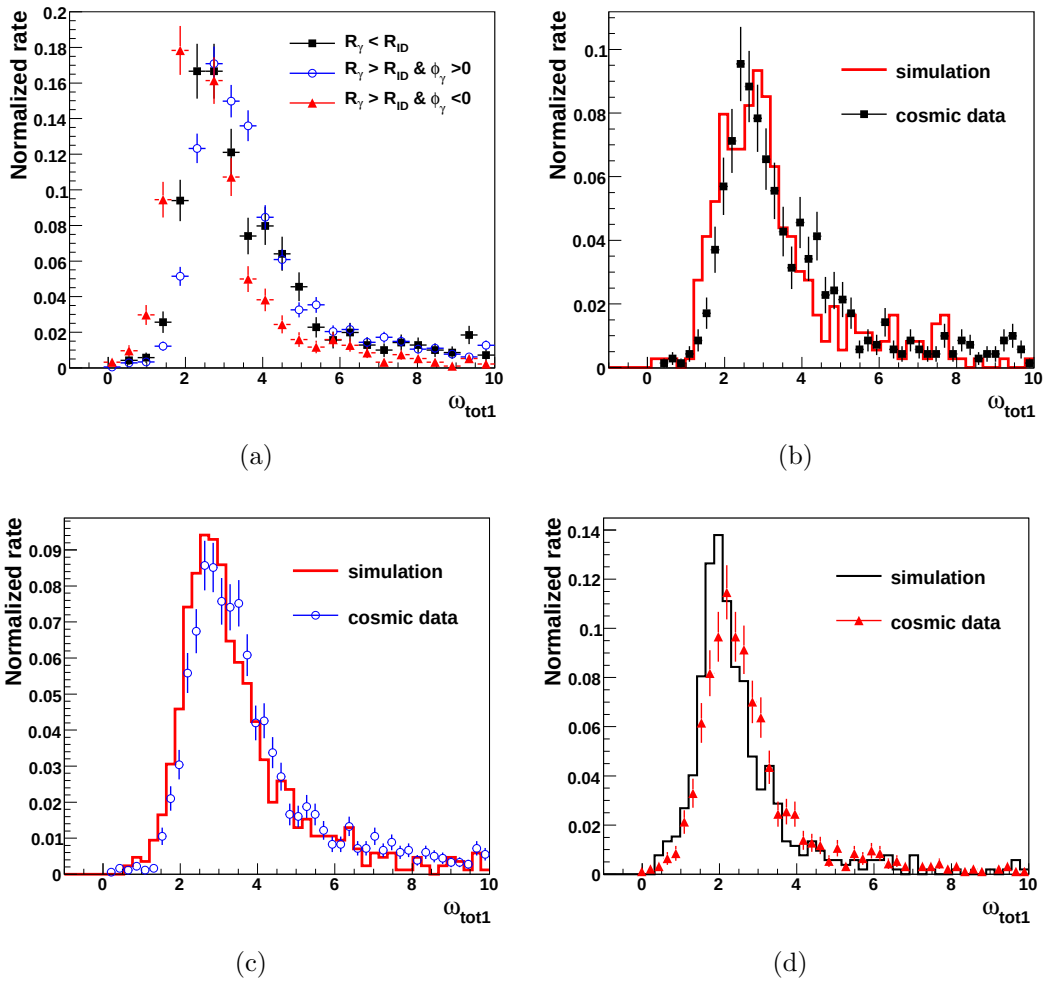

Figure 7.19. (a) ω_{tot1} distributions for sample A ($R_\gamma < R_{ID}$), sample B ($R_\gamma > R_{ID}$ and $R_\gamma > 0$) and sample C ($R_\gamma > R_{ID}$ and $R_\gamma < 0$) from data. The comparison of ω_{tot1} distributions in data and simulation are shown in (b), (c) and (d) for sample A, B and C, respectively.

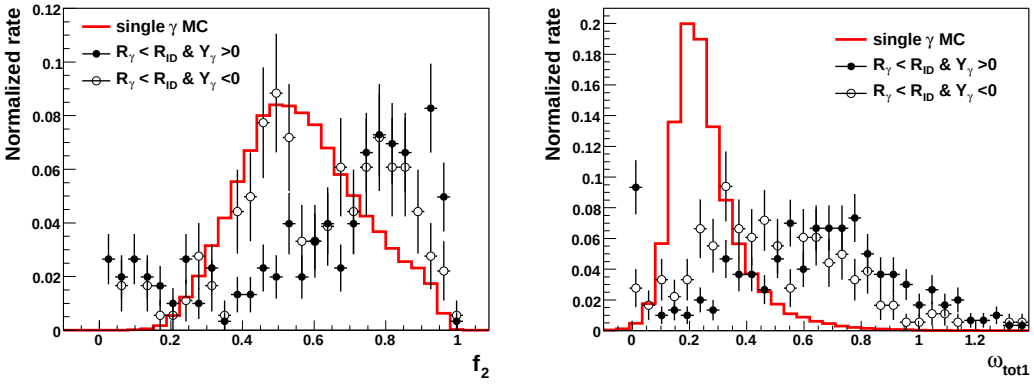

(a) (b)

Figure 7.20. (a) f_2 and (b) ω_{tot1} distributions for photon candidates in sample A. The sample are consists of two samples, $\phi > 0$ (open circles) and $\phi < 0$ (closed circles). Both plots are produced by cosmic-ray data. Monte Calo sample used here is the single photon sample with $E = 10$ GeV (line histogram).

CHAPTER 8

PROSPECT FOR HIGGS SEARCH USING $H \rightarrow \gamma\gamma$

8.1 Introduction

The Higgs decaying to two photon final state is one of the cleanest discovery channels for the Standard Model Higgs boson in the low mass range $115 < m_H \leq 150$ GeV/c^2. The signal of this channel would be observed as narrow peak in the invariant mass distribution of two photons over a large background continuum. The background can be divided into irreducible background containing two real photons and reducible backgrounds, in which at least one of the identified photon is in fact a fake from a jet. Even after using the full photon identification capability of ATLAS, the minimized reducible background of this channel is still challenging due to the its low branching ratio times cross section and the high QCD cross-section of the background.

This chapter presents the prospects for observing $H \rightarrow \gamma\gamma$ and the significance of this signal, when using the photon H-matrix. The simulation of signal and background and the analysis tools are also described.

8.2 Data Samples

The signal and background Monte Calo samples are processed with the full detector simulation of ATLAS based on GEANT4 [64]. The background Monte Carlo samples are produced with a fast detector simulation [89] which are used primarily for the evaluation of the analysis sensitivity to the $H \rightarrow \gamma\gamma$ signal.

8.2.1 Signal Process

As shown in Fig. 2.5, there are four Higgs production processes: Gluon Fusion, Vector Boson Fusion (VBF), Higgs-strahlung with W/Z and $t\bar{t}(b\bar{b})H$ associated production (ttH). In this study, the signal sample produced by gluon fusion process is used.

The gluon fusion process simulated with MC@NLO is used here [72, 73]. The MC@NLO gives a QCD Next Leading Order (NLO) matrix element in addition to a good description of multiple soft gluon emission at the next-to-next-to-leading logarithmic level (NNLL) [90, 91, 92]. This higher order consideration is relevant to the evaluation of the discriminating power of the E_T of diphoton and jets distributions. The signal process are modelled with fully simulated samples. The leading order (LO) and NLO cross-sections of $H \rightarrow \gamma\gamma$ channel for several Higgs boson masses are listed in Table 8.1. The NLO cross-section is obtained by [93]: $\sigma_{NLO} \times (1 + \delta_{QCD} + \delta_{EW})$. The δ_{QCD} and δ_{EW} are NLO electroweak and QCD correction [94], respectively.

Table 8.1. Summary of cross-sections for the $H \rightarrow \gamma\gamma$ signal used in the study.

m_H (GeV/c^2)	LO cross-section (fb)	NLO cross-section (fb)
115	48.4	90.5
120	47.6	88.5
130	41.1	77.2
140	30.5	57.6

8.2.2 Background Process

The background to the $H \rightarrow \gamma\gamma$ channel can be separated into irreducible background and reducible backgrounds as follows:

- Irreducible background
  - two prompt photons from $q\bar{q} \rightarrow \gamma\gamma$ or $gg \rightarrow \gamma\gamma$
  - quark bremsstrahlung from $qg \rightarrow q\gamma \rightarrow q\gamma\gamma$.
- Reducible background
  - γ+jet events where a leading π^0 in a jet has been misidentified as one photon
  - jet-jet events where both jets have been misidentified as photons.

Irreducible backgrounds come directly from two isolated photons and reducible backgrounds come from events with at least one fake photon. These fake photons are mostly due to the misidentification of a leading π^0 resulting from the fragmentation of a quark or a gluon. The irreducible backgrounds are shown in Fig 8.1 and mainly produced by the Born ($q\bar{q} \rightarrow \gamma\gamma$), box ($gg \rightarrow \gamma\gamma$) and bremsstrahlung ($qg \rightarrow q\gamma \rightarrow q\gamma\gamma$) processes.

The reducible backgrounds are coming from QCD jet processes which haves cross-sections many orders of magnitude above the $H \rightarrow \gamma\gamma$ cross-section. The dominant contribution to the reducible background consists of jet-jet events which are dominated by gluon initiated jets which are easier to reject with respect to the quark initiated jets. In the case of the γ+jet process, quark initiated jets are the dominant contribution (see Fig. 8.2).

For QCD correction to background the DIPHOX [95] and REBOS [96, 97] programs can evaluate the irreducible background. DIPHOX computes the cross-section at NLO but without the resumption effects. Moreover, it includes the fragmentation from quark and gluon to photons at NLO. REBOS covers the Born and box contributions at NLO except that fragmentation from quarks or gluons is only at LO as well

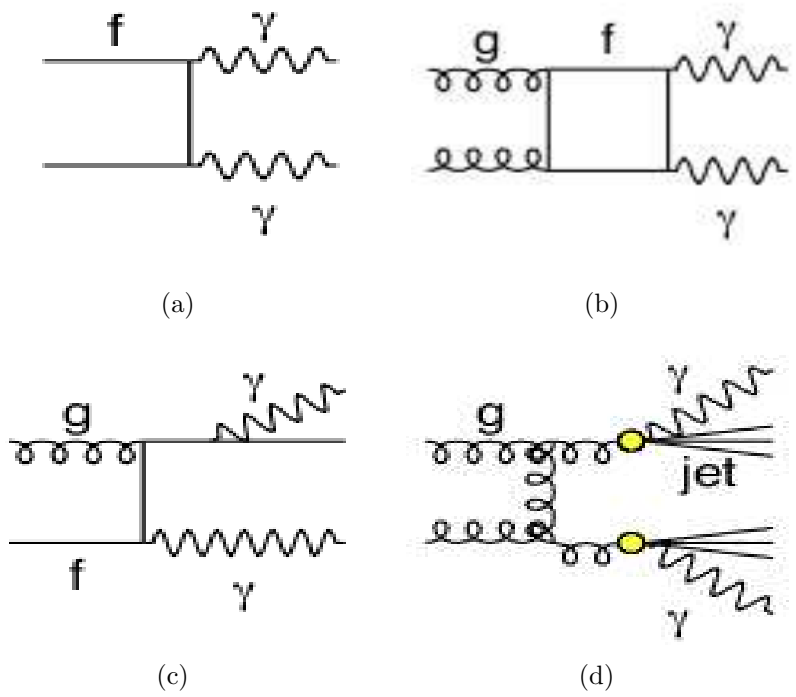

Figure 8.1. Diagrams of irreducible process to the two photon decay of a Higgs boson from the (a) Born, (b) box and bremsstrahlung (c and d) processes.

as resummation effects to NNLL. The prediction of DIPHOX and RESBOS for the total irreducible background agree to better than 10% [50].

ALPGEN is used to generate sample of $\gamma\gamma$+jets with a fast detector simulation. This generator produces $2 \rightarrow N$ tree level matrix elements, where N = 2 - 5. The MLM prescription for the merging of the parton shower and the matrix elements is also implemented

The inclusive cross-section for the γ+jet process is obtained using the package JETPHOX [98]. This package provides a next-to-leading fixed order (NLO) prediction of the differential cross sections for the γ+jet processes, and the fragmentation of final-state partons into a leading photon. The differential cross section obtained with

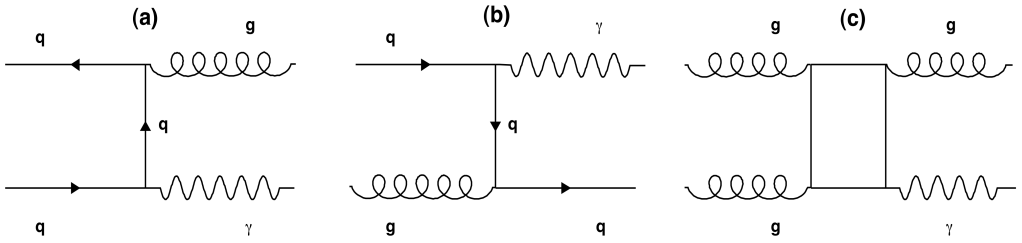

Figure 8.2. Feynman diagrams of γ-jet production process.

JETPHOX is found to be a factor of 2.1 larger than that obtained with PYTHIA with weak E_T dependence for p_{T_γ} larger than 25 GeV [99].

The inclusive cross-section for dijet production is computed with the NLOJET++ package [100, 101] which considers QCD NLO corrections. It is observed that the cross-section obtained is a factor of 1.3 larger than the one obtained with PYTHIA with $p_{T_{jet}} > 25$ GeV.

The γ+jet and jet-jet backgrounds are simulated by PYTHIA. Jets are considered as photon candidates when a neutral pion passing the basic kinematical selection criteria is found in the event. The Bremsstrahlung events are considered to be those γ+jet events where a second prompt photon is observed.

The cross-sections of the irreducible and reducible backgrounds used in the $H \to \gamma\gamma$ analysis are sumarrized in Tab. 8.2.

Table 8.2. Summary of the cross-sections of the backgrounds samples used in $H \to \gamma\gamma$ analysis.

Process	**Cross-section (pb)**	**Generator**
$q\bar{q}, qg \to \gamma\gamma$X	20.1	PYTHIA
$gg \to \gamma\gamma$	8.0	ALPGEN
γ+jets	2.893 $\times 10^5$	PYTHIA
jj	9.261 $\times 10^8$	PYTHIA

8.3 Event Selection

In the standard inclusive analysis the following kinematical cuts are applied in order to optimize the signal significance:

- **Cut** I: Both photons are required to hit the electromagnetic calorimeter in the region $|\eta| < 2.5$. Two η regions, $1.37 < |\eta| < 1.52$ and $2.37 < |\eta| < 2.5$ have been excluded where the EM calorimeter response is not optimal (see section 3.3.3).
- **Cut** II: The two photon candidates are required to have a transverse energy greater than 40 (for leading photon) and 25 GeV (for sub-leading photon), respectively;

The fiducial Cut I are motivated by the quality of the off-line photon identification and the fake photon rate. The values of photon transverse momentum cuts are obtained by previous optimization studies. [44, 102].

The E_T distribution of the photons after Cut I and Cut II is shown in Fig. 8.3. The distribution for signal is produced by $H \rightarrow \gamma\gamma$ sample with Higgs mass of 120 GeV/c^2. The E_T distribution of the leading photon corresponds to Fig. 8.3(a) and that of the sub-leading photons to Fig. 8.3(b) for signal (solid histogram) and background (dashed histogram). The background processes are added together according to cross-sections and the signal and background histograms are normalized to unity. Most photon events in the signal have E_T of $\sim$ 60 GeV for leading photons, of $\sim$ 50 GeV for sub-leading photons while those from the background shows a rapidly decreasing spectrum. The E_T cuts for the photons are set to be 25 GeV and 40 GeV cutting away part of the soft photon events in the background, and keeping 67% of the signal events.

Figure 8.4 shows the diphoton invariant mass distributions after applying both the selection cuts. The expected contribution from a Higgs boson signal for $m_H =$

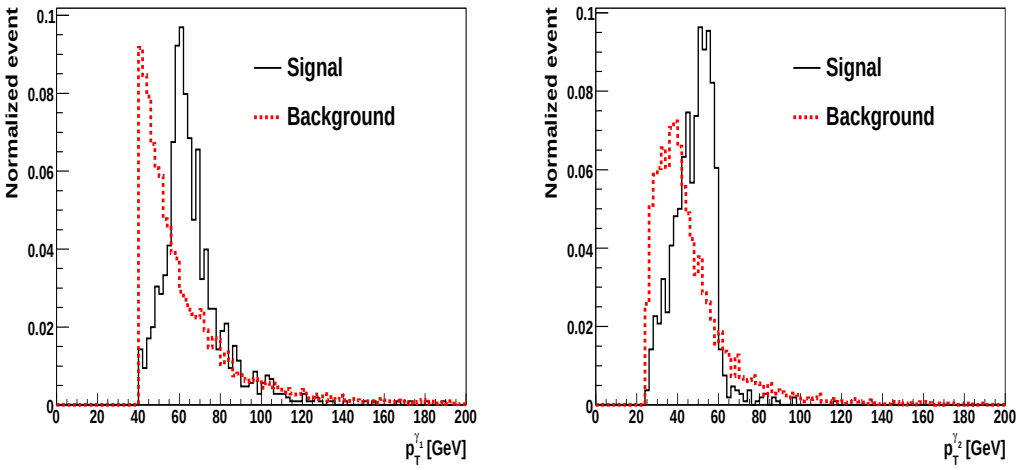

(a) (b)

Figure 8.3. Transverse momentum distributions of the (a) leading photon ($p_T^{\gamma 1}$)and (b) sub-leading photon ($p_T^{\gamma -2}$) for signal and background after all the cuts are applied. The histograms are produced by Higgs samples with mass, $m_H = 120$ GeV/c^2. Histograms are normalized to unity.

120 GeV/c^2 is shown in Fig. 8.4(a) and for $m_H = 140$ GeV/c^2 in Fig. 8.4(b). The line histograms in the both plots show a Gaussian fit to the peak of $M_{\gamma\gamma}$. The measured invariant mass of two photons are 119 ± 2.2 and 136 ± 2.5 for single samples with $m_H = 120$ GeV/c^2 and $m_H = 140$ GeV/c^2, respectively.

Figure 8.5 shows the expected diphoton mass spectrum after the application of cuts I and II. The hashed histogram in the bottom corresponds to the total contributions from events with one and two fake photons and irreducible backgrounds. The background contributions are obtained with MC samples normalized to their cross-sections.

8.4 Signal Significance in $H \rightarrow \gamma\gamma$

Signal significance of the Higgs signal in the two photon decay channel is given from the expected number of signal and background events. Signal significance are

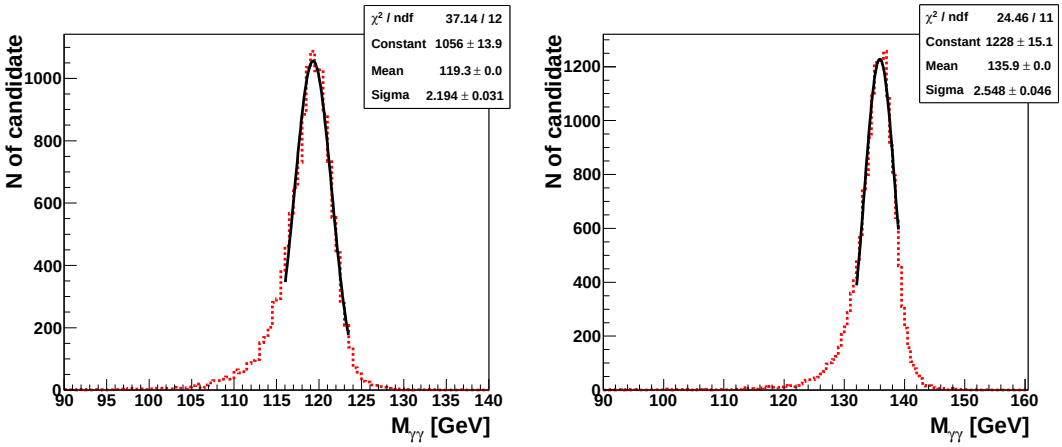

(a) (b)

Figure 8.4. $m_{\gamma\gamma}$ distributions for Higgs boson samples with (a) $m_H = 120$ and (b) $m_H = 140$ GeV/c^2, fit to a Gaussian (line histograms). The measured invariant mass of two photons are 119±2.2 for $m_H = 120$ GeV/c^2 and 136±2.5 for $m_H = 140$ GeV/c^2 signal samples, respectively.

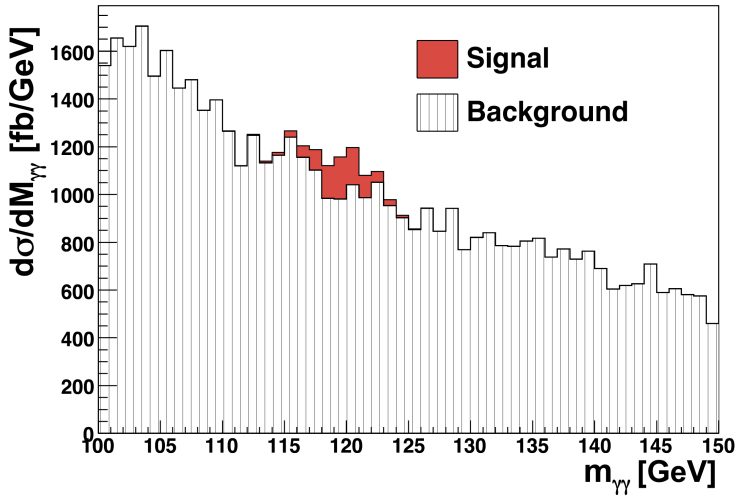

Figure 8.5. $H \rightarrow \gamma\gamma$ signal on the top of the background process after cuts, in the case of a 120 GeV/c^2 Higgs boson. Histograms are normalized to an integrated luminosity of 100fb^{-1}.

Table 8.3. Number of diphoton event candidates for 100fb^{-1} after Cuts I, II and the H-matrix $\chi^2_{\gamma-\text{jet}}$ cuts, $\chi^2_{\gamma-\text{jet}} < 3$ and $\chi^2_{\gamma-\text{jet}} < 5$. The column B_{tot} gives the total number of background events and the last column gives the significance of the expected signal excess of the background

m_H	Signal	Background process			B_{tot}	$S/\sqrt{B_{tot}}$
(GeV)	(S)	$\gamma\gamma$	γj	jj		
$\chi^2_{\gamma-\text{jet}} < 3$						
115	375	7593	34.88	1438	9066	3.9
120	455	10431	85.62	3529	14046	3.8
130	409	5180	52.85	2178	7411	4.8
140	301	6244	29.07	1198	7471	3.5
$\chi^2_{\gamma-\text{jet}} < 5$						
115	446	9036	51.68	2549	11637	4.1
120	541	12414	126.59	6243	18784	3.9
130	487	6165	78.31	3862	10105	4.9
140	358	7431	43.07	2124	9598	3.7

considered for different Higgs masses, 115, 120, 130 and 140 GeV/c^2. It is reported that the highest significance is obtained with a mass bin of width $\pm 1.4\sigma$ (m_{H}) [76]. Thus cut values on invariant mass are chosen within this window, $m_{\gamma\gamma}$ of $\pm 1.4\sigma$ of each masses.

In addition this, the rejection power of H-matrix for irreducible and reducible backgrounds are calculated based on the performance result from section 5.3.3. Using the fake rates and efficiency for two different χ^2 cut values the expected number of photon events at 100 fb^{-1} are obtained. The summary table of the number of signal and background events, and the total significance $S/\sqrt{B}$ after one year at high luminosity is shown in Tab. 8.3.

Figure 8.3 shows the signal significance for 100 fb^{-1} of integrated luminosity as a function of the Higgs mass at 3 and 5 of $\chi^2_{\gamma-\text{jet}}$ cut values. It has been found, that the result of cut $\chi^2_{\gamma-\text{jet}} < 5$ shows a higher significance than the result of the cut

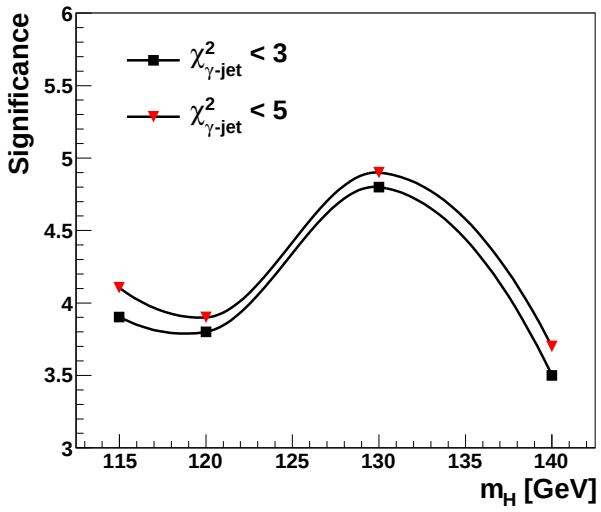

Figure 8.6. Expected signal significance for a Higgs boson using the $H \to \gamma\gamma$ decay for an integrated luminosity of 100 fb^{-1} as a function of the mass.

$\chi^2_{\gamma-\text{jet}} < 3$. Therefore the highest significance at given Higgs mass can be achieved by optimizming the cut value on $\chi^2_{\gamma-\text{jet}}$.

8.5 Conclusions

The $H \to \gamma\gamma$ decay mode of a Standard Model Higgs boson is the most promising detection channel for a Higgs boson in the mass range $115 < m_H < 150$ GeV. Nevertheless it is still very challenging and its discovery will require both ATLAS and the LHC accelerator to reach nominal design performance.

The signal of two isolated photons from $H \to \gamma\gamma$ can be discovered with integrated luminosities of several 100 fb^{-1}, but both the irreducible $\gamma\gamma$ background and the reducible jet-jet and γ+jet backgrounds are mucher large than the signal. After requiring highly transverse energetic photons, a very large fraction of the QCD-jets is removed, and the remaining reducible background mostly comes from single π^0. A photon identification tool such as H-matrix, that uses the detailed information of the

high granularity and high resolution ATLAS EM Calorimeter is crucial to make the discovery of $H \rightarrow \gamma\gamma$ possible.

CHAPTER 9

CONCLUSIONS

With the performance of the ATLAS detector and the expected signal and background rates at LHC, the ATLAS experiment will be able to discover the Standard Model Higgs over the entire Higgs mass range $115 - 1000$ GeV/c^2. An integrated luminosity of 10 fb^{-1} and center of mass of 14 TeV may be sufficient if the Higgs particle mass is in the range $150 - 500$ GeV/c^2. The LHC is expected to be able to deliver this amount of integrated luminosity in the years to come, once the accelerator can provide an instantaneous luminosity of $L = 10^{33}\text{cm}^{-2}\text{s}^{-1}$. The two most demanding mass regions for the Higgs discovery are the low mass range below $m_H = 140$ GeV/c^2 and the high mass end above $m_H = 600$ GeV/c^2. In the low mass range, the cleanest signature of the Higgs is the $H \rightarrow \gamma\gamma$ channel. This channel requires an excellent energy resolution and angular resolution for photons, and a powerful photon identification to reject the huge multijet and γ+jets backgrounds.

Based on the need for powerful photon identification, a covariant matrix based algorithm has been developed to identify electrons and photons. This method exploits the high granularity of the ATLAS electromagnetic calorimeter and the expected correlations between various EM shower shape variables. To take into account the specific features of electron and photon showers, two H-matrix discriminants have been in practice developed, one specialized in photon identification and one specialized in electron identification. To enhance further the jet rejection a jet H-matrix has been built and combined with the photon H-matrix. The electron H-matrix shows significantly better performance than the current standard ATLAS cut-based electron

discriminant. The combined photon-jet H-matrix shows also excellent jet rejection but is comparable to the ATLAS cut-based method. Since the H-matrix discriminant provides a continuous variable to cut on, the cut value on the H-matrix can be adjusted to the needed efficiency versus rejection working point, optimal to a certain analysis. The ATLAS cut-based discriminant is less flexible.

A new calibration process has been studied that will allow to measure the photon identification efficiency directly with the ATLAS data. By selecting the inner bremsstrahlung photons in $Z \to \mu\mu\gamma$ events a pure sample of prompt photons can be isolated. Already with a few hundreds pb^{-1} it should be possible to precisely extract efficiencies for photons with E_T below 40 GeV. The contamination by other Standard Model processes is about 7% with the presented selection and between 7% and 14% of fake photons from the $Z \to \mu\mu\gamma$ events themselves, depending on the tightness of the selection on the $m_{\mu\mu\gamma}$ mass. The contamination by other processes or by fake photons would lead to an underestimate of the in-situ photon efficiency if it is not taken into account or reduced to a negligible level. These backgrounds could be reduced further by considering the angle $\Delta\phi_{Z\gamma}$ between the Z momentum and the photon candidate, or tighter cuts on $m_{\mu\mu\gamma}$, or $m_{\mu\mu}$. The total background contribution in data could also possibly be removed using side band technique to measure the area under the $m_{\mu\mu\gamma}$ mass peak at m_Z, before and after the selection on H-matrix or cut-based photon discriminant.

The $Z \to \mu\mu\gamma$ channel is promising in terms of statistics given the large integrated luminosity expected at the LHC. Before the 1 fb^{-1} at $\sqrt{s} = 7$ TeV LHC target is reached at the end of 2011, this channel should become important for in-situ photon efficiency calculations in ATLAS.

The outlook for measurements with photons and electrons in the early ATLAS data is excellent. The data to simulation comparisons show already good agree-

ment at this early stage of the experiment. In addition calibration processes such as $Z \rightarrow ee$ and $Z \rightarrow \mu\mu\gamma$ will become available within the coming 1.5 years, in large enough statistics that the efficiencies of electron and photon H-matrix can be measured directly in data.

Prior to the LHC beam, considerable amount of cosmic data were collected with the ATLAS detector. These data have provided a great opportunity to study the detector response and compare it to the predictions of the simulation. The interaction of cosmic muons with the material of the ATLAS detector produces in a very small fraction of cosmic ray events, high energy bremsstrahlung photons. It was possible to isolate these photons in data and compare their shower properties with the simulation of cosmic rays in ATLAS.

The shower shapes measured in the ATLAS calorimeter are sensitive to the amount of material crossed by the photon before it reaches the various layers of the calorimeter. Thus by comparing the shower shapes in data and simulation, one can test whether the material description of ATLAS in the simulation is correct or if it needs adjustment. Classes of photons were selected based on their approximate point of emission along the muon track. Photons produced in the top half or the lower half of the calorimeter could be studied separately as well as photons produced in the volume of the inner detector. For each class of photon the data and cosmic ray simulation are in good agreement. These results give confidence that the simulation already gives an accurate description of the material distribution in ATLAS and that the shower shape variables produced by the GEANT simulation of ATLAS can be relied on. Small discrepancies between data and the cosmic simulation were observed and the effect of such discrepancies on the H-matrix efficiency has been estimated. It appears that the effect of the observed discrepancies on the H-matrix efficiency is negligible.

One of the most important motivations for the construction of the highly performing ATLAS electromagnetic calorimeter is to be able to discover a low mass Higgs boson decaying into two isolated photons. This channel is very challenging due to small production rate, and it will only be possible to discover this signal once the ATLAS and the LHC have reached their design performance. The photon H-matrix developed in this thesis provides a powerful tool to reject the γ+jet and jet-jet backgrounds to the $H \rightarrow \gamma\gamma$ signal. With the upcoming data ATLAS will soon be possible to measure the photon identification performance in real data, complementing the studies that have been done using the bremsstrahlung photons from cosmic-ray muons in this thesis. The validation of the photon H-matrix should become possible in data with the $Z \rightarrow \mu\mu\gamma$ events well before the search for $H \rightarrow \gamma\gamma$ becomes statistically competitive.

APPENDIX A

ALGORITHM TO CALCULATE H-MATRIX χ^2

The algorithm of χ^2 claculation for photon is presented in this section. For electron case, same algorithm is used with different parameters, which are saved at TMatrix format.

A.0.1 Header File

```
#ifndef HMatrixPhoton_h
#define HMatrixPhoton_h

#include <TH2.h>
#include <TStyle.h>
#include <TFile.h>
#include <TH1F.h>
#include <TCanvas.h>
#include <TString.h>
#include <TMatrixD.h>
#include <iostream>

using namespace std;

class HMatrixPhoton {
  public :

   HMatrixPhoton();
  ~HMatrixPhoton();

  const int NHMvars;
  const int Netabins;
  const int Nebins;
  const int Npars;
```

```
  const int Nptbins;

  TString RootDir;

  TMatrixD *MeanPhotonArray      [7][12][2];
  TMatrixD *CovariantPhotonArray[7][12][2];

  TMatrixD AddTMatrix(TMatrixD & MatrixA, TMatrixD & MatrixB);

  Int_t    GetEtaBin(Float_t eta);
  Int_t    GetPtBin (Float_t pt);
  Int_t    GetEnergyBin(Double_t ene);
  Int_t    GetEnergyBin_BasedOnSinglegamma(Double_t ene);
  Double_t GetCutvalue(Float_t pt);

  // photon HM
  void     GetHMParameter();
  TMatrixD GetHMMean(Int_t etabin,Int_t enebin,Double_t en);
  Double_t GetHMChi2(Int_t etabin,Int_t ebin, Double_t ene, Double_t
      Hdel[14]);
  Double_t HmatrixPhoton(Double_t etot, Float_t eta, Double_t HMval[14])
      ;
  Double_t GetCutvaluePhoton(Float_t pt);

};

#endif // HMatrixPhoton.h
```

A.0.2 Source Code

```
#include <TH2.h>
#include <TStyle.h>
```

```
#include <TFile.h>
#include <TH1F.h>
#include <TCanvas.h>
#include <TString.h>
#include <TMatrixD.h>
#include <iostream>
#include ``HMatrixPhoton.h''

using namespace std;

HMatrixPhoton::HMatrixPhoton() : NHMvars(14), Netabins(12), Nebins(8),
    Npars(2), Nptbins(4)
{
  GetHMParameter();
}

HMatrixPhoton::~HMatrixPhoton()
{

}

void HMatrixPhoton::GetHMParameter()
{
  TString MatrixName;
  TString RootFile;
  RootFile = ``HM14photon_MeanMatrix_v0.root'';
  cout << ``mean para root = '' << RootFile<<endl;
  TFile* MeanPhotonFile = new TFile(RootFile,``READ''); //bassed on Mean

  for(Int_t iene=0;iene<Nebins-1;++iene)
  {
```

```
  for(Int_t ieta=0;ieta<Netabins; ++ieta)
  {
     MatrixName = ``HM_Mean_ebin'';
     MatrixName+=iene;
     MatrixName+=``_eta'';
     MatrixName+=ieta;
     MatrixName+=``_a'';
     MeanPhotonArray[iene][ieta][0]
              = (TMatrixD*)MeanPhotonFile->Get(MatrixName);

     MatrixName =``HM_Mean_ebin'';
     MatrixName+=iene;
     MatrixName+=``_eta'';
     MatrixName+=ieta;
     MatrixName+=``_b'';
     MeanPhotonArray[iene][ieta][1]
              = (TMatrixD*)MeanPhotonFile->Get(MatrixName);

     MatrixName =``HM_Mean_ebin'';
     MatrixName+=iene;
     MatrixName+=``_eta'';
     MatrixName+=ieta;
     MatrixName+=``_c'';
     MeanPhotonArray[iene][ieta][2]
              = (TMatrixD*)MeanPhotonFile->Get(MatrixName);
  }// ietabin
}// ienebin

RootFile = ``HM14photon_CovariantMatrix_v0.root'';
TFile* CovariantPhotonFile = new TFile(RootFile,``READ'');
```

```
  for(Int_t iene=0;iene<Nebins-1;++iene)
    {
      for(Int_t ieta=0;ieta<Netabins;++ieta)
        {
          MatrixName =``HMatrix_ebin'';
          MatrixName+=iene;
          MatrixName+=``_eta'';
          MatrixName+=ieta;
          MatrixName+=``_a'';

          CovariantPhotonArray[iene][ieta][0]
             = (TMatrixD*)CovariantPhotonFile->Get(MatrixName);

          MatrixName =``HMatrix_ebin'';
          MatrixName+=iene;
          MatrixName+=``_eta'';
          MatrixName+=ieta;
          MatrixName+=``_b'';

          CovariantPhotonArray[iene][ieta][1]
             = (TMatrixD*)CovariantPhotonFile->Get(MatrixName);
        }
    }
}

Int_t HMatrixPhoton::GetEtaBin(Float_t eta)
{
  Int_t bin;
  if(fabs(eta)>=0. && fabs(eta)<0.2) bin = 0;
  else if (fabs(eta)>=0.2 && fabs(eta)<0.4) bin = 1;
  else if (fabs(eta)>=0.4 && fabs(eta)<0.6) bin = 2;
```

```
  else if (fabs(eta)>=0.6 && fabs(eta)<0.8) bin = 3;
  else if (fabs(eta)>=0.8 && fabs(eta)<1.0) bin = 4;
  else if (fabs(eta)>=1.0 && fabs(eta)<1.2) bin = 5;
  else if (fabs(eta)>=1.2 && fabs(eta)<1.37)bin = 6;
  else if (fabs(eta)>=1.52 && fabs(eta)<1.8) bin = 7;
  else if (fabs(eta)>=1.8 && fabs(eta)<2.0) bin = 8;
  else if (fabs(eta)>=2.0 && fabs(eta)<2.2) bin = 9;
  else if (fabs(eta)>=2.2 && fabs(eta)<2.37) bin = 10;
  else if (fabs(eta)>=2.37 && fabs(eta)<2.47)bin = 11;
  else {bin = 12;}
  return bin;
}

Int_t HMatrixPhoton::GetEnergyBin(Double_t ene)
{
  Int_t bin;
  if(ene >460.129) bin = 0;
  else if(ene<=460.129 && ene >182.797) bin = 1;
  else if(ene<=182.797 && ene >90.6885) bin = 2;
  else if(ene<=90.6885 && ene >67.6994) bin = 3;
  else if(ene<=67.6994 && ene >44.4463) bin = 4;
  else if(ene<=44.4463 && ene >21.7713) bin = 5;
  else if(ene<=21.7713 && ene >8.66207) bin = 6;
  else bin =7;
  return bin;
}

Int_t HMatrixPhoton::GetPtBin(Float_t pt)
{
 Int_t bin;
  if(pt<=25) bin =0;
```

```
  else if(pt<=30) bin =1;
  else if(pt<=40) bin =2;
  else if(pt<=50) bin =3;
  else if(pt<=60) bin =4;
  else if(pt<=70) bin =5;
  else if(pt<=80) bin =6;
  else bin =7;
  return bin;
}

TMatrixD HMatrixPhoton::GetHMMean(Int_t etabin,
                          Int_t enebin, Double_t en)
{
  TMatrixD meanPara_a(1,14);
  TMatrixD meanPara_b(1,14);
  TMatrixD meanPara_c(1,14);
  TMatrixD Mean(1,14);

  for(int ivar=0; ivar<NHMvars; ++ivar)
  {
    if(ivar ==1 || ivar ==7 || ivar==8)
    {
      meanPara_a(0,ivar)
        = (*MeanPhotonArray[enebin][etabin][0])[0][ivar];
      meanPara_c(0,ivar)
        = (*MeanPhotonArray[enebin][etabin][1])[0][ivar];

      meanPara_a(0,ivar) *= en;  // a = a * energy
    }
    else
    {
```

```
      meanPara_a(0,ivar) = (*MeanPhotonArray[0][etabin][0])[0][ivar];
      meanPara_b(0,ivar) = (*MeanPhotonArray[0][etabin][1])[0][ivar];
      meanPara_c(0,ivar) = (*MeanPhotonArray[0][etabin][2])[0][ivar];
      if(ivar == 6)
      {
         meanPara_a(0,ivar)*= sqrt(en);
         meanPara_b(0,ivar)*= sqrt(1/en);
         meanPara_a(0,ivar) += meanPara_b(0,ivar);
      }
      else
      {
         meanPara_a(0,ivar)*= (1/en);
         meanPara_b(0,ivar)*= sqrt(1/en);
         meanPara_a(0,ivar) += meanPara_b(0,ivar);
      }

      Mean = AddTMatrix(meanPara_a, meanPara_c);  //mean = a + b;
    }
  return Mean;
}

Double_t HMatrixPhoton::GetHMChi2(Int_t etabin,
        Int_t ebin, Double_t ene, Double_t Hdel[NHMvars])
{
  double sum=0;
  double temp, det1;

  TMatrixD Mmatrix_a  (NHMvars,NHMvars);
  TMatrixD Mmatrix_b  (NHMvars,NHMvars);
  TMatrixD Mmatrix    (NHMvars,NHMvars);
  TMatrixD HM         (NHMvars,NHMvars);
```

```
TMatrixD Mmatrix13_a(NHMvars-1,NHMvars-1);
Mmatrix13_b(NHMvars-1,NHMvars-1);
TMatrixD Mmatrix13  (NHMvars-1,NHMvars-1);
TMatrixD HM13       (NHMvars-1,NHMvars-1);
TMatrixD Mmatrix9_a (NHMvars-5,NHMvars-5);
Mmatrix9_b (NHMvars-5,NHMvars-5);
TMatrixD Mmatrix9   (NHMvars-5,NHMvars-5);
TMatrixD HM9        (NHMvars-5,NHMvars-5);

// get parameter for given ebin and etabin
for(int irow=0; irow<NHMvars; ++irow)
  {
    for(int icolumn=0; icolumn<NHMvars; ++icolumn)
      {
        Mmatrix_a(irow,icolumn)
          = (*CovariantPhotonArray[ebin][etabin][0])[irow][icolumn];
        Mmatrix_b(irow,icolumn)
          = (*CovariantPhotonArray[ebin][etabin][1])[irow][icolumn];
      }
  }

Mmatrix_a *= ene;  // para_a = para_a * energy

// some values are not difined at certain etabins so dim of HM is
   reduced
if(etabin ==11)
  {
    for(int irow=0; irow<NHMvars-5; ++irow)
      {
        for(int icolumn=0; icolumn<NHMvars-5; ++icolumn)
          {
```

```
            Mmatrix9_a(irow,icolumn) = Mmatrix_a(irow,icolumn);
            Mmatrix9_b(irow,icolumn) = Mmatrix_b(irow,icolumn);
          }//icol
        }//irow

      Mmatrix9 = AddTMatrix(Mmatrix9_a, Mmatrix9_b);

      HM9=Mmatrix9;
      HM9.Invert(&det1);

      for(int irow=0; irow<NHMvars-5; ++irow)
        {
          for(int icolumn=0; icolumn<NHMvars-5; ++icolumn)
            {
              temp = Hdel[irow] *HM9(irow,icolumn) *Hdel[icolumn];
              sum += temp;
            }//icolumn
        }//irow

    }//eta12
  else if(etabin>7 && etabin<11)
    {
      for(int irow=0; irow<NHMvars-1; ++irow)
        {
          for(int icolumn=0; icolumn<NHMvars-1; ++icolumn)
            {
              Mmatrix13_a(irow,icolumn) = Mmatrix_a(irow,icolumn);
              Mmatrix13_b(irow,icolumn) = Mmatrix_b(irow,icolumn);
            }
        }
```

```
      Mmatrix13 = AddTMatrix(Mmatrix13_a, Mmatrix13_b);

      HM13=Mmatrix13;
      HM13.Invert(&det1);
      for(int irow=0; irow<NHMvars-1; ++irow)
        {
          for(int icolumn=0; icolumn<NHMvars-1; ++icolumn)
            {
              temp = Hdel[irow]*HM13(irow,icolumn) *Hdel[icolumn];
              sum += temp;
            }//icolumn
        }//irow

    }// eta10 to eta11
  else
    {
      Mmatrix = AddTMatrix(Mmatrix_a, Mmatrix_b);

      HM = Mmatrix;
      HM.Invert(&det1);

      for(int irow=0; irow<NHMvars; ++irow)
        {
          for(int icolumn=0; icolumn<NHMvars; ++icolumn)
            sum = sum  + Hdel[irow]*HM(irow,icolumn)*Hdel[icolumn];
        }
    } //eta 1 to eta 9

  return sum;
}
```

```
Double_t HMatrixPhoton::HmatrixPhoton(Double_t etot,
                                      Float_t eta, Double_t HMval[NHMvars])
{
  Double_t Hchi2, del[NHMvars];
  TMatrixD HMean(1,NHMvars);
  Int_t etabin,ebin;

  //determine index eta & energy
  etabin = GetEtaBin(eta);
  ebin = GetEnergyBin(etot);

  if(etabin !=12 && ebin !=7)
    {
      if(ebin == 6 && etabin > 7) Hchi2=999999999.;
      else
        {
          HMean = GetHMMean(etabin,ebin,etot);

          for(Int_t ivar=0; ivar<NHMvars; ++ivar)
            {
              if(HMval[ivar] <= -9999999.|| HMval[ivar] == -999.)
                 {     del[ivar]=0;     }
              else del[ivar] = HMval[ivar] - HMean(0,ivar);
            }
          //calculation of chi2
          Hchi2 = GetHMChi2(etabin,ebin,etot,del);
        }//
    }// not crack region
  else
    {
      Hchi2 = 999999999.;
```

```
    }
  return Hchi2;
}

TMatrixD HMatrixPhoton::AddTMatrix(TMatrixD & MatrixA,
                                   TMatrixD & MatrixB)
{
  if((MatrixA.GetNcols() != MatrixB.GetNcols()) ||
     (MatrixA.GetNrows() != MatrixB.GetNrows()))
    {
      cout << `` cannot add two Matrices '' <<endl;
    }

  TMatrixD MatrixSum(MatrixA.GetNrows(),MatrixA.GetNcols());
  for(int irow=0; irow<MatrixA.GetNrows(); ++irow)
    {
      for(int icol=0; icol<MatrixB.GetNcols(); ++icol)
        {
          MatrixSum(irow,icol) = MatrixA(irow,icol) + MatrixB(irow,icol)
              ;
        }//icol
    }//irow
  return MatrixSum;
}
```

APPENDIX B

ALGORITHM TO MEASURE PHOTON EMISSION POINT (R_γ)

In this appendix, the algorithm for R_γ calculatrion is presented.

B.1 R_γ Algorithm

```
void GetParameterOfLine(float d0, float phi, float para[2],
                        float point1[2], float point2[2])
{
  float _phi;
  float slope, Yintercept;

  if(phi<0) _phi = phi;
  else _phi = phi +PI;

  slope = TMath::Tan(_phi);
    Yintercept = d0/(TMath::Cos(_phi));

  para[0] = slope;                  para[1] = Yintercept;
  point1[0] = -Yintercept/slope;    point1[1] = 0;
  point2[0] = 0;                    point2[1] = Yintercept;
}

int GetParameterOfLine(bool newparameter, bool geterror,
                       float eta1, float eta2, float phi1, float phi2,
                       float para[4], float point1[2], float point2[2],
                       float radius[2])
{
  float radius1, radius2;
  float temp1, temp2, temp3, temp4;
  float x1, x2, y1, y2;
  float phoA, phoB, phi, _phi, d0;
```

```
float _phi1, _phi2;

if(eta1 == -999|| eta2 == -999 || phi1 == -999 || phi2 == -999)
{
  para[0] = -9999999; para[1] = -9999999;
  para[2] = -9999999; para[3] = -9999999;
  point1[0] = -9999999; point1[1] = -9999999;
  point2[0] = -9999999; point2[1] = -9999999;
  return 0;
}
else
{
  eta2 = fabs(eta2) ;
  eta1 = fabs(eta1) ;
  if(newparameter)
  {
    if(eta2 < 0.8)
    {
      radius2 = (1697.1 - 15.311*eta2 - 64.153*eta2*eta2);
      temp4 = (-15.311 - 64.153*eta2);
    }
    else
    {
      radius2 = (1739.1 - 75.648*eta2 - 18.501*eta2*eta2);
      temp4 = ( -75.648- 18.501*eta2);
    }
    if(eta1 < 0.8)
    {
      radius1 = (1567.8 - 18.975*eta1 - 17.668*eta1*eta1);
      temp3 = (-18.975 - 17.668*eta1);
    }
```

```
  else
  {
    radius1 = (1503.2 + 71.716*eta1 - 41.008*eta1*eta1);
    temp3 = (71.716 - 41.008*eta1);
  }
} // newparameter
else
{
// ========== optimise for csc ==========================
  radius2 = (1698.990944 - 49.431767*eta2 - 24.504976*eta2*eta2);
  temp4 = (- 49.431767 - 24.504976*eta2);
  if(eta1 < 0.8)
  {
    radius1 = (1558.859292 - 4.990838*eta1 - 21.144279*eta1*eta1);
    temp3 = (- 4.990838 - 21.144279*eta1);
  }
  else
  {
    radius1 = (1522.775373 + 27.970192*eta1 - 21.104108*eta1*eta1);
    temp3 = (27.970192 - 21.104108*eta1);
  }
}//oldparameter

if(phi1>0) _phi1 = phi1-PI;
else _phi1 = phi1;
if(phi2>0) _phi2 = phi2-PI;
else _phi2 = phi2;

radius[0] = radius1, radius[1] = radius2;
x1 = radius1*TMath::Cos(phi1); y1 = radius1*TMath::Sin(phi1);
x2 = radius2*TMath::Cos(phi2); y2 = radius2*TMath::Sin(phi2);
```

```
    phoA = (y1-y2)/(x1-x2);
    phoB = ((x1*y2)-(x2*y1))/(x1-x2);
    phi = TMath::ATan(phoA);

    if(phi1>0 && phi<0) _phi = PI + phi;
    else if(phi1<0 && phi>0) _phi = -PI + phi;
    else _phi = phi;

    if(((phi1>=-PI/2||phi1<=-PI) || (phi2>=-PI/2 && phi2<=-PI) || (_phi
        <=-PI/4))
       && ((phi1>=0||phi1<=-PI/2) || (phi2>=0 && phi2<=-PI/2) || (phi
           >=-(3*PI)/4)))
    {
       d0 = (phoB/phoA) * TMath::Sin(_phi);
       para[2] = _phi;    para[3] = d0;
    }
    else
    {
      para[2] = -9999999;    para[3] = -9999999;
    }
    point1[0] = x1;    point1[1] = y1;
    point2[0] = x2;    point2[1] = y2;
    para[0] = phoA;    para[1] = phoB;

    return 1;
  }
}
```

```
int GetRgamma(bool newparameter, float mud0, float muphi, float eta1,
    float eta2,
                float eta3, float phi1, float phi2, float phi3,
                float e[3] , float & xgamma, float  & ygamma, float  &
                    radius,
                float phox[2], float phoy[2], float mux[2], float muy[2],
                    float Para[6])
{
  float mupara[2], phopara[4], Error[2];
  float NewX, NewY, phoA, phoB, muA, muB;
  int isget;
  float point1[2], point2[2], R[2];

  GetParameterOfLine(true, mud0, muphi, mupara, point1, point2);
  mux[0] = point1[0]; muy[0] = point1[1];
  mux[1] = point2[0]; muy[1] = point2[1];
  muA = mupara[0];     muB =  mupara[1];

  isget = GetParameterOfLine(newparameter, true, eta1, eta2, phi1, phi2,
                                phopara, point1, point2, R, Error);
  phoA = phopara[0];   phoB = phopara[1];
  phox[0] = point1[0]; phoy[0] = point1[1];
  phox[1] = point2[0]; phoy[1] = point2[1];

  // parameter
  // slope and Yintercept of muon
  Para[0] = mupara[0];   Para[1] = mupara[1];
  //slope and Yintercept of photon
  Para[2] = phopara[0]; Para[3] = phopara[1];
```

```
// phi and d0 of photon
Para[4] = phopara[2]; Para[5] = phopara[3];
// deltaphi(phi1, phi2) & deltaphi(eta1,eta2)
//Para[6] = Error[0]; Para[7] = Error[1];

if(e[0]>200)
{
  if(e[0]>e[2])
  {
     NewX = -(muB-phoB)/(muA-phoA); NewY = (muA*phoB - muB*phoA)/(muA-
         phoA);

     xgamma = NewX;
     ygamma = NewY;

     radius = sqrt(NewX*NewX + NewY*NewY);

     if(ygamma>0 && point1[1]<0 )
     {
        if(ygamma>point1[1]) return 1;
        else return -1;
     }
     else if(ygamma<0 && point1[1]<0)
     {
       if(radius<R[0]) return 1;
       return -1;
     }
     else if(ygamma>0 && point1[1]>0)
     {
       if(radius<R[1]) return 1;
       return -1;
```

```
        }
        else return -1;
      }//e1>e3
      else {radius = -999; return 0;}
    }//e1 > 200MeV
    else {radius = -999; return 0; }

}//
```

REFERENCES

[1] G. Abbiendi et al. Phys. Lett. **B 565** (2003) 61.

[2] B. W. Lee et al. Phys. Rev. Lett. **38** (1977) 883.

[3] M. Quiros, Constraints on the Higgs boson properties from the effective potential hep-ph/9703412.

[4] A. Ghinculov and T. Binoth Acta Phys **B30** (1999) 99.

[5] S. Weinberg Phys. Rev. Lett. **19** (1967) 1264.

[6] S. L. Glashow Nucl. Phys. **22** (1961) 579.

[7] J. I. S. L. Glashow and L. Maiani Phys. Rev. **D** (1970) 1285.

[8] R. C. Fernow, *Introduction to experimental particle physics*. Cambridge University Press, New York, 1986.

[9] D. Griffiths, *Introduction to Elementary Particles*. Wiley-VCH, Weinheim, 1987.

[10] J. Zinn-Justin, *Quantum Field Theory and Critical Phenomena*. Oxford University Press, 2002.

[11] V. Pasquier, *From Perturbative to Constructive Renormalization*. Princeton University Press, 2002.

[12] R. P. Feynman, *Quantum Electrodynamics*. Westview Press, 1998.

[13] Addison-Wesley, ed., *Gauge theories of the strong, weak, and electromagnetic interactions*. Addison Wesley Publishing Company, 1997.

[14] Addison-Wesley, ed., *Foundations Of Quantum Chromodynamics: An Introduction to Perturbative Methods in Gauge Theories*. World Scientific Publishing Company, 1998.

[15] A. Salam, *Elementary Particle Theory*. Almquist and Wiksell, Stockholm, 1968.

[16] C. A. et al., *The review of particle physics*, Phys. Lett. **B 667** (2008) .

[17] LEP Electroweak Working Group web page: http://lepewwg.web.cern.ch/LEPEWWG/.

[18] W.-M. Yao et al. J. Phys. **G 33** (2006) 1.

[19] P. Higgs Phys. Rev. Lett. **12** (1964) 132–134.

[20] P. Higgs Phys. Rev. Lett. **13** (1964) 508–509.

[21] F.Englert and R.Brout Phys. Rev. Lett. **13** (1964) 321–323.

[22] G. Guralnik, C. R. Hagen and T. W. B. Kibble Phys. Rev. Let. **13** (1964) 585–87.

[23] T. W. B. Kibble Phys. Rev. Let. **155** (1967) 1554–1561.

[24] P. Publishing, ed., *The Higgs Hunter Guide*. Cambridge, 2000.

[25] N. Cabibo, L. Maiani, G. Parisi and R. Petronzio Nucl. Phys. **B 158** (1979) 295.

[26] R. A. Flores and M. Sher Phys. Rev. **D 27** (1983) 1679.

[27] M. Lindner Z. Phys. **C 31** (1986) 273.

[28] M. Sher Phys. Rept. **179** (1989) 273.

[29] T. Hambye and K. Riesselmann Phys. Rev. **D 55** (1997) 7255.

[30] G. Altarelli and G. Isidori Phys. Lett. **B 337** (1994) 141.

[31] J. A. Casas, J. R. Espinosa and M. Quiros Phys. Lett. **B 342** (1995) 171.

[32] K. Riesselmann, Limitations of a Standard Model Higgs Boson hep-ph/9711456, 1977.

[33] page: http://sl-div.web.cern.ch/sl-div/.

[34] Fermi National Accelerator Laboratory http://www.fnal.gov.

[35] T.Appelquist and C.Bernard Phys. Rev. **D 22** (1980) 200.

[36] The ALEPH, CDF, D0, DELPHI, L3, OPAL, SLD Collaborations, the LEP Electroweak Working Group, the Tevatron Electroweak Working Group, and the SLD Electroweak and Heavy Flavour Group, *Precision Electroweak Measurements and Constraints on the Standard Model*, 2009. `hep-ex/0911.2604`.

[37] M. Spira and P. M. Zerwas, *Electroweak Symmetry Breaking and Higgs Physics*, 1997. `hep-ex/9803257`.

[38] M. Spira Nucl. Instrum. Meth. **A 389** (1997) 357–360.

[39] M. Benedikt et al., *The Large Hadron Collider, Conceptual Design*, Tech. Rep. CERN-AC-95-05, 1995.

[40] ATLAS Collaboration, *ATLAS : technical proposal for a general-purpose pp experiment at the Large Hadron Collider at CERN*, Report, CERN-LHCC-94-43, 1994.

[41] CMS collaboration Collaboration, *CMS, the Compact Muon Solenoid : technical proposal*, Tech. Rep. CERN-LHCC-94-38, 1994.

[42] ALICE collaboration Collaboration, *ALICE : Technical proposal for a Large Ion collider Experiment at the CERN LHC*, Tech. Rep. CERN-LHCC-95-71, 1995.

[43] LHCb collaboration Collaboration, *LHCb: Technical proposal for a Large Ion collider Experiment at the CERN LHC*, Tech. Rep. CERN-LHCC-98-4, 1998.

[44] ATLAS Collaboration, *Detector and Physics Performance Technical Design Report*, Tech. Rep. CERN-LHCC-99-14, 1997.

[45] ATLAS Collaboration, *Liquid Argon Calorimeter Technical Design*, Tech. Rep. CERN-LHCC-96-41, 1996.

[46] ATLAS Collaboration, *Tile Calorimeter Technical Design*, Tech. Rep. CERN-LHCC-96-42, 1996.

[47] ATLAS Collaboration, *Pixel Detector Technical Design*, Tech. Rep. CERN-LHCC-98-13, 1998.

[48] ATLAS Collaboration, *Inner Detector Technical Design*, Tech. Rep. CERN-LHCC-97-16, 1997.

[49] ATLAS Collaboration, *Muon Spectrometer Technical Design*, Tech. Rep. CERN-LHCC-97-22, 1997.

[50] A. Yamamoto et al., *The ATLAS central solenoid*, NIM **A 584** (2008) 53.

[51] ATLAS Collaboration, *Central solenoid toroid Technical Design Report*, Tech. Rep. CERN-LHCC-97-021, 1997.

[52] ATLAS Collaboration, *Barrel toroid Technical Design Report*, Tech. Rep. CERN-LHCC-97-019, 1997.

[53] ATLAS Collaboration, *End-cap toroid Technical Design Report*, Tech. Rep. CERN-LHCC-97-020, 1997.

[54] R. Wigmans., *Calorimetry Energy Measurement in Particle Physics*. Oxford University Press, 2000.

[55] W. Christian NIM **75(4)** (2003) 1243–1286.

[56] S. M. Seltzer and M. J. Berger Int. J. of Applied Rad **33** (1982) 1189.

[57] S. M. Seltzer and M. J. Berger Int. J. of Applied Rad **35** (1984) 665.

[58] J. C. et al NIM **A 550** (2005) 96–115.

[59] M. A. et al., *Energy linearity and resolution of the ATLAS electromagnetic barrel calorimeter in an electron test-beam*, NIM **A 568** (2006) 601–623.

[60] R. W. et al. NIM **A 487** (2002) 621–628.

[61] R. W. et al. NIM **A 409** (1998) 621–628.

[62] ATLAS Collaboration, *ATLAS computing Technical Design Report*, Tech. Rep. CERN-LHCC-2005-22, 2005.

[63] S. A. et al., *Geant4: A simulation toolkit*, **A506** (2003) 250–303.

[64] J. et al., *Geant4 developments and applications*, IEEE Transaction on Nuclear Science **53(1)** (2006) 270–278.

[65] T. Sjostrand, S. Mrenna, and P. Skands, *A brief introduction to PYTHIA 8.1.*, Comput. Phys. Commun. **178** (2008) .

[66] T. Sjostrand, S. Mrenna, and P. Skands, *PYTHIA 6.4 physics and manual*, JHEP **05** (2006) 026.

[67] The PythiaB manual.

[68] M. M. et al. JHEP **07** (2003) 001.

[69] G. C. et al, HERWIG 6.5 release note hep-ph/0210213.

[70] J. F. J. Butterworth and M. Seymour Z. Phys **C72** (1996) 637–646.

[71] G. C. et al. ZHEP **01** (2001) 010.

[72] S. Frixione and R. B. Webber, The MC@NLO 3.2 event generator hep-ph/0601192.

[73] S. Frixione and R. B. Webber JHEP **06** (2002) 029.

[74] Z. Marshall, *The ATLAS simulation software*, Tech. Rep. ATL-SOFT-PROC-2008-001, 2008.

[75] ATLAS Collaboration, *The ATLAS experiment at the CERN Large Hadron Collider*, JINST **3** (2008) .

[76] ATLAS Collaboration, *Expected performance of the ATLAS experiment: detector, trigger and physics*, Tech. Rep. CERN-OPEN-2008-020, 2009.

[77] R. A. Fisher Annals Eugenics **7** (1936) 179.

[78] P. Mahalanobis Proc. Nat. Inst. Sci. India **2A** (1936) 49.

[79] P. C. Bhat, *Search for the Top Quark at D0 using Multivariate Methods*, AIPConf.Proc **357** (1996) 308–319.

[80] ATLAS Collaboration, *Expected performance of the ATLAS experiment: Electrons and Photons*, Tech. Rep. CERN-OPEN-2008-020, 2009.

[81] M. Wielers, *Photon identification with the Atlas detector*, .

[82] W. Lampl, The LAr EM Scale: From ADC counts to a calibrated energy measurement available at: http://esmane.physics.lsa.umich.edu/wl/atlas/meetings/2007/physics-americas/20070822-umwlcd0011-02/real/f001.htm, 2007.

[83] T. Binoth and the others JHEP **12** (2006) 046.

[84] J. M. Butterworth, J. R. Forshaw and M. H. Seymour, *Multiparton Interactions in Photoproduction at HERA*, Z. Phys. **C 72** (1996) 637 (hep–ph/9601371).

[85] ATLAS Collaboration, Expected Performance of the ATLAS Experiment CERN-OPEN-2008-020.

[86] CDF Collaboration, D. E. A. et al. Phys. Rev. Lett. **94** (2005) 091803.

[87] DØ Collaboration, V. A. et al. Phys. Rev. D **76** (2007) 012003.

[88] ATLAS Collaboration, Observation of $W \to \ell\nu$ and $Z \to \ell\ell$ production in proton-proton collisions at $\sqrt{s} = 7$ TeV with the ATLAS detector ATLAS Conference note, ATLAS-CONF-2010-044, available at: https://atlas.web.cern.ch/Atlas/GROUPS/PHYSICS/CONFNOTES/ATLAS-CONF-2010-044/.

[89] E. Richter-Was, D. Froidevaux and L. Poggioli, *Froidevaux and L. Poggioli, ATLFAST2.0 a Fast Simulation package for ATLAS*, Tech. Rep. ATL-PHYS-98-131, 2007.

[90] C. Balazs and C.-P. Yuan Phys. Lett **B 478** (2000) 192.

[91] C. Balazs, J. Huston and I. Puljak Phys. Rev. **D 63** (2001) 014021.

[92] S. Corcella et al. JHEP **0307** (2003) 028.

[93] ATLAS Collaboration, *Expected performance of the ATLAS experiment: Higgs Boson*, Tech. Rep. CERN-OPEN-2008-020, 2009.

[94] G. Bozzi, *IFAE 2006 : QCD corrections to Higgs physics at the LHC.* Springer Milan, 2007.

[95] T. Binoth, J.P. Guillet, E.Pilon and M. Werlen Eur.Phys.J. **C16** (2000) .

[96] C. Balazs and C.P. Yuan Phys.Rev. **D56** (1997) .

[97] P. Nadolsky, C. Balazs, Edmond L. Berger, C.-P. Yuan Phys. Rev. **D76** (20007) .

[98] S. Catani et al. HEP. **0205** (2002) .

[99] P. Bernat, L. Fayard, M. Kado and F. Polci, *Normalization of the γ-jet background to the $H \to \gamma\gamma$ inclusive analysis*, Tech. Rep. ATL-COM-PHYS-2009, 2009.

[100] Z. Nagy Phys. Rev. Lett. **88** (2002) .

[101] Zoltan Nagy and Zoltan Trocsanyi Phys. Rev. Lett. **87** (2001) .

[102] L. Fayard and G. Unal, *Search for Higgs decay into photons with EAGLE*, Tech. Rep. PHYS-NO-001, 1998.

BIOGRAPHICAL STATEMENT

Hyeon Jin Kim was born in Kimhae, Republic of Korea, in 1968. She received her B.S and M.S. degrees from Gyeonsang National University, Republic of Korea, in 1990, majoring physics and in 1998, majoring elementary particle physics, repectively. From 1998 to 2002, she was with the department of Physics, Gyeongsang National University as an Instructor. She got addimission in University of Texas at Arlington in 2003 for graduate stuy and in 2005 she completed the requirements for Ph.D. She carried out her doctoral research at CERN in Geneva, Switzerland, and graduated with a Ph.D. in Physics from UTA in the summer of 2010. She looks forward to a successful research career as a physicist.